Faculty of Science and Engineering

Department of Imaging and Applied Physics

Hydrogen Storage Studies of Mesoporous and Titanium Based Materials

Drew A Sheppard

This thesis is presented for the Degree of
Doctor of Philosophy
of
Curtin University of Technology

July 2008

Declaration

This thesis contains no material which has been accepted for the award of any other degree or diploma in any university.

To the best of my knowledge and belief this thesis contains no material previously published by any other person except where due acknowledgement has been made.

Signature:

Date:

Acknowledgements

Firstly, I wish to thank my supervisor, Prof. Craig Buckley for his guidance that he has given to me throughout the duration of this thesis. His door has always been open to me.

A special thankyou must go to Annie. Her help, patience and understanding put my feet on the path needed to finish this thesis. I am indebted to her.

I must also extend a very large thank you to Glen Lawson, the Senior Scientific Officer and Technical Manager for the Department of Imaging and Applied Physics. When ever I had a question or needed help with advice on anything from chemical safety to equipment access to anything associated with working in a research laboratory environment, Glen was happy to help.

I'd also like to thank all the staff in the Department of Imaging and Applied Physics who have helped me over the years but I must make special mention of Carmel McManus, Dr. Nigel Kirby, Dr. Rob Hart and Mark Paskevicius.

I must also thank the Australian Government for the receipt of an Australian Postgraduate Research Award (APRA) and and the Australian Institute of Nuclear Science and Engineering (AINSE) for a Postgraduate Research Award (PGRA) during the course of my Ph.D.

Abstract

Concerns over green house gas emissions and their climate change effects have lead to a concerted effort into environmental friendly technologies. One such emphasis has been on the implementation of the hydrogen economy. There are four major impediments to the implementation of a hydrogen economy: hydrogen production, distribution, storage and conversion. This thesis is focused on exploring the hydrogen storage problem.

Hydrogen can be stored by a wide range of methods. One of these methods involves using a secondary material that stores hydrogen by either physisorbing hydrogen onto its surfaces or by reacting with it to form a new compound. Of the wide variety of materials that can interact with hydrogen, three different materials were chosen; (1) nano-structured materials of high surface area; mesoporous silica (MCM-41) and titanate nanotubes, and (2) hydrides of Ti-Mg-Ni alloys.

Results of the hydrogen on mesoporous silica (MCM-41) showed 1 wt.% H_2 to a maximum of 2 wt.% H_2 for 500 to 1060 m^2/g surface area, respectively, at 77 K. Doping these samples with Al or Zn did not make an appreciable difference but rather they reduced the surface area available for hydrogen adsorption. Adorption of hydrogen at room temperature was neglifible (0.1 wt.% up to an equilibrium pressure of 5 MPa).

Sodium titanate nanotubes showed hydrogen adsorption that increased with increasing hydrogen pressure at 77 K. Hydrogen adsorption reached 0.4 wt.% at an hydrogen equilibrium pressure of 2.6 MPa. Exchange of sodium ions in the titanate nanotubes with Zn and Li did not have an impact on hydrogen adsorption. However, partial substitution of Na ions for H ions resulted in an increase in hydrogen adsorption from 0.4 wt.% to 0.8 wt.% while decreasing the pressure required for maximum hydrogen uptake from 2.6 MPa to 0.5 MPa at 77 K. Desorption from this sample also showed strong hysteresis indicating hydrogen adsorption into the interlayer spacing of the

nanotube wall. Hydrogen adsorption at room temperature was negligible for all samples being below 0.1 wt.%, up to a hydrogen equilibrium pressure of 5 MPa.

Ti-Mg-Ni alloys are interest as 11 wt.% hydrogen has been reported in the literature; specifically for $Ti_{53}Mg_{47}Ni_{20}$. Samples with various stoichiometries of Ti, Mg and Ni were produced via balling and their hydrogen sorption properties examined. Measured hydrogen absorption ranged from 2.5 wt.% to 5.0 wt.%. Measurements were hindered by the high temperature (723 K) used during the activation process. The high temperature ensured decomposition of titanium hydride but resulted in the vaporisation and deposition of magnesium on the sample cell filter. This had the duel effect of reducing the total hydrogen absorption and to sporadically block the sample cell filter. However, in those cases where the hydrogen flow was not impeded, absorption kinetics were measured to be extremely rapid. For example, greater than 95 % of the total hydrogen uptake of 3.7 wt.% for the sample ball-milled in the molar ratio of 65:133:20 (Ti:Mg:Ni) occurred within 60 seconds at room temperature. However, the low equilibrium pressure meant a negligible amount of hydrogen could be desorbed at this temperature. X-ray diffraction revealed that after hydriding, the samples comprised varius mixtures of MgH_2, TiH_2 and hydrides of the intermetallic compounds Mg_2Ni and Ti_2Ni. The amount of each of these hydride phases changed according the intial starting stoichiometries of each sample.

List of Abbreviations

XRD	X-ray diffraction
TEM	Transmission electron microscopy
SEM	Scanning electron microscopy
MOF	Metal organic framework
DOE	(U. S.) Department of Energy
INS	Inelastic neutron scattering
PCT	Pressure-composition-temperature
H/M	Hydrogen to metal ratio
PEM	Proton exchange membrane
NPT	National pipe-thread tapered – a standard tapered thread used to join pipes and fittings
EOS	Equation of state
PDF	Powder Diffraction File
NIST	National Institute of Standards and Technology
FOM	Figure of merit
HSRG	Hydrogen Storage Research Group
CSIRO	Commonwealth Scientific and Industrial Research Organisation
NHMA	National Hydrogen Materials Alliance
GCMC	Grand Canonical Monte Carlo
GULP	General Utility Lattice Program
NRI	Nanochemistry Research Institute
SAXS	Small angle X-ray scattering
NMR	Nuclear magnetic resonance
CTAB	Cetyltrimethylammonium bromide
DTAB	Decyltrimethylammonium bromide
ANSTO	Australian Nuclear Science and Technology Organisation
BJH	Barret – Joyner – Halenda
KJS	Kruk – Jaroniec – Sayari
LED	Light emitting diode
FTIR	Fourier transform infra red
TPD	Temperature programmed desorption
BET	Brunauer – Emmett – Teller
BTP	Ball to powder
DSC	Differential scanning calorimetry
HIMA	Hydrogen induced mechanical alloying
EDS	Energy dispersive spectroscopy

Table of Contents

List of Figures

List of Tables

1. The Hydrogen Storage Problem

1.1. Introduction

Large-scale mining, transportation, processing and usage of fossil fuels and the associated pollution and environmental problems are the driving forces behind research into alternative energy carriers for use with automobiles[1].

Hydrogen is the ideal energy source. Hydrogen contains more chemical energy per weight than any hydrocarbon fuel. It can be used in a fuel cell or carefully burnt in an internal combustion engine to produce water as the only emission[2]. Given the concern over environmental pollution and the diminishing reserves of hydrocarbons, hydrogen would make the ideal replacement. Production of hydrogen is also a straight-forward process from renewable energy such as hydroelectricity, wind, solar and geothermal sources – with water being the only necessary starting material.

While hydrogen has many advantages, there are a number of hurdles that need to be overcome before a hydrogen economy becomes a reality. The four main challenges to overcome are production, delivery, storage and conversion. This thesis is concerned with examining the hydrogen storage problem.

A fuel cell powered car would require approximately 4 kg of hydrogen to have a 400 km driving range[2]. At room temperature and atmospheric pressure, 4 kg of hydrogen takes up 45 m^3 and so a suitable means of storing hydrogen is a must. There are a number of possible ways to store hydrogen including: compression, liquefaction, adsorption in porous materials, interstitial absorption by metal hydrides and as a complex hydride[3]. Currently none of these methods meet all the efficiency, size, weight, cost, safety and operating conditions required for use in the transportation industry.

1.1.1. Hydrogen Storage Targets – DOE FreedomCar Goals

The United States Department of Energy has set forth a timeline for a number of specifications required for a hydrogen based vehicle to be viable on a large scale.

These specifications relate to both scientific and consumer orientated goals. In summary though, the 2010 targets require the storage system to store 6 wt.% of hydrogen and 9 wt.% by 2015. Volumetric density must reach 45 kg/m^3 by 2010 and 81 kg/m^3 by 2015. As well as these specifications, the storage system must also be able to operate at near ambient temperature (233 – 333 K) and pressure (< 10 MPa). Other considerations include rapid refuelling (3 - 5 minutes), long cyclically stability (1500 cycles) and cost competitiveness with current fuels[4].

1.2. Hydrogen Storage Methods

1.2.1. Liquid Hydrogen

Liquid hydrogen is stored in cryogenic tanks at ~21 K. It has the advantage of high gravimetric capacity (100 wt.% of H_2) and high volumetric density (~71 kg/m^3). It is also a proven technology and has been used in the space industry for many years. There are two main drawbacks to liquid hydrogen. The first is losses due to evaporation while the second is the large amount of energy required for liquefaction. Because of hydrogen's low critical temperature it must be stored in an open container and vented to avoid a large pressure build up[3]. This results in boil-off of hydrogen during periods of vehicle dormancy[5]. Inevitable heat flow from the external environment induces boil-off of hydrogen in a variety of ways while sloshing of the hydrogen (as would occur in vehicular applications) also contributes to boil-off[6]. The boil off rate due to heat leakage is strongly dependent on the surface to volume ratio of the tank. For large cryogenic tanks, this boil off rate may be as low as 0.06% per day for large 20 000 m^3 tanks [3]. Aceves et al.[5] have claimed that complete boil off of liquefied hydrogen can occur in as little as 16 days regardless of the driving conditions (corresponding to 6% loss per day). More recently, information from BMW [2] has suggested that this loss can be reduced to as little as 1.5% per day while the addition of a recooling system can reduce this further to 0.3% per day[7]. In addition to these losses, evaporation losses can also occur during refilling due to necessary cooling of any connecting hoses to the fuel tank[5].

The theoretical energy required to liquefy hydrogen is 14.3 MJ/kg but is complicated by a number of factors. Hydrogen must first be cooled to below 202 K with liquid nitrogen before successive expansion-cooling cycles finally results in liquid hydrogen.

Hydrogen also has two different nuclear spin arrangements; orthohydrogen and the lower energy parahydrogen, with the relative amount of each being temperature dependent. At low temperature the parahydrogen form dominates and the spontaneous conversion from ortho- to parahydrogen is exothermic[8] releasing more energy than the latent heat of vaporisation of hydrogen[9]. The result of all this that the actual energy required to liquefy hydrogen is more than 2.5 times greater than the theoretical value[10] corresponding to as much as 30% of the energy contained within the hydrogen.

1.2.2. Compressed Gas

Since hydrogen is the lightest molecule known, it raises unique issues not present in the compression and storage of other gases. Its small size means that it readily diffuses through gaps in the seals of a storage vessel and directly through solid materials.

Storage of hydrogen as a gas phase has a long history. Aluminium and stainless steel tanks that can store hydrogen up to pressures of 25 MPa are commercially available. But because of hydrogen's low density the energy density of these tanks is quite low. More recently though, Dynetek Industries Ltd have developed composite tanks for transport applications with working pressures up to 70 MPa [3], which have a two to four-fold weight saving as compared to conventional tanks. These 70 MPa ambient temperature tanks can store 3.9 mass% of hydrogen at a volumetric density of 36 kg m^{-3}.

One recent publication has cast doubt on compressed hydrogen gas ever being viable for vehicle use, at least at ambient temperature[11]. Even considering an infinitely strong and infinitely light material, a working pressure of 255 MPa would be required to meet the 2015 DOE targets for mass% and volumetric density. The only other means of increasing the mass% and volumetric density is to cool the hydrogen[11,12]. While reducing the operating temperature adds complexity to the system, an empty tank at 150 K holds twice as much hydrogen as one at 300 K and a tank at 77 K holds almost 4 times as much as one at 300 K. Based on calculations of various hydrogen tank scenarios, Aceves and Berry[5] concluded that low temperature (80 K) pressure

vessels (25 MPa) showed substantial promise as compared to liquid hydrogen and ambient compression technologies. One large advantage of compressed and cooled hydrogen over liquid hydrogen is that the fuel tanks retain up to 1/3 of their hydrogen even if warmed to ambient temperatures. The result is that periods of vehicle dormancy will not leave the car without fuel. This method of cooling pressurised tanks is currently being examined by Dynetek[13] for their very high pressure tanks.

1.2.3. Adsorption on Porous Solids

Hydrogen molecules can interact with the atoms of a surface through dispersive forces known as physisorption. Due to its weak nature, significant physisorption is only observed at temperatures below 273 K [3]. In physisorption, a monolayer of adsorbate may form on the adsorbent with which molecules in the gas phase can subsequently interact with. To maximise their interaction with hydrogen, materials with a high surface area are desired. In addition to this, materials with sufficiently small pores results in an increased strength of interaction due to the overlap of potentials from walls on opposite sides of the pore. To this end, a number of porous materials have been explored for their possible use as a hydrogen storage medium. These include activated carbon, carbon nanotubes, zeolites and metal organic framework materials.

When considering hydrogen adsorption on porous materials, a number of terms need to first be defined before the suitability of a material can be evaluated. Excess adsorption is defined as the amount of hydrogen adsorbed on a sample in excess of the hydrogen that would be there due to the hydrogen gas pressure alone. Total adsorption (also often referred to as gravimetric adsorption) is defined as the hydrogen contained within an adsorbent, which is there due to compression and the hydrogen that is present as excess adsorption. Adsorption enthalpy, or heat of adsorption, is a measure of the strength of interaction between the hydrogen molecule and the adsorbent substrate. For hydrogen interacting with activated carbon, this value has been measured to be in the range of 4 – 6.5 $kJmol^{-1}$ [14,15]. The adsorption enthalpy is an important factor when considering hydrogen adsorption on porous materials as the stronger the interaction, the higher the temperature at which an adsorbent can retain hydrogen. Simulations suggest that an adsorbent with a heat of adsorption of ~15 $kJmol^{-1}$ [16] would be suitable for room temperature operation.

1.2.3.1. Carbon Based Adsorbents

Carbon forms a rich variety of compounds and a variety of porous carbon variants have been examined for hydrogen adsorption including activated carbon, carbon nanotubes, and carbon aerogels.

Activated carbons are comprised of micropores (< 2 nm) with surface areas generally larger than 1000 m^2/g and as high as 2800 m^2/g [14]. They are made from a wide range of source materials including coal, peat, petroleum-based residues, coconut shells, fruit stones, nut shells and wood to name but a few[17, 18]. There are two main production routes for activated carbon. The first production method involves carbonizing the raw material at temperatures of up to 873 K (600^{o}C) followed by activation by an oxidising agent such as steam or carbon dioxide[17]. The second method uses pyrolysis followed by impregnation with chemicals such as potassium hydroxide or phosphoric acid before activation at high temperatures (1073 – 1173 K) [18].

Activated carbon has been considered as a hydrogen storage candidate since the 1960's [19]. Due to the weak interaction between activated carbon and hydrogen, the amount adsorbed is highly temperature dependent[14] with storage densities of practical interest only occuring at low temperatures. This is illustrated by Figure 1-1 for a sample of activated carbon, AX-21, which shows the change in hydrogen uptake as a function of temperature. At 77 K excess hydrogen sorption for activated carbons generally range between 2.2 wt.%[19] and 5 wt.%[14] with the peak adsorption usually occurring in the pressure range of 3 to 4 MPa[14,20,21].

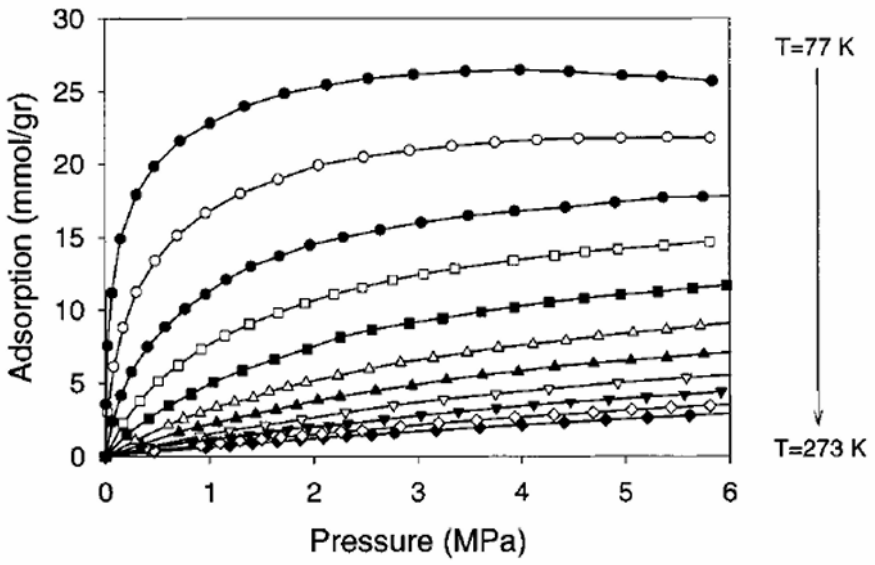

Figure 1-1: Adsorption isotherms of hydrogen on activated carbon at 77 K and covering the range 93 – 273 K separated by 20 K intervals. Reprinted with permission from [14]. Copyright 2001 American Chemical Society.

Despite the disadvantage of working at 77 K, arguments have been made that hydrogen tanks cooled with liquid nitrogen and filled with pelletized activated carbon, which can volumetrically store 41 gl^{-1} and gravimetrically store 5.7 wt.% of hydrogen, could be viable for mobile applications[21].

Hydrogen uptake at room temperature is less encouraging[22] and simulations[23] have shown that even optimisation of the pore size will result in excess adsorption of only 0.9 wt% and a volumetric density of just 14 kgm^{-3} at a temperature of 300 K and a pressure of 10 MPa.

Carbon aerogels are comprised of mesopores, tailorable mass densities, continuous porosities, and high surface area. These materials are synthesized by the sol-gel polymerization of resorcinol with formaheldahyde in aqueous solution to produce an organic gel. This gel is subsequently supercritically dried and pyrolysed in an inert atmosphere followed by activation with CO_2 at 1223 K (950^oC)[24]. This final activation process introduces microporosity and a consequent increase in the surface area. The ultimate surface area is dependent on activation time and can reach as high as 3200 m^2/g [24].

Activated carbon aerogels as well as metal doped carbon aerogels have recently been examined for their hydrogen storage properties[24]. They found that, similar to activated carbon, the amount of hydrogen uptake was proportional to the surface area and measured a maximum of 5.3 wt.% hydrogen uptake at 3.5 MPa and 77 K. Nickel was incorporated into the carbon aerogels and its effect on hydrogen uptake was monitored as a function of the carbonization temperature. Despite having a lower surface area, the low carbonization temperature sample resulted in a sample with increased hydrogen uptake as compared to the high temperature carbonized sample. The low temperature carbonisation was believed to result in more accessible metal sites that lead to increased hydrogen uptake via the hydrogen spillover effect[25]. These metal doped samples also yielded a higher hydrogen enthalpy of adsorption than the undoped samples (~7 $kJ.mol^{-1}$), but the introduction of the metal particles resulted in a substantial reduction in the surface area (from 3200 m^2/g to ~1000 m^2/g).

Single walled carbon nanotubes consist of a sheet of graphene rolled up to form a seamless cylinder and have been considered for hydrogen storage. Their cylindrical geometry leads to the potentials from the carbon atoms in the walls combining to produce a deeper potential well in the centre. Theoretical calculations have shown that this potential well inside the nanotubes can reach as high as 12.3 $kJmol^{-1}$ while confined geometry effects between nanotubes can raise this to as high as 15 $kJmol^{-1}$ [22]. Experimental measurements of hydrogen adsorption in carbon nanotubes has evoked much controversy with early reports suggesting 5 - 10 wt.% could be stored at room temperature[26]. Room temperature adsorption is now generally accepted to be below 1 wt.% [27]. Reports of adsorption at low temperature (77 K) have varied between 1.5 and 8 wt.%[22] while simulations of optimized nanotube size and separation distance has suggested that 6 wt.% can be adsorbed[28]. Much of the variation in adsorption reported for carbon nanotubes can now be attributed to erroneous measurements, sample contamination (both of the samples themselves and of the hydrogen gas used in the experiments), insufficiently pure or characterized samples as well as to differences in sample preparation[22,27].

1.2.3.2. Zeolites

Zeolites are crystalline materials whose synthesis conditions (including chemical composition, temperature and structure directing agents) result in crystalline porous materials with pores ranging in size from 0.25 to 1.5 nm. The most common building blocks for zeolites consist of tetrahedrally co-ordinated aluminium, silicon and oxygen atoms. The cations in the lattice structure of zeolites can also be readily exchanged with other cations such as Na^+, K^+, Mg^{2+}, Ca^{2+} etc.

Research into hydrogen storage in zeolites has followed two main paths. The first involves physisorption of molecular hydrogen into the porous framework and is typically done at low temperature (77 K). The second approach uses the idea of encapsulation. In this approach, the zeolite is heated up to temperatures between 150 and 573 K (300^{o}C) and hydrogen pressure of up to 90 MPa is applied before being cooled[29]. The premise behind this method is that the heating of the zeolite leads to thermal expansion and a consequent increase in pore size. The result is that pores that were previously too small to allow hydrogen to penetrate can now do so. Then, as the sample is cooled, the pores contract and trap the hydrogen. This trapped hydrogen can then be released when required by heating the zeolite[29,30,31,32]. To date, the application of this form of hydrogen storage has been limited by the high encapsulation temperatures (573 K), high encapsulation pressures (up to 90 MPa) and low hydrogen storage content (< 1 wt.%)[29, 31].

Hydrogen adsorption in zeolites at room temperature as well as 77 K has been extensively studied[19, 33, 34, 35, 36, 37, 38, 39, 40, 41, 42]. A list of some of the data published on hydrogen adsorption by zeolites, at both liquid nitrogen temperatures and room temperature, are presented in Table 1-1.

Table 1-1: A list of hydrogen adsorption measurements performed on various zeolites.

Zeolite Type[Reference]	Exchange Ion	BET Surface Area (m^2/g)	wt.% of H_2	Temperature (K)	Pressure (MPa)	Enthalpy of Adsorption ($kJ.mol^{-1}$)
Molecular Sieve 5A[19]	-	616	1.2	77	1.5	-
Zeolite X[34]	Ca	669	2.19	77	1.5	-
Zeolite X[34]	K	607	1.96	77	1.5	-
Zeolite A[33]	Na	Negligible	1.54	77	1.5	-
Zeolite A[33]	Na	Negligible	0.28	298	1.5	-
Zeolite X[33]	Mg	-	1.61	77	1.5	-
Zeolite X[33]	Mg	-	0.28	298	1.5	-
SSZ-13[35]	H	638	1.28	77	0.092	-9.7
SAPO-34[35]	H	547	1.09	77	0.092	-
Low Silica Type X[36]	Li	717	1.50	77	0.1	-
Low Silica Type X[36]	Li	717	0.60	298	10	-
Low Silica Type X[36]	Li	717	1.60	298	10	-
SAPO-34[37]	H	547	1.09	77	0.092	-
Chabazite (Si:Al =2.1)[37]	H	490	1.10	77	0.092	-
Zeolite X (Si:Al =1.05)[38]	Na	-	1.22	77	0.06	-
Zeolite X (Si:Al =1.40)[38]	Na	-	0.73	77	0.06	-
Zeolite Y (Si:Al =2.4)[38]	Na	-	0.30	77	0.06	-
Zeolite A[39]	Na	-	1.24	77	0.105	-10.0
ZSM-5[40]	Li	-	-	-	-	-6.5
ZSM-5[41]	Na	-	-	-	-	-10.3
ZSM-5[41]	K	-	-	-	-	-9.1
Zeolite Y[42]	Mg	-	-	-	-	-18.2

Hydrogen uptake by zeolites is, in general, significantly less than that by activated carbons and metal-organic frameworks, with reported values ranging up 2.19 wt.% at 1.5 MPa [34] and 77 K. Much of the published data of 77 K adsorption measurements are only performed up to 0.1 MPa. A number of these samples do not show hydrogen saturation in this pressure range while the highest adsorbing zeolite [34] does not show saturation at 1.5 MPa. The result is that a definitive evaluation of the suitability of these zeolites as hydrogen storage media is difficult. However, a number of these zeolite samples do saturate before 1.5 MPa and the relatively low hydrogen uptake in these zeolites can be explained by their relatively modest surface area (< 800 m^2/g) and pore volume.

Despite the modest hydrogen uptake reported, interest in zeolites and their interaction with hydrogen continues. In hydrogen adsorption on activated carbon, the hydrogen and carbon mainly interact via van der Waals interactions. However, in zeolites the polarized cation sites also interact with the quadrupole moment of hydrogen resulting

in a stronger enthalpy of adsorption. The enthalpy of adsorption of hydrogen on these cation sites is strongly dependent on the type of ion and the structure of the zeolite framework[34,41]. Heats of adsorption between -6.5 and -10 $kJ.mol^{-1}$ (see Table 1-1) have been reported with the highest reported value being -18.2 $kJ.mol^{-1}$ for a Mg^{2+} ion exchanged zeolite[42]. However, this publication does not present hydrogen adsorption measurements but merely suggests that Mg based materials may present a viable adsorption media. The oxygen contained in the zeolite framework has also been shown to act as a binding site at high hydrogen loading, although with a lower enthalpy of adsorption[36,38]. It is hoped that understanding hydrogen's interactions with the highly polarized cations in zeolites will lead to a tailored material capable of working at near ambient temperatures.

Hydrogen adsorption at room temperature by zeolites, like other porous materials, is somewhat modest. However, the Li exchanged ZSM-5 zeolite combined with a carbon supported catalyst has been shown to adsorb 1.6 wt.% of hydrogen at 10 MPa, an increase by a factor of 2.6 over the pure Li-ZSM-5[36]. The improved hydrogen uptake is attributed to hydrogen spillover in a process that has also been applied to increase the room temperature uptake of activated carbon[43] (1.8 wt.% at 298 K and 10 MPa) and MOF's [44] (also at 1.8 wt.% at 298 K and 10 MPa).

1.2.3.3. Metal Organic Frameworks

Metal organic frameworks (MOFs) consist of transition metal oxide clusters bridged by flexible organic linkers[45]. Control of the pore size via a change in the length of the organic linkers is facile while the surface area of different MOFs has been measured to generally be between 1000 and 4500 m^2/g [46]. Nearly 5000 two dimensional and three dimensional MOF structures have been identified in the literature. Few have had their porosity characterised and fewer still have had their hydrogen adsorption properties analysed[46].

A number of metal organic framework materials have had their hydrogen adsorption properties examined (Table 1-2). For approximately half of these materials, hydrogen adsorption measurements where made at 77 K using the same apparatus as that used for nitrogen adsorption[47-51] which limits adsorption isotherms to 101.3 kPa. For

samples measured in this way hydrogen adsorption ranged between 0.9 wt.%[51] and 2.48 wt.%[49]. For hydrogen adsorption on MOFs measured at higher pressures (5 - 10 MPa) an interesting trait is that those MOFs that have relatively low gravimetric uptake at saturation show enhanced uptake at low pressures as compared to those samples with higher surface area and higher gravimetric uptake[52]. This suggests that gravimetric adsorption is determined by hydrogen binding energy at low pressure and surface area at high pressure[22].

The strength of interaction between hydrogen and MOFs has been measured to be between 2.3 and 4 kJ.mol^{-1} [53,54]. This is substantially below the 15 – 20 kJ.mol^{-1} [16,46] required for room temperature hydrogen adsorption on porous materials. Consequently, room temperature measurements on MOFs up to 10 MPa have yielded only around 1 wt.% of hydrogen uptake or less[54-56].

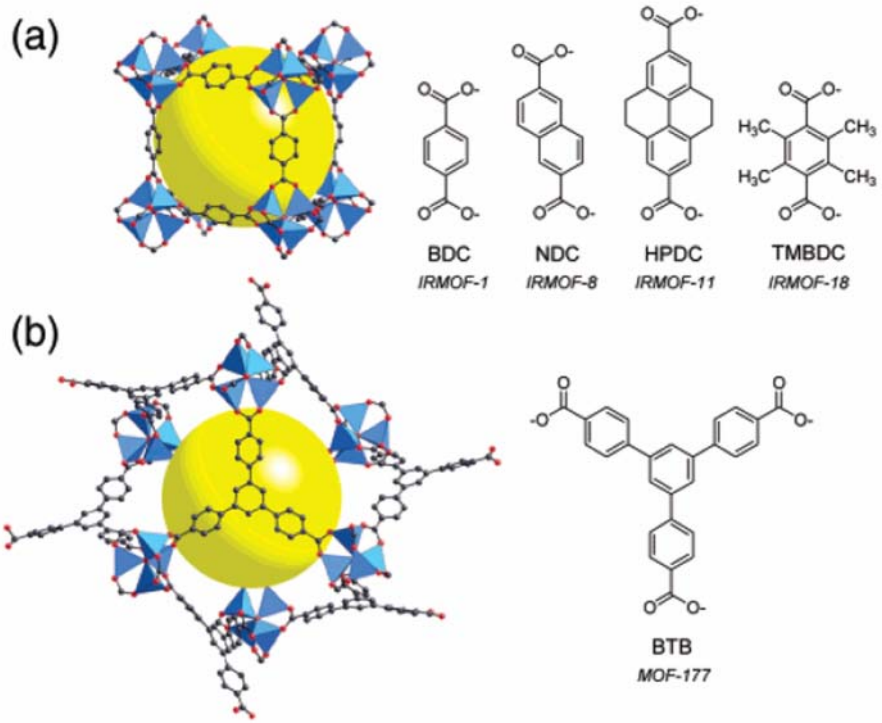

Figure 1-2: (a) Isoreticular (having the same underlying topology) metal-organic frameworks, Zn4O(L)3, are constructed by linking zinc oxide clusters with linear carboxylates L such as those shown. (b) The structure of MOF-177, Zn4O(BTB)2, is formed by linking the same clusters with a trigonal carboxylate. The large void regions are illustrated by yellow spheres with diameters equal to the distance of separation between the frameworks' van der Waals surfaces. Reprinted with permission from [47]. Copyright 2004 American Chemical Society.

A number of possibilities exist for increasing the hydrogen storage of metal-organic frameworks. Inelastic neutron scattering (INS) has shown that MOFs generally contain an adsorption site associated with the metal ion and a number of adsorption sites of similar energy associated with the organic linkers[57]. Rosi et al.[57] used the approach of lengthening the linkers to introduce more hydrogen binding sites. While this approach does increase the gravimetric wt.% of hydrogen adsorbed, it does so at the expense of volumetric density[46]. Producing co-ordinately unsaturated metal sites in MOFs has been suggested as a means of increasing the strength of interaction with hydrogen[46]. Simulations have shown that co-ordinatedly unsaturated Cu atoms in MOF-505 have binding energies of between 8 and 13.4 $kJ.mol^{-1}$ [58]. Recent experiments using this approach in conjunction with exceptionally high surface areas have resulted in hydrogen uptake at 77 K of 7.5 wt. % (at 7 MPa)[52] with a volumetric density of 53 kgm^{-3} [52] and 6.9 wt. % (at 9 MPa)[56] with a volumetric density of 60 kgm^{-3} and a heat of adsorption of 10.1 $kJ.mol^{-1}$.

Table 1-2: Summary of hydrogen adsorption in MOFs.

Material[(a) Reference]	Apparent Langmuir Surface Area (m^2/g)	Wt.% of H_2	Temperature (K)	Pressure (MPa)
IRMOF-1[47]	3362	1.32	77	0.1
IRMOF-1[57]		1.00	296	2.0
IRMOF-1		1.65	296	4.8
IRMOF-6[57]	2630	1.00	296	1.0
IRMOF-8[47]	1466	1.50	77	0.1
IRMOF-8[57]		2.00	296	1.0
IRMOF-11[47]	1911	1.62	77	0.1
IRMOF-18[47]	1501	0.89	77	0.1
MOF-177[47]	4526	1.25	77	0.1
MIL-53(Al)[59]	1590	3.80	77	1.6
MIL-53(Cr)[59]	1500	3.10	77	1.6
Ni(cyclam)(bpydc)[60]	817	1.10	77	1.1
$Zn_2(bdc)_2(dabco)$[48]	1450[(b)]	2.00	77	0.1
$Ni_3(btc)_2(3\text{-}pic)_6(pd)_3$[61]	-	2.10	77	1.4
$Zn_4O(L^1)_3$[55]	-	1.12	296	4.8
$Zn_4O(L^2)_3$[55]	-	0.98	296	4.8
MOF-505[49]	1646	2.48	77	0.1
Cu-(tbc)[50]	-	2.10	77	0.1
$NaNi_3(OH)(SIP)_2$[51]	-	0.90	77	0.1
Mn(BTT)[56]	2100	2.20	77	0.1
Mn(BTT)[56]		6.90	77	9.0
Mn(BTT)[56]		0.95	298	9.0
MOF-177[52]	5640	7.50	77	7.0
IRMOF-20[52]	4593	6.70	77	8.0

(a) Acronyms; cyclam = 1,4,8,11-tetraazacyclotetradecane, bpydc = 2,2'-bipyridyl-5,5' -dicarboxylate, bdc = benzene-1,4-dicarboxylate, dabco = 1,4- diazabicyclo [2.2.2] octane, btc = benzene-1,3,5-tricarboxylate, 3-pic = 3-picoline, pd = 1,2-propanediol, L^1 = 6,6'-dichloro -2,2'-diethoxy-1,1'-binaphthyl-4-4'-dibenzoate, L2 = 6,6'-dichloro-2,2'-dibenzyloxy-1,1' -binaphthyl-4,4'-dibenzoate, (b) Measured using BET rather than Langmuir method

Another method for increasing the hydrogen uptake of MOFs is to increase the strength of interaction between the organic linkers and hydrogen via functionalisation. Although not shown in Figure 1-2, hydrogen is bonded to the benzene rings of the organic linkers and recent theoretical work has shown that electronegative atoms, such as chlorine, can be exchanged for these hydrogen atoms to produce a polarised organic linker with increased affinity for hydrogen[62].

1.2.4. Metal and Intermetallic Hydrides

Many transition metals and their intermetallic alloys can react with hydrogen to form hydrides. Molecular hydrogen is dissociated at the surface of a metal with the subsequent hydrogen ions diffusing into the bulk of the material. Upon entering the

metal, the resulting hydrogen atoms occupy one or more of the available interstitial sites in the metal lattice[63]. This hydrogen absorption is most pronounced in the early transition metals and the lanthanide rare earths. The alloys of these compounds also show a strong affinity for hydrogen and are known as intermetallic hydrides. They usually consist of an element, A, with a high affinity for hydrogen and an element, B, that has a low affinity for hydrogen. The element, A, usually consists of a rare earth or alkaline metal while element, B, is usually a transition metal[3].

The absorption/desorption process can be described by pressure-composition-temperature (PCT) graphs (see Figure 1-3). These plot the amount of hydrogen absorbed (hydrogen to metal ratio, H/M) at a given pressure and temperature. At low hydrogen concentrations (H/M ratio < 0.1), hydrogen is absorbed by the metal and forms a solid solution, known as the α-phase (between point (a) and (b)), with an associated expansion of the metal lattice. As the hydrogen to metal ratio exceeds ~0.1 (this value varies from material to material), the metal hydride phase begins to forms (β-phase). While the α–phase and β-phase co-exists (between point (b) and (c)), there is a plateau in the isotherm and how long this plateau is determines how much hydrogen can be stored[3]. The absorption process is exothermic while the desorption process is endothermic. Completion of the β-phase is associated with a steep rise in the equilibrium pressure (beyond point (c)). Re-examining the PCT diagram with this in mind shows us that absorption/desorption is relatively straightforward with changes in temperature and/or pressure[1,64].

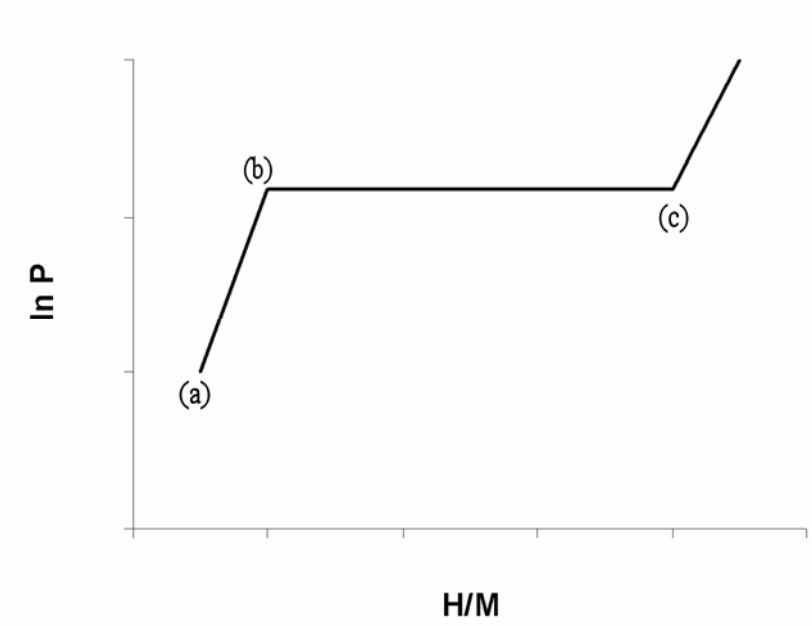

Figure 1-3: Example Pressure-Composition-Temperature Isotherm. Point (a) reprents the beginning of α-phase formation. Point (b) marks the beginning of β-phase formation. Point (c) represents the completion of β-phase formation.

There are a number of advantages to metal hydrides including storing hydrogen at high density. For example, $LaNi_5$ has a volumetric density of hydrogen of 115 kg/m^3. Even accounting for the void space that exists in powdered metal hydrides, the density of hydrogen in metallic hydrides significantly exceeds that of liquid hydrogen[3]. The hydrogen can also be stored at relatively modest pressures, often in the range of 0.1 - 1 MPa[1]. This is a significant positive in terms of safety as a rupture of the containment vessel will result in little hydrogen loss unless a significant and sustained heat source is present[63]. However, the fine powder formed by decrepitation of the hydride can, like any fine powder, be pyrophoric on exposure to air[64]. A further advantage of metal hydrides is that the released hydrogen is extremely pure. This is an important factor when considering hydrogen for mobile applications, based on PEM (Proton Exchange Membrane) fuel cells, as the catalysts used in these are susceptible to poisoning from impurities.

Since the majority of the intermetallic alloys consist of transition metals, they are relatively heavy when compared to hydrogen. The result, the greatest drawback of metal hydrides, is that they store a relatively low gravimetric amount of hydrogen. Table 1-3 lists a number of hydrides and their gravimetric capacities. As this table

shows, the hydrides with the most favourable operating temperatures and pressure, such as $LaNi_5$ and FeTi, contain less than 2 wt.% of hydrogen and so suffer when considered for mobile applications. Magnesium hydride stores enough hydrogen to meet the 2010 DOE gravimetric target but requires impractical operating temperatures for mobile applications. The hydrogen supplied to the metal hydrides must also be very pure as impurities can cause poisoning. The poisoning can take the form of segregation of the constituent elements at the surface of intermetallic compounds rendering it inert towards dissociation of hydrogen[65]. Impurities may also form a monolayer on the surface of the metal particle which also acts as a barrier to dissociative chemisorption[64].

Table 1-3: Selected metal hydrides and their properties[63,66].

Metal Hydride	wt.% of H_2	Operating Pressure (MPa)	Temperature (K)
LiH	12.7	0.02	1076
MgH_2	7.7	0.60	613
TiH_2	4	0.08	902
AlH_3	10.1	2500	413
$VH_{1.91}$	3.6	0.48	313
$TiFeH_2$	1.9	0.52	303
Mg_2NiH_4	3.5	0.11	523
$Ti(V_{0.8}Mn_{0.2})_2H_6$	3.8	2.00	453
$LaNi_5H_{6.4}$	1.5	0.17	298
$BaReH_9$	2.7	0.10	< 373
$Ti_{0.9}Zr_{0.1}Cr_{1.8}H_{5.1}$	3.4	200	293

1.2.5. Complex Hydrides

Complex hydrides can broadly be categorised into alanates $(AlH_4)^{-1}$, borohydrides $(BH_4)^{-1}$ and nitride based materials $(NH_2)^{-1}$ (amides and imides). These compounds are of interest due to their high hydrogen content as illustrated in Table 1-4.

Table 1-4: Selected complex hydrides.

Compound	wt. % of H_2
$LiAlH_4$	10.5
$NaAlH_4$	7.5
$KAlH_4$	5.8
$Mg(AlH_4)_2$	9.3
$Ca(AlH_4)_2$	7.7
$LiBH_4$	18.5
$NaBH_4$	10.6
$Mg(BH_4)_2$	14.9
$Ca(BH4)_2$	11.4
$Al(BH_4)_3$	16.9
$LiAlH_2(BH_4)_2$	15.2
Li_2NH	6.6
$LiNH_2$	5.7

1.2.5.1. Alanates

Alanates, as a class, have been known for more than 50 years. Until recently, these materials have received little attention as potential hydrogen storage materials for mobile applications due to their lack of reversibility. However, in 1996, Bogdanivec et al.[67] discovered that sodium alanate, $NaAlH_4$, doped with a suitable Ti based catalyst could undergo dissociation followed by reversible hydrogen absorption. Unlike the case for intermetallic hydrides, the desorption of hydrogen from complex hydrides follows a multistep decomposition process. The two step desorption for $NaAlH_4$ is shown in equation (1-1) and (1-2) along with the theoretical amount of hydrogen released.

$$3NaAlH_4 \Leftrightarrow Na_3AlH_6 + 2Al + 3H_2 \text{ (3.7 wt. \% H)} \qquad (1\text{-}1)$$

$$Na_3AlH_6 \Leftrightarrow 3NaH + Al + 3/2H_2 \text{ (3.0 wt. \% H)} \qquad (1\text{-}2)$$

In practice, for the decomposition of $NaAlH_4$, only 5.6 wt.% of hydrogen has been shown to be reversible with operating temperatures of ~473 K (200^{o}C) and 533 K

(260°C) for the first and second reaction respectively[68]. In practise, operation below 373 K (100°C) yields a reversible capacity of 3 – 4 wt. %.[67,68]

In theory lithium alanates are candidates for hydrogen storage applications due to their high hydrogen content. $LiAlH_4$ has a theoretical hydrogen content of 10.5 wt.% while Li_3AlH_6 has a theoretical hydrogen content of 11.2 wt. %. In practise however, $LiAlH_4$ is an unstable hydride with a high equilibrium pressure, even at room temperature, resulting in it being irreversible. Further to this some of the hydrogen is locked up as LiH which requires temperatures above 953 K (680°C) for decomposition. Chen et al.[69] did however, obtained limited reversibility by introducing $TiCl_3.1/3AlCl_3$ as a catalyst via a vibratory-milling technique. Li_3AlH_6 is also not reversible, at least up to a pressure of 5 MPa at a temperature of 473 K (200°C)[70].

Magnesium alanate has also been examined by Fichtner et al.[71] and was found to follow a desorption process different to the alkali based alanates. $Mg(AlH_4)_2$ first decomposed to MgH_2 and Al below 474 K (200°C) followed by desorption of hydrogen from MgH_2 with further heating yielding the intermetallic Al_3Mg_2. The reversibility of this system was not studied.

Despite their high content of hydrogen, alanates in general suffer from poor kinetics and problems with reversibility. To a large extent the problem of kinetics has been addressed via incorporation of suitable titanium based catalysts in combination with ball-milling[67,72,73,74].

1.2.5.2. Borohydrides

Sodium borohydride ($NaBH_4$) and lithium borohydride ($LiBH_4$) have also been considered as possible hydrogen storage materials[75,76]. Sodium borohydride has, theoretically, 10.8 wt.% of hydrogen and has been commercially developed to produce hydrogen via a hydrolysis reaction as follows[76]:

$$NaBH_4 + 2H_2O \rightarrow 4H_2 + NaBO_2 \qquad (1\text{-}3)$$

In practise, this reaction yields 7.5 wt.% of hydrogen and has the advantage that the reaction can be precisely controlled and that the by-product, a solution of $NaBO_2$, is relatively inert. The main drawbacks of this method are that regeneration needs to be performed off-board resulting in a current price of US$80/kg for $NaBH_4$[77] and that the large amount of heat produced during hydrogen production inevitably limits the energy efficiency of the process[77].

Lithium borohydride has also been considered as a hydrogen storage material via hydrolysis[78] as well as direct pyrolysis[75]. Hydrolysis has been excluded for $LiBH_4$ due to the large amount of acid required to push the reaction to completion[78] and also due to the large amount of heat generated during hydrogen production[79]. In the pyrolysis reaction, $LiBH_4$ undergoes melting at ~583 K before desorbing 50% of its contained hydrogen at ~763 K with a further 25% of its contained hydrogen being released at ~953 K with the remaining 25% being contained within LiH. Experiments involving temperature programmed desorption[80] suggested a desorption process involving intermediate steps which have now been attributed to the formation of $Li_2B_{12}H_{12}$ [81]. The addition of silica (SiO_2) has been shown to initiate hydrogen desorption at 473 K with a peak centred at ~633 K with a second small desorption peak at ~723 K [82]. However, this effect has been shown to be a catalytic effect rather than a destabilization of the hydride[80]. Rehydrogenation for lithium borohydride has been achieved at 873 K (600^{o}C) and 35 MPa of hydrogen pressure[75] which is still too high a temperature for mobile applications.

Another factor that may eventually limit the application of light metal complexes for hydrogen storage for transport applications is the large amount of heat generated during hydrogenation[83]. Calculations show that a typical car will require several megawatts of cooling for it to be refuelled in the time frame specified by the DOE targets[77]. However, not all complex hydrides have large heats of formation. $Al(BH_4)_3$, a liquid at room temperature, has a relatively low heat of formation and pure $Al(BH_4)_3$ as well as partially substituted $Al(BH_4)_3$ are now under investigation[84,85].

1.2.5.3. Lithium Nitrides

Lithium nitride based materials have recently come under scrutiny as a possible hydrogen storage material[86]. Li_3N undergoes two absorption plateaux corresponding to equation (1-4) and (1-5).

$$Li_3N + 2H_2 \rightarrow Li_2NH + LiH + H_2 \quad (1\text{-}4)$$

$$Li_2NH + LiH + H_2 \Leftrightarrow LiNH_2 + 2LiH \quad (1\text{-}5)$$

Equation (1-4) is only considered reversible at extreme temperatures (> 693 K)[87] but equation (1-5) represents reversible hydrogen absorption of ~6 wt.% in the temperature range of 423 – 573 K (150 - 200^{o}C). The thermodynamics of equation (1-4) are such that, to be useful for vehicular applications, a temperature of 523 K (250^{o}C) is required to generate an equilibrium pressure of 100 kPa [87]. The kinetics of absorption/desorption are also somewhat sluggish but have been shown to improve with the addition of a suitable catalyst[88].

A ternary compound of Li-Mg-N, has also been examined[87]. The Li-Mg-N compounds were produced via mixing of $LiNH_2$ and MgH_2 [89] and have been shown to have a reversible hydrogen capacity of 4.5 – 5.5 wt.% in the temperature range of 433 - 473 K (160 - 200^{o}C) with a substantial increase in both the absorption and desorption plateaux pressure. This indicates a substantial destabilisation as compared to pure $LiNH_2$ but the kinetics are still below that required for onboard applications.

1.3. Measuring Hydrogen Adsorption/Absorption

Numerous techniques are available for measuring the hydrogen sorption properties of a material. Two terms are used to describe hydrogen sorption. These are adsorption and absorption. Adsorption refers to the binding of molecular hydrogen to the surface of material and is the term used in describing the interaction of hydrogen with porous materials. Absorption refers to the chemical binding of a hydrogen atom and the formation of a new compound. Absorption is the term used in describing the interaction of hydrogen with materials such as metal hydrides, alanates, borohydrides

and nitrides etc. Sometimes the term "adsorption" is used when discussing these materials. In this case, adsorption refers the sorption of molecular hydrogen onto the surface of the material that precedes dissociation and absorption.

The most common types of hydrogen sorption measurement apparatuses are: the gravimetric method, which directly measures the hydrogen absorbed by a sample; the Sieverts-type volumetric method, which measures the change in hydrogen pressure in response to hydrogen sorption and; the flow-controlled volumetric method, which measures amounts of gas by integrating gas flow over the time period required to fill the sample cell.

1.3.1. Gravimetric Method

The gravimetric method is based on measuring the change in mass of an absorbent as it absorbs hydrogen. This system typically has a sensitivity of 1 μg in several grams [90,91] and gives a direct and sensitive measure of the hydrogen uptake of a sample. Due to this sensitivity, the technique is ideally situated for low mass samples in the order of 3 mg to tens of milligrams[91,92]. The gravimetric technique is, however, fraught with complicating factors. The buoyancy effect arises from the displacement by the sample of the absorbate gas and increases with increasing absorbate density. The buoyancy effect can also be further complicated with low density samples whose density isn't accurately known[93]. The addition of gas to the system can also create temperature gradients and convection currents that can result in signals being generated that are as large as the values that are to be measured[91,92]. Finally, the gravimetric technique requires very pure hydrogen for its measurements as contaminants that preferentially adsorb/absorb over hydrogen can produce erroneous results. This was illustrated in the results of Chen et al.[94] who published data for hydrogen uptake in alkali doped nanotubes. These results were subsequently shown to be caused by water vapour contamination of the hydrogen gas[92,95].

1.3.2. Volumetric Methods

1.3.2.1. Sieverts

Figure 1-4 shows a generic setup for a Sieverts apparatus. Hydrogen absorption proceeds in a stepwise function. In the first step, the entire system pressure and temperature is measured. The calibrated reference volume is then separated from the calibrated sample cell volume by a Valve S and the reference volume is filled to a new pressure. Valve S is then opened and the system is allowed to come to equilibrium with new values being measured for the pressure and temperature. The amount of hydrogen absorbed by the sample is then measured via the change in the pressure of the system[23,91,93,96]. This technique has the advantages of being cheap, simple and relatively robust. Furthermore, it is also relatively insensitive to contamination of the hydrogen supply[91]. The major source of uncertainty in such a system is the calibration of the constituent volumes. In addition, care must be exercised when measuring hydrogen of porous samples with low or unknown density[88].

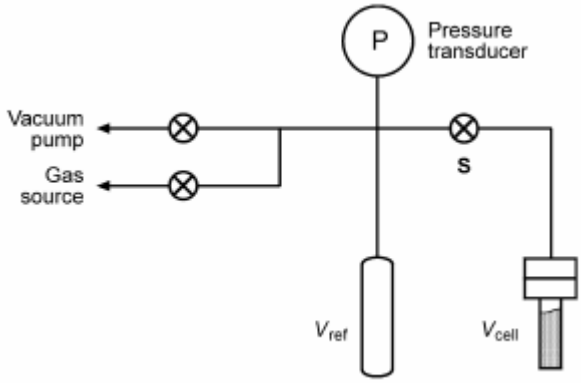

Figure 1-4: Minimal Sieverts apparatus for determining the uptake of gas atoms or molecules by the sample contained in a cell with empty volume V_{cell}, based on the initial pressure of gas in V_{ref} and a further measurement of pressure after the valve S has been opened[93].

1.3.2.2. Flow Controlled

In more sophisticated volumetric apparatus a flow controlled method is used. "In the flow-based approach, amounts of gas are measured by integrating a constant gas flow over the time period required to fill the sample cell. The hydrogen excess sorption is then calculated from the difference between the amount of hydrogen and helium sent to the sorbing system under the same flow, pressure, and temperature conditions." [91]

This apparatus is particularly useful for measuring absorption or desorption rates at a constant hydrogen pressure. For this system, the uncertainty of hydrogen sorption is typically better than 5% with the largest uncertainty arises from measuring the flow rate of hydrogen in the system.

2. Methodology

2.1. Motivation

Hydrogen storage is currently a burgeoning field of research and, as illustrated by the literature review of Chapter 1, a multitude of materials may be considered as hydrogen storage materials. Therefore, a process must be implemented for deciding what materials will be considered as part of this thesis. Factors to take into consideration include; the potential of the material as a hydrogen storage material; the extent to which the material has previously been investigated; whether or not it is currently being researched; and whether or not we have the appropriate facilities here at Curtin University of Technology to produce, handle and characterise a particular material.

2.2. Hydrogen Apparatus

2.2.1. Apparatus

The first goal of this thesis was to design and construct a apparatus for performing hydrogen sorption measurements. The apparatus constructed here at Curtin University of Technology employs the volumetric (also called manometric and Sievert's) method to determine hydrogen sorption of a sample. In this method, a calibrated reference volume is filled to a measured pressure of hydrogen gas and then opened to the sample chamber. The amount of hydrogen sorbed by the sample is then determined via the change in the gas pressure in the system. The apparatus consists of 316 stainless steel components, stainless steel manually operated diaphragm valves, a Rosemount 3051S pressure transducer and a K-type thermocouple with all components rated up to a gas pressure of 24 MPa. The unit comprises 3 distinct volumes: the calibration volume, the reference volume and the sample cell volume.

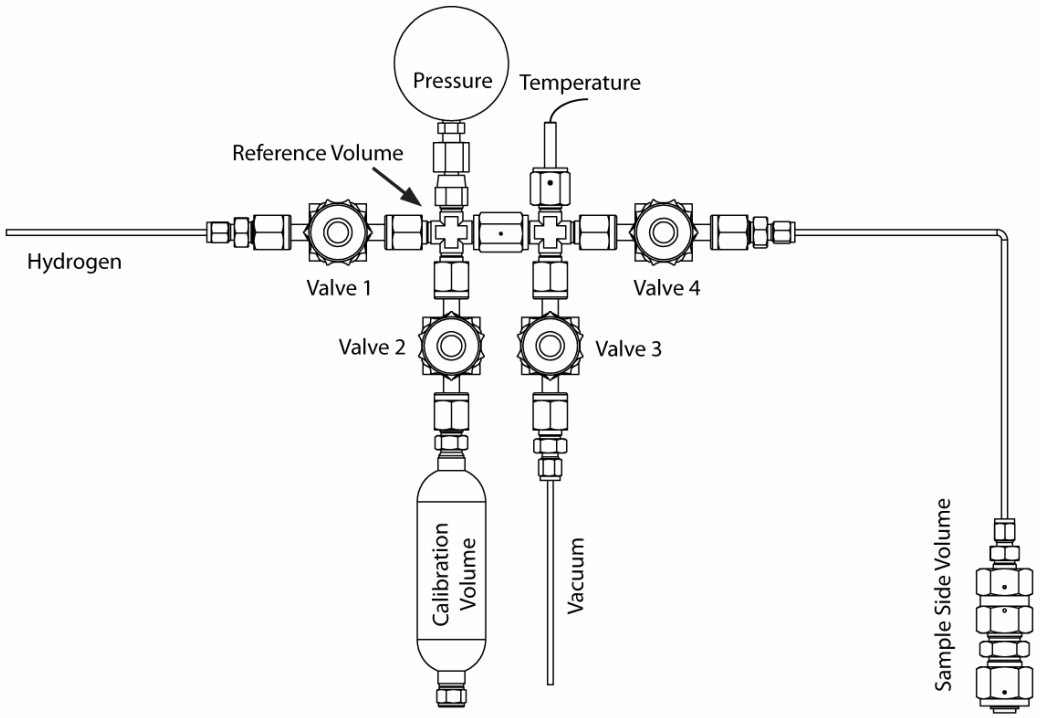

Figure 2-1: Schematic of the Sievert's apparatus used for hydrogen measurments in this work. The reference volume is comprised of the volume enclosed by Valve 1, Valve 2, Valve 3 and Valve 4 while the sample volume is that volume to the right of Valve 4. Image courtesy of Mark Paskevicius.

2.2.2. Pressure Transducer and Thermocouple

The pressure gauges consist of Rosemount pressure transducers model 3051S. Due to circumstances beyond our control, some are setup as gauge pressure while others are setup as absolute pressure. All the pressure gauges have a precision of 0.01% of the full scale. Calibration certificates supplied with the pressure transducers show that the pressure transducer purchased in 2003 has an accuracy of 0.02% of full scale while that purchased in 2006 has an accuracy better than 0.01% of full scale. So that an absolute pressure reading could be obtained from the gauge pressure transducers, a Baromec Type N^{o}: M1975 atmospheric barometer, produced by Mechanism Ltd., was used to measure atmospheric pressure.

The thermocouples consist of standard K-type thermocouples calibrated against both a mercury thermometer and a four-point platinum resistor in the temperature range of 293 to 333 K (20 to 60^{o}C). They measure the temperature inside the reference volume only. If the sample cell is also at ambient temperature and relatively small (<25 cm^{3})

then the sample cell temperature is taken to be the same as the reference volume temperature. If a large volume (>75 cm^3) is used as either the calibration volume or sample cell volume then a second K-type thermocouple is attached and used to measure its temperature.

2.2.3. Volume Calibrations

Two versions of a calibration volume were used during the course of this thesis. Both calibration volumes consists of a double ended, 304 type stainless steel cylinder (~75 cm^3) sealed at one end with an NPT style plug while the other consists of a NPT style fitting attached to either a ball or diaphragm valve. The calibration volume is determined by measuring the mass of the fluid which fills the container and its temperature. Initially, an attempt to use water as the calibration fluid was made. The nozzle on the inlet tube to the valve has a small diameter (3.2 mm) and the large surface tension of water made it difficult to insert the water into the calibration volume. A second complicating factor of water's high surface tension is that small bubbles can form on the surface of the stainless steel which are difficult to dislodge. Even with submersing the calibration volume in a water bath and subjecting the entire water bath to vacuum, it was difficult to ascertain if the calibration volume was completely filled with water. The lower surface tension of ethanol meant it was an ideal replacement for water as a calibration medium.

Ethanol was inserted into the calibration volume with a syringe before using a K-type thermocouple to measure its temperature. The valve was then closed and any excess ethanol allowed to evaporate before the change in mass was measured. An evaluation version of the program AlcoDens©[97] was used to calculate the density of ethanol at a given temperature and a given mass percent of water. Adsorption of atmospheric moisture was assumed to be negligible and therefore the purity of ethanol was taken as 99.8% with the remainder being water.

2.3. The Combressibility of Hydrogen

A modified version of the ideal gas law is required to accurately relate the variables of pressure, temperature, volume and number of moles of a gas (equation 2-1).

$$n = \frac{PV}{ZRT} \qquad (2\text{-}1)$$

where n = the number of moles of gas

P = the pressure of the gas (Pa)

V = the volume that the gas occupies (m^3)

T = the temperature of the gas in Kelvin

R = the universal gas constant (8.3145 $JK^{-1}mol^{-1}$)

Z = the compressibility factor.

The compressibility factor is a measure of how much a gas deviates from the ideal gas law and is defined by:

$$Z = \frac{V_m}{V_m^i} \qquad (2\text{-}2)$$

Here V_m is the molar volume (V/n) as determined by an accurate equation of state (EOS) for the range of temperatures and pressures of interest while V_m^i is the molar volume as determined from the ideal gas law. A detailed explanation of the implementation of the compressibility factor may be found in McLennan and Gray[98].

The EOS used when the temperature exceeds 100 K and the pressure is above 0.1 MPa is the Hemmes equation of state[99]. This EOS was derived from a number of sets of data on hydrogen available in the literature spanning the temperature range of 100 to 1000 K and the pressure range of 0.1 MPa to 10^5 MPa. The EOS reproduces most of the experimental data to within 0.1% and practically all the data within 0.5% indicating its appropriateness for determining the compressibility factor in the modified ideal gas law. A detailed explanation of the Hemmes EOS may be found in Appendix 7.1. A simple iterative piece of software was created which used the Hemmes EOS to determine the compressibility factor, Z, for any given temperature and pressure using equation (2-2).

Initially, the EOS derived by Hemmes et al.[99] was applied to adsorption measurements performed at 77 K. However, it became clear that there was a systematic error in this EOS that increased with increasing pressure. A thorough examination of the literature revealed a number of sets of data that could possibly be used to generate compressibilities at 77 K. Vargaftik[100] has extensive tabulated data for the molar volume of hydrogen over a range of temperatures and pressures. However, we are interested in data at 77 K and over a range of pressures while Vargaftik's data is limited to 70 K and 80 K and to 200 kPa increments below 2 MPa and to 1 and 2 MPa increments from 2 to 10 MPa. Interpolation of this data to the desired temperature of 77 K and to any pressure between 100 kPa and 12 MPa would prove inadequate.

Further examination of the literature reveals a Virial equation to describe hydrogen that covers the temperature range between 55 and 100 K and for pressures between 0.2 and 34 MPa [101]. The accuracy of this Virial equation is hard to ascertain due to the difficulty in obtaining the original document. However, subsequent work by one of the authors states that this Virial equation derived from the experimental data has a 0.1% uncertainty in the density[102]. This work was performed under the auspice of the United States National Bureau of Standards which is now known as the National Institute of Standards and Technology (NIST). An updated interactive database is available from NIST[103] which can generate the density of hydrogen covering the temperature range of 14 to 400 K and the pressure range of 0 to 121 MPa. The maximum uncertainty in the density is quoted as 0.2%. From the density of hydrogen for a given temperature and pressure the compressibility, Z, can be determined. The NIST database was used to generate a tabulated data set of the hydrogen density at 77 K in the pressure of 0 to 12 MPa in 100 kPa increments. The compressibility as a function of pressure was then fitted using a 5 term polynomial inside the software package Igor Pro[104]. The residuals between the tabulated values from the NIST database and the polynomial fit were no more than 0.03%, approximately an order of magnitude better than the error in the density provided by the database.

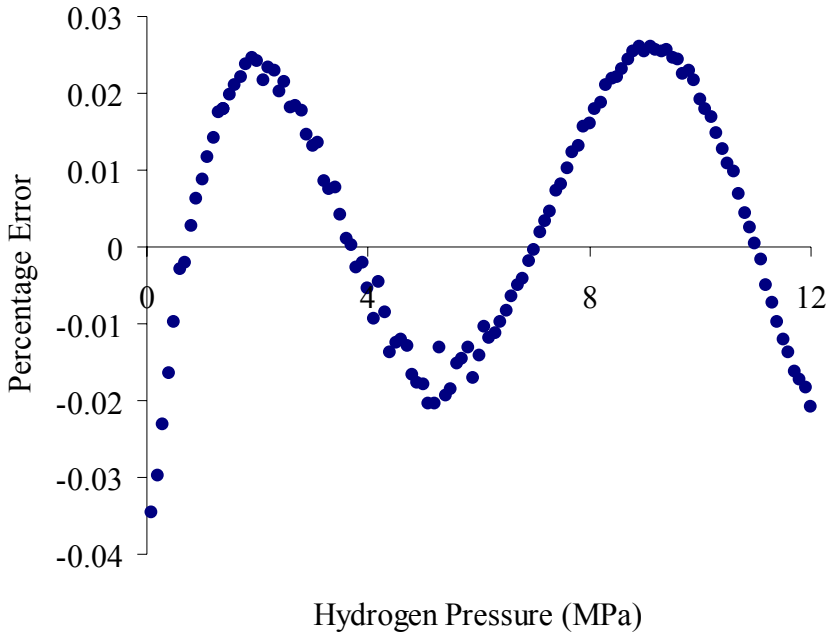

Figure 2-2: Percentage error in the 5 term polynomial fit to the NIST database[103] compressibility for hydrogen at 77 K.

2.4. Hydrogen Sorption Measurement Technique

The explanation of the hydrogen sorption measurements will be made with regards to the volumetric hydrogen apparatus depicted in Figure 1-4. The explanation is based on that of Blach and Gray[93]. The sorption of hydrogen is performed in a step wise manner. Suppose that, at the end of the i-1th step, a pressure P_e^{i-1} is present throughout the hydrogen apparatus (which consists of the reference volume, V_{ref}, and the sample cell volume, V_{cell}). The valve between the reference volume and sample cell volume (Valve S) is then closed and a new pressure, P_r^i, is established in the reference volume. Valve S is then opened and a new pressure, P_e^i, is established for the system. The number of moles sorbed by the sample for the i^{th} step, n^i_{sor}, is then given by equation (2-3).

$$n^i_{sor} = \frac{P_r^i V_r}{Z_r^i R T_r^i} + \frac{P_e^{i-1} V_s}{Z_e^{i-1} R T_e^{i-1}} - \left(\frac{P_e^i V_r}{Z_e^i R T_e^i} + \frac{P_e^i V_s}{Z_e^i R T_e^i} \right) \qquad (2\text{-}3)$$

Where n^i_{sor} = the number of moles of gas sorbed by the sample for the i^{th} step.

P_r^i = the pressure of gas in the reference volume for the i^{th} step.

V_{ref} = the reference volume.

T_r^i = the temperature in the reference volume for the i^{th} step.

Z_r^i = the compressibility factor associated with P_r^i and T_r^i.

$P_e^{i\text{-}1}$ = the system equilibrium pressure associated with the i^{th}-1 step.

V_{cell} = the sample cell volume.

$T_e^{i\text{-}1}$ = the temperature in the sample cell volume for the i^{th}-1 step.

$Z_e^{i\text{-}1}$ = the compressibility factor associated with $P_e^{i\text{-}1}$ and $T_e^{i\text{-}1}$.

P_e^i = the system equilibrium pressure associated with the i^{th} step.

T_e^i = the temperature associated with the equilibrium pressure for the i^{th} step.

Z_e^i = the compressibility factor associated with P_e^i and T_e^i.

When a measurement is being performed on an actual sample, the sample itself occupies a volume and so must be subtracted from the sample cell volume, V_s. The volume of a sample can be defined in terms of its mass, m_s, and density, ρ_s, resulting in:

$$n_{sor}^i = \frac{P_r^i V_r}{Z_r^i R T_r^i} + \frac{P_e^{i-1}\left(V_s - \frac{m_s}{\rho_s}\right)}{Z_e^{i-1} R T_e^{i-1}} - \left(\frac{P_e^i V_r}{Z_e^i R T_e^i} + \frac{P_e^i\left(V_s - \frac{m_s}{\rho_s}\right)}{Z_e^i R T_e^i}\right) \qquad (2\text{-}4)$$

The total amount of hydrogen sorbed by the sample after N steps is then given by:

$$n_{sor}^N = \sum_{i=1}^{N} n_{sor}^i \qquad (2\text{-}5)$$

When considering using a Sievert type apparatus, the performance of the system based on the system volume, the sensitivity of the pressure transducer, the mass of the sample available for experimentation and its density are all important design factors. Blach and Gray[93] have developed a means to determine a figure of merit, η, for a Sievert's apparatus which can be used as a guide to the appropriateness of the experimental setup.

$$\eta = \frac{s_i}{\delta p} \qquad (2\text{-}6)$$

Where s_i is given by;

$$s_i = \frac{\Delta n_H R}{2\sum_j \frac{V_j}{Z\left(P_e, T_j^i\right) T_j^i}} \qquad (2\text{-}7)$$

where Δn_H = the number of moles of hydrogen atoms sorbed for the i^{th} sorption step.

R = the universal gas constant

V_j = the sum of all the volumes that comprise the hydrogen sorption apparatus

Z = the compressibility factor associated with each volume in the system which is dependent on P_e and T_j^i.

T_j^i = the temperature associated with each of the volumes that comprise V_j.

s_i is basically the pressure change induced by a sample sorbing hydrogen for the i^{th} step in a hydrogen sorption run. δp is the useable resolution of the pressure transducer and is a measure of the sensitivity of the pressure transducer to a change in pressure induced by the hydrogen uptake of a sample.

The author's[93] deduced, through experience, that a value for η greater than 100 was adequate to produce reliable data that would be relatively robust in the face of uncertainties in the sample density. However, this figure of merit should only be used as a guide for the following reasons. The variable s_i is, in effect, a measure of the number of moles of hydrogen sorbed by a sample for a given pressure step. For a porous material, hydrogen uptake may be highly pressure dependent with usually large uptake at low pressure followed by slower uptake at increasing pressure. This adsorption may even plateau or decrease at sufficient pressure. The result is that the figure of merit is dependent on the size of the pressure step and the amount of hydrogen taken up by a sample and is not constant for a fixed experimental setup or sample. With a sufficiently large pressure step and with the sample adsorbing hydrogen, the figure of merit (FOM) will be large but as the peak or plateau is reached the number of moles adsorbed for the pressure steps will approach zero. In this case the FOM will also approach zero and suggests that the experimental setup is

insufficient to acquire useful data. Therefore, a qualitative approach is suggested to be used in conjunction with the FOM as follows; if the hydrogen uptake of a sample for a given pressure step is small relative to the total hydrogen content adsorbed by the sample from previous steps, then the measurement can be counted as relatively robust.

2.5. Uncertainties and Error Analysis

An appreciation and identification of uncertainties, possible sources of error and error propagation are integral when presenting results of any scientific experiment. This is particularly true in the hydrogen storage field where controversial hydrogen uptake for a variety of materials[26,94,105] has been published in the literature that have now been generally excepted to be due to experimental errors.

The Sievert's technique for determining hydrogen uptake of a sample relies on measurements of pressure, temperature and volume to determine the number of moles of hydrogen in the gas phase and consequently within the sample. Hence we are ultimately interested in the uncertainty of the number of moles of hydrogen in the gas phase of our Sievert's system.

2.5.1. Maximum Uncertainty Method

The maximum uncertainty method is one of the simplest methods available for determining uncertainties. Each quantity in the formula is varied by its uncertainty to create a maximum and minimum value[106]. As it applies to our case, the variables in equation (2-4) are increased or decreased by an amount equal to their uncertainties in such a way as create the largest change in the number of moles adsorbed by the sample, n^{i}_{sor} for any given pressure step.

2.5.2. Differential Uncertainty Method

Let us consider a variable X that is a function of the variables a and b. The uncertainty, ΔX, in the variable X is then given by:

$$\Delta X = \left(\left(\frac{\partial X}{\partial a} \Delta a \right)^2 + \left(\frac{\partial X}{\partial b} \Delta b \right)^2 \right)^{1/2} \qquad (2\text{-}8)$$

The modified ideal gas law is used to describe the number of moles, n, in the gas phase and has variables as defined for equation (2-1).

$$n = \frac{PV}{ZRT}$$

Taking R as constant, the resulting uncertainty in the moles, Δn, is consequently:

$$\Delta n = \left(\left(\frac{\partial n}{\partial P} \right)^2 \Delta P^2 + \left(\frac{\partial n}{\partial V} \right)^2 \Delta V^2 + \left(\frac{\partial n}{\partial Z} \right)^2 \Delta Z^2 + \left(\frac{\partial n}{\partial T} \right)^2 \Delta T^2 \right)^{1/2} \qquad (2\text{-}9)$$

Substituting in the partial derivatives yields:

$$\Delta n = \left(\left(\frac{V}{ZRT} \right)^2 \Delta P^2 + \left(\frac{P}{ZRT} \right)^2 \Delta V^2 + \left(\frac{-PV}{Z^2 RT} \right)^2 \Delta Z^2 + \left(\frac{-PV}{ZRT^2} \right)^2 \Delta T^2 \right)^{1/2}$$

2.5.3. Results of Uncertainty Analysis

The uncertainty in the pressure is better than 0.02% of the full scale of the pressure gauge. The pressure gauge with the largest scale has a 15.1 MPa range resulting in ΔP having a value of 3 kPa. Since the uncertainty is 0.02% of the full scale we see that as the pressure decreases, the relative uncertainty actually increases. The K-type thermocouple was calibrated against both a 4-point platinum thermistor and a mercury thermometer and has an accuracy of ± 0.2^o C in the temperature range 293 – 333 K (20 – 60^{o}C). The uncertainty in the compressibility, Z, is more difficult to estimate. This compressibility is dependent on the pressure and temperature of the system and so, theoretically, its uncertainty can be determined based on their uncertainties. However, the Hemmes EOS must be solved numerically and is intractable to the partial differentiation method. Applying the maximum uncertainty method to the Hemmes EOS shows that the uncertainties associated with pressure and temperature varies the corresponding Z by less than 0.005%. The uncertainty in the calibration volume is expected to be quite low given that the mass of the ethanol is measured with an uncertainty of 0.01%. Given the temperature and density of ethanol are also quite well known, the total uncertainty of the calibration volume is taken to be not worse than 0.1%.

The simplest form of a hydrogen sorption measurement involves raising the reference volume to a known pressure and temperature while maintaining the sample cell (containing the sample) at vacuum and then opening the valve between the two volumes and measuring the pressure change. The maximum uncertainty method and partial derivative method can be considered to produce reasonable estimates of the uncertainty in the number of moles of hydrogen initially in the reference volume as displayed in Figure 2-2. Even if variables are dependent, such as pressure and compressibility (changes in P make only small changes in Z), using the partial derivative method will provide an upper bound on the uncertainty in the system.

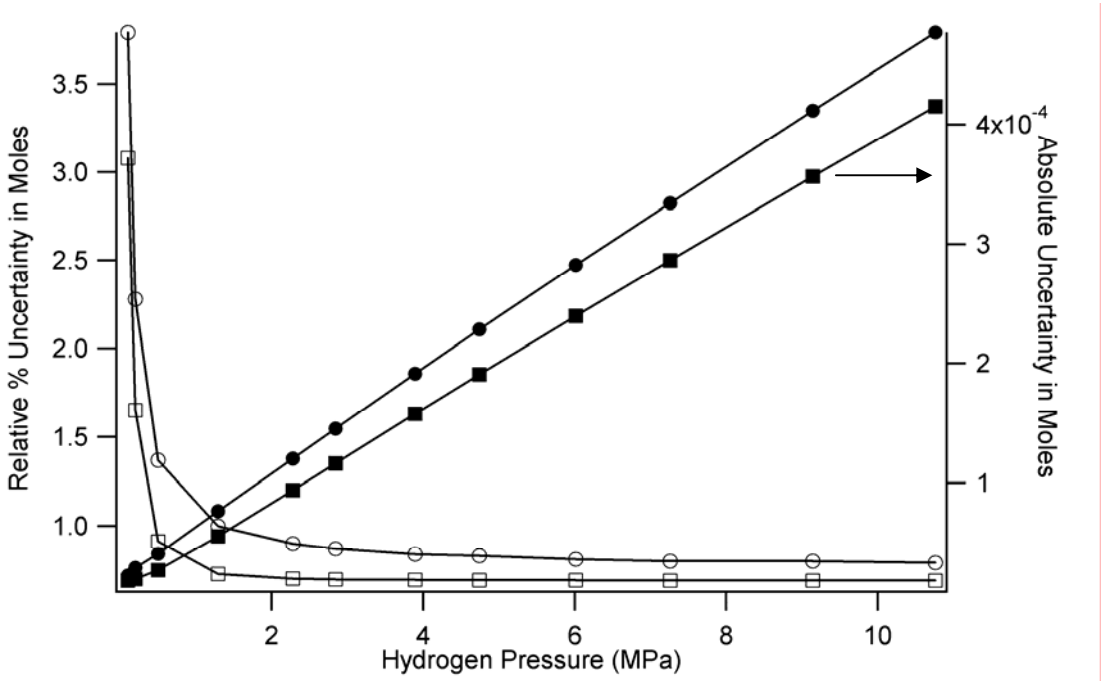

Figure 2-3: The uncertainty in the number of moles in the reference volume as a function of pressure for a particular Sievert's apparatus. (○) is the relative uncertainty in moles calculated via the maximum uncertainty method. (●) is the absolute uncertainty in the number of moles calculated via the maximum uncertainty method. (□) is the relative uncertainty in moles calculated via the partial derivative method. (■) is the absolute uncertainty in moles calculated via the partial derivative method.

However, a subsequent sorption step involves closing the valve between the reference volume and sample cell volume and measuring this pressure as the equilibrium pressure. A new pressure is then introduced into the reference volume before the valve between the reference volume and sample cell volume is opened and a new equilibrium pressure is established. For N sorption steps then the maximum

uncertainty or partial derivative method are applied to equation (2-5) resulting in a total uncertainty of[106]:

$$\pm n_{sor}^{N} = \sum_{i=1}^{N} \pm n_{sor}^{i} \qquad (2\text{-}10)$$

Because the number of moles sorbed by a sample is the difference between two relatively large numbers (n_r+n_s being one while n_e is the other) the maximum uncertainty and partial derivative method suggest that the uncertainty in the number of moles sorped is therefore of similar magnitude to the quantity we are interested in. Subsequent sorption steps merely compound this large uncertainty. However, both maximum uncertainty and partial derivative methods work on the assumption that any systematic uncertainties have been identified and minimised and that the variables are independent of each other. This is the case for when we are considering the number of moles in the gas phase in a particular volume but performing sorption steps introduces dependencies. The most obvious is that the equilibrium pressure for a current sorption step is dependent on the initial reference pressure, initial sample cell volume pressure and the number of moles sorped by the sample.

Let us now consider the uncertainties for the general case where we have a function, q, with dependent variables x and y. The uncertainty may then be defined by[107]:

$$\sigma_q = \left(\left(\frac{\partial q}{\partial x} \right)^2 \sigma_x^2 + \left(\frac{\partial q}{\partial y} \right)^2 \sigma_y^2 + 2 \frac{\partial q}{\partial x} \frac{\partial q}{\partial y} \sigma_{xy} \right)^{1/2} \qquad (2\text{-}11)$$

Where σ_q = the standard deviation in the function q.

$\frac{\partial q}{\partial x}$ = the partial derivative of q with respect to variable x.

σ_x = the standard deviation with respect to N measurements $x_1, \ldots, x_N$.

σ_{xy} = the covariance between x and y given by

$$\sigma_{xy} = \frac{1}{N} \sum_{i=1}^{N} (x_i - \bar{x})(y_i - \bar{y}) \qquad (2\text{-}12)$$

Where x_i = the i^{th} measurement of the quantity x.

$\bar{x}$ = the mean of all x measurements.

y_i = the i^{th} measurement of the quantity y.

$\bar{y}$ = the mean of all y measurements.

In the case when x and y are independent we can see that the covariance, σ_{xy}, should approach zero. Whatever the value of y_i, the quantity $x_i - \bar{x}$ is just as likely to be negative as it is positive. Consequently, after numerous measurements, the positive and negative terms in equation (2-12) should nearly balance resulting in the familiar equation for independent and random uncertainties (equation 2-6).

If the measurements of x and y are not independent then the covariance σ_{xy} may not be zero. We can envisage in the case of dependence between x and y in which an overestimate in the measurement of x is accompanied with an overestimate in the variable y, and vice versa. In either case the number ($x - \bar{x}$) and ($y - \bar{y}$) will always have the same sign, whether they be positive of negative, with the resulting covariance being non-zero and positive. The overall uncertainty derived from equation (2-11) will therefore be larger than the uncertainty derived from equation (2.6) for independent variables.

However, we can also envision the case where an overestimate in the number ($x - \bar{x}$) is associated with an underestimate in the number ($y - \bar{y}$) resulting in a covariance, σ_{xy}, that is negative. The resulting uncertainty, σ_q, for the dependent variables can be smaller than for the case of independent variables.

The general case described above is applicable to when numerous repeat measurements are made of the same quantity. However, in the process used to make a hydrogen sorption measurement we can only make the one measurement and so a quantitative assessment of equation (2-11) is impossible. Given this, a practical estimate of the uncertainties is best made with equation (2-10) in conjunction with Figure 2-3. For any measurement in which the initial reference pressure is above 0.5 MPa, the uncertainty in the number of moles of hydrogen in the gas phase is less than 1% (but greater than 0.8 wt% regardless of pressure) with the uncertainty in the volume being the largest contributor. The uncertainty for any particular sorption measurement is then calculated with equation (2-10) and is therefore dependent on the number of steps made.

However, adsorption measurements made at 77 K present a further complication with regards to determining uncertainties. In this case, the uncertainty in the volume of the sample cell at 77 K becomes the dominant factor. This is due to the fact that the density of bulk hydrogen gas is ~4 times higher at 77 K than it is at room temperature for the same pressure. For these measurements, the uncertainty displayed in plots of hydrogen adsorption as a function of pressure is determined by applying the maximum uncertainty method to the volume calibration of that volume of the adsorption apparatus at 77 K.

2.6. Modelling

In the search of a hydrogen storage material that fulfils the requirements of onboard vehicular storage, as well as experimental techniques, modelling of the materials and their interaction with hydrogen will play a crucial role.

Curtin's Hydrogen Storage Research Group (HSRG) has joined CSIRO's National Hydrogen Materials Alliance (NHMA) in a coordinated effort to examine ways to improve the efficiency of hydrogen storage, generation and end use. As part of this collaborative effort, Curtin's HSRG is focused on hydrogen storage in porous materials. One computational technique to examine hydrogen adsorption by porous materials is the Grand Canonical Monte Carlo (GCMC) method. The Monte Carlo method is one that uses intermolecular potentials to compute equilibrium properties of classical many body systems. GCMC computer algorithms are typically tailor written for the particular system under study. Given this, a single piece of software capable of modelling a wide variety of adsorbents and their interactions with hydrogen is desirable. This thesis will examine the suitability of one such piece of software.

2.6.1. Basic Principles of the Grand Canonical Monte Carlo Method

In terms of Monte Carlo software the algorithms are relatively simple, as compared to say quantum chemistry codes, and so often the algorithm will be tailor-made to a specific application[108]. The result is that there is no such thing as a standard Monte Carlo implementation but the foundations upon which software are developed are, if not identical, at least very similar.

The GCMC method can be used to determine information about molecules confined within pores which are at equilibrium with an infinite reservoir of identical molecules at a fixed chemical potential (μ) and temperature (T). If the pressure of the bulk gas at a given μ and T is known via a suitable equation of state (EOS) then a simulation can be performed in a similar manner to an adsorption experiment[109]. The pressure and temperature of the bulk gas determines the chemical potential. This chemical potential is then used as an input to the simulation and will determine the weight of hydrogen adsorbed at equilibrium in a given pore. The interactions between hydrogen molecules and between the hydrogen molecules and the adsorbate can be modelled by the Lennard-Jones potential.

$$U(r) = 4\varepsilon\left[\left(\frac{\sigma}{r}\right)^{12} - \left(\frac{\sigma}{r}\right)^{6}\right] \qquad (2\text{-}13)$$

where σ and ε are experimentally determined parameters for the interaction of interest and r is the distance between interacting particles.

The simulation consists of generating an initial configuration of molecules inside a volume. If the chemical potential (μ), the pore volume (V) and the temperature (T) are fixed, then the number of molecules within the volume becomes a variable and will vary throughout the simulation[109] in an attempt to find a minimum energy configuration. This fluctuation in particle number is achieved with trials of random translation, insertion or deletion of molecules. If the energy of the system after one of these trials is such that it satisfies certain conditions then the trial is accepted, else it is rejected. In this way the system gradually moves towards an energy minimum.

2.6.2. Software Choice

The software chosen with which to perform Monte Carlo simulations was GULP (General Utility Lattice Program)[110]. GULP is an input driven program that is designed to perform a variety of tasks related to three dimensional solids including energy minimisations, crystal properties, defect analysis, genetic algorithm optimisation, molecular dynamics and structure analysis. The author of the software,

Professor Julian Gale, is now based in the Nanochemistry Research Institute (NRI) within the Department of Applied Chemistry at Curtin University of Technology. This association with Curtin has allowed access to the formulas and their implementation, a task that may prove difficult for third party software.

To assess the suitability of GULP for use in GCMC simulations of hydrogen adsorption of porous materials, confirmation was first required as to whether the software was working as intended. To this end, simulations of bulk hydrogen gas were performed over a range of temperatures and pressures and compared to data in the literature. Rzepka et al.[23] published GCMC simulations of hydrogen adsorption in graphitic slit pores and carbon nanotubes. The data they used to generate a relationship between chemical potential (μ), temperature (T) and pressure was used as a comparison[111]. This data is available in Appendix 7.2. Due to a difference in the implementation of the equations that dictate creation, destruction and translation between Rzepka et al.[23] and GULP, the chemical potential obtained from Rzepka[111], μ, had to first be adjusted according to the following equation:

$$\mu_{adj} = kT \ln\left(L_D e^{\left(\frac{\mu}{kT}\right)} \right) \qquad (2\text{-}14)$$

Where μ_{adj} = the adjusted chemical potential (J)

k = Boltzmann's constant (1.381 x 10^{-23} J/K)

T = temperature (K)

μ = chemical potential from Rzepka's[111] data (J)

The term L_D is given by:

$$L_D = \frac{1\text{Å}^3}{M^{3/2}\lambda^3} \qquad (2\text{-}15)$$

Where M = the molar mass of molecular hydrogen (g/mole)

λ = the de Broglie wavelength of molecular hydrogen at temperature T (Å).

2.6.3. Monte Carlo Modelling

2.6.3.1. The Simulation

The simulation consists of generating an initial configuration of molecules inside the simulation volume. If the chemical potential (μ), the simulation volume (V) and the temperature (T) are fixed, then the number of molecules within the simulation becomes a variable and will vary throughout the simulation[109].

2.6.3.2. Trial Displacements

A molecule is chosen at random and moved a small random distance. The configurational energy is then calculated by summing all the pair-wise interactions via the Lennard-Jones potential. For a trial displacement the number of molecules, N, the temperature, T, and volume are kept constant. The new energy (U_{NEW}) is then compared to the old energy (U_{OLD}) and the decision to accept or reject the trial is given by:

$$\Pr = MIN\left[1, e^{\frac{-(U_{NEW}-U_{OLD})}{kT}}\right] \qquad (2\text{-}16)$$

If $U_{NEW} < U_{OLD}$ then Pr = 1 and the new configuration is accepted. If Pr < 1 then the new configuration is accepted if $e^{\frac{-(U_{NEW}-U_{OLD})}{kT}} > R$, where R is a random number, else the old configuration is retained[109].

2.6.3.3. Trial Creation

In this case, a new molecule is created at a random position within the volume and the new energy is calculated and compared to the old. GULP uses the following probability in its creation step:

$$\Pr = MIN\left[1, e^{\frac{-(U_{NEW}-U_{OLD})}{kT}} \frac{M_S^{\frac{3}{2}}}{N+1} e^{\frac{\mu}{kT}} \left(\frac{AkT}{N_A\hbar^2}\right)^{\frac{3}{2}} V\right] \qquad (2\text{-}17)$$

where M_S = molecular mass per mole (g/mole)

N = number of particles in the simulation volume

k = Boltzmann's constant, 1.381×10^{-23} J/K

μ = the chemical potential (J)

N_A = Avogadro's number, 6.022×10^{23} (mol^{-1})

$\hbar = 1.055 \times 10^{-34}$ Js

V = volume of system available to hydrogen ($Å^3$)

A = a constant,

Again, if the potential of the system is lowered then the trial is accepted (i.e.Pr = 1). The trial may still be accepted if $e^{\frac{-(U_{NEW}-U_{OLD})}{kT}} \frac{M_S^{\frac{3}{2}}}{N+1} e^{\frac{\mu}{kT}} \left(\frac{AkT}{N_A \hbar^2} \right)^{\frac{3}{2}} V > R$, where R is a randomly generated number, else the old configuration is retained.

2.6.3.4. Trial Destruction

In this case a molecule is destroyed at random, the new energy compared to the old is accepted or rejected following the guidelines outlined in the previous section.

$$P = MIN\left[1, e^{\frac{-(U_{NEW}-U_{old})}{kT}} e^{-\frac{\mu}{kT}} \left(\frac{N_A \hbar^2}{AkT} \right)^{\frac{3}{2}} \frac{N}{M_S^{\frac{3}{2}} V} \right] \qquad (2\text{-}18)$$

2.6.4. Modelling Parameters

For the Lennard-Jones potential, the parameters used for the hydrogen-hydrogen interaction are σ = 0.297 nm and ε = 2.8272 x 10^{-3} eV[23]. All computer simulations require a compromise between accuracy and computation time. Examining the Lennard-Jones potential for the hydrogen-hydrogen interaction (Figure 2-3) shows negligible interaction at a separation of 10 Å. This was therefore taken as the cut-off for interaction between hydrogen molecules. The simulation cell used was 25Å × 25Å × 25Å. This resulted in simulations that typically took 8 to 9 hours to complete.

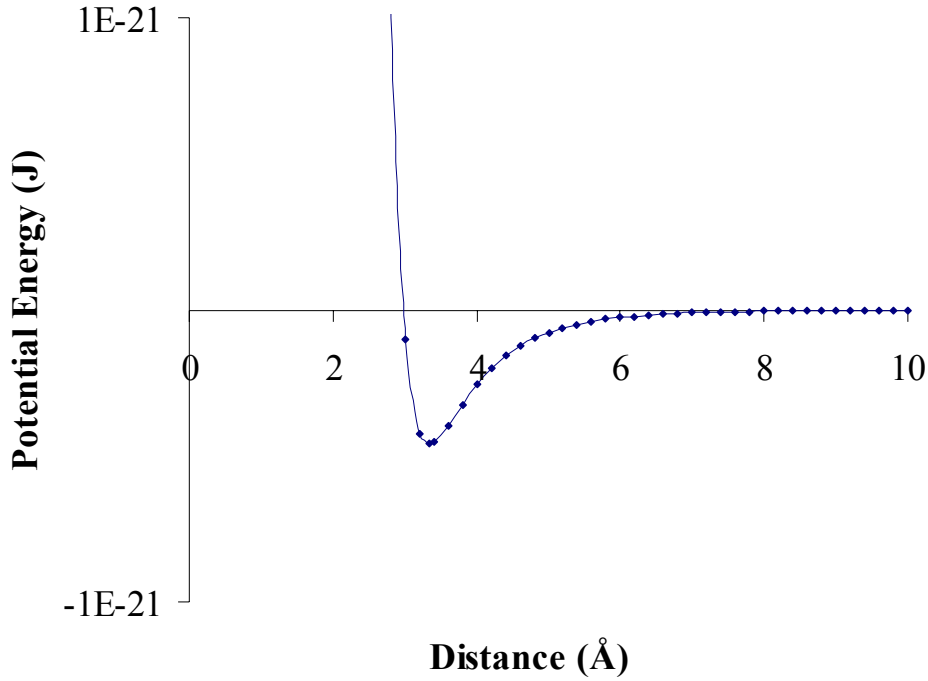

Figure 2-4: Lennard-Jones potential function for a hydrogen-hydrogen interaction.

2.6.5. Results of Modelling

At the conclusion of a simulation GULP generates a table of the molecular configuration of the hydrogen gas inside the simulation volume. Based on the temperature of the simulation, the simulation volume and the number of molecules in the simulation volume, the quantity *P/Z* can be determined.

$$\frac{P}{Z} = \frac{NkT}{V} \qquad (2\text{-}19)$$

Where P = the final gas pressure of the simulation (Pa)

Z = the compressibility associated with P and T

T = the temperature of the simulation (K)

N = the number of molecules of hydrogen gas in the simulation volume

k = Boltzmann's constant (1.381×10^{-23} J/K)

V = the volume of the simulation cell (m^3)

The pressure (P) can then be iteratively solved for and compared to the pressure used to generate the chemical potential that was used to run the simulation.

Table 2-1 shows the results of modelling bulk hydrogen gas with GULP at a variety of pressures and temperatures. Column one is the input chemical potential (μ_{adj}) associated with the target pressure of the simulation (as derived from Rzepka[111]). Column 2 is the temperature of the simulation and Column 3 is the pressure associated with the input chemical potential and temperature. If working correctly, a GULP simulation will result in the number of molecules in the simulation volume that corresponds to the target pressure (Column 3). The target n^o of molecules (Column 4) is the number of molecules required in the simulation volume to correspond to the target pressure. Column 5 is the number of hydrogen molecules, as simulated by GULP, for the input chemical potential and temperature, while Column 6 is the pressure calculated from Column 5.

Table 2-1: Results of simulating bulk hydrogen gas using GULP.

Target Chemical Potential (eV)	Temperature (K)	Target Pressure (MPa)	Target n^o of H_2 Molecules	Calculated n^o of H_2 Molecules	Calculated Pressure (MPa)
-0.141	250	9.8	41.6	45	10.7
-0.077	150	5.2	37.6	38	5.2
-0.037	100	10.0	107.6	108	10.1
-0.029	77	5.0	77.0	114	7.5
-0.029	77	5.0	77.0	111	7.3

As can be seen from Table 2-1, GULP's calculated pressure is within 9% of the target pressures for the simulations run at 250 K, 150 K and 100 K respectively. However, the simulation at 77 K is in disagreement with the target pressure of 5 MPa by 50%. To exclude the possibility of an anomalous result, the simulation was repeated (Row 5 of Table 2-1) and it generated a result commensurate with the first simulation at 77 K.

There are only two possible explanations for the deviation of the pressure calculated at 77 K by GULP and that expected based on the data of Rzepka[111]. The first is that there was either an error in the initial data from Rzepka[23] or that there is an error in the way that GULP is running the GCMC simulation that is accentuated at low temperature. The second possibility is that quantum mechanical effects are significant enough at 77 K for there to be a deviation from a result calculated using a classical

approximation. Simulations of hydrogen adsorption on single walled carbon nanotubes (SWNT)[112] showed that classical simulations over estimated the density of hydrogen within the SWNTs by 17% when compared to quantum mechanical simulations. Simulations using GULP that incorporate a wider range of temperatures and pressures are required to determine why the calculated pressure at 77 K deviates from the expected pressure.

3. Mesoporous Silica – MCM-41

3.1. Motivation

MCM-41 is a mesoporous material with a surface area of between 700 and 1200 m^2/g. Given that this material would be expected to interact with hydrogen via van der Waals interactions, adsorption is expected to be highest at a low temperature (77 K). Upon commencement of this thesis only one article in the literature[113] had looked at hydrogen adsorption in MCM-41 at 77 K and only up to a pressure of 0.1 MPa. MCM-41 is produced by a relatively simple process and samples are readily characterised with X-ray diffraction (XRD), small angle X-ray scattering (SAXS), transmission electron microscopy (TEM), scanning electron microscopy (SEM) and nitrogen adsorption.

Recently, experiments with zeolites[114,115,116] have shown that co-ordinately unsaturated metal sites have increased interaction strength with hydrogen. Simulations of negatively charged single-walled carbon nanotubes have also shown an increased affinity for hydrogen[117]. Zinc incorporation into MCM-41 is believed to create a negative charge on the pore wall[118] and so it is of interest to see if this charge creates any increased strength of interaction with hydrogen. Doping with aluminium[119] is also a common method used to alter the catalytic effect of MCM-41 and its effect on hydrogen adsorption is also of interest.

3.2. General

MCM-41 is one member of the family of porous materials known collectively as M41S[119,120]. MCM-41 is a silica based material with a regular hexagonal array of cylindrical pores that can be tailored in size to be between 1.5 and 10 nm. The pore walls are amorphous but the array of mesopores generates diffraction peaks at low scattering angles (Figure. 3-1 (a)). The planes of pores responsible for the peaks labelled in Figure 3-1(a) are depicted in Figure 3-1(b).

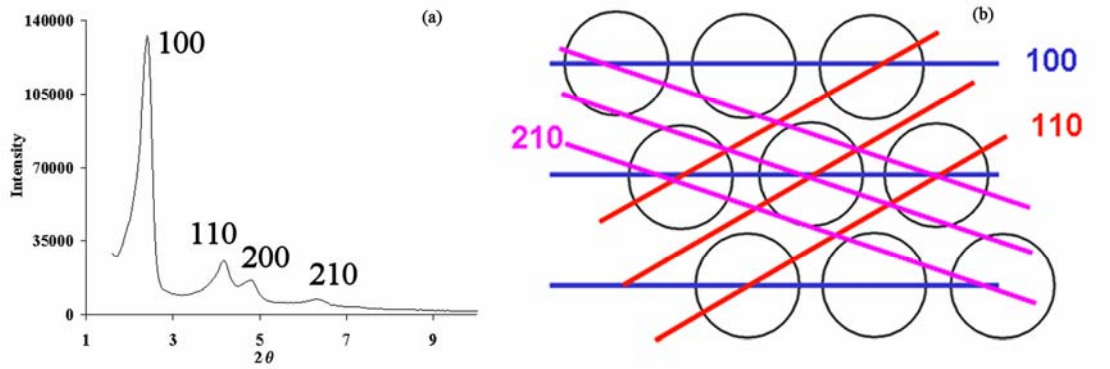

Figure 3-1: (a) X-ray diffraction pattern of MCM-41. (b) End on view of cylindrical pores depicting diffraction planes.

MCM-41 is currently finding use in such fields as a heterogeneous catalysis, separation processing, guest-host chemistry, adsorption and biocatalysis[121,122].

3.3. Production Techniques

In general, synthesis of MCM-41 requires four reagents: a solvent (water and/or ethanol), a silica precursor, a structure directing agent and a catalyst[122]. The multitude of available silica precursors, structure directing agents, reaction temperatures, reaction times, additives and structure directing agent removal techniques means a bewildering number of methods are available for the production of MCM-41.

The most common structure directing agents used for MCM-41 production are surfactants. A surfactant, as it relates to MCM-41 production, can be defined as a material that has two distinct chemical structures. The first is a molecular component that is hydrophobic while the second is a molecular component that is hydrophilic. In aqueous systems the hydrophobic component is usually a long chain hydrocarbon radical while the hydrophilic part will be an ionic or highly polar group that can impart the desired water solubility. In water, to minimise the overall energy of the system, surfactants can agglomerate into structures of various shapes, called micelles, based on temperature, concentration and shape of the surfactant[123]. These structures can take on the following shapes; Isotropic micellar phases that include spheres and rod-shapes; hexagonally packed rod-shaped micelles; cubic packed micelles and a lamellar phase (See Figure 3-2).

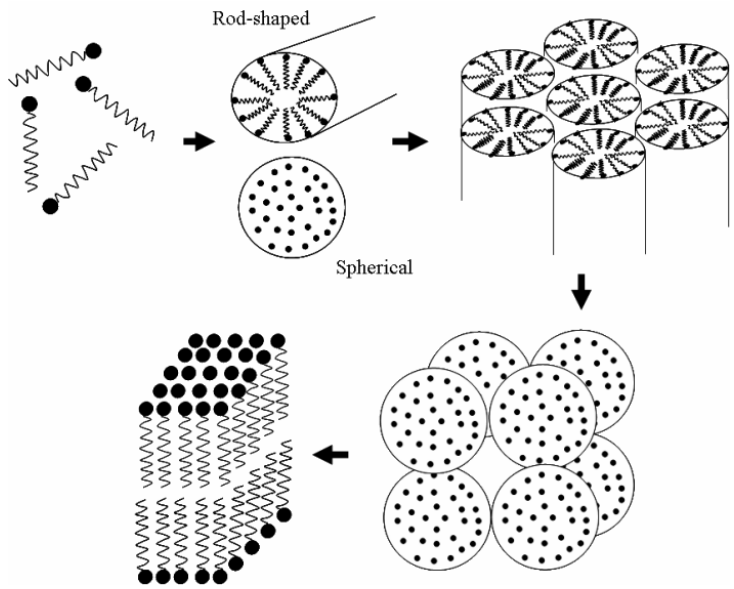

Figure 3-2: Progression of micelle shape in water with increasing surfactant concentration. Based on Zhao et al.[121]

Two similar mechanisms were initially suggested for MCM-41 formation (See Figure 3-3)[119]. In the first case, as the surfactant concentration in solution is increased the micelles accumulate into different liquid crystal templates that thus form the basis for the structure. However, the concentration of surfactant used by most authors is insufficient to form the in-solution liquid crystal template of the known structures of M41S materials [124]. Chen et al.[125] showed via Nuclear Magnetic Resonance (NMR) and Vartulli et al.[126] showed via altering the silica level in the synthesis process that it was the interaction of the silicate species in solution with the surfactant that resulted in the ordering of the surfactant into a structure directing agent and hence supporting the second formation pathway (see Figure 3-3).

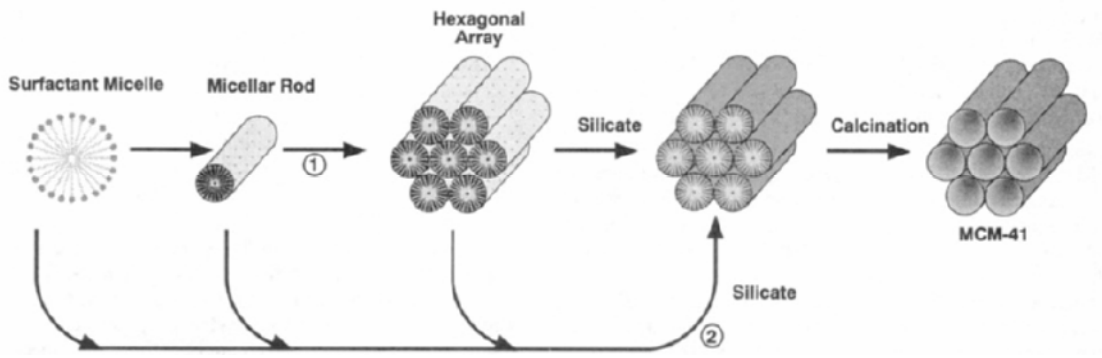

Figure 3-3: Possible formation pathways of MCM-41. (1) indicates liquid crystal phase initiated and (2) indicates silicate anion initiated. Reprinted with permission from [119]. Copyright 1992 American Chemical Society.

3.3.1. Doping MCM-41

The controlled pore size and surface area of MCM-41 makes it an ideal candidate for a catalyst support. To change the catalytic effect of MCM-41 it has been doped with a multitude of different elements. The most common method of doping employs the dissolution of a water soluble salt of the desired dopant into the surfactant solution before the addition of the silica source[127,128,129,130]. Aluminium doped MCM-41 has also successfully been ion exchanged for Na^+, K^+, Ca^{2+} and Y^{3+} [131]. Examples of doped MCM-41 include; Vanadium doped MCM-41 for selective oxidation of hydrocarbons over H_2O_2[127]; Zirconium doped MCM-41 for photocatalytic generation of hydrogen[129]. MCM-41 doped with cobalt[132], iron[130], nickel[133] has been used as a support for the production of single-walled carbon nanotubes with uniform length and width while pure MCM-41 has been shown to be capable of producing multi-walled carbon nanotubes[134]. Mg doped MCM-41 has also been used to produce single-walled boron nanotubes[135].

3.3.2. Calcination Methods

Calcination refers to the removal of surfactant from the solid sample resulting in the porous structure of MCM-41. A number of calcination methods are used for the surfactant extraction. Heating of the as-produced samples in flowing nitrogen for 2 hours followed by flowing air for at least 5 hours at 813 K (540^{o}C) was the initial method used[120,136]. Mere heating in a muffle furnace at 823 K (550^{o}C) for at least 5 hours has also been shown to be effective[137]. Marler et al.[138] and Voegtlin et al.[139] were early proponents of a two stage calcination process. This first involves calcination at a modest temperature (423 – 473 K) to decompose the surfactant followed by calcination at a higher temperature (743 – 873 K) to remove the decomposed organic component. He et al.[140] went one step further and suggested that calcination at high temperatures resulted in transient pressure increases due to surfactant decomposition that were high enough to damage the structure. To assess this possibility they examined the decomposition process of the surfactant using Temperature Programmed Desorption (TPD). They found two peaks at 418 K (145^{o}C) and 698 K (425^{o}C) respectively. The first was attributed to the decomposition of the cetyltrimethylammonium surfactant while the second was attributed to the desorption

or decomposition of hexadecene and trimethylamine readsorbed on the surface of the MCM-41. Their resultant two-step calcination method involved calcining the sample at 423 K (150^{o}C) for two hours followed by a further six hours of heating at 873 K (600^{o}C) with a subsequent increase in the quality of the MCM-41 samples as determined from XRD patterns (Figure 3-4).

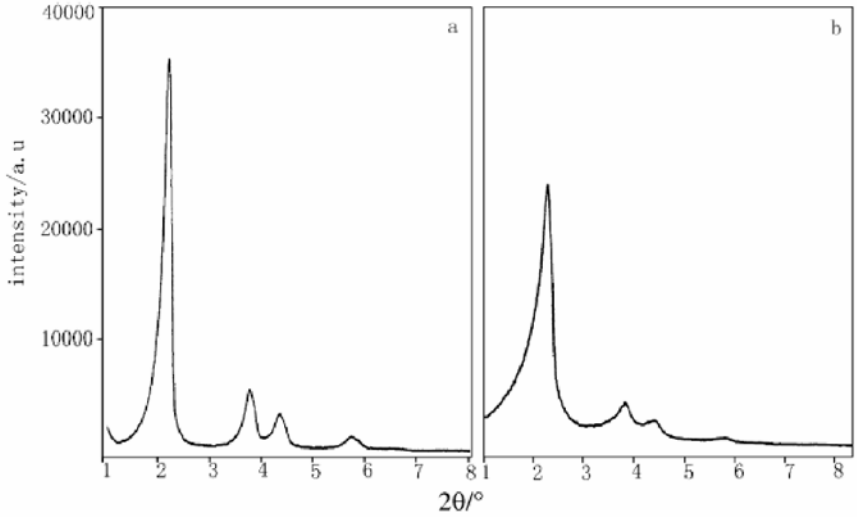

Figure 3-4: XRD patterns of MCM-41: (a) treated by two-step calcination; (b) calcined directly at 773 K (500°C)[140].

In an attempt to remove the variability that air calcination imparts to surface area, pore size and pore volume, a number of other techniques have been developed for surfactant removal[141]. The simplest method involves using ethanol[142,143] but other organic solvents have been used[144]. A modification of this method includes the use of dilute acid, such as sulphuric, acetic, ammonium nitrate[144] or hydrochloric acid[145]. Even acetic acid by itself has been used as a surfactant extractor[146]. However, all these approaches except that of Tanev et al.[142], who used hot ethanol, required further calcination at elevated temperatures to remove residual surfactant. One further method that has been examined is that of supercritical drying[145,147]. This involves exposing the as-produced sample to supercritical CO_2 modified with methanol at pressures of up to 35 MPa. This method can extract up to 93% of the surfactant and has the benefit that the surfactant can then be recovered for future synthesis[147].

3.4. Experimental Method

3.4.1. Production Methods

A list of all the chemicals used in the production of MCM-41, their chemical purities and supplies is listed in Table 3-1. The notation used for different samples is MCM-41-X where X is the sample number. If a sample is doped with an element, Y, the sample name also contains the ratio between silicon and the dopant such as MCM-41-X-Si:Y=10:1.

Table 3-1: Chemicals used in MCM-41 production.

Chemical Name	Abbreviation	Purity	Supplier
Cetyltrimethylammonium Bromide	CTAB	95%	Sigma-Aldrich
Decyltrimethylammonium Bromide	DTAB	>98%	Fluka
Sodium Silicate Solution	-	-	Sigma-Aldrich
Tetraethyl Orthosilicate	TEOS	>99%	Fluka
Alumiun Chloride Hexahydrate	$AlCl_3 6H_2O$	99%	Sigma-Aldrich
Zinc Sulphate Heptahydrate	$ZnSO_4.7H_2O$	>99.5	Univar
Sulphuric Acid	H_2SO_4	98%	Univar

3.4.1.1. Pure Mesoporous Silica - MCM-41

A number of MCM-41 production methods were tried. Initial attempts were focused on using the method of Edler and White[148]. The reagents used were cetyltrimethylammonium bromide (CTAB, 99%), sulphuric acid (analytical reagent grade, 98%), sodium silicate (27 wt.% SiO_2, 59 wt.% H_2O, 14 wt.% NaOH) and milliQ water. The procedure is as follows: Sodium silicate and water were weighed out to desired amounts with the water being added drop-wise to the sodium silicate. Sulphuric acid is diluted to a ~1M solution before being added drop-wise to the sodium silicate solution under stirring. A separate solution is made by heating water to ~308 K (35^{o}C) before adding the surfactant to the desired composition. The sodium silicate solution is then added drop-wise to the surfactant solution under continuous magnetic stirring. Once all the sodium silicate solution has been added to the CTAB, the entire mixture is stirred for a further 20 minutes before being placed in an autoclave at 343 K (70^{o}C). Some samples had their pH adjusted to 10 with 1M sulphuric acid before being placed in the autoclave similar to the process first used by Ryoo and Kim[149], and Edler and White[148]. Subsequent pH adjustments to 10 were

made every 24 hours thereafter with the sample being placed in a water bath at 343 K (70^{o}C) to avoid temperature induced changes in pH. Unlike for the samples of He et al.,[150] two step calcination made virtually no difference to the XRD patterns of the samples produced for this thesis made via the method of Edler[148]. Consequently calcination was performed at 773 K (500^{o}C) in a muffle furnace for at least 12 hours. Table 3-2 summarises the chemical compositions used to produce pure MCM-41

Table 3-2: Summary of MCM-41 samples produced, the molar compositions used, ageing time and whether a pH adjustment was used.

Sample Name	Si	CTAB	Ageing Time	pH Adjustment
MCM-41-1	1	0.09	<1 min	No
MCM-41-3	1	0.09	96 hours	Yes
MCM-41-7	1	0.17	96 hours	Yes
MCM-41-8	1	0.26	96 hours	Yes
MCM-41-11	1	0.26	96 hours	Yes
MCM-41-16	1	0.26	1 hour	Yes
MCM-41-18	1	0.26	8 hours	Yes
MCM-41-20	1	0.26	24 hours	Yes
MCM-41-22	1	0.26	48 hours	Yes
Sample Name	Si	DTAB	Ageing Time	pH Adjustment
MCM-41-13	1	0.26	96 hours	Yes
MCM-41-14	1	0.26	96 hours	Yes
MCM-41-29	1	0.19	48 hours	Yes

3.4.1.2. Zinc Doped MCM-41

Samples of zinc doped MCM-41 were produced using the same method as that for pure MCM-41. The zinc source was zinc sulphate heptahydrate ($ZnSO_4.7H_2O$) added to the surfactant solution prior to the addition of sodium silicate. The pH was then reduced to 10 with the addition of 1 M sulphuric acid before the samples were aged at 343 K (70^{o}C) for 48 hours with a pH adjustment to 10 after 24 hours. The pH after 48 hours was at 10 indicating that the polymerisation of the silica had finished [148] and hence the ageing process was halted at this point. Table 3-3 shows the chemical compositions of the zinc doped MCM-41 samples.

Table 3-3: Summary of molar compositions used to produced zinc doped MCM-41.

Sample Name	Si	CTAB	Zn	Si:Zn
MCM-41-26	1	0.18	0.16	6.3:1
MCM-41-27	1	0.17	0.08	12.2:1
MCM-41-28	1	0.17	0.41	2.4:1
MCM-41-30	1	0.17	0.02	49.8:1

3.4.1.3. Aluminium Doped MCM-41

Aluminium doped samples of MCM-41 were produced based on the method of Yu et al[151]. The method can be summarised as follows: aluminium chloride hexahydrate ($AlCl_3.6H_2O$) is dissolved in a solution of CTAB and sodium hydroxide. Tetraethyl orthosilicate was then added dropwise to this solution under stirring for 1-2 hours during which time a precipitate begins to form. Following stirring, 1 M sulphuric acid was used to reduce the pH to 10 before the mixture was put into the autoclave at 343 K (70^oC) and aged. Table 3-4 summarises the synthesis conditions of two aluminium doped MCM -41 samples.

Table 3-4: Summary of Al-doped MCM-41 samples produced, the molar compositions, ageing time and whether a pH adjustment was used.

Sample Name	Si	CTAB	H_2O	Al	Si:Al	Ageing Time	pH Adjustment
MCM-41-10	1	0.12	111	0.10	10.1:1	96 hours	Yes
MCM-41-31	1	0.13	112	0.02	46.4:1	48 hours	No

3.4.2. X-ray Diffraction

X-ray diffraction was performed on a Siemen's D500 using a wavelength, λ, of 0.154056 nm. After some experimentation, a step size of 0.04^o 2θ with a collection time of 6 seconds per step over the 2θ range of 1.5 to 10^o was used. Due to the relatively low angle used, scattering from the sample holder and air was significant. Consequently a blank run was performed for each sample holder used and was subtracted from subsequent patterns.

3.4.3. Nitrogen Adsorption/Desorption Isotherms

Nitrogen adsorption/desorption curves were performed at ANSTO on a Micromeritics ASAP 2400 instrument at 77 K. All samples were outgassed at 473 K (200°C) overnight prior to measurements being performed.

Nitrogen adsorption/desorption curves can be used to give useful information about the surface and area and pore size distribution of MCM-41 samples. When combined with X-ray diffraction data, information on wall thickness can also be derived. Figure 3-5 shows the nitrogen adsorption and desorption curve for a purely siliceous MCM-41, sample MCM-41-7.

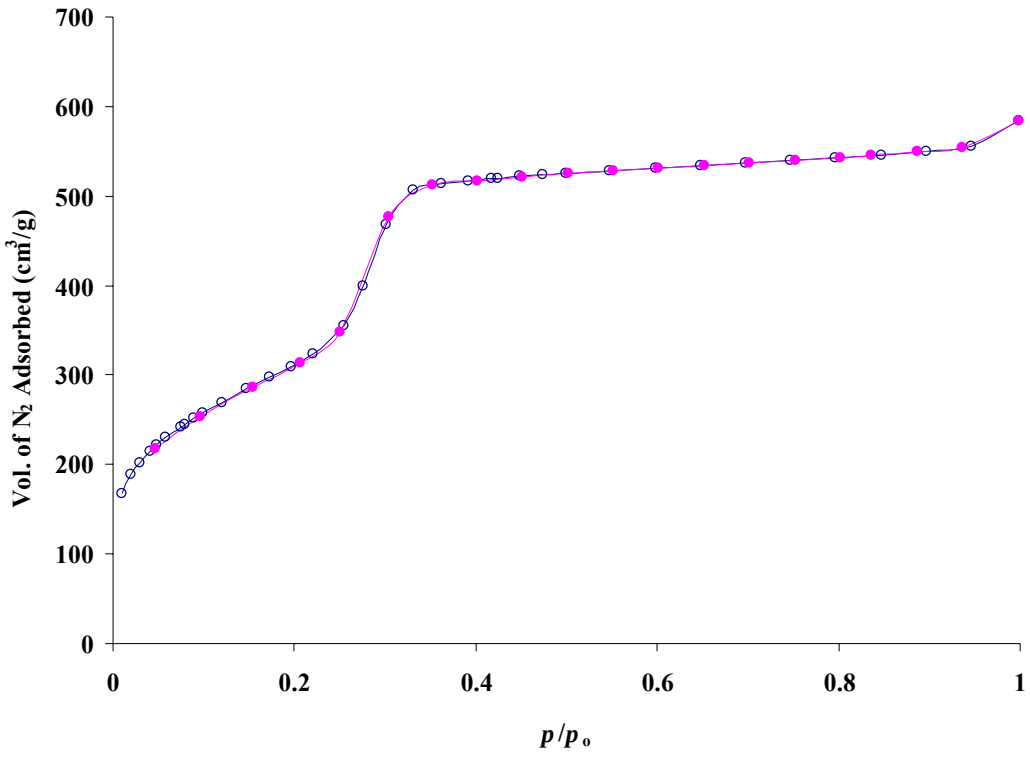

Figure 3-5: Nitrogen adsorption/desorption curves obtained at 77 K for sample MCM-41-7. (○) indicates adsorption while (●) indicates desorption.

The typical features of an adsorption/desorption curve on MCM-41 include nitrogen monolayer formation on all surfaces of the sample at pressures below $p/p_o < 0.2$ followed by capillary condensation in the cylindrical pores of the MCM-41 in the pressure range 0.2 - 0.4 (with the exact pressure being dependent on the pore size of

the material) associated with a steep uptake in nitrogen. A relatively flat plateau follows due to all surfaces being saturated with a monolayer of nitrogen and mesopores being filled with nitrogen. Above a pressure of p/p_o = 0.9 there may be condensation of nitrogen in the macropores of the sample. That is, the pores formed between grains are subject to nitrogen condensation. One interesting feature of the nitrogen adsorption/desorption curves in MCM-41 is that, for pores less than 4 nm in size, there is no hysteresis in the desorption curve.

The nitrogen adsorption data for MCM-41 was analysed using the Barrett-Joyner-Halenda (BJH) method[152]. The BJH method uses the assumption that the equilibrium pressure between a gas phase and an adsorbed phase is influenced by physical adsorption on the pore walls and capillary condensation within the pores. The result is that a specific equilibrium pressure is related to a specific pore size via the Kelvin equation. The original BJH method has been shown to be problematic in its application to MCM-41 and so an implementation known as Kruk-Jaroniec-Sayari (KJS) method[153] was utilised. The KJS method uses the form of the Harkins – Jura equation, as shown in equation (3-1), to estimate the film thickness of nitrogen at a given pressure;

$$t(p/p_o) = 0.1\left[\frac{60.65}{0.03071 - \log(p/p_o)}\right]^{0.3968} \qquad (3\text{-}1)$$

Where t = the statistical film thickness of nitrogen for a given p/p_o (nm)

p = the actual vapour pressure

p_o = the saturated vapour pressure

From this the pore radius that will be filled with nitrogen at a particular pressure, $r(p/p_o)$, is given by the addition of equation (3-1) to a modified form of the Kelvin equation;

$$r(p/p_o) = \frac{2\gamma V_L}{RT\ln(p_o/p)} + t(p/p_o) + 0.3nm \qquad (3\text{-}2)$$

Where γ = the surface tension of the adsorbate

V_L = the molar volume of the liquid adsorbate

R = the universal gas constant

T = the temperature in Kelvin

The BJH method usually employs the desorption branch of nitrogen isotherms for pore size analysis but, due to its unique properties, MCM-41 requires that the adsorption branch be used. A detailed explanation of the derivation of these equations may be found in Kruk, Jaroniec and Sayari[153].

Due to the limited number of adsorption points, the peak of the pore size distribution often falls between data points. To interpolate between these points and to determine an estimate of the peak position, a double Gaussian function was fitted to the data, an example of which is displayed in Figure 3-6.

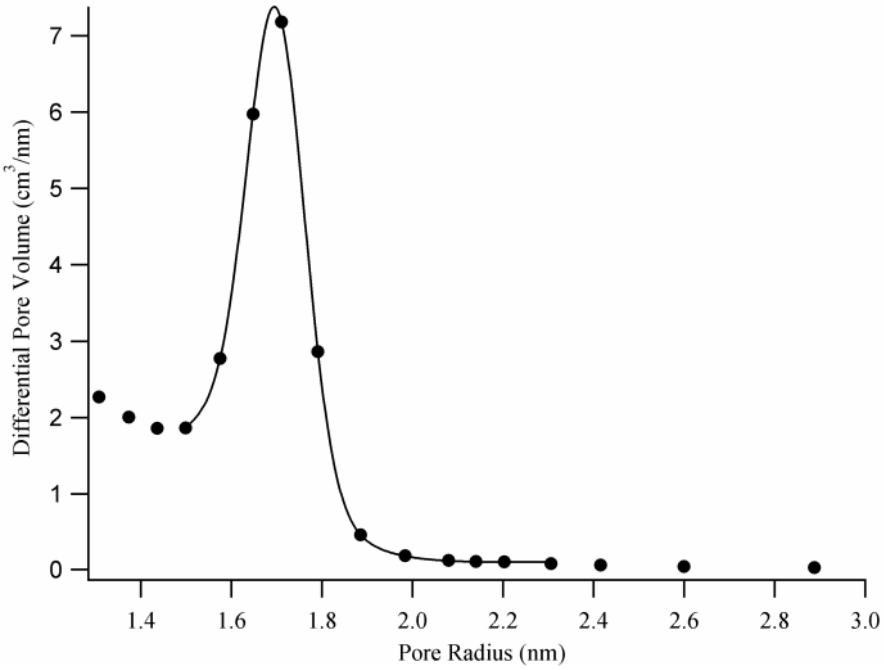

Figure 3-6: Pore size distribution derived from N_2 adsorption at 77 K on MCM-41-7. Solid circles indicate data points while the solid line indicates the fitted curve.

Where multiple peaks were present or the peak was poorly defined, a best guess estimate was used based on the shape of the peak and the position of the two points either side of the peak.

The uncertainty on the average pore size quoted from this method is ± 0.1 nm. This number is derived based on the results of Jaroniec and Solovyov[154] who showed that the KJS method, the pore size derived from modelling of X-ray diffraction patterns and that nitrogen adsorption used in conjunction with geometric considerations agreed with each other to within 0.1 nm for pore sizes less than 4.5 nm. This number must be used with caution as it is merely the average pore size and does not give information about the pore size distribution.

3.4.4. Hydrogen Adsorption

Sample masses used typically varied between 0.5 and 0.9 g depending on the bulk density of the samples. All samples were compressed into the sample cell by hand as much as possible to increase the amount of sample inside the sample-cell. Broyer et al.[155] have shown that 100 MPa of uniaxial compression is required before MCM-41 suffers noticeable structural damage and such a pressure is unlikely in manual compression. All hydrogen measurements were preceded by out-gassing of the sample under vacuum at 473 K (200^{o}C) for at least 12 hours prior to any adsorption measurements being performed. The density of the silica was taken to be 2.2 g/cm^{3} [138,156] though other values have been reported[157]. Given that the desorption curves follow the adsorption curves for MCM-41, the desorption curves have been excluded from the figures to improve clarity.

3.5. Results

3.5.1. Pure MCM-41 Made with CTAB

3.5.1.1. Effect of surfactant:silica ratio

The first goal was to produce a sample of MCM-41. Given the variety of methods available for MCM-41 production, a method from the literature was required. The method of Edler and White[148] was initially chosen because their samples exhibited better long range order than most others reported in the literature. However, ignorance of the Krafft Temperature lead to early experimental difficulties.

After trying different solubilities of the CTAB surfactant, a sample was made with only a relatively low level of surfactant dissolved in water with the surfactant solution

mixed with the sodium silicate and aged for less than one minute at room temperature. The uncalcined X-ray diffraction pattern for this sample is labelled as (a) in Figure 3-1. Typical synthesis conditions in the literature use substantially more CTAB, longer mixing and ageing times as well as higher ageing temperatures. Despite this, four broad diffraction peaks were evident in the X-ray diffraction pattern (Figure 3-7 (a)) of the uncalcined material, sample MCM-41-1

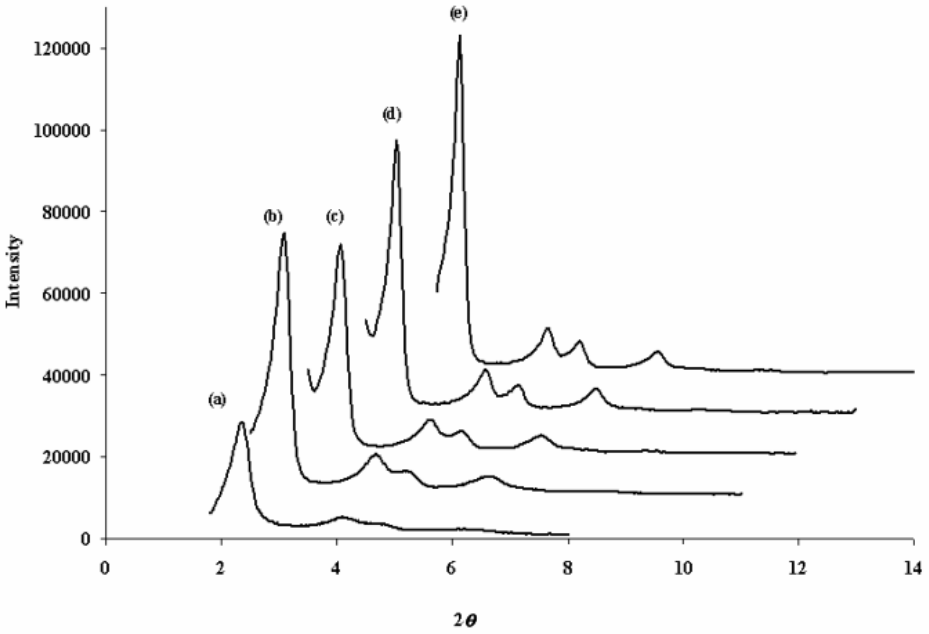

Figure 3-7: XRD pattern of uncalcined MCM-41 samples. (a) MCM-41-1, (b) MCM-41-3, (c) MCM-41-7, (d) MCM-41-8 and, (e) MCM-41-11. Each pattern is offset by 1° 2θ and 10,000 counts from the previous pattern.

In the literature, the main factor that varies between sample preparations is the molar ratio between the template surfactant, the silica and the water content. Once awareness of the Krafft temperature was taken into account, the same molar ratio of reagents were used as for MCM-41-1 in producing sample MCM-41-3 but using the pH adjustment method of Edler and White[148]. To explore the effect different surfactant, silica and water ratios may have on the final product, a number of samples were produced using the same ageing time, temperature and pH adjustment, but with different molar ratios. These molar ratios are displayed in Table 3-5. As a comparison, the molar ratio of Si:CTAB:H_2O used by Edler and White[148] was 1:0.53:85. The XRD patterns of the resulting samples are displayed in Figure 3-7.

Table 3-5: Molar compositions for the MCM-41 samples whose XRD patterns are shown in Figure 3-7.

Sample Name	Si	CTAB	H_2O	Ageing Time
MCM-41-1	1	0.09	282	<1 min
MCM-41-3	1	0.09	282	96 hours
MCM-41-7	1	0.17	281	96 hours
MCM-41-8	1	0.26	283	96 hours
MCM-41-11	1	0.26	52	96 hours

Figure 3-8 shows X-ray diffraction patterns of the calcined samples from Figure 3-7. The broadening of the d_{210} diffraction peak for all the samples after calcination indicates a decrease in the long range pore ordering. The sample aged for less than one minute showed almost total loss of long range pore order upon calcination with all peaks beyond the main d_{100} having been removed. There was no significant difference between the XRD patterns of the calcined samples (c) MCM-41-7 (d) MCM-41-8 and (e) MCM-41-11

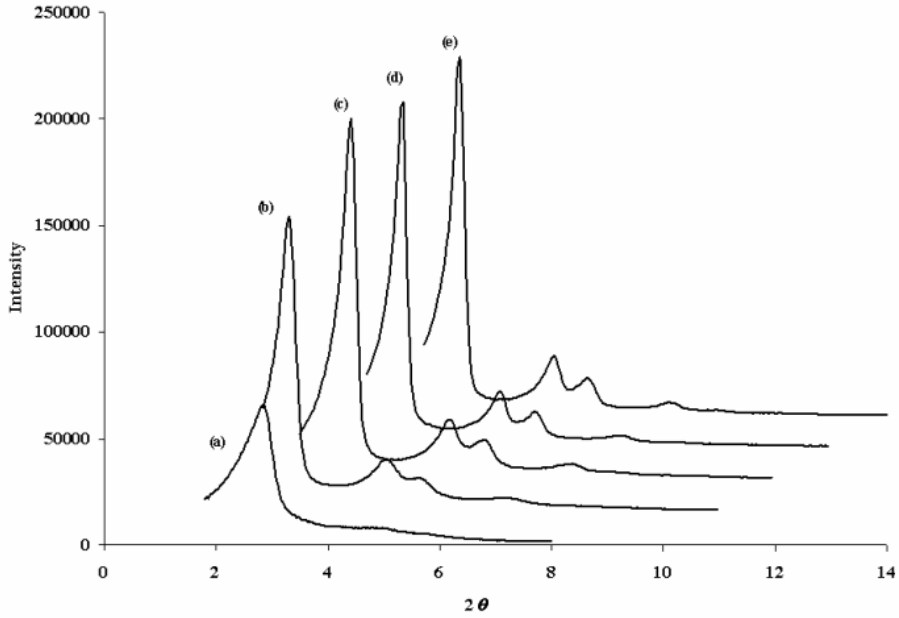

Figure 3-8: XRD pattern of calcined MCM-41 samples. (a) MCM-41-1, (b) MCM-41-3, (c) MCM-41-7, (d) MCM-41-8 and, (e) MCM-41-11. Each pattern has been offset by 1^o 2θ and 15000 counts for clarity.

An important experimental observation was made during the production of the samples listed in Table 3-5. The samples go through a very noticeable gelation point

while the silica source is being added to the surfactant solution. This gelation phenomenon has previously been reported by Edler and White[148]. Their observation was that the addition of sulphuric acid to the surfactant/silica mixture resulted in gelation as the pH decreased through a value of ~11. For the samples in Figure 3-8, the gelation occurs during the addition of the silica source to the surfactant. Given that the silica source (which is highly basic) results in an increase in pH of the surfactant solution, it is conceivable that the gelation experienced is the result of the pH transitioning upwards through a pH of 11. This would also explain why a more dilute surfactant solution (i.e. one with more water) shows less pronounced gelation than a more concentrated surfactant solution. At times during mixing the gelation resulted in impaired movement or even complete cessation of the magnetic stirring bar. Given this tendency for gelation in surfactant rich solutions and that there is no significant difference in the end product when using a lower surfactant concentration, low surfactant concentrations similar to those of samples MCM-41-7 and MCM-41-8 were used for all subsequent samples unless otherwise noted.

3.5.1.2. Effect of Ageing Time

The effect of ageing time on the structure of MCM-41 was also examined. Using the same molar composition as for sample MCM-41-8, samples were made with ageing times of 1, 8, 24, 48 and 96 hours at 343 K (70^{o}C) respectively.

Table 3-6: MCM-41 samples made with the same chemical composition but aged for different periods of time.

Sample Name	Si	CTAB	H_2O	Ageing Time (hrs)	pH Adjustment
MCM-41-16	1	0.26	282	1	Yes
MCM-41-18	1	0.26	282	8	Yes
MCM-41-20	1	0.26	282	24	Yes
MCM-41-22	1	0.26	281	48	Yes
MCM-41-8	1	0.26	283	96	Yes

Figure 3-9 shows the resulting XRD patterns for the uncalcined samples while Figure 3-10 shows the XRD patterns for the calcined products.

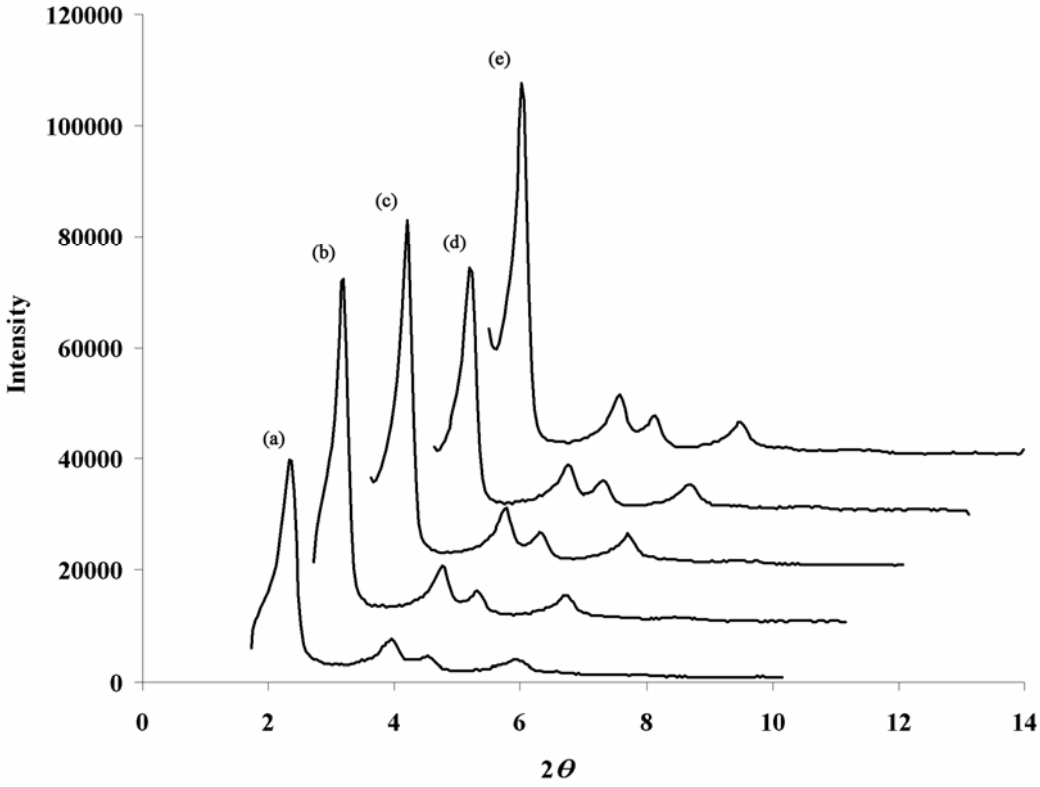

Figure 3-9: XRD pattern of uncalcined MCM-41 (a) MCM-41-16, (b) MCM-41-18, (c) MCM-41-20, (d) MCM-41-22 and (e) MCM-41-8. Each pattern is offset by 1° 2θ and 20,000 counts.

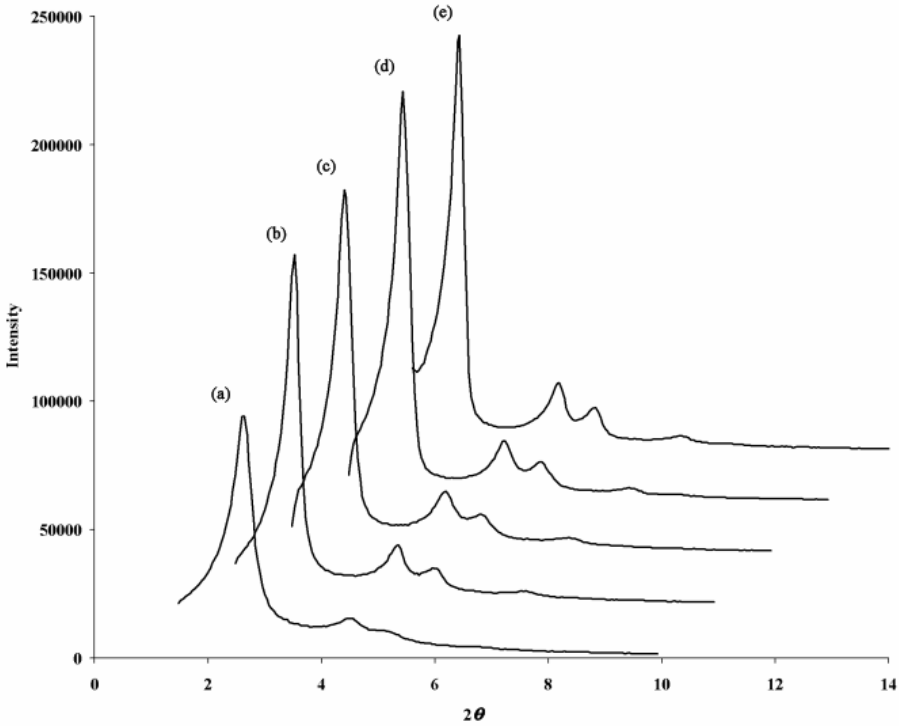

Figure 3-10: XRD pattern of calcined MCM-41 (a) MCM-41-16, (b) MCM-41-18, (c) MCM-41-20, (d) MCM-41-22 and (e) MCM-41-8. Each pattern is offset by 1° 2θ and 20,000 counts.

From Figure 3-10 it can be seen that, for the samples aged for 1 to 24 hours, there is a sharpening of the main d_{100} diffraction peak with increasing ageing time. The d_{110}, d_{200}, and d_{210} peaks also become more resolved. The samples aged for 24, 48 and 96 hours show little difference in their XRD patterns.

3.5.1.3. Nitrogen Isotherm Data

Nitrogen adsorption experiments were performed to assess the surface area and pore size distribution of MCM-41 samples. The nitrogen adsorption isotherms performed at 77 K for samples MCM-41-16, MCM-41-18, MCM-41-20, MCM-41-22 and MCM-41-8 are presented in Figure 3-11. The desorption curves have been excluded for clarity.

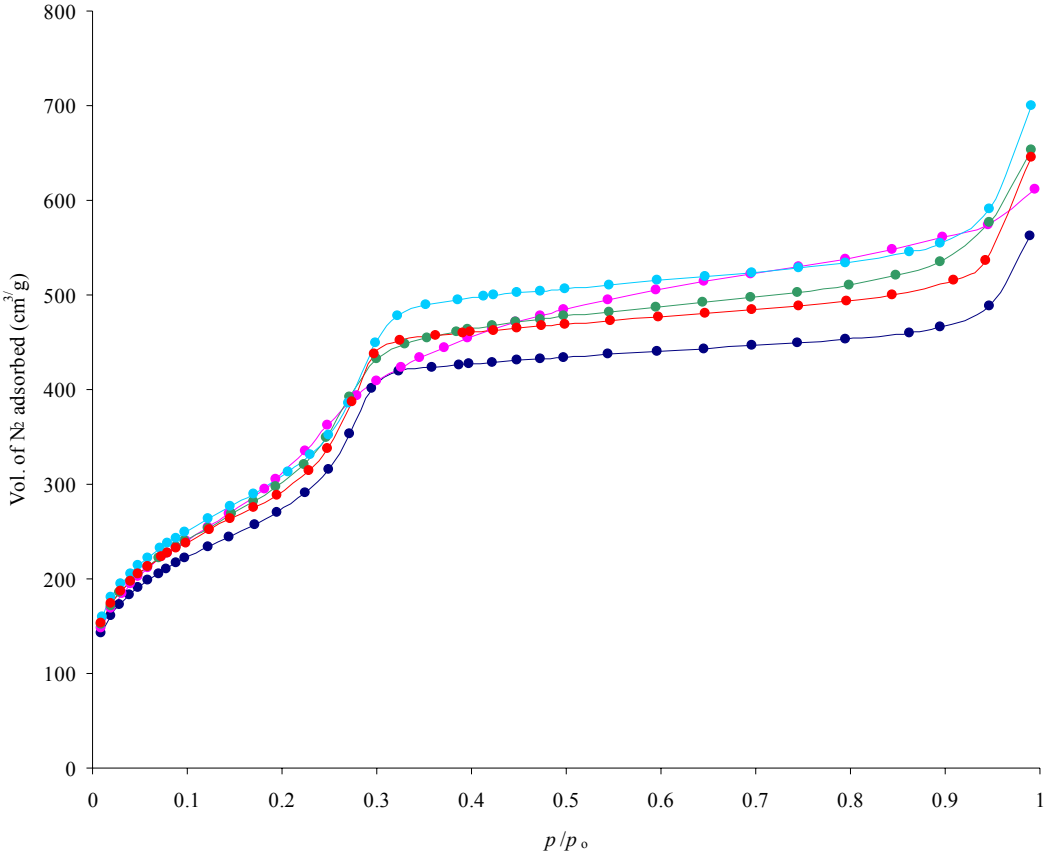

Figure 3-11: Nitrogen adsorption curves performed at 77 K on MCM-41-16 (●), MCM-41-18 (●), MCM-41-20 (●), MCM-41-22 (●) and MCM-41-8 (●).

Figure 3-11 shows nitrogen adsorptions isotherms typical for that of MCM-41. Sample MCM-41-16 shows a slight deviation from the typical isotherm in that rather than a flat plateau for a pressure $p/p_o > 0.3$ there is a sloping plateau. This suggests

incomplete filling of the mesopores. The isotherms of the other samples show slight variations in the level of their plateaux as their only differentiating features.

Figure 3-12(a) shows the BJH pore size distributions derived from Figure 3-11 for the samples MCM-41-18, MCM-41-20, MCM-41-22 and MCM-41-8 respectively. This shows that the samples aged for 24 hours or longer have comparable pore sizes with the average pore size for these samples ranging between 3.34 and 3.40 nm. For sample MCM-41-18, aged for 8 hours, the average pore size is 3.26 nm.

The BJH pore size for MCM-41-16, this time based on adsorption and desorption data, is shown separately in Figure 3-12(b). These pore size distributions were not amenable to the Gauss peak fitting as used for those samples in Figure 3-12(a). Adsorption yields an average pore size of 3.14 nm but the pore size distribution is significantly broader than those samples shown in Figure 3-12(a). Figure 3-12(a) shows that for all these samples, the pore size distribution shows no pores larger than 3.8 nm while Figure 3-12(b) indicates that MCM-41-16 has some pores as large as ~4.8 nm. This is commensurate with the sloping rather than flat plateau for MCM-41-16. This is further confirmed by the BJH analysis of the desorption isotherm for this sample which yields a secondary pore structure of ~4.4 nm.

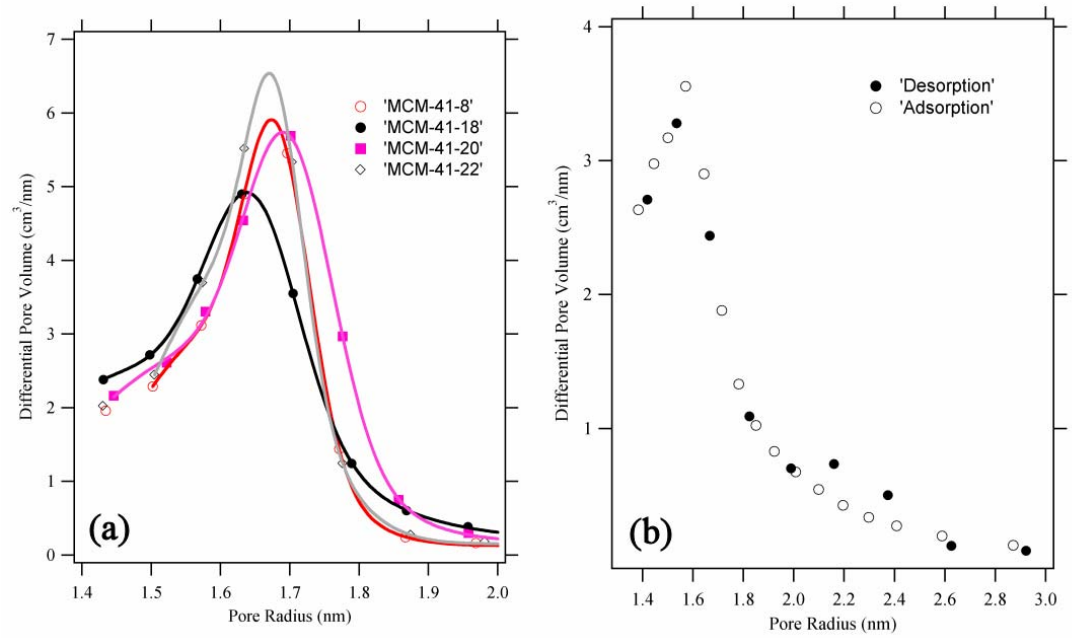

Figure 3-12: (a) Pore size distributions determined from N_2 adsorption isotherm at 77 K for MCM-41-8, MCM-41-18, MCM-41-20, MCM-41-22. (b) Pore size distribution for MCM-41-16 as determined by the adsorption and desorption curve from the N_2 isotherm at 77 K.

Surface area analysis of these samples, via the BET method, yielded surface area's ranging between 916 and 1032 m^2/g. These values appear to be independent of ageing time. Table 3-7 shows a summary of the data obtained from XRD, BET and BJH data.

Table 3-7: Data derived from XRD and N_2 adsorption/desorption isotherms.

Sample Name	Pore Repeat Distance (nm)	Pore Size (nm)	Wall Thickness (nm)	Surface Area (m^2/g)
MCM-41-16	3.89	3.14	0.75	993
MCM-41-18	4.05	3.26	0.79	991
MCM-41-20	4.25	3.40	0.85	1032
MCM-41-22	4.18	3.34	0.84	982
MCM-41-8	4.18	3.40	0.78	916

3.5.2. Pure MCM-41 made with DTAB

In an attempt to produce MCM-41 with smaller pores, the shorter chain surfactant decyltrimethylammonium bromide (DTAB) was used. Three samples were produced and their synthesis details are listed in Table 3-8.

Table 3-8: The chemical composition of MCM-41 samples made with decyltrimethylammonium bromide (DTAB) as the structure directing agent.

Sample Name	Si	DTAB	H_2O	Ageing Time	pH adjustment
MCM-41-13	1	0.26	281	96 hours	Yes
MCM-41-14	1	0.26	147	96 hours	Yes
MCM-41-29	1	0.19	282	48 hours	Yes

The first sample produced was MCM-41-13 and used the same molar ratio of reagents as that for the sample MCM-41-8 but with DTAB instead of CTAB. The XRD pattern of the calcined product is shown in Figure 3-13 (a). From this we see a distinct difference to previous patterns in that there is an overlap of two distinct strong peaks at $2\theta \sim 3.0^o$. The pattern is suggestive of a duel phase system comprising poorly defined hexagonal and cubic phases[119]. However, a subsequent sample was made (MCM-41-14) containing a higher wt.% of DTAB which resulted in a poorly defined hexagonal phase.

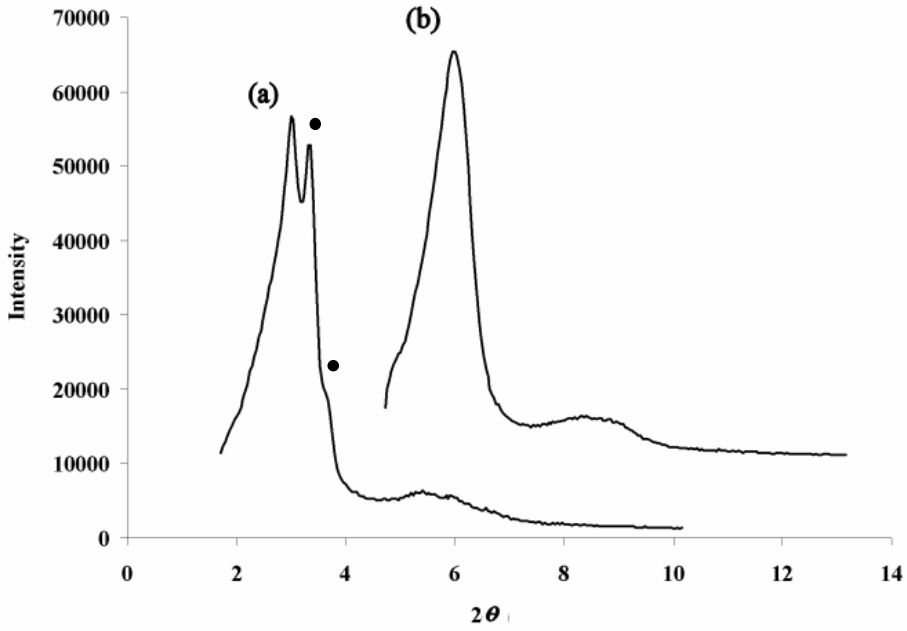

Figure 3-13: XRD pattern of calcined MCM-41. (a) MCM-41-13, (b) MCM-41-14. (b) is offset by 3° 2θ and 10,000 counts for clarity. • Indicates cubic phase known as MCM-48.

The d_{100} peak position position of sample MCM-41-14 is consistent with the first peak position of MCM-41-13 supporting the idea that the first peak position in the XRD pattern of MCM-41-13 is the hexagonal phase.

Though a phase diagram for decyltrimethylammonium bromide could not be obtained, phase diagrams for the similar surfactants dodecyltrimethylammonium chloride(DDTAC)-water, CTAB-water and cetyltrimethylammonium sulphate-water were obtained[158, 159, 160]. The CTAB-water phase diagram is relatively uninformative showing a progression from isotropic to hexagonal to cubic and finally a lamellar micelle shape progression. DDTAC is chemically very similar to DTAB but has a carbon chain two atoms longer and it contains chlorine instead of bromine. Examination of the phase diagram of DDTAC reveals a slightly different micelle phase progression to that for CTAB-water. In this case the progression goes from an isotropic solution at low surfactant concentration to a cubic phase, then hexagonal, then another cubic phase and finally a lamellar phase as the surfactant concentration is increased. Given that sulphate ions are added to the mixture via the use of sulphuric acid, parallels can also be drawn with the phase diagram for cetyltrimethylammonium

sulphate and water. This phase diagram also shows a cubic phase at low surfactant concentration.

It must be kept in mind that all of the preceding discussion has been applied to the case where we only have a binary system: surfactant and water. In reality we have a multi component system which consists of surfactant, water, silica source, sulphuric acid as well as the 5% impurity from the surfactant, all of which will have an effect on phase equilibria[158].

A sample (MCM-41-29) was produced using DTAB utilising the very dilute molar composition of sample MCM-41-7 to examine the resultant mesoporous phase. As has been the case for some other samples, gelation was an issue despite the silica source being added drop-wise to the surfactant solution. It was observed that after mixing and ageing, a portion of the MCM-41 sample remained floating on the top of the reaction solution. The sample that settled on the bottom of the reaction vessel was labelled as MCM-41-29a while the floating portion was collected and labelled as MCM-41-29b. A comparison between the uncalcined samples MCM-41-14, MCM-41-29a and MCM-41-29b is shown in Figure 3-14.

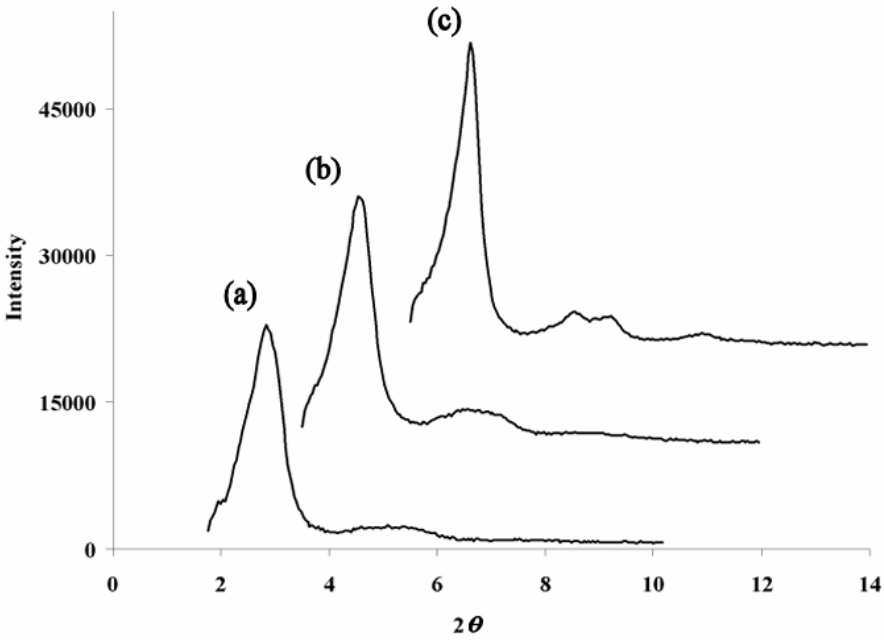

Figure 3-14: XRD pattern of uncalcined MCM-41 produced using DTAB as a surfactant. (a) MCM-41-14, (b) MCM-41-29a, (c) MCM-41-29b. Each pattern is offset by 2^{o} 2θ and 10,000 counts for clarity.

From this we see that MCM-41-14 (Figure 3-14 (a)) and MCM-41-29a (Figure 3-14(b)) have similar XRD patterns consisting of a distinct d_{100} peak. Where the second and third diffraction peaks would be expected for a highly ordered hexagonal phase we find a single broad hump. Sample MCM-41-29b (Figure 3-14(c)) extracted from the surface of the reaction liquid, however, shows a noticeably narrowing of the d_{100} diffraction peak while the broad hump has resolved into two peaks with a fourth peak also being evident. This suggests that the mixing method may have a significant impact on the long range pore ordering. An insufficient mixing speed may result in poor homogenisation of the sample while a high mixing speed results in shear forces that may disrupt long range structuring. However, a reasonable high mixing speed is required to prevent total gelation of the sample.

3.5.3. Zinc Doped MCM-41

Four samples were examined with the different zinc content and the synthesis conditions are shown in Table 3-9. All samples underwent pH adjustment

Table 3-9: The molar composition of MCM-41 samples doped with zinc.

Sample Name	Si	CTAB	H_2O	Zn	Si:Zn
MCM-41-26	1	0.18	280	0.16	6.3:1
MCM-41-27	1	0.17	282	0.08	12.2:1
MCM-41-28	1	0.17	281	0.41	2.4:1
MCM-41-30	1	0.17	282	0.02	49.8:1

There were noticeable differences during the production of the zinc doped samples compared to pure MCM-41. During ageing of the pure MCM-41 samples, the white precipitate settles to the bottom of the sample container. However, for zinc doped MCM-41 the precipitate remained suspended in solution. The typical ageing time for MCM-41 is 4 days but the ageing of the zinc doped samples produced for this thesis were halted at 48 hours. This is because the pH of the solution had not changed between 24 and 48 hours suggesting that the hydrolysis of silica was completed[148]. Lastly, the colour of the final calcined product was found to be dependent on zinc content. The lowest zinc loading of Si:Zn = 49.8:1 was white as is the case for pure MCM-41. The sample with a zinc loading of Si:Zn = 12.2:1 was, however, a pale

brown and the samples became progressively darker brown with increasing zinc content.

Figure 3-15 shows the uncalcined X-ray diffraction patterns for the four zinc doped samples while Figure 3-16 shows the calcined XRD patterns. MCM-41-31 (Si:Zn = 29.8:1) has a relatively well defined hexagonal pore structure indicated by four diffraction peaks. Increasing the zinc content to Si:Zn = 12.2:1 (MCM-41-27) yields a decreased long range pore ordering with noticeable broadening of and a reduction in the number of peaks to three. The increase in zinc content to Si:Zn = 6.3:1 and 2.4:1 removes almost all features beyond the d_{100} diffraction peak.

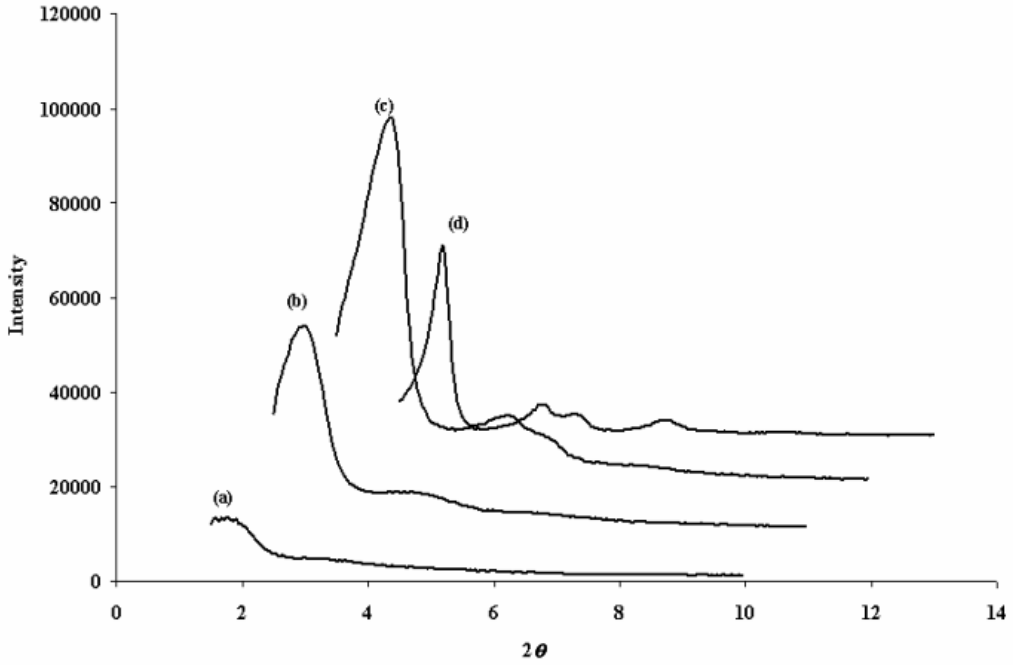

Figure 3-15: XRD pattern of uncalcined zinc-doped MCM-41 (a) sample MCM-41-28-Si:Zn = 2.4:1, (b) sample MCM-41-26-Si:Zn = 6.3:1, (c) sample MCM-41-27-Si:Zn = 12.2:1 and (d) sample MCM-41-30-Si:Zn = 49.8:1. Each pattern is offset by 1° 2θ and 10,000 counts for clarity.

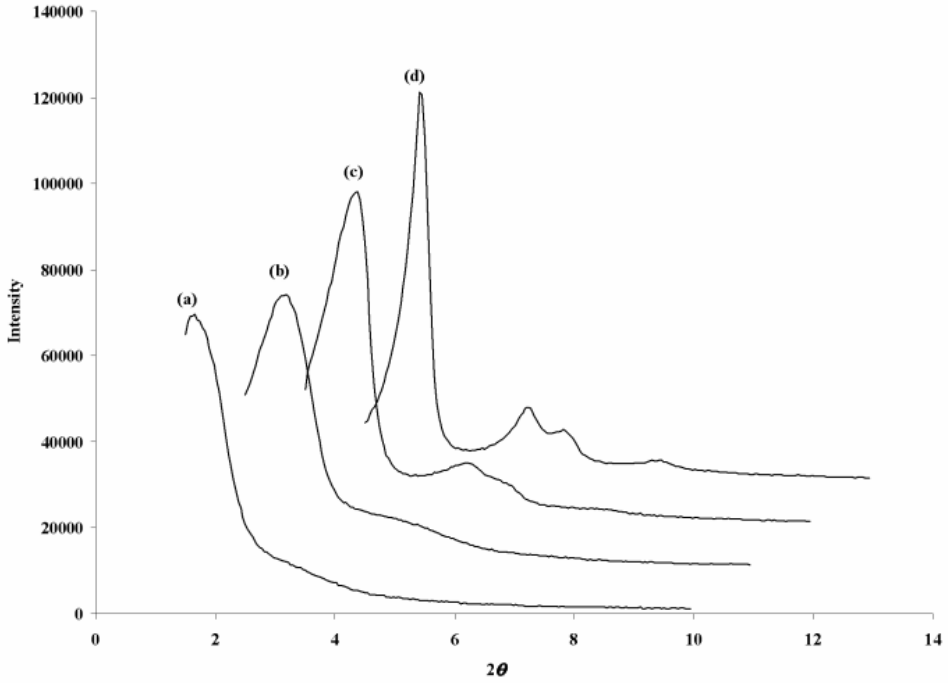

Figure 3-16: XRD pattern of calcined zinc-doped MCM-41. (a) sample MCM-41-28-Si:Zn = 2.4:1, (b) sample MCM-41-26-Si:Zn = 6.3:1, (c) sample MCM-41-27-Si:Zn = 12.2:1 and (d) sample MCM-41-30-Si:Zn = 49.8:1. Each pattern is offset by 1° 2θ and 10,000 counts for clarity.

The position of the d_{100} diffraction peak shows a correlation with zinc content. The d_{100} peak position for MCM-41-31 (Si:Zn rato of 49.8:1) has a *d*-spacing of 3.65 nm. This peak position shows a shift to lower 2θ angles with increasing zinc content and has a *d*-spacing of 5.39 nm for MCM-41-28 doped with a Si:Zn ratio of 2.4:1.

3.5.3.1. Nitrogen Isotherm Data

The nitrogen adsorption and desorption isotherms, performed at 77 K, for the zinc doped MCM-41 samples is shown in Figure 3-17. The adsorption/desorption isotherm for the sample with the lowest zinc loading (MCM-41-30-Si:Zn=49.8:1) is typical of that for MCM-41. As the zinc content increases, the characteristic steep uptake between a pressure of p/p_o = 0.25 – 0.35 becomes less pronounced suggesting a decrease in the uniformity of the pore size. In addition, the characteristic flat plateau above a pressure of p/p_o > 0.35 becomes progressively more sloped with increasing zinc content.

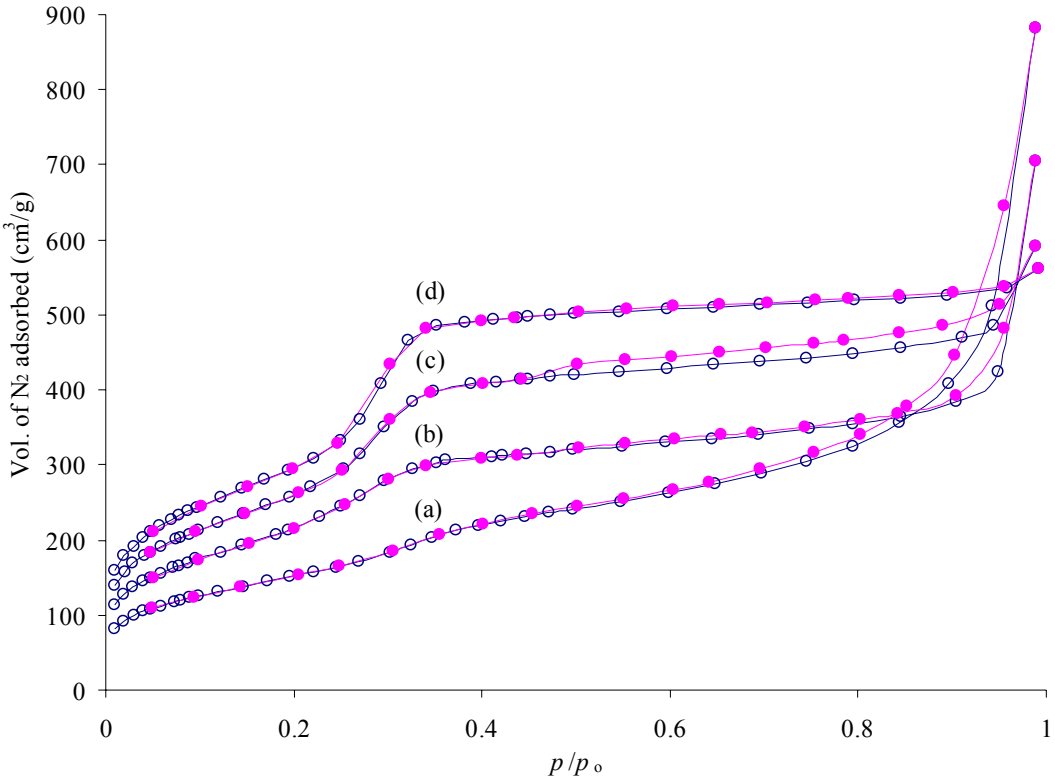

Figure 3-17: Nitrogen adsorption/desorption isotherms performed at 77 K on Zn-doped calcined MCM-41. (a) sample MCM-41-28-Si:Zn=2.4:1, (b) sample MCM-41-26-Si:Zn=6.3:1, (c) sample MCM-41-27-Si:Zn=12.2:1 and (d) sample MCM-41-30-Si:Zn=49.8:1. (○) indicates adsorption while (●) indicates desorption.

The BJH pore size distributions are shown in Figure 3-18 with that of pure MCM-41-7 shown as a comparison. The average pore size varies little with zinc content. The largest average pore size, 3.56 nm, is for the highest level of zinc while the smallest average pore size, 3.28 nm, is for MCM-41-26 containing a Si:Zn ratio of 6.3:1. The pore size for the other samples doped with zinc and that of pure MCM-41-7 fall within this range. Despite the pore size being relatively constant with zinc loading, the intensity of the pore size distribution peak reduces with increasing zinc content indicating that there are fewer pores with a similar size. We also see the presence of secondary pore systems in MCM-41-26-Si:Zn=6.3:1 (indicated by the arrows) of ~2.9 and ~3.8 nm in size respectively. In addition, though not shown in Figure 3-18, the hysteresis evident for MCM-41-27-Si:Zn=12.2:1 in the nitrogen desorption curve (Figure 3-17(c)) corresponds to a secondary pore structure of ~4.8 nm in size.

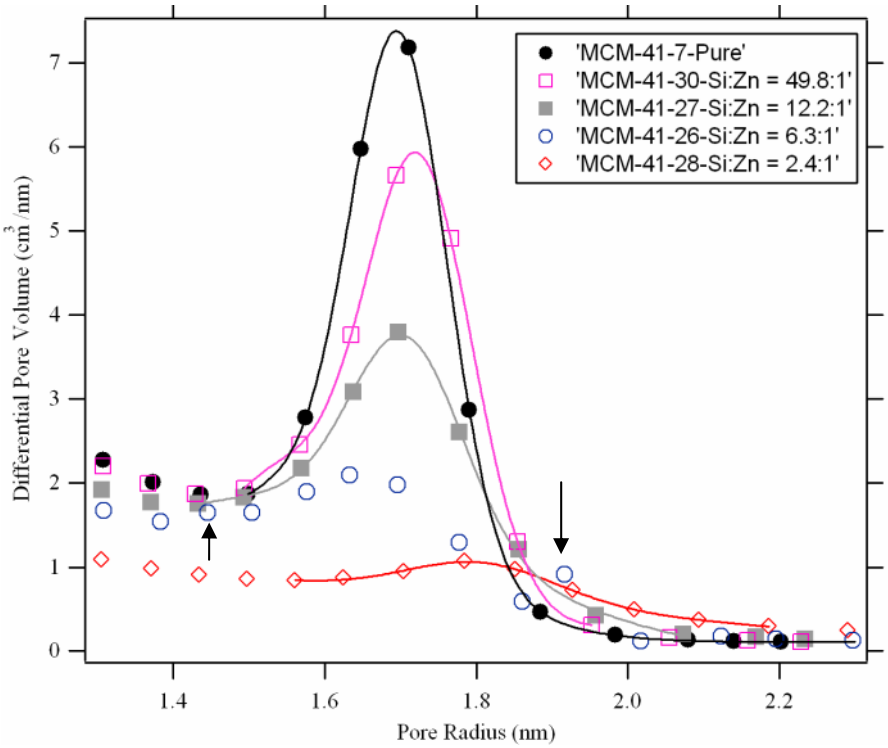

Figure 3-18: Pore size distributions for zinc doped MCM-41. Solid lines indicate interpolation between data points.

Though there is no obvious correlation between zinc loading and pore size, there is a clear effect on surface area. Figure 3-19 plots the surface area versus zinc content for samples MCM-41-26-Si:Zn=6.3:1, MCM-41-27-Si:Zn=12.2:1, MCM-41-28-Si:Zn=2.4:1 and MCM-41-30-Si:Zn=49.8:1. The horizontal line represents the surface area for pure MCM-41-7. As can be seen, a zinc loading of Si:Zn = 49.8:1 has negligible impact on the surface area. As the zinc content increases, the effect on surface area becomes more pronounced. At a Si:Zn ratio of 2.4:1 the surface area has approximately halved as compared to pure MCM-41.

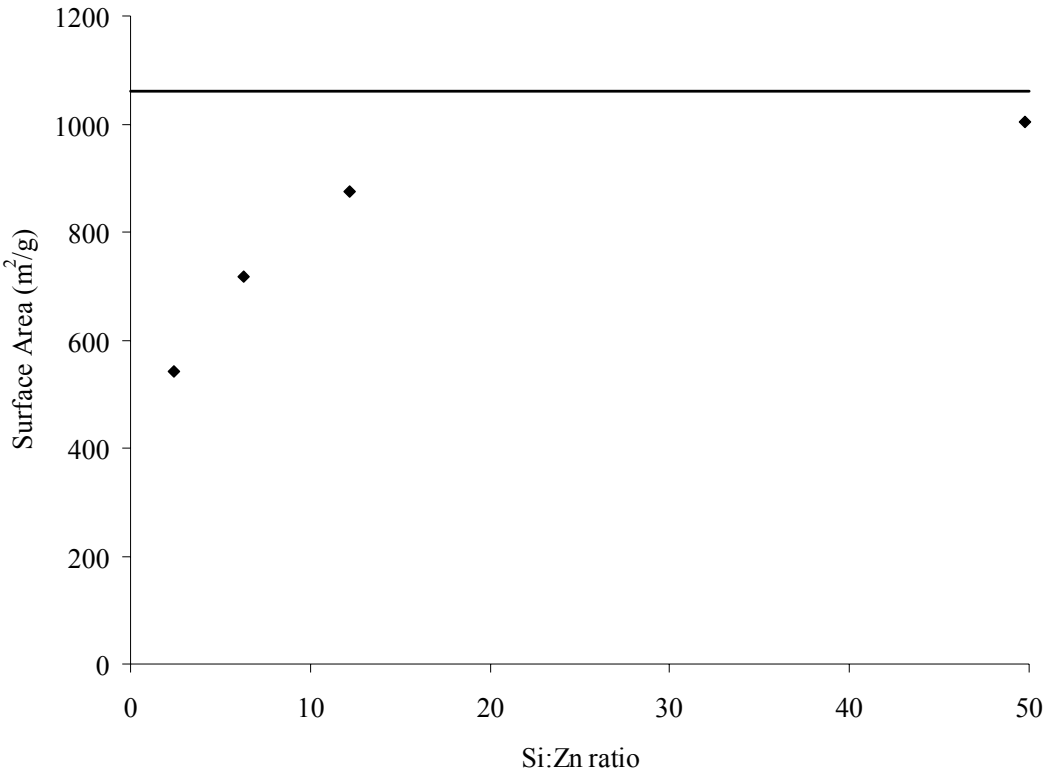

Figure 3-19: Surface area of zinc doped MCM-41 samples measured via the BET method as a function of zinc loading. The solid line indicates the surface area of a purely siliceous MCM-41-7 made without zinc.

A summation of the data obtained from XRD and nitrogen adsorption/desorption isotherms is shown in Table 3-10. The data for pure MCM-41-7 is also included as a comparison.

Table 3-10: Data derived from XRD and nitrogen adsorption/desorption isotherms. The data for pure MCM-41-7 is included as a comparison.

Sample Name	Si:Zn Ratio	Pore Repeat Distance (nm)	Pore Size (nm)	Wall Thickness (nm)	Surface Area (m^2/g)
MCM-41-28	2.4:1	6.22	3.62	2.60	516
MCM-41-26	6.3:1	4.72	3.28	1.44	717
MCM-41-27	12.2:1	4.29	3.42	0.87	875
MCM-41-30	49.8:1	4.22	3.44	0.78	1004
MCM-41-7	-	4.22	3.40	0.82	1060

Given that the BJH pore size analysis reveals the pore sizes to be reasonably consistent regardless of zinc loading, we find that the wall thickness increases with

increasing zinc content. Given that the Zn – O bond is longer than the Si – O bond[161], this suggests that zinc is being incorporated into the pore wall.

3.5.4. Al-doped MCM-41

Figure 3-20(a) shows the uncalcined XRD pattern for MCM-41-10 doped at a Si:Al ratio of 10.1:1 while Figure 3-20(b) shows the uncalcined pattern for MCM-41-31 doped at a Si:Al ratio of 46.4:1. The patterns are typical of MCM-41, comprising one strong and three weaker diffraction peaks.

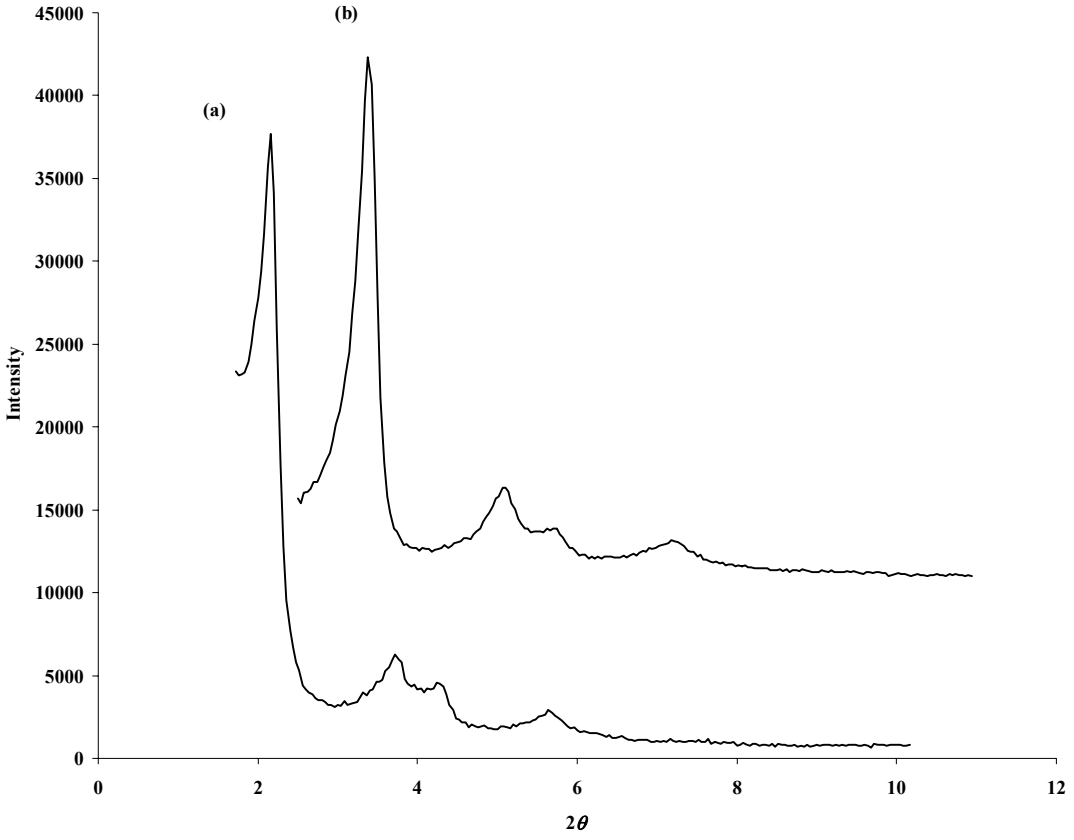

Figure 3-20: XRD pattern of uncalcined aluminium-doped MCM-41 (a) sample MCM-41-10-Si:Al = 10.1:1 and (b) MCM-41-31-Si:Zn = 46.4:1. (b) is offset by 1° 2θ and 10,000 counts for clarity.

Despite their similar XRD patterns prior to calcination, sample MCM-41-10-Si:Al=10.1:1 and MCM-41-31-Si:Al=46.4:1 show distinct differences after calcination (Figure 3-21(a) and (b) respectively). Sample MCM-41-10-Si:Al=10.1:1

shows a typical XRD pattern after calcination while MCM-41-31-Si:Al=46.4:1 shows an almost total loss of diffraction peaks beyond that of the main d_{100} peak.

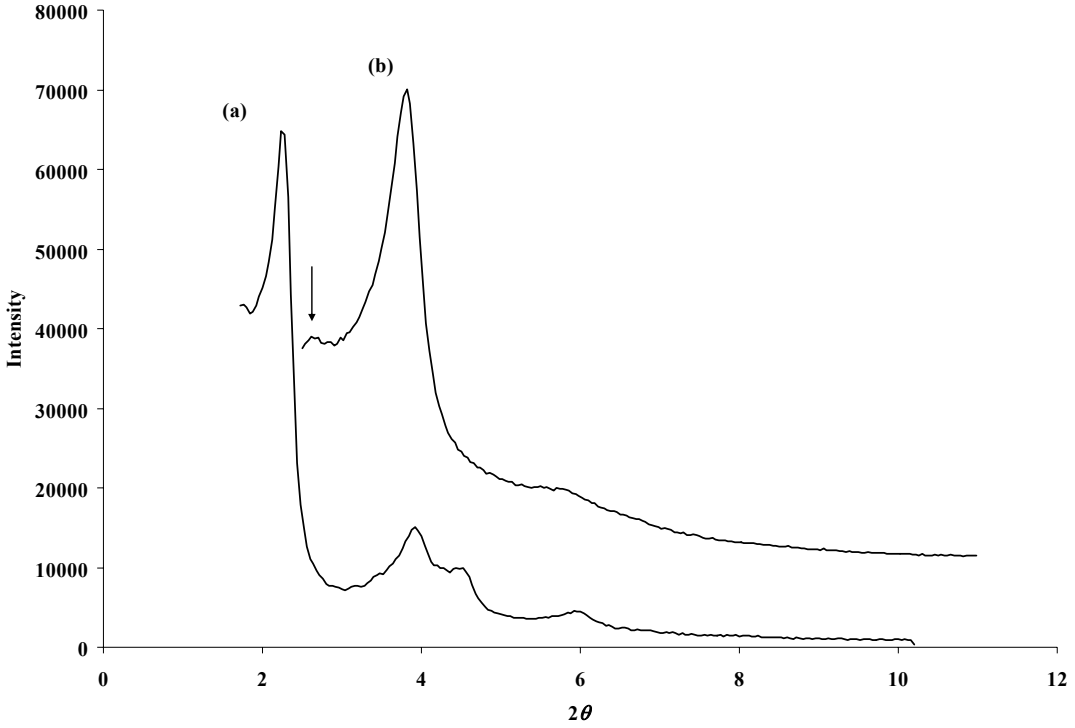

Figure 3-21: XRD pattern of calcined aluminium-doped MCM-41. (a) sample MCM-41-10-Si:Al = 10.1:1 and (b) MCM-41-31-Si:Al = 46.4:1. (b) is offset by 1° 2θ and 10,000 counts for clarity.

3.5.4.1. Nitrogen Isotherm Data

The N_2 isotherm for MCM-41-31-Si:Al=46.4:1 is shown in Figure 3-22(a) and is markedly different to that of pure MCM-41-7 shown in Figure 3-22(b). Up to a pressure of p/p_o = 0.1 the adsorption curves of MCM-41-31 and MCM-41-7 are similiar. However, instead of the sharp uptake that occurs between p/p_o = 0.25 and 0.35 for MCM-41-7, associated with capillary condensation in similar size pores, we see a continuous curve up to a p/p_o of ~0.55 for MCM-41-31. At this point the adsorption curve for MCM-41-31 flattens indicating the completion of mesopore filling. Desorption from MCM-41-31also shows minor hysteresis between p/p_o = 0.55 and 0.40.

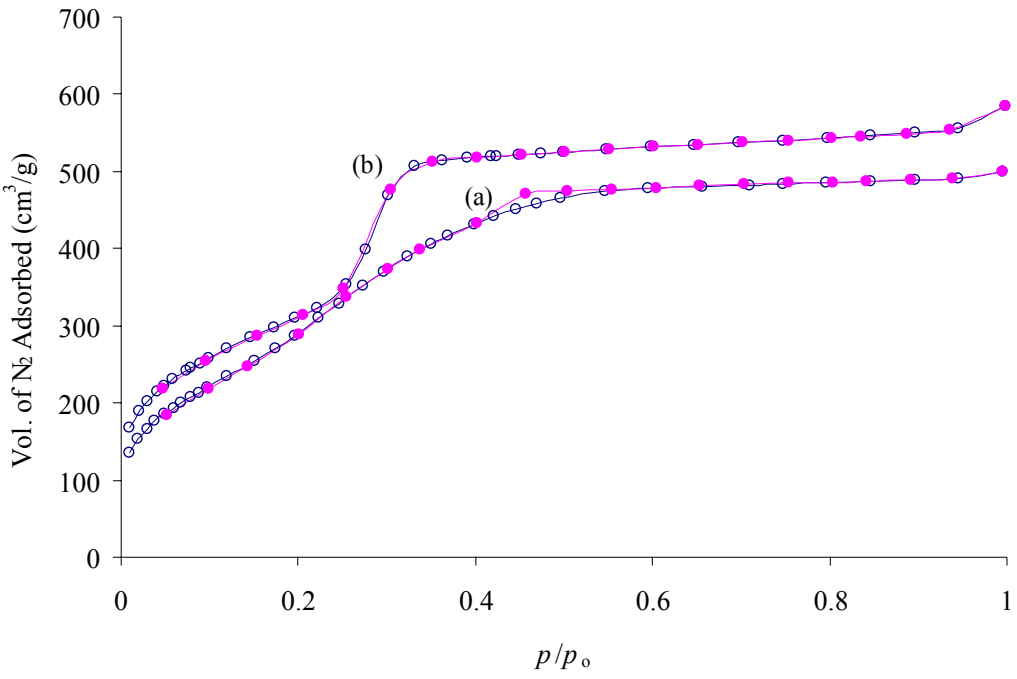

Figure 3-22: Nitrogen adsorption/desorption curves obtained at 77 K for (a) sample MCM-41-31-Si:Al = 46.4:1 and (b) pure MCM-41-7 as a comparison. (○) indicates adsorption (●) indicates desorption.

The BJH pore size analysis of MCM-41-31 derived from both the adsorption and desorption isotherms are shown in Figure 3-23. The adsorption curves yields an average pore size of ~2.94 nm but the distribution is significantly broader than those for pure MCM-41 samples (See Figure 3-12). This is borne out by the desorption analysis which shows a small secondary peak corresponding to a pore size of ~4.4 nm. A closer examination of the XRD pattern of calcined MCM-41-31-Si:Al=46.4.1 (Figure 3-21) yields a small peak (indicated by the arrow) at $2\theta \sim 1.7^{o}$ (once the 1^{o} offset has been accounted for) corresponding to a *d*-spacing of 5.2 nm. Given that the typical pore wall thickness for both low-level zinc doped MCM-41 and pure MCM-41 was determined to be ~0.8 nm, these two features seem to correlate well with each other.

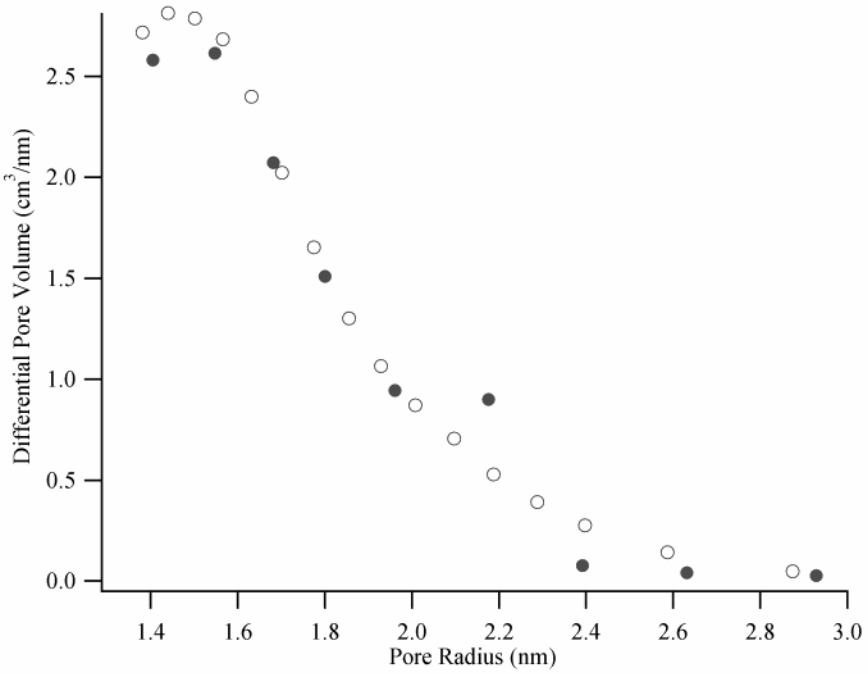

Figure 3-23: Pore size distribution for MCM-41-31. (○) indicates adsorption data while (●) indicates desorption data.

3.5.5. Hydrogen Adsorption Results

Figure 3-24 shows the hydrogen uptake at 77 K for samples MCM-41-8, MCM-41-16, MCM-41-18, MCM-41-20 and MCM-41-22. Hydrogen uptake for these samples ranges between 1.68 and 1.98 wt.% at ~4.5 MPa. However, the highest uptake, for sample MCM-41-20, must be viewed with some caution due to the large uncertainty associated with the measurements. This large uncertainty arises from the relatively small sample mass used for the hydrogen adsorption measurement.

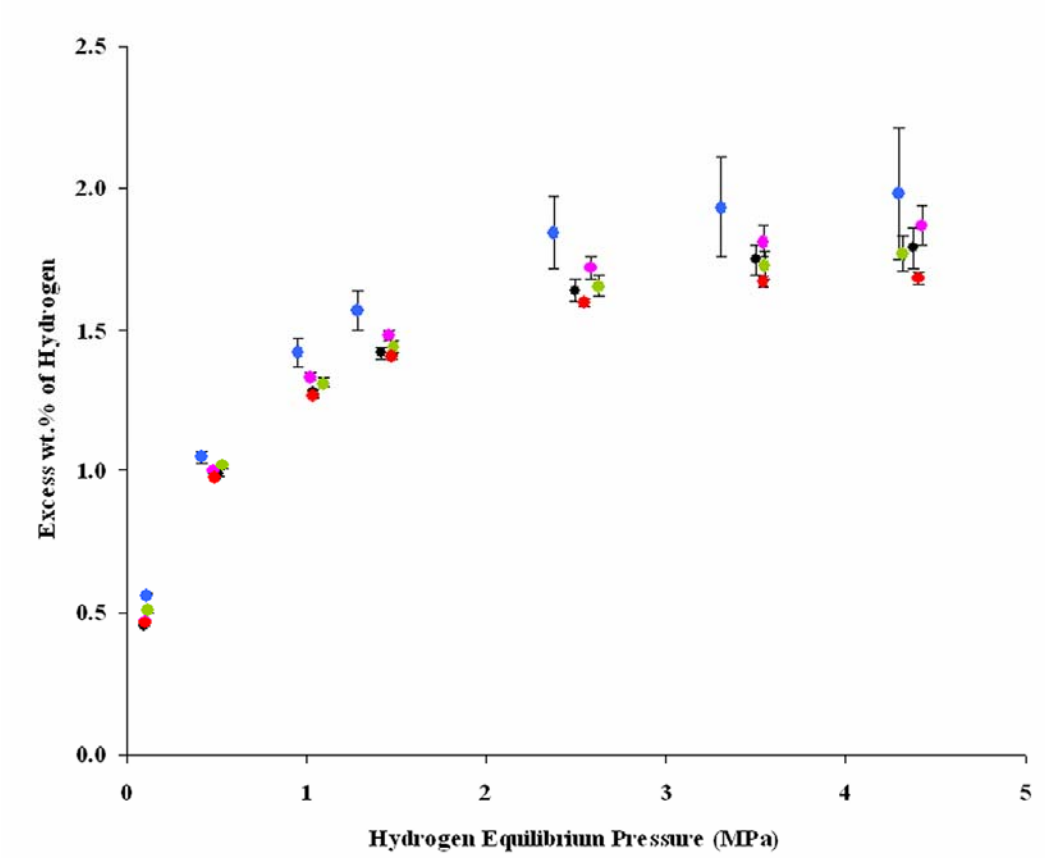

Figure 3-24: Hydrogen adsorption at 77 K on MCM-41-8 (●), MCM-41-16 (●), MCM-41-18 (●), MCM-41-20 (●) and MCM-41-22 (●).

Figure 3-25 shows the hydrogen uptake, measured at 77 K, for the two samples made with DTAB surfactant, MCM-13 and MCM-14, compared to the hydrogen uptake of sample MCM-41-7 made using CTAB surfactant. The hydrogen uptake is near identical for MCM-41-13 and MCM-41-14 despite the significant difference in their respective XRD patterns (Figure 3-13(a) and (b) respectively). The hydrogen uptake for these samples at ~4.5 MPa is 1.48 and 1.50 wt.% respectively and is characterised by hydrogen uptake curves that approach a plateau at lower pressure than for samples made with CTAB

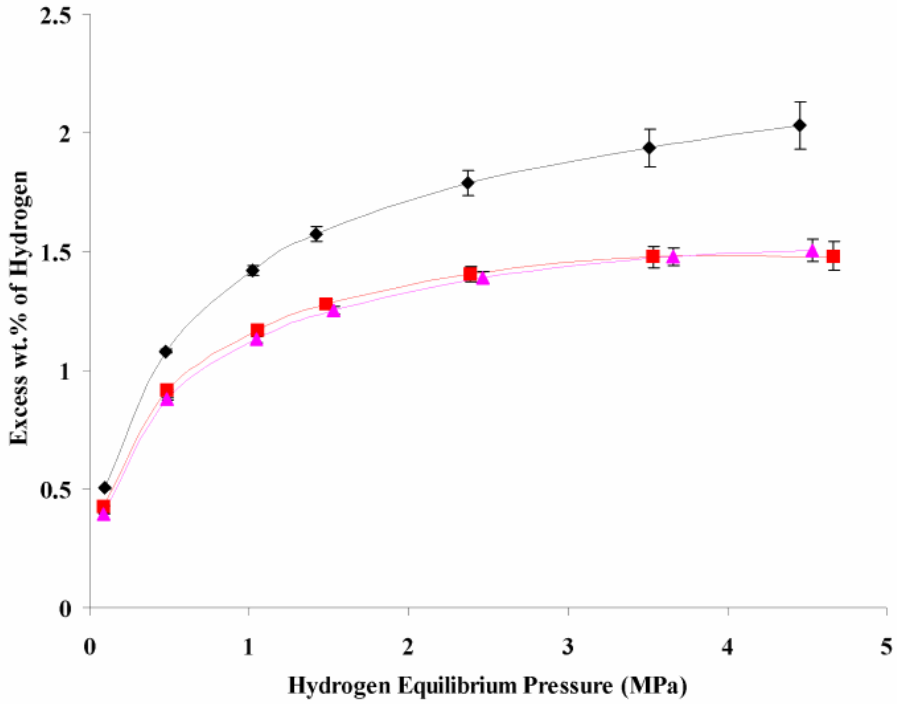

Figure 3-25: Hydrogen adsorption at 77 K on MCM-41-7 (◆), MCM-41-13 (■),MCM-41-14 (▲).

Figure 3-26 shows the hydrogen uptake, measured at 77 K, for the four samples doped with zinc with the uptake of pure MCM-41-7 shown as a comparison. The hydrogen uptake for the two lowest zinc doped samples, MCM-41-30-Si:Zn=49.8:1 and MCM-41-27-Si:Zn=12.2:1 show comparable uptake to the pure MCM-41 samples with 1.83 wt.% and 1.90 wt.% respectively at ~4.5 MPa. The two samples with the highest zinc doping, MCM-41-28-Si:Zn=2.4:1 and MCM-41-26-Si:Zn=6.3:1, show a significant reduction in hydrogen uptake. However, this reduction is not unexpected given the reduction in long-range pore ordering, decreased surface area (compared to pure MCM-41) and increased pore wall thickness.

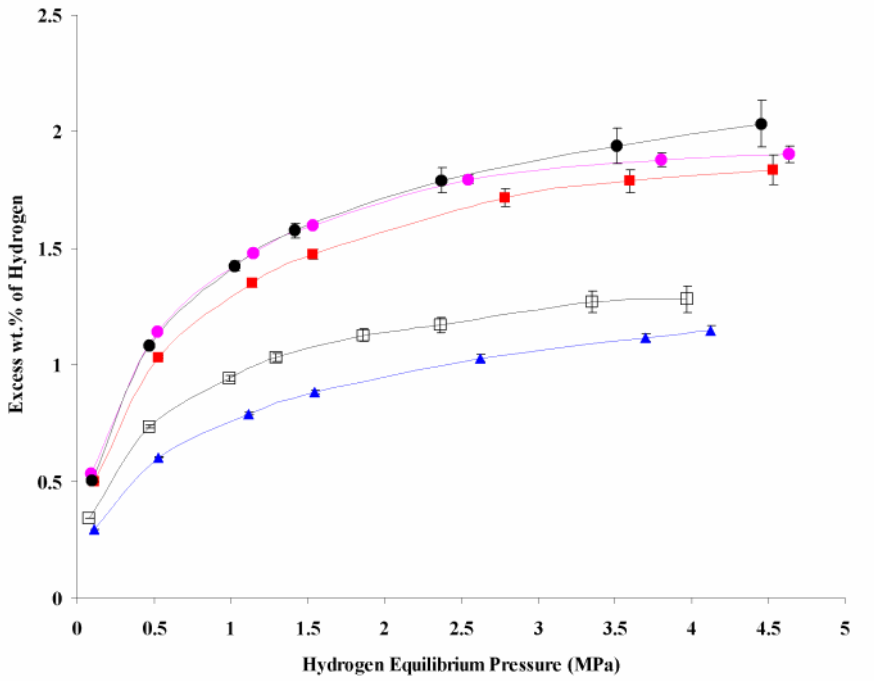

Figure 3-26: Hydrogen adsorption performed at 77 K on zinc-doped MCM-41 samples: MCM-41-28-Si:Zn=2.4:1 (▲); MCM-41-26-Si:Zn=6.3:1 (□); MCM-41-30:Si:Zn=49.8:1 (■). MCM-41-27-Si:Zn=12.2:1 (●). MCM-41-7-Pure Silica MCM-41 (●).

Figure 3-27 shows the hydrogen adsorption, performed at 77 K, on aluminium doped MCM-41 samples, MCM-41-10-Si:Al=10.1:1 and MCM-41-31-Si:Al=46.4:,1 with the adsorption of pure MCM-41-7 shown as a comparison. Hydrogen uptake for MCM-41-10-Si:Zn=10.1:1 and MCM-41-31-Si:Zn=46.4:1 at ~4.5 MPa is 1.09 wt.% and 1.35 wt.% respectively at ~4.5 MPa.

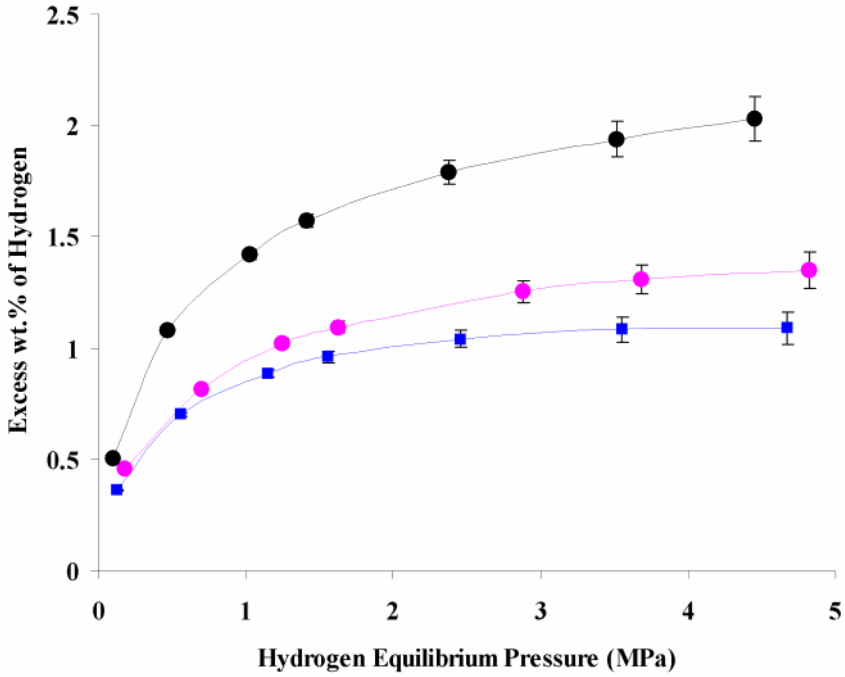

Figure 3-27: Hydrogen adsorption at 77 K on aluminium doped MCM-41-31-Si:Al=46.4:1 (●) and MCM-41-10-Si:Al=10.1:1 (■). The hydrogen adsorption of pure MCM-41-7 (●) is shown for comparison.

3.6. Discussion

3.6.1. Pure MCM-41

For pure MCM-41 made with CTAB, hydrogen adsorption is independent of parameters such as the reagent ratios, ageing time and apparent quality as determined by XRD. The hydrogen uptake is, however, strongly correlated with surface area. Figure 3-28 shows the hydrogen uptake for the samples MCM-41-7, MCM-41-8, MCM-41-16, MCM-41-18, MCM-41-20 and MCM-41-22 plotted against their surface area. The line in Figure 3-28 corresponds to the general guide for hydrogen uptake per unit of surface area of a porous material [3]. The data for MCM-41 falls below this line and may do so for a number of reasons;

(1) The line is determined based on the assumption of a monolayer of hydrogen on a graphene sheet. In considering an actual hydrogen adsorption measurement, some hydrogen would occupy sites on the surface of the graphene due to compression alone. Hence, hydrogen adsorption measured as excess wt.% will automatically be lower than this level.

(2) For these samples, hydrogen adsorption was near but not yet at a maximum value at the final pressure measurements of ~4.5 MPa. Hence, the maximum excess hydrogen adsorption for these MCM-41 samples will actually be slightly higher than the values reported here.

(3) The uptake per unit surface area is quoted for a flat sheet of graphene. As noted by Wang and Johnson[112], the curvature of a circular pore can introduce steric effects that reduces the effective surface area.

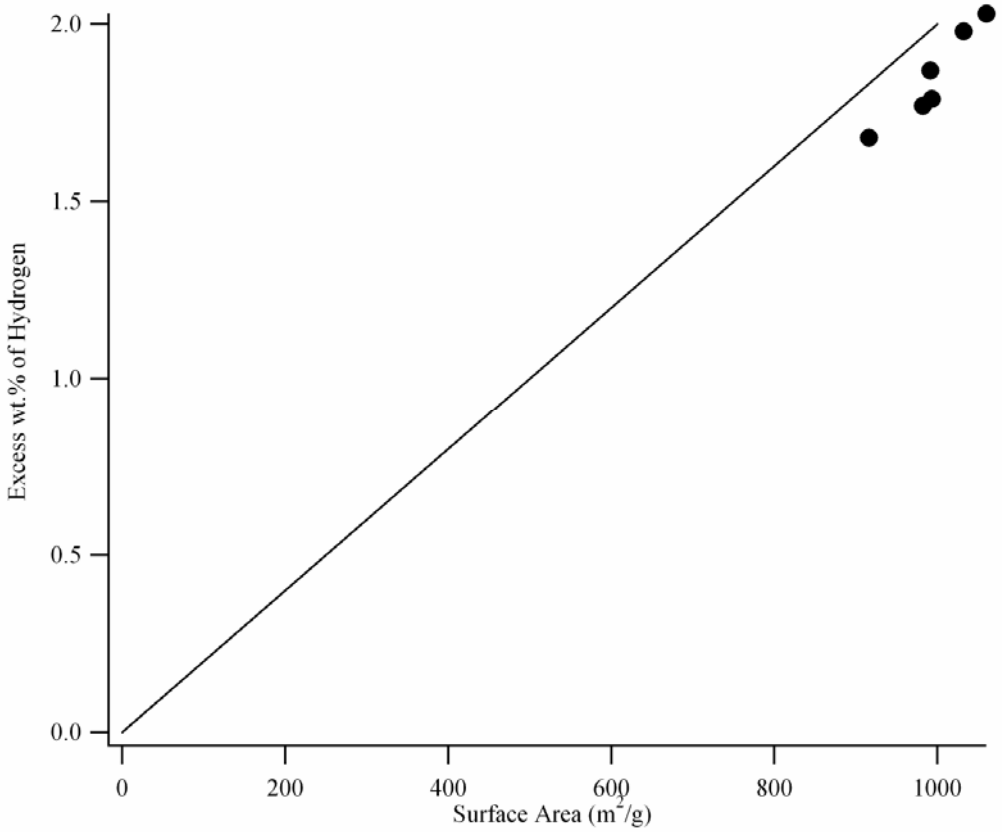

Figure 3-28 Hydrogen adsorption versus surface area for the samples MCM-41-7, MCM-41-8, MCM-41-16, MCM-41-20 and MCM-41-22.

Given the cylindrical geometry of the pores in MCM-41, one way to increase the interaction strength with hydrogen is to reduce the pore size. This results in a deeper potential well inside the pore and an enhancement of the hydrogen density. Without having performed nitrogen adsorption/desorption and pore size analysis on the samples made with DTAB, a direct comparison between the hydrogen adsorption results on samples made with CTAB and those made with DTAB is difficult. However, based on the literature[162], a number of statements about how pore size and surface area change with the shorter surfactant, DTAB, can be made.

(1) The pore size for MCM-41 made with DTAB by Kruk et al.[162] was ~72% of the size of the pores for MCM-41 made with CTAB.
(2) The wall thickness increases slightly with decreasing pore size. Even if the pore size remains constant, the consequence is a decrease in surface area due to an increase in the skeletal density of silica. Kruk et al.[162] measured the surface area of MCM-41 made with DTAB to be approximately 86% of the value for MCM-41 made with CTAB.

The pore sizes for most samples of MCM-41 made with CTAB for this thesis are approximately 3.4 nm. Based on this, the pore size of samples made with DTAB may be expected to be approximately 2.4 nm. This is an insufficient reduction in pore size to result in an enhancement of hydrogen density within the pore[112].

The hydrogen adsorption for MCM-41-13 and MCM-41-14, made with DTAB, is ~75% of the value measured for MCM-41-7 made with CTAB (~1.5 wt.% versus ~2.0 wt. %). Given that there is a ~15% variation in surface area for samples made from CTAB, the decrease in hydrogen uptake for MCM-41-13 and MCM-41-14 is broadly in line with expectations for adsorption that is primarily determined on surface area.

3.6.2. Doped MCM-41

Figure 3-29 shows the hydrogen adsorption versus surface area of all pure MCM-41, zinc doped MCM-41 and aluminium doped samples for which a surface area measurement has been made. This figure shows an enhancement in hydrogen uptake per unit surface area for two of the zinc doped samples, MCM-41-26-Si:Zn=6.3:1 and MCM-41-27-Si:Zn=12.2:1, and a decrease in the hydrogen uptake for the aluminium doped sample, MCM-41-31-Si:Al=46.4:1, as compared to pure MCM-41. However, the other two zinc doped samples, MCM-41-28-Si:Zn=2.4:1 and MCM-41-30-Si:Zn=49.8:1, showed comparable hydrogen uptake per unit surface area as the pure MCM-41 samples. The relatively poor hydrogen adsorption results for aluminium doped MCM-41 may be due to an effect reported by Biz and White[163], who suggested that Al-doped MCM-41 may contain regions of poorly condensed silica that may be prone to collapse. Consequently, the compression used in packing the MCM-41 powder into the sample cell before hydrogen adsorption may have resulted in a certain

amount of pore collapse. The variability in the hydrogen uptake of the zinc doped samples can not be so readily explained. Pore collapse cannot be used as an explanation since the zinc doped samples with lower uptake per unit surface have comparable uptake to pure MCM-41. Nor is any trend dependent on the level of zinc doping evident.

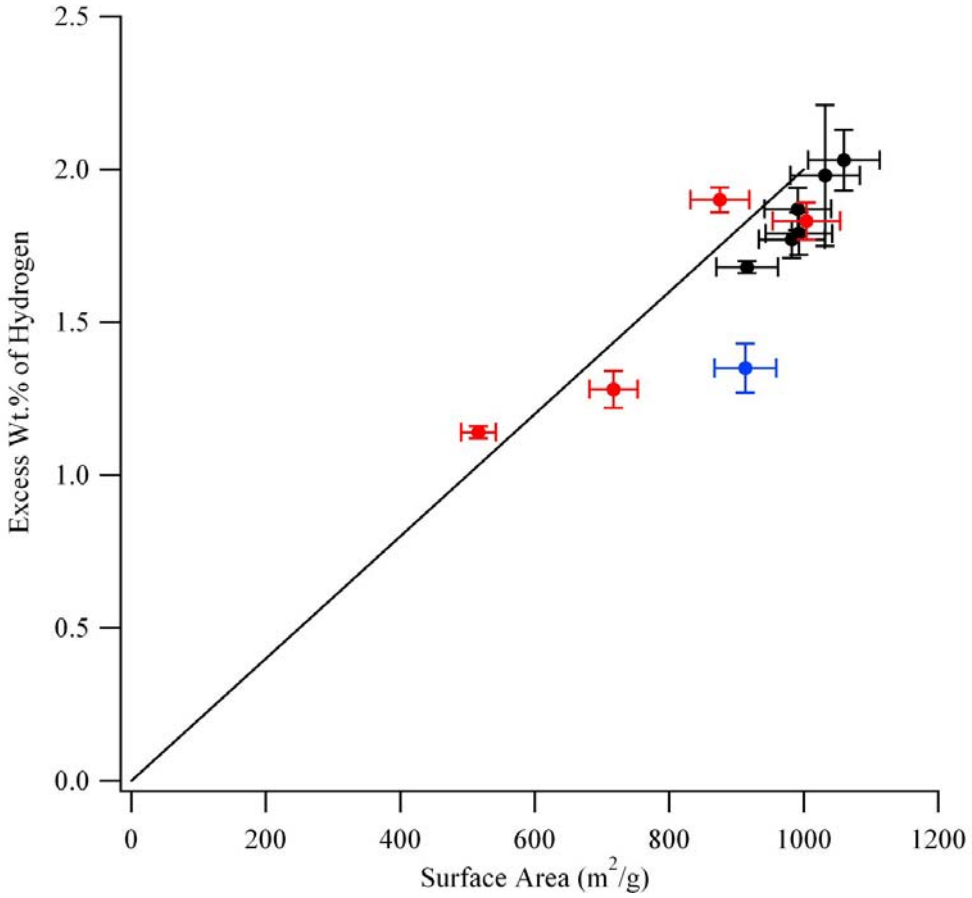

Figure 3-29: Hydrogen adsorption versus surface area for pure MCM-41-7, MCM-41-8, MCM-41-16, MCM-41-20 and MCM-41-22 (●), the zinc doped samples MCM-41-26-SI:ZN=6.3:1, MCM-41-27-Si:Zn=12.2:1, MCM-41-28-SI:Zn=2.4:1, MCM-41-30-Si:Zn=49.8:1 (●) and the aluminium doped sample MCM-41-31(●). The uncertainty in the surface area was taken to be 5%.

3.7. Conclusions

The highest hydrogen uptake at 77 K was for sample MCM-41-7 being 2.03 wt.% at a hydrogen equilibrium pressure of 4.45 MPa. The shape of the adsorption curve showed that adsorption was near but not yet at a maximum. For pure MCM-41

samples, the hydrogen uptake was most closely associated with surface area. The long range pore structure or quality of the sample, as determined by XRD, as well as the pore size had no obvious bearing on hydrogen uptake. The use of DTAB as a structure directing agent results in reduced hydrogen uptake. This is most likely due to the decreased surface area, associated with shorter chain surfactant, that is not offset by the pores being reduced in size sufficiently to result in an increased potential well within the pores.

The influence of doping on hydrogen adsorption properties was more difficult to elucidate. Two of the zinc doped samples, MCM-41-27-Si:Zn=12.2:1 and MCM-41-28-Si:Zn=2.4:1, showed an increase in the uptake per unit of surface area as compared to pure MCM-41 while the other two samples, MCM-41-26-Si:Zn=6.3:1, MCM-41-30-49.8:1 showed comparable uptake per unit surface area as pure MCM-41. However, zinc doping at all but the lowest level (MCM-41-30-Si:Zn=49.8:1) resulted in a degradation of the long range pore structure, a thickening of the pore walls and, consequently, a decrease in the surface area. Any possible increase in interaction strength of zinc-doped MCM-41 with hydrogen is off-set by the decrease in surface area that the zinc-doping leads to. The natural variability that occurs between samples makes any definitive determination impossible. Aluminium doping seems to have a negative impact on hydrogen uptake regardless of the level of doping. The surface area of MCM-41-31-Si:Al=46.4:1, was comparable to pure MCM-41 but showed a significant decrease in hydrogen uptake. This is either a consequence of the aluminium having a negative impact on hydrogen uptake or that the pore structure of MCM-41-31 is more prone to collapse.

3.8. Directions for Future Work

To increase the hydrogen adsorption of any porous material, three main factors ultimately determine the hydrogen storage: the surface area, the pore size and the strength of interaction between the adsorbate (hydrogen) and the pore wall. MCM-41 created with CTAB has a reasonably high surface area, ~1000 m^2/g, but suffers from relatively large pores, ~3.4 nm, that results in the density of hydrogen in the centre of those pores being comparable to that of bulk hydrogen gas for a given pressure. Reducing the size of the surfactant used to make MCM-41 reduces the pore size, but

also thickens the pore wall and decreases surface area. Therefore, it seems that methods for increasing hydrogen uptake in MCM-41 are limited. However, an exhaustive search of the literature reveals a zeolite with similarities, in terms of pore structure, to MCM-41[164]. Figure 3-30 shows the structure of this zeolite projected down the c-axis.

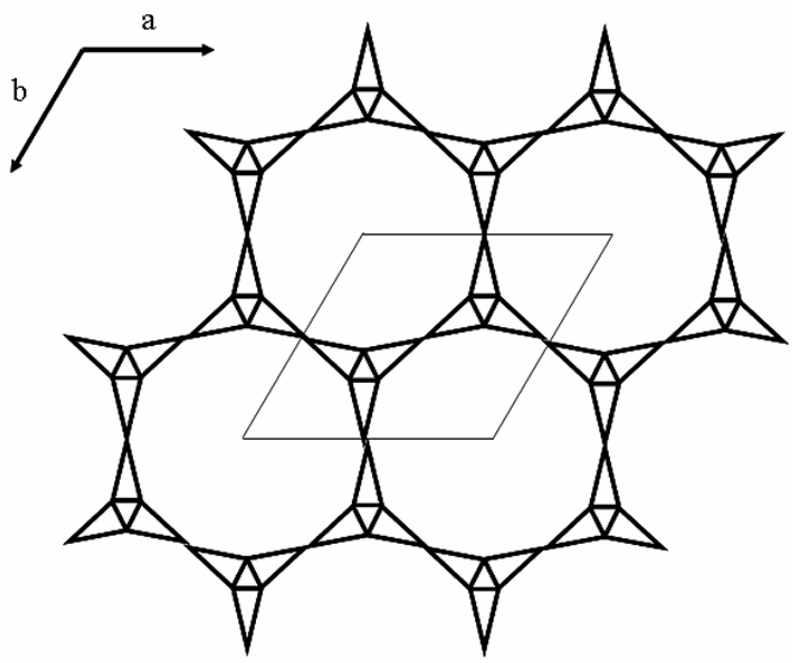

Figure 3-30: Projection along the c-axis of the zeolite OSO.

This structure has a pore repeat distance of just 1 nm with single atoms constituting the walls between pores. In addition, the structure also contains additional pore structure in the c-direction. This zeolite has the advantage of small pores and a three dimensional pore structure. With a pore repeat distance of just 1nm, the actual pore size will be smaller than this (no nitrogen adsorption/desorption has been done). In addition, this zeolite is based on beryllium, a highly toxic element. However, the authors note that the same structure should be obtainable using zinc.

Unlike some zeolites that have cage structures that prevent permeation and the interaction of an adsorbate with every atom in the structure, this zeolite has a very open structure that allows all atoms in the structure to interact with an adsorbate. Given that zinc has also previously been shown to act as an adsorption site for hydrogen, the hydrogen sorption properties of this zeolite should be researched if it can be produced with zinc instead of beryllium.

4. Titanate Nanoscrolls

4.1. Introduction/Motivation

A veritable explosion of research into nanostructured materials as hydrogen storage agents has occurred in recent years. As addressed in Chapter 1, these include activated carbon, carbon nanotubes, carbon aerogels, zeolites and metal-organic frameworks. In addition to this graphite nanofibres, intercalated graphite and nanostructured materials based on various forms of carbon nitride[165, 166], boron oxide[167], boron nitride[168] and titanium disulphide[169] have also been explored. Titanate nanotubes are a recently synthesised nanoscale material[170]. In this thesis we explore their viability as a medium for hydrogen storage. As of the commencement of this thesis, titanate nanotubes had not been explored as a hydrogen storage medium. The simple synthesis process, handling and characterisation as well as the layered nanostructure of the titanate nanotubes make them a possible candidate for hydrogen storage.

4.2. Literature Review

4.2.1. General

Titanate nanotubes were first produced in 1998 [170] via a soft chemical process that involves ageing TiO_2 powder in a concentrated NaOH solution. The resultant nanotubes, once filtered and washed, are typically 8 - 10 nm in diameter and hundreds of nanometers long. The walls consist of 3 - 5 layers and the diameter of the hollow centre is typically ~5 nm [171]. The layered structure is the result of the rolling up of a continuous titanate sheet. A typical TEM image showing longwise and end-on nanotubes is shown in Figure 4-1 while a typical XRD pattern is displayed in Figure 4-2.

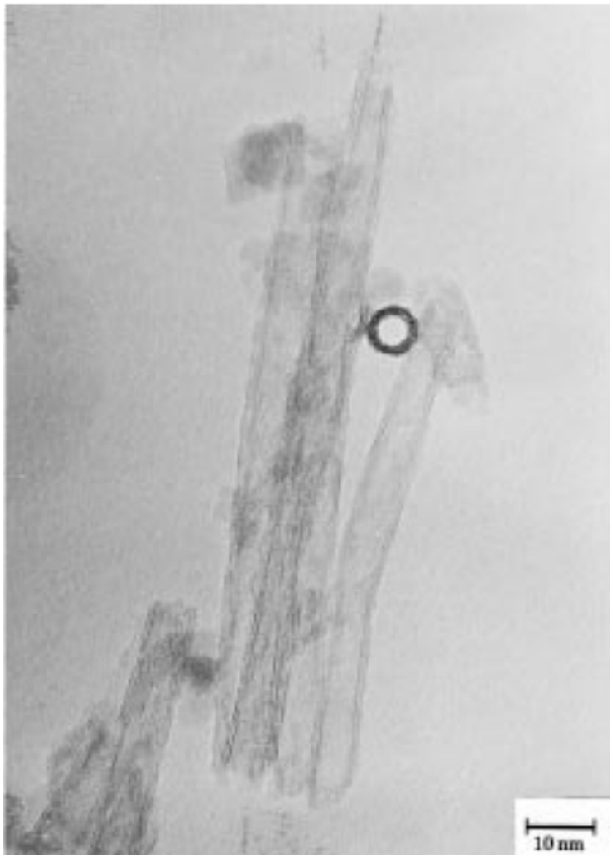

Figure 4-1: TEM of nanotubes produced using a 10 M NaOH solution held at 383 K (110°C) for 20 hours. Reprinted with permission from [170]. Copyright 1998 American Chemical Society.

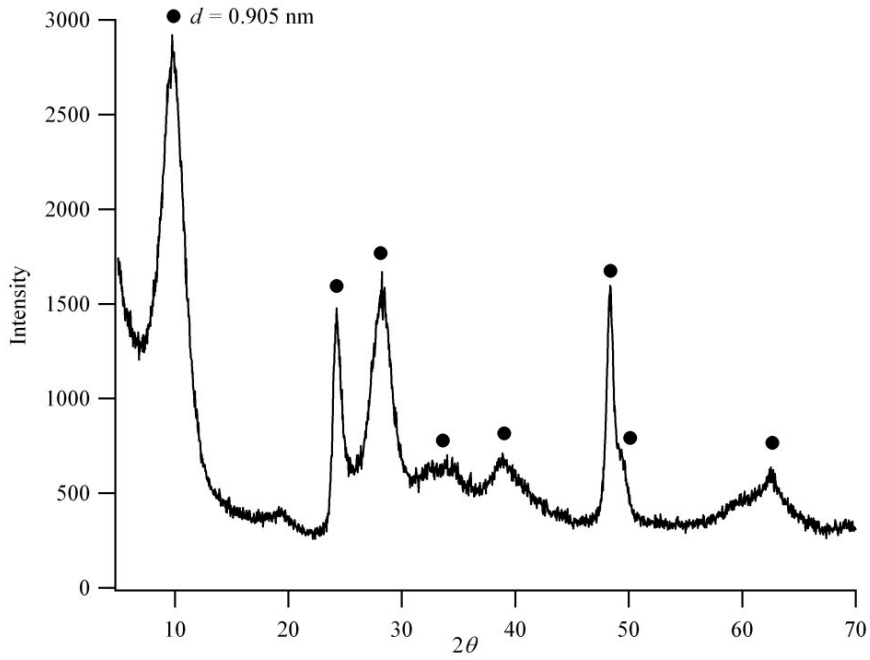

Figure 4-2: A typical XRD pattern of titanate nanotubes. • indicates nantoube phase as shown in reference 165.

4.2.2. Synthesis

Kasuga et al.[170] first explored the formation of titanate nanotubes by placing the anatase polymorph of titania (TiO_2) in solutions of NaOH at concentrations of 2.5, 5, 10 and 20 M. These mixtures were then placed in stainless steel containers and held for 20 hours at 293, 333 or 383 K (20, 60 or 110^{o}C). The treated powders were washed well with 0.1 M HCl aqueous solution and distilled water and were subsequently separated from solution by centrifugation. The results of their experiments showed that temperatures of at least 333 K (60^{o}C) and NaOH concentration greater than 5 M were required for the formation of nanotube-type structures. Subsequent work [171] confirmed that titanate nanotubes could also be derived from another polymorph of titania, rutile. XRD and selected area electron diffraction measurements performed by Kasuge et al.[170] were said to confirm that the nanotubes were composed of anatase but no patterns or *d*-spacing information were presented to confirm this.

A range of synthesis conditions have since been tested and their impact on nanotube formation examined. The most commonly used synthesis conditions are as follows[171, 172, 173, 174, 175]: Anatase or rutile powder is added to a 10M NaOH solution that is subsequently heated at between 383 K (110^{o}C) and 403 K (130^{o}C) for 20 to 72 hours. The resulting powder is separated from solution by centrifugation followed by washing with copious quantities of distilled water. The nanotubes are then ion-exchanged by washing with dilute acid. The acid wash step has been cited as a crucial step in the formation process of titanate nanotubes[170, 171, 174]. However, a number of authors have shown that the nanotubes form during the ageing process. Production processes that use a less concentrated NaOH solution results in incomplete transformation to nanotubes[170,176] while the use of temperatures above 433 K (160^{o}C) results in the formation on nanoribbons and nanofibres[177].

Chen et al.[178] found a disordered phase containing Na from TEM investigations of samples of titanate nanotubes retrieved during the ageing process. To further explore the role that this sodium plays in the formation of titanate nanotubes, they performed to the same experiment but replaced NaOH with KOH or LiOH. XRD revealed sharp diffraction peaks, very different from that of the nanotubes. From TEM, nanorods and

nanoplates were observed in the KOH treated sample and nanoparticles were observed in the LiOH sample. Replacement of NaOH with NaCl or $NaNO_3$ also did not result in nanotube formation. The conclusion drawn was that a high concentration of Na^+ cations and a strongly basic solution is required for nanotube formation. Bavykin et al.[179], however, showed that titanate nanotubes could be formed using KOH if the synthesis temperature was low enough (<60^{o}C) and long enough (12 days). This long reaction time was not enough to result in complete transformation to nanotubes and the nanotubes formed were highly defected.

4.2.2.1. Ion-Exchange

Titanate nanotubes have also been the subject of ion-exchange research in an attempt to alter their catalytic and structural stability properties. The original experiments of Kasuga et al.[170] substituted sodium ions for hydrogen by rinsing the sample with dilute hydrochloric acid. These titanates are typically referred to as acid-exchanged titanates, protonated titanate or just acid titanates.

Li, Na, K, Rb and Cs have all been ion exchanged into nanotubes[180, 181] by adding the acid-exchanged nanotubes to solutions of the desired hydroxide (i.e. LiOH for Li^+ exchange). Cd, Zn, Co, Ni and Cu have also been exchanged into nanotubes by soaking the nanotubes in a solution of the desired metal salt complexed with ammonia solution[174].

4.2.3. Structure

There are a number of factors that contributed to the difficulty in ascertaining the true structure of titanate nanotubes. The first is that there are a large number of crystal polymorphs for pure TiO_2, the protonated forms of polytitanic acid, ($H_{2m}Ti_nO_{2n+m}$), and their hydrates. Secondly, the small size of the nanotubes leads to peak broadening in XRD patterns. Lastly, titanate nanotubes are relatively unstable and can undergo further phase transformations upon heating or acid treatment both during and after preparation[182].

Despite these difficulties, a number of different structures have been assigned to titanate nanotubes produced via the soft chemical process. These include anatase

[170,171], $H_2Ti_3O_7$ [173], lepidocrocite-type ($H_xTi_{2-x/4}\square_{x/4}O_4$ where x~0.7 and $\square$ is a vacancy) structure [183], $H_2Ti_4O_9.H_2O$ [184] and $Na_2Ti_2O_4(OH)_2$ [185].

With the exception of the anatase phase, the other proposed structures have a number of elements in common such as:

1) they all consist of a well defined layer structure with an interlayer spacing of 0.7-0.8 nm. This results in a characteristic XRD peak at $2\theta \sim 10^o$;
2) the as-produced titanate nanotubes containing sodium ions that can be exchanged for a wide variety of alkali and metal ions;
3) the layers being comprised of edge- and corner-sharing TiO_6 octahedra.

Figure 4-3 shows the crystal structure of trititanic acid ($H_2Ti_3O_7$) [182] projected along each of the crystallographic directions. The trititanic acid has three edge sharing TiO_6 octahedra before "stepping down" to the next group of three TiO_6 octahedra via a corner sharing process. The nanotubes are formed by wrapping around the b-axis. The only difference between this and the $H_2Ti_4O_9.H_2O$ structure proposed by Nakahira et al.[184] is that their structure consists of four edge sharing TiO_6 octahedra before "stepping down." The structures proposed by Ma et al.[183] and Yang et al.[185] differ only in that the layer is comprised of a continous array of edge sharing TiO_6 octahedra.

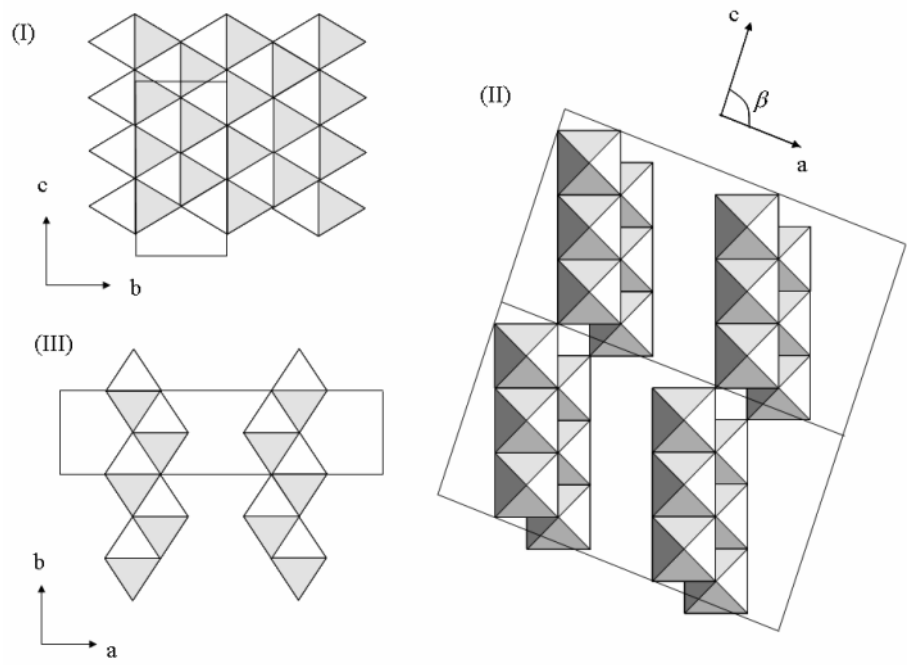

Figure 4-3: Structure of trititanate nanotubes, $H_2Ti_3O_7$ as viewed down the (I) a-, (II) b- and (III) c-axis of the unit cell. Derived from [182].

4.2.4. Applications

Due to the unique structure of titanate nanotubes, a number of applications are currently being explored for this material. Liu et al. examined titanate nanotubes as a biosensor[186] for selective dopamine detection in extra-cellular fluid - a key process for detecting Parkinson's disease. Other biomedical applications include using the nanotubes as an improved platform for bone regrowth[187]. LED type applications have also been explored due to the strong photoluminescence of titanate nanotubes[188], while application in solar cells is also being explored[189]. The layered nature of titanates also means that they have been explored as a proton conducting fuel cell electrolyte[190] and as an electrode for lithium ion batteries[191]. Metal intercalation or substitution is also possible, which leads to variations in the electronic, optical and magnetic properties particularly with regards to improving photocatalysis [174,192].

4.2.5. Hydrogen Adsorption

During the course of this thesis, two papers have been published regarding the hydrogen adsorption properties of titanate nanotubes [193,194]. Bavykin et al.[193] used a synthesis typical for production of titanate nanotubes [170,175] resulting in XRD patterns common in the literature. Lim et al.[194] used a similar method of production, but

followed synthesis with an extended acid wash step believed to promote anatase formation [174]. XRD performed on this sample is somewhat inconclusive but suggests the transformation to anatase while N_2 adsorption/desorption and BJH analysis confirms that the as-produced material maintains its tubular morphology upon conversion from titanate to anatase [194].

Bavykin et al.[193] performed hydrogen adsorption measurements at four different temperatures: 77 K (-196^{o}C) , 353 K (80^{o}C) , 383 K (110^{o}C) and 398 K (125^{o}C) over the pressure range of 0 to 0.6 MPa. The measurement at 77 K showed a large uptake of 3.8 wt.% at an equilibrium pressure of 0.2 MPa with no further adsorption with increasing pressure. Desorption showed large hysteresis with more than 3 wt.% remaining in the sample upon reduction of the hydrogen pressure (Figure 4-4). Given the modest surface area of this sample (199 m^2/g), the large hydrogen uptake suggests that the hydrogen is entering the interstitial spacing between the walls of the nanotubes. Heating of the sample to 473 K lead to a complete desorption of the remaining hydrogen. XRD performed on the as-produced nanotubes and fully hydrogen saturated nanotubes showed no significant changes. The repeat distance between nanotube layers is 0.72 nm but it is unclear how large the actual pore is that is available to hydrogen. Given that the pore is available to hydrogen but not nitrogen[175] and that no expansion of the interlayer spacing occurs, as may be expected if the pore is slightly smaller than the size of molecular hydrogen[195], then the pore can be estimated to be between 0.24 and 0.3 nm in size (i.e. between the size of a hydrogen and nitrogen molecule).

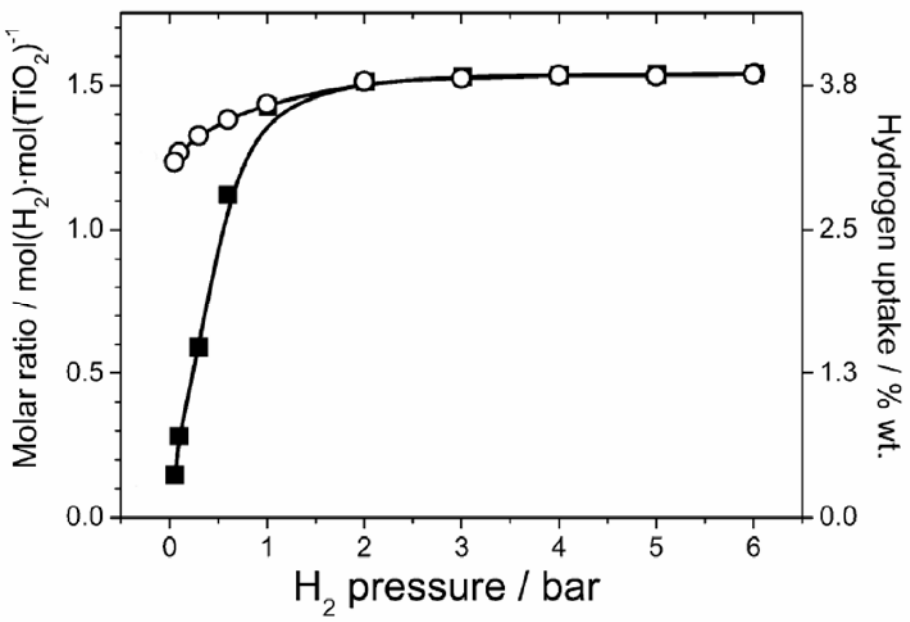

Figure 4-4: Hydrogen adsorption/desorption for titanate nanotubes at 77 K. Adsorption is indicated by (■) while (○) indicates desorption. Reprinted with permission from [193]. Copyright 2005 American Chemical Society.

The apparatus used by Bavykin et al.[193] allowed for constant pressure experiments which in turn could be used to determine the kinetics of hydrogen adsorption. Kinetic adsorption measurements performed at 398 K and 383 K at a constant pressure of 0.1 MPa showed a maximum of approximately 1 wt.% and 1.2 wt.% hydrogen uptake respectively within 2 hours. The measurement performed at 353 K presented a somewhat different result (Figure 4-5). After 2 hours, total uptake was greater than for either the 383 K or 398 K measurement but equilibrium conditions were not reached even after 12 hours at which time the sample had adsorbed >2.5 wt.% of hydrogen. Based on these measurements, an estimate was made of the diffusion coefficient of molecular hydrogen into the nanotube layers and was found to be dependent on the both the temperature and the length of the tube. For carbon nanotubes, it has been shown[196] that an increase in hydrogen pressure from 2 to 11.5 MPa resulted in an increase in the diffusion coefficient by a factor of ~ 4 and such a measurement performed on the titanate nanotubes may prove enlightening. To my knowledge no such measurement has been done. Desorption was not specifically focused on at near ambient temperatures, however it was noted that desorption is particularly slow at room temperature.

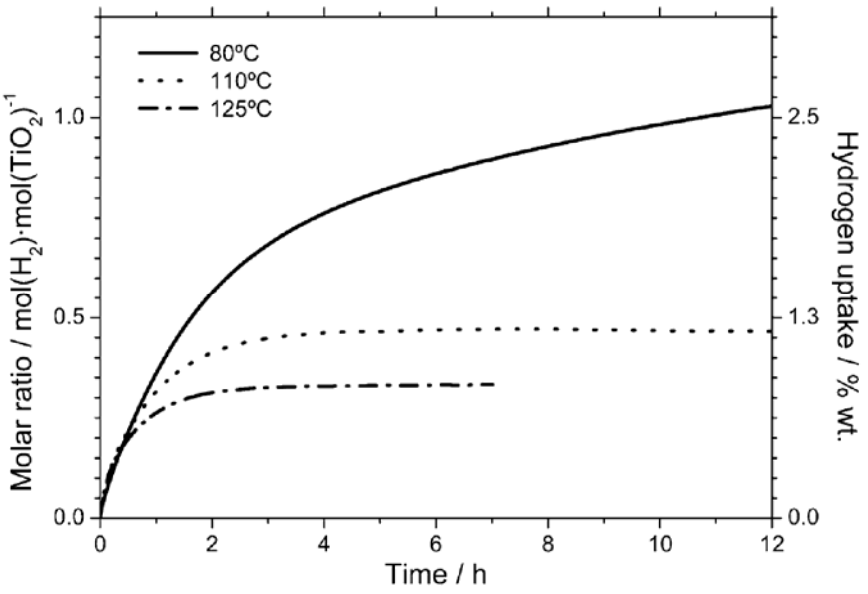

Figure 4-5: Kinetic curves for hydrogen intercalation into the titanate nanotubes at temperatures in the range 353 to 398 K (80 to 125°C) and at a constant pressure of 0.1 MPa. Reprinted with permission from [193]. Copyright 2005 American Chemical Society.

Hydrogen adsorption measurements on the anatase converted nanotubes were performed by Lim et al.[194] at 298 K (25°C), 343 K (70°C) and 393 K (120°C) up to a pressure of 6 MPa. Their measurement at 298 K (25°C) showed an uptake of ~2 wt. % of hydrogen but showed hysteresis with only 75% of this hydrogen being recoverable upon reduction of the hydrogen pressure. The measurements at 343 K (70°C) and 393 K (120°C) resulted in hydrogen uptake of 1.45 and 1.10 wt. % respectively with a reduction in the amount of hysteresis with an increase in temperature. To examine the nature of the adsorbed hydrogen, TPD (temperature programmed desorption) and FTIR (Fourier transform infra red) spectroscopy was performed on a sample saturated with hydrogen. FTIR revealed a large increase in the signal associated with –OH bonds. TPD showed a strong H_2 desorption peak centered at 343 K (70°C) that tailed off to 433 K (160°C) suggesting a range of hydrogen binding energies. TPD also revealed water desorption above 393 K (120°C), which suggests the decomposition of the –OH bonds revealed by FTIR. Approximately 12% of the entire hydrogen uptake could be accounted for by –OH formation. The water formation proves to be a point of interest not expounded on by the authors. It would have been informative to see if the removal of oxygen, presumably from the structure of anatase, was present in consecutive hydrogen adsorption/desorption cycles or whether it was an artefact of the first adsorption. If it is present in every adsorption/desorption cycle then the

repeated oxygen removal may be expected to have an effect on the overall structure of the nanotubes.

4.3. Experimental

4.3.1. Sample Production

The starting materials for this investigation consisted of the anatase polymorph of titanium dioxide (>98%) supplied by BDH Laboratory Supplies. Sodium hydroxide (NaOH) was an AnalaR brand at a purity of 99%.

All samples produced used ~ 40 g of NaOH added to 80 mL of water under stirring to produce a 10 M solution. The container of this sodium hydroxide solution was immersed in water during the stirring process to lower the risk of the container melting due to the highly exothermic nature of NaOH dissolution in water. Details of specific samples follow below.

Sample TNT-1 was produced by adding ~0.5 g of anatase to 100 mL of a 10 M NaOH solution in polypropylene bottle and ageing it under constant stirring at 343 K (70^{o}C) for 24 hours. This temperature was chosen for two reasons. The first was that, at this stage, the only suitable vessels available for handling concentrated sodium hydroxide were polypropylene which had a temperature rating of 373 K (100^{o}C). Given that Kasuga et al.[170] showed that a temperature of 333 K (60^{o}C) yielded nanotube formation, 343 K (70^{o}C) seemed a reasonable compromise between the temperature required for nanotube formation and the maximum temperature rating of the polypropylene bottles.

Sample TNT-2 consisted of the same quantity of reagents but was aged in a polypropylene bottle at 363 K (90^{o}C) under constant stirring for 24 hours.

Sample TNT-3 used the same molar ratio of reagents as for TNT-1 and TNT-2. In this case a Teflon® bottle was used and the sample was statically aged for 72 hours at a temperature of 383 K (110^{o}C).

It was noted at this point that a sample left to stand for 72 hours agglomerated into a single solid mass. Given that titanate nanotubes are believed to form by the rolling up of a single titanate sheet, it was hypothesised that this agglomeration could hinder nanotube formation. Consequently, samples were produced with an additional step as outlined below.

For sample TNT-4 and TNT-5, ~2g of anatase was added to a 100 mL solution of 10M NaOH. The samples were aged in a Teflon® container for 72 hours. However, after each successive 24 hour period the container was removed from the autoclave and stirred with a magnetic bar for 30 minutes before being returned to the autoclave.

The washing process to separate the titanate nanotubes from solution was as follows: The solids were allowed to settle out of solution with the excess liquid decanted. MilliQ water was then added and the solids were resuspended in solution via agitation. The solution, with suspension, was transferred to centrifuge tubes and separated out. The excess liquid was siphoned off and MilliQ water was added to the centrifuge tubes and the nanotubes were resuspended via agitation before the centrifuge process was again used. This process was repeated until the pH of the solution reached 10.4 beyond which point further washing resulted in negligible further change in pH. Sample TNT-3 was, at this point, separated from solution by filtration and 100 mL of 0.1 M HCl was filtered through the sample. For sample TNT-4 and TNT-5, the samples were filtered from solution without acid treatment. Once separated from solution, all samples were dried at 383 K (110^{o}C).

4.3.2. Ion-Exchange

The process for ion exchange was different for each ion and was based on the ion-exchange work on titanate nanotubes of Sun and Li[174] and Morgado et al.[197] and the ion-exchange work on layered titanates of Cardoso et al.[198].

For the zinc exchanged sample, designated Zn-TNT-4, 100 mL of a 1M solution was made with $ZnSO_4.7H_2O$ and 0.632g of TNT-4 was added and stirred at room temperature for 24 hours. For the lithium exchanged sample, designated Li-TNT-5,

100mL of a 1M solution was made with LiCl. Due to its hygroscopic nature, LiCl was weighed inside an argon filled glove-box. To this solution 1.005g of TNT-5 was added and the solution was stirred at room temperature for 24 hours. For the hydrogen exchanged sample, designated H-TNT-5, 0.971g of TNT-5 was slurried in 100 mL of a 0.1M HCl acid solution. This agitation in acidic solution was kept to two hours to minimise degradation of the titanate nanotube structure[190, 197]. At this point, aggregates (estimated at ~10% of the material) that had not broken up in the short stirring process were removed. Following the ion-exchange process the samples where centrifuged with the excess liquid drawn off. The samples were then re-slurried with Milli Q water and dried in a petri dish at 383 K (110^{o}C) for at least 12 hours.

4.3.3. X-ray Diffraction

For X-ray diffraction, a number of different measurement variables were used in an attempt to maximise the quality of the obtained pattern. For TNT-1, a step size of 0.04^{o} 2θ was used with a scan rate of 4^{o} 2θ per minute. For TNT-2, TNT-3 and TNT-4 a step size of 0.02^{o} 2θ was used with a scan rate of 1^{o} 2θ per minute was used. In an attempt to reveal more detail, a step size of 0.04^{o} 2θ and a scan rate of 0.4^{o} 2θ per minute was used for selected 2θ regions. Due to a change in the XRD instrument's software, the conditions used for all subsequent XRD measurements consisted of a step size of 0.04^{o} 2θ and a scan rate of 0.48^{o} 2θ per minute (5 seconds per step).

4.3.4. Hydrogen Adsorption

Between 0.46 and 0.93 grams of titanate nanotubes was used for each hydrogen adsorption measurement. All samples were outgassed at 473 K (200^{o}C) for at least 12 hours prior to measurements. Due to the lack of a well defined structure, the correct density to use for hydrogen adsorption measurements was somewhat difficult to determine. The density of the as-produced titanate nanotubes was taken to be that of $Na_2Ti_3O_7$ and equal to 3.44 g/cm^3 (PDF n^{o} 31-1329). The reasoning behind this choice will be expounded upon in the discussion. For the acid exchanged nanotubes, H-TNT-5, the density was taken to be that of $H_2Ti_3O_7$ and equal to 3.163 g/cm^3 (PDF n^{o} 47-0561). The density of the lithium exchanged nanotubes was taken to be that of $Li_2Ti_3O_7$ and equal to 3.17 g/cm^3 (PDF n^{o} 34-0393). Given that no layered zinc

titanate exists in the ICCD Powder Diffraction File, the density of the zinc exchanged nanotubes was taken to be that of TNT-1 and equal to 3.44 g/cm^3.

4.3.5. Nitrogen adsorption/desorption Isotherm

Nitrogen adsorption/desorption measurements were performed on sample TNT-3 and were performed at ANSTO on a Micromeritics ASAP 2400 instrument at 77 K. TNT-3 was outgassed at 473 K (200^{o}C) overnight prior to measurements being performed. The surface area was determined using the BET formula[199] and data from the pressure range covering p/p_o = 0.01 - 0.1.

4.4. Results

4.4.1. Samples TNT-1, TNT-2 and TNT-3

XRD of TNT-1 (Figure 4-6) revealed a very small degree of nanotube transformation (indicated by ♦) with the majority of the sample remaining as anatase.

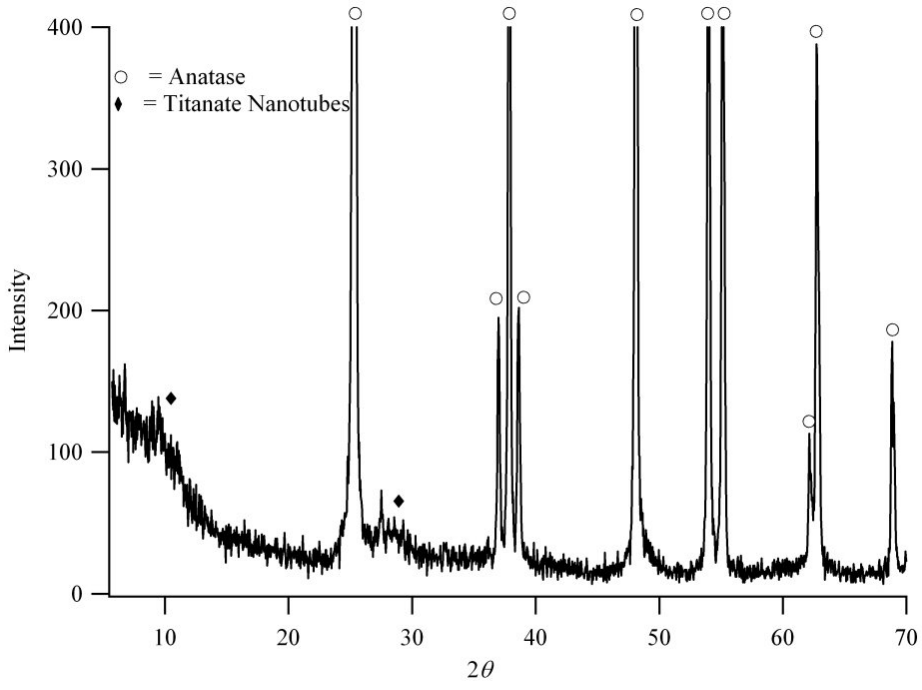

Figure 4-6: XRD pattern of sample TNT-1. ♦ Indicates titanate nanotube phase and ○ indicates anatase phase.

Figure 4-7 shows the XRD pattern for TNT-2 aged under constant stirring conditions at 363 K (90^{o}C). The sample is still predominantly anatase, however there are three

peaks corresponding to titanate nanotube formation at 2θ ~ 10°, 24° and 28° respectively as well as the beginning of a characteristic nanotube shoulder at 2θ ~ 49°.

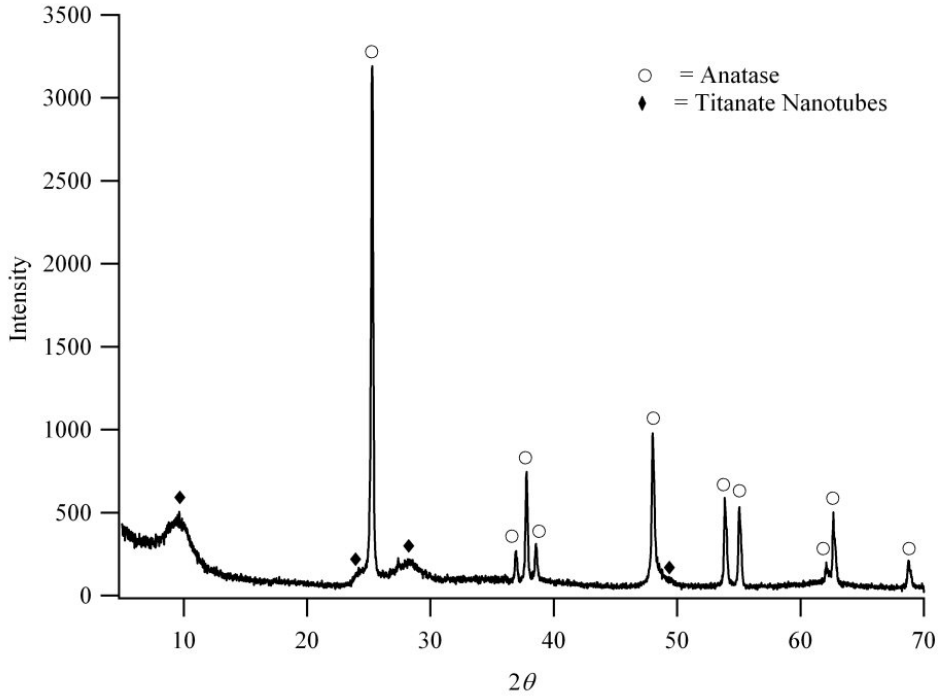

Figure 4-7: XRD pattern of sample labelled sample TNT-2. . ♦ Indicates titanate nanotube phase and ○ indicates anatase phase.

Figure 4-8 shows the XRD pattern of sample TNT-3 aged statically for 3 days at 383 K (110°C). The pattern is characterised by four strong diffraction peaks at 2θ ~ 9.6°, 25.0°, 28° and 48°. Broad, diffuse peaks are also evident at 2θ ~ 35° and 38° while a weak, asymmetric peak extends between 2θ ~ 56° and 66°.

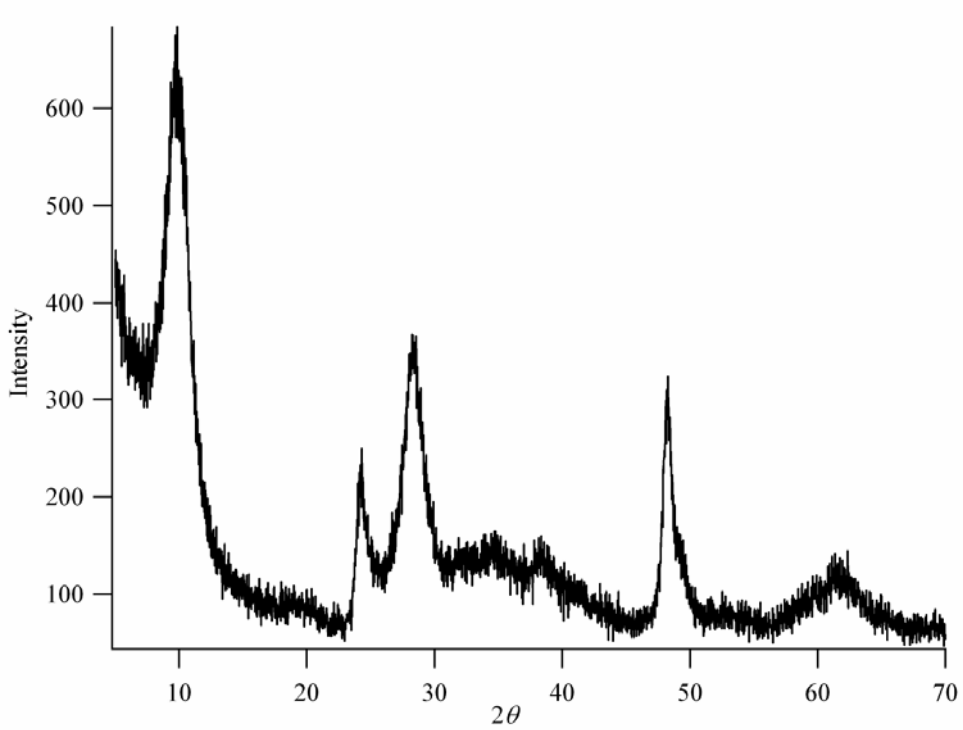

Figure 4-8: XRD pattern of sample TNT-3.

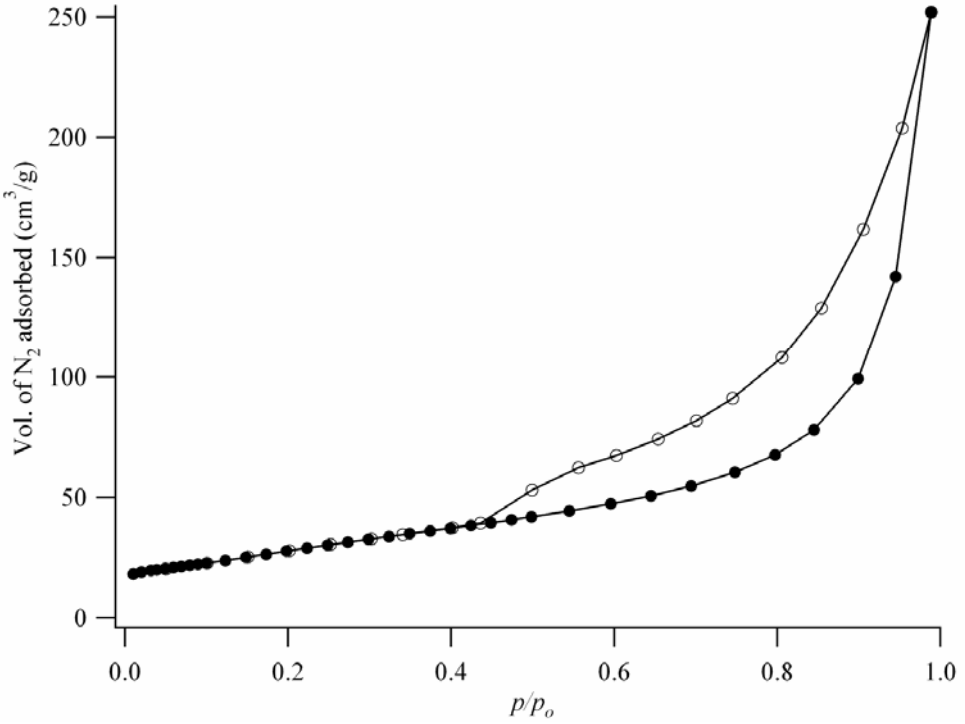

Figure 4-9: Nitrogen adsorption/desorption curves for titanate nanotube sample TNT-3. (●) indicates adsorption (○) indicates desorption.

Figure 4-9 shows the nitrogen adsorption/desorption curve for TNT-3 performed at 77 K. The curve shows both similarities and differences to the isotherm of Bavykin et al.[175] (Figure 4-10). Based on a knowledge of the geometry of titanate nanotubes the hysteresis, as shown in Figure 4-9 and 4-10, is likely to be the convolution of two hysteresis loops that have different foundations[175,200]. The hysteresis between p/p_o equal to ~0.5 and 0.8 is associated with capillary condensation inside cylindrical pores that are open at both ends. The hysteresis between p/p_o of ~0.8 and 1.0 corresponds to large pores that are not being completely filled. Hence, the hysteresis above p/p_o ~ 0.8 corresponds to condensation between nanotubes while the hysteresis below p/p_o ~ 0.8 corresponds to condensation within the central pores of the nanotubes.

The surface area for TNT-3 was calculated as being 91 m^2/g. The value for the surface area of titanate nantoubes quoted in the literature generally range between 200 m^2/g [175] and 270 m^2/g [176].

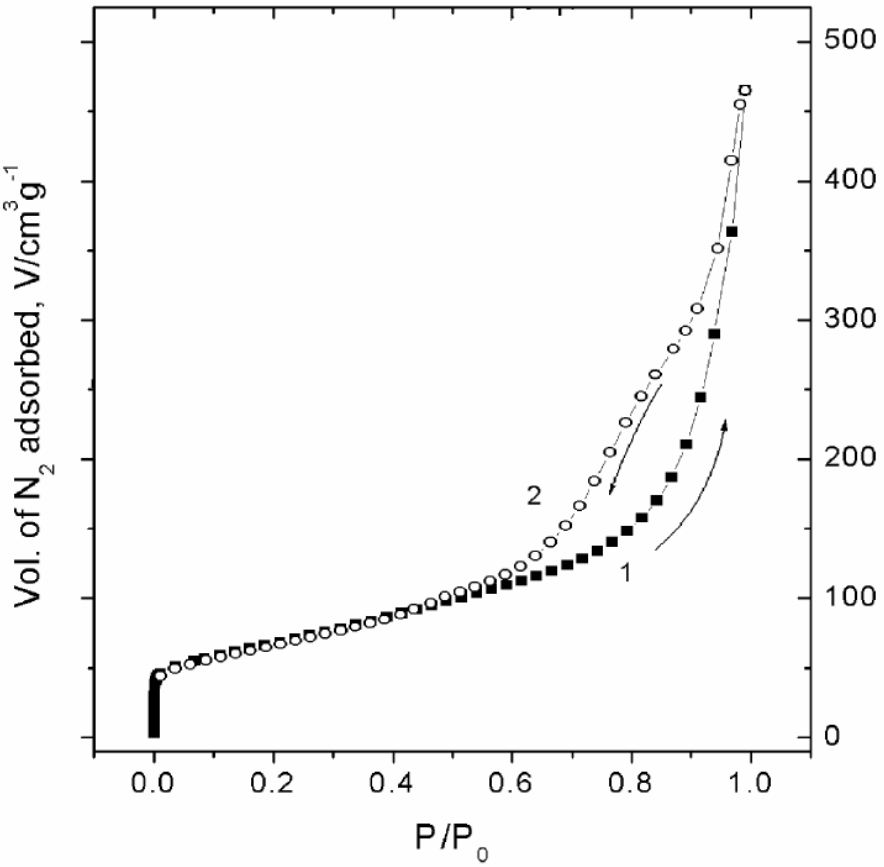

Figure 4-10: Nitrogen isotherm on titanate nanotubes performed at 77 K from Bavykin et al.[175] Solid squares indicate adsorption and open circles indicate desorption. Reproduced with permission of The Royal Society of Chemistry (http://dx.doi.org/10.1039/b406378c).

Notable difference between the nitrogen sorption isotherm obtained in this work and that of Bavykin et al.[175] are as follows:

1) The desorption curve for TNT-3 is near parallel to the desorption curve between $p/p_o \sim 0.7$ and ~0.56 at which point a weak shoulder is evident before the desorption curve meets the adsorption curve at $p/p_o \sim 0.44$.

2) The total uptake of nitrogen is higher along all points of the isotherm for Bavykin et al.'s commensurate with the higher surface area.

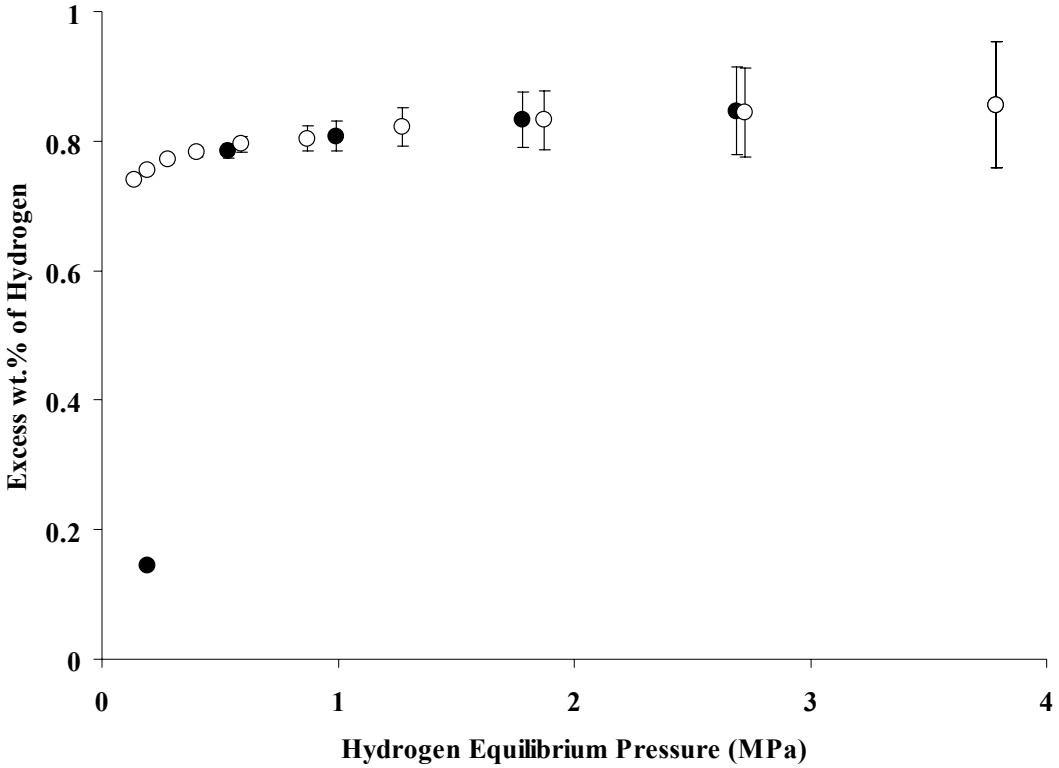

Figure 4-11: Hydrogen adsorption (●) and desorption (○) on TNT-3 performed at 77 K.

Figure 4-11 shows the hydrogen adsorption and desorption isotherm of TNT-3 performed at 77 K. Adsorption is characterised by a steep initial uptake with adsorption plateauing above an equilibrium pressure of ~0.5 MPa. The maximum uptake was just 0.83 wt.%. Desorption is characterised by pronounced hysteresis below a pressure of ~0.5 MPa. The final desorption point has an equilibrium pressure of 0.1387 MPa with 0.74 wt.% of hydrogen remaining in the sample. This is

compared to the first adsorption point that has an equilibrium pressure of 0.1916 MPa with a hydrogen uptake of 0.14 wt.%.

4.4.2. TNT-4 and TNT-5

Figure 4-12 shows the XRD pattern of sample TNT-4 from which the zinc exchanged titanate nanotubes, Zn-TNT-4, were produced. Figure 4-13 shows the XRD pattern of sample TNT-5 from which from which the hydrogen and lithium exchanged nanotubes were produced. The patterns differ slightly from the literature in that there is a small diffraction peak at $2\theta \sim 19.6^{o}$. This peaks corresponds to the nanotube structure propsoed by Yang et al. [185] Of note also is that the relative height of the four strongest peaks vary with respect to each other.

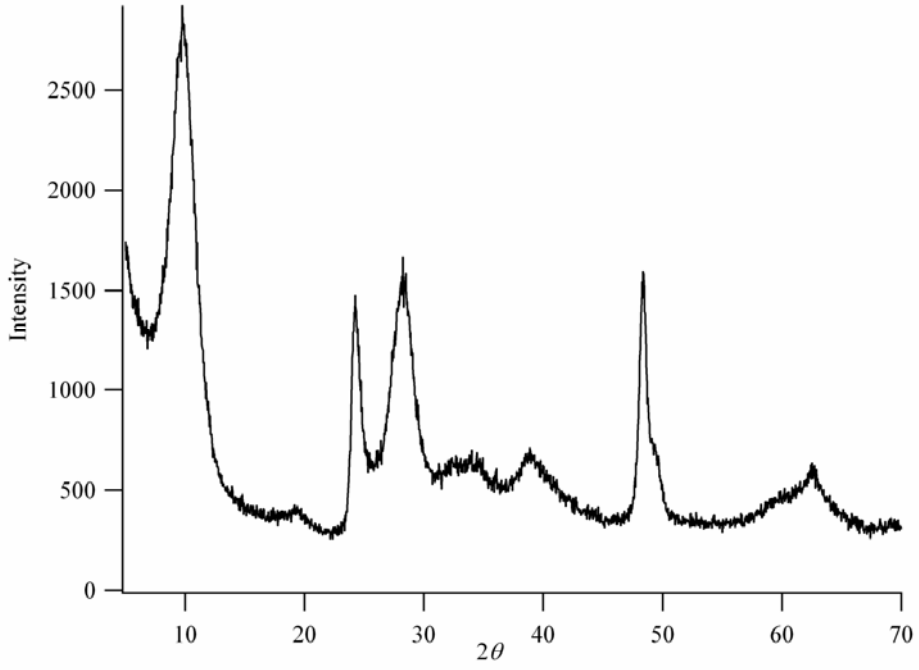

Figure 4-12: XRD pattern of TNT-4.

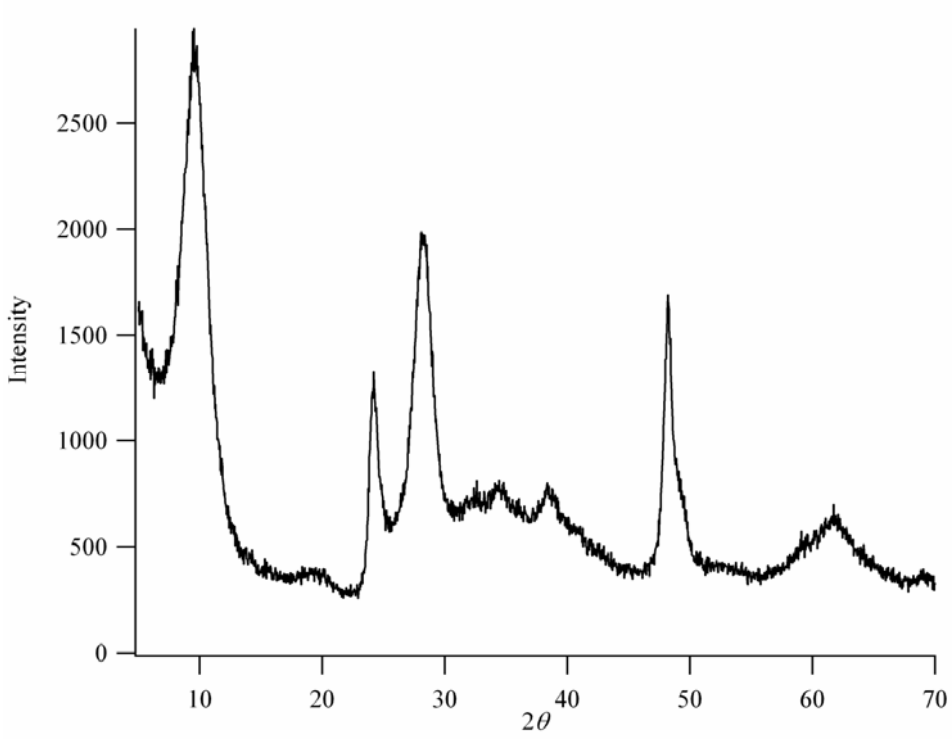

Figure 4-13: XRD pattern of TNT-5.

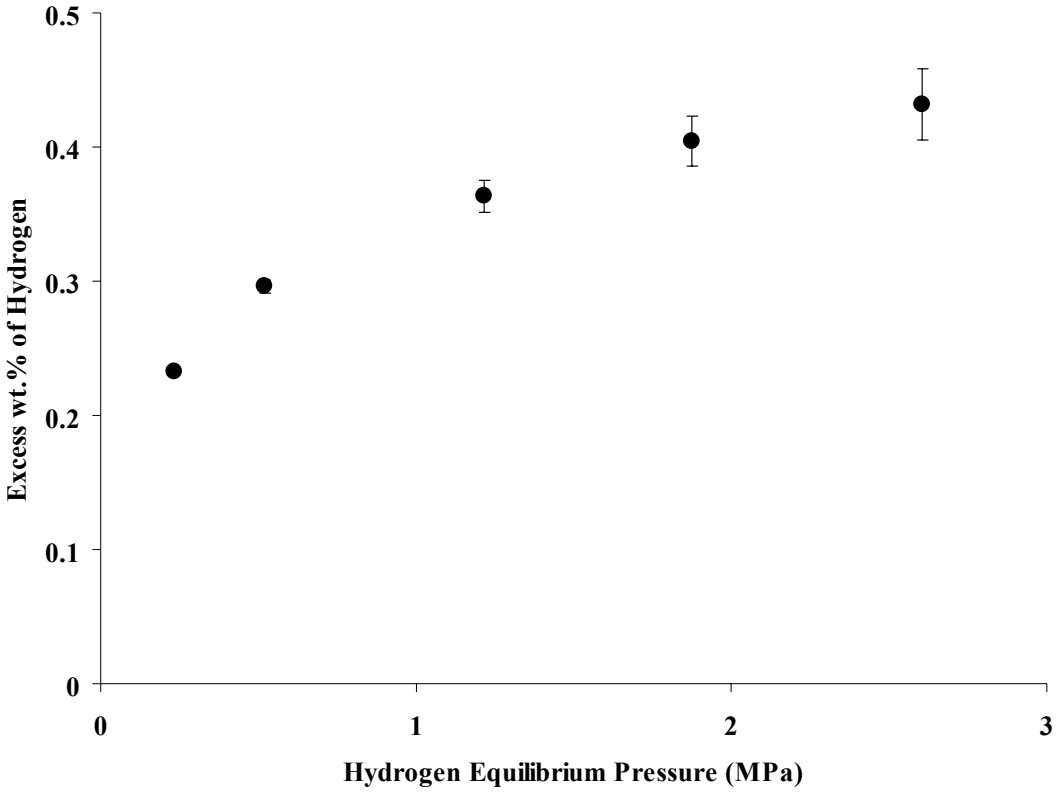

Figure 4-14: Hydrogen adsorption performed at 77 K on sample TNT-4.

Figure 4-14 shows the hydrogen adsorption performed at 77 K on the sample TNT-4. The adsorption curve is distinctly different to that of TNT-3 in a number of ways. The first is the shape of the adsorption isotherm. TNT-3 shows a steep initial uptake of hydrogen followed by a plateau above an equilibrium pressure of 5 MPa. For TNT-4 there is a reasonably steep uptake associated with the first equilibrium pressure at ~0.2 MPa. Beyond this pressure there is a gradual increase in uptake with pressure. The final equilibrium pressure point at ~2.6 MPa yields a hydrogen adsorption of 0.43 wt.%, a value nearly half that for TNT-3.

4.4.3. Ion-exchanged Nanotubes: Zn-TNT-4, H-TNT-5 and Li-TNT-5

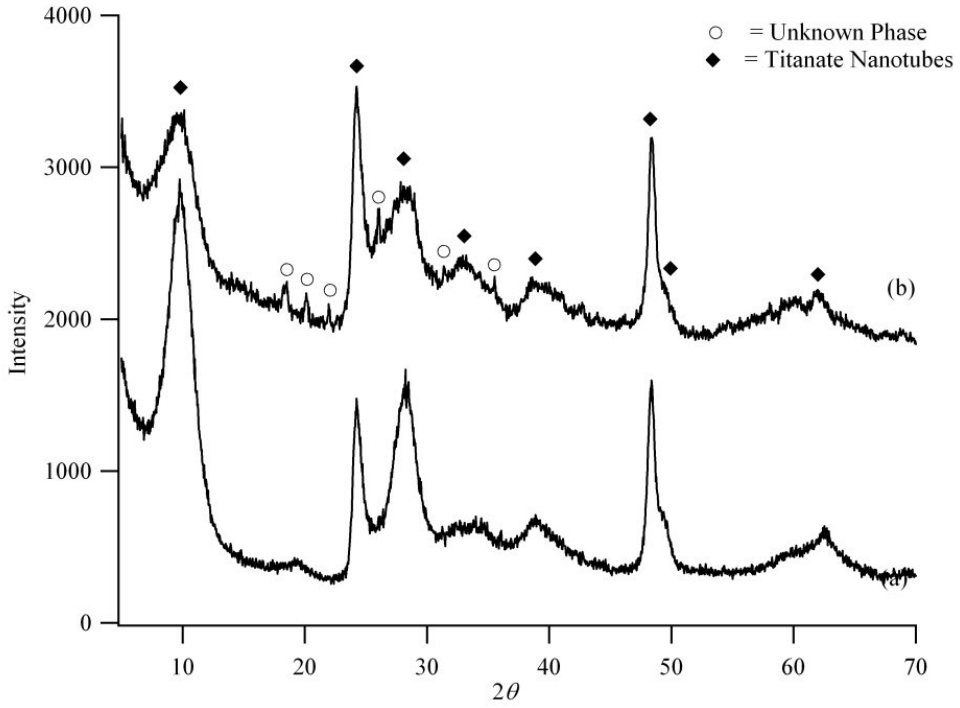

Figure 4-15: XRD patterns of: (a) as produced titanate nanotubes, TNT-4, and (b) zinc exchanged titanate nanotubes, Zn-TNT-4. The Zn-TNT-4 pattern is offset by 1500 counts for clarity. ♦ Indicates titanate nanotube phase and ○ indicates an unknown phase or phases.

The XRD pattern of zinc exchanged titanate nanotubes, Zn-TNT-4, is shown in Figure 4-15(b). There is a reduction in the intensity of the peaks at $2\theta \sim 9.8^{o}$ and 28^{o}. The most pronounced change is the presence of six small but relatively sharp peaks at $2\theta \sim 18.3^{o}$, 20.1^{o}, 22.0^{o}, 26.0^{o}, 31.4^{o} and 35.5^{o} respectively. These peaks remain unidentified. Zinc sulphate monohydrate ($ZnSO_4.H_2O$, PDF = 33-1476) has peak positions that align with three of these peaks but the intensities are inconsistent. All

other zinc sulphates, sulphites and their hydrates as well as sodium sulphates, sulphites and their hydrates can be excluded as possible phases remaining from incomplete washing of the sample.

These changes in the XRD pattern of Zn-TNT-4 are also distinctly different to the changes for the zinc exchanged titanate nanotubes of Sun and Li[174]. Their method of zinc exchange used a solution of a dissolved zinc salt that had been complexed with ammonia. Their XRD pattern showed a significant sharpening in the peak at $2\theta \sim 10^{o}$ and the appearance of a higher order reflection of this peak at $2\theta \sim 20^{o}$ while their peak at 2θ ~ 28.0 showed a decrease in intensity as compared to starting nanotubes. TGA further revealed that ammonia was also intercalated into the crystal lattice.

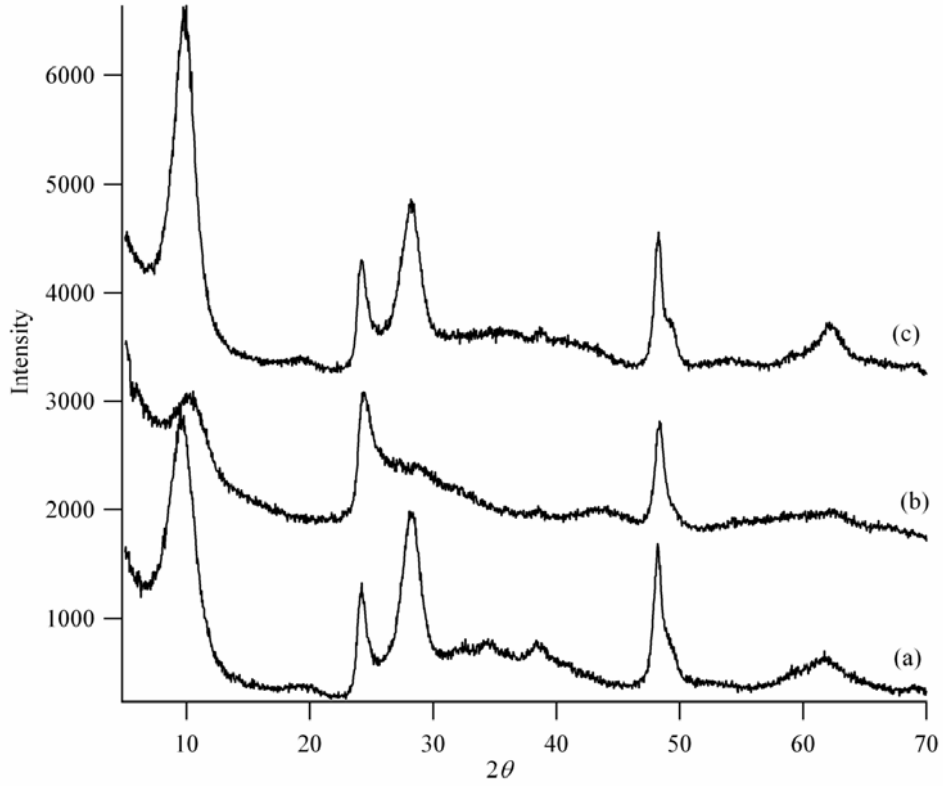

Figure 4-16: XRD patterns of: (a) As produced titanate nanotubes, TNT-5, (b) hydrogen exchanged nanotubes, H-TNT-5, and (c) lithium exchanged nanotubes, Li-TNT-5. Each pattern is offset by 1500 counts for clarity.

Figure 4-17 shows the XRD patterns of the hydrogen exchanged nanotubes, H-TNT-4, the lithium exchanged nanotubes, Li-TNT-5, and the original starting nanotubes, TNT-5.

The H-TNT-5 pattern (Figure 4-16(b)) shows a marked deterioration in the structure. The strongest peak in TNT-5 at $2\theta \sim 9.6^{o}$ has shifted to $2\theta \sim 10.4^{o}$ and has been significantly reduced in intensity. The peaks at $2\theta \sim 28^{o}$, 35.5^{o}, 38.5^{o} and 61.5^{o} are practically absent in the hydrogen exchanged sample while the shoulder at $2\theta \sim 49.5^{o}$ has also been reduced in intensity. A broad and weak peak at $2\theta \sim 43.5^{o}$ also becomes evident. This pattern is similar to that obtained by Morgado et al.[197] who treated 1g of nanotubes with 375g of 0.1M HCl. They determined that their nanotubes had a residual sodium content of 1.22 wt.%.

The lithium exchanged nanotubes, Li-TNT-5, (Figure 4-17(c)) show little changed as compared to the TNT-5. The strongest peak at $2\theta \sim 9.8^{o}$ shows a minor increase in intensity as compared to the starting nanotubes. A minor shift in the peak ($\Delta 2\theta < 0.2^{o}$) position may be present but the strong background through this region of the XRD pattern makes definitive determination difficult. The peaks at $2\theta \sim 35.5^{o}$ and 38.5^{o} are no longer evident, instead an elevated background is present between $2\theta \sim 30.5^{o}$ and 45.5^{o}.

Also of note is the mass change after lithium exchange. 1.005g of TNT-5 was used for the exchange process while 0.91g of nanotubes were recovered. After 5 months of storage at ambient conditions and atmospheric humidity, this mass had increased to 0.93g.

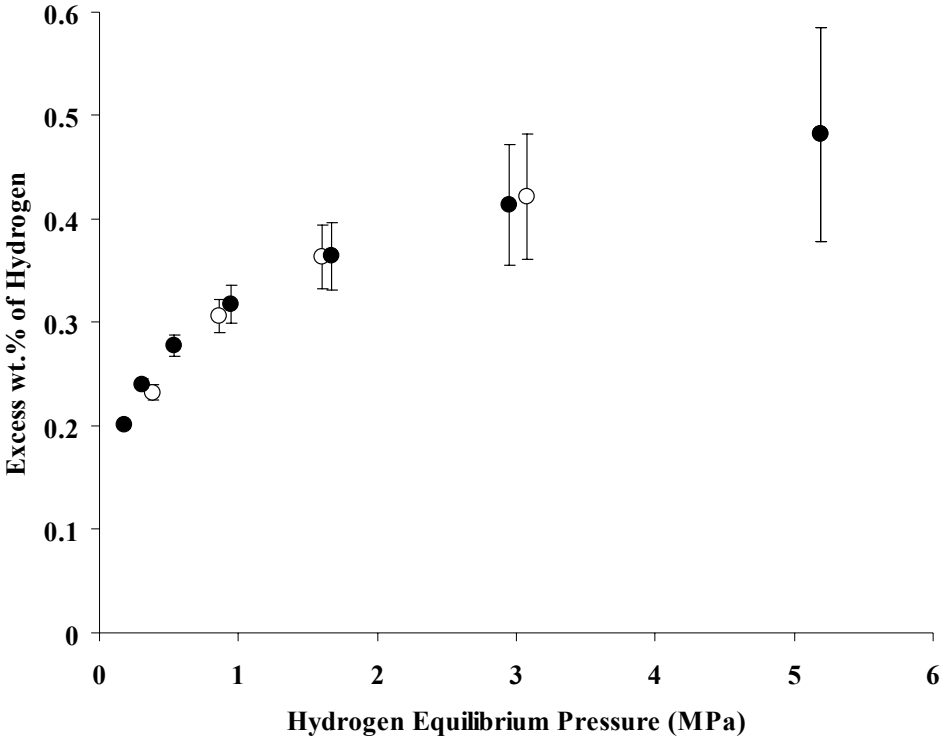

Figure 4-17: Hydrogen adsorption (●) and desorption (○) on zinc exchanged titanate nanotubes, Zn-TNT-4, performed at 77 K.

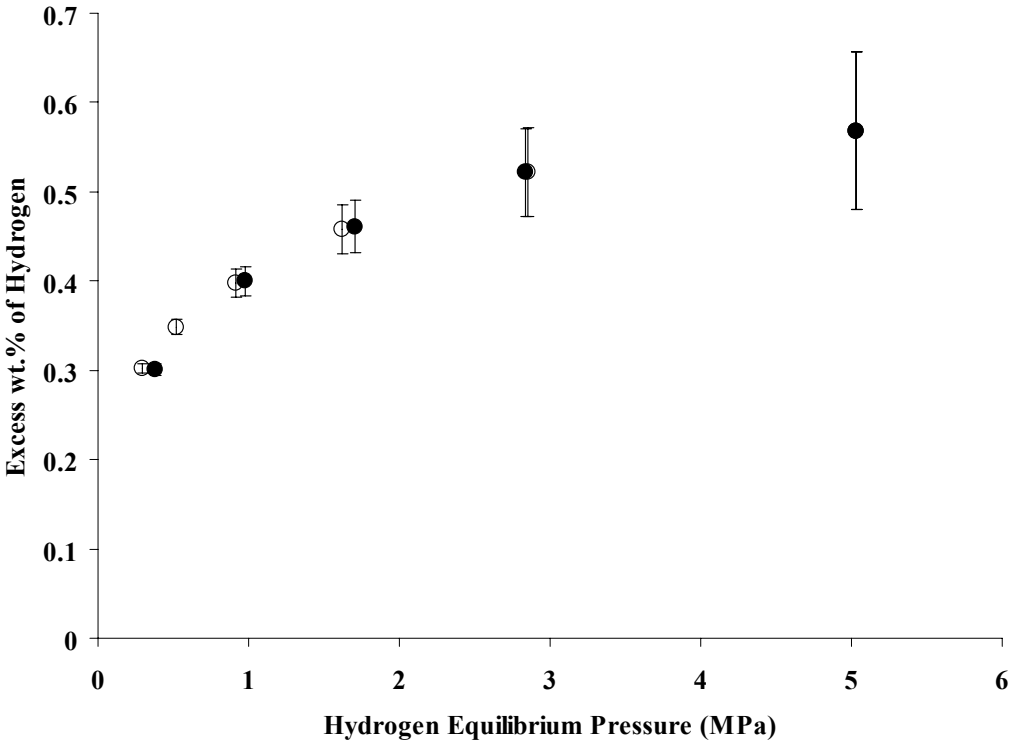

Figure 4-18: Hydrogen adsorption (●) and desorption (○) on hydrogen exchanged titanate nanotubes, H-TNT-5, performed at 77 K.

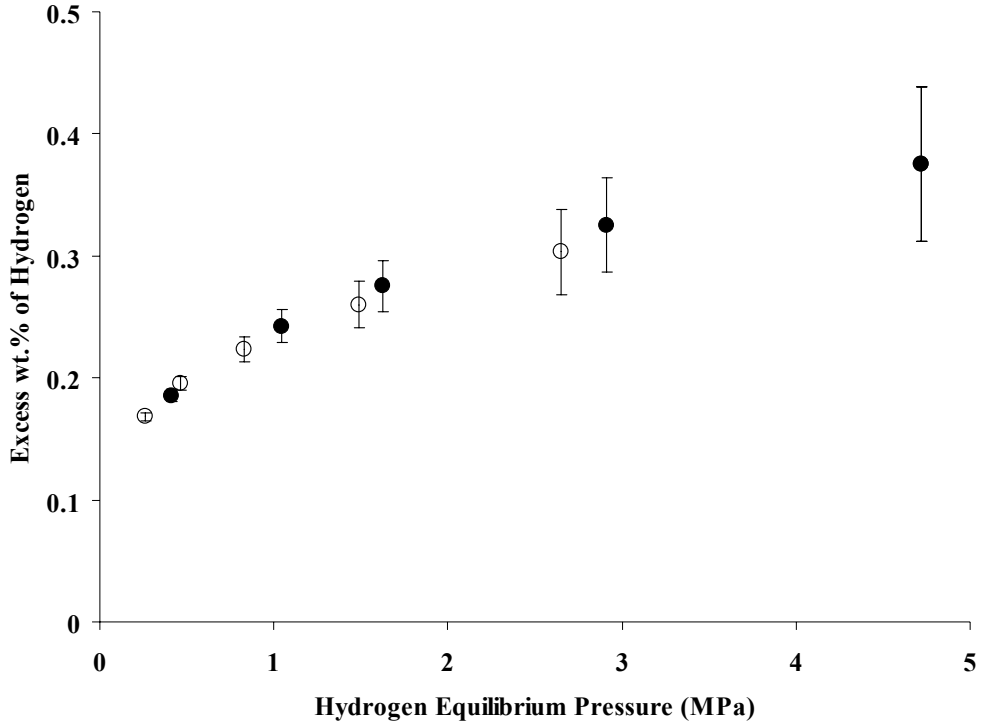

Figure 4-19: Hydrogen adsorption (●) and desorption (○) on lithium exchanged titanate nanotubes, Li-TNT-5, performed at 77 K.

Hydrogen adsorption/desorption measurements performed at 77 K on the Zn-TNT-4, H-TNT-5 and Li-TNT-5 are shown in Figure 4-17, 4-18 and 4-19 respectively. Hydrogen adsorption was measured to reach 0.48% (at ~5.2 MPa), 0.57% (at ~5.0 MPa) and 0.37% (at ~4.7 MPa) respectively. The adsorption and desorption curves are consistent in shape between Zn-TNT-4, H-TNT-5 and Li-TNT-5 but are distinctly different to TNT-3. The desorption curves for Zn-TNT-4, H-TNT-5 and Li-TNT-5 show slight hysteresis below ~2 MPa when compared to the adsorption curves.

4.5. Discussion

4.5.1. Sodium Content and the Effect of Acid Washing

A significant problem with comparing hydrogen adsorption results from this thesis and that from the literature is due to sample characterisation. The initial synthesis process of ageing TiO_2 in concentrated sodium hydroxide is straightforward. However, the washing process in the literature is systematically dearth of detail. Kasuga et al.'s[170] original paper merely stated that after the as-produced nanotubes

had been washed with water and then with with 0.1 M HCl. Other publications use dilute nitric and sulphuric acid[175], again, without specific details. The complication of this lack of detail in the acid wash is due to the fact that acid treatment is known to result in degradation of the titanate nanotube structure. Du et al.[172] reported that TEM observations of nanotubes "washed" with 0.1 M HCl, as advocated by Kasuga et al.,[170] resulted in more stuctural defects than nanotubes washed only with water, Stirring of nanotubes in 0.1 M HNO_3 for 2 hours[174] was shown to result in a slight degradation of the nanotube structure, as determined by XRD, while alternatively washing 1 g of nanotubes with water and 0.1 M HCl until 375 g of HCl was used resulted in significant degradation of the nanotube structure. XRD of the 0.1 M HCl treated sample showed that the two strongest diffraction peaks at $2\theta \sim 10^{o}$ and 28^{o} are almost totally removed. Increasing the stirring time of nanotubes in 0.1 M HCl up to 48 hours results in total destruction of the titanate structure and a transformation to anatase[194]

Despite the lack of specific washing details in the literature, some conclusions can be drawn based on the characterisation of samples in the literature and their comparison to the samples examined for this thesis. Morgado et al.[197] showed that, though an extensive acid wash resulted in degradation of the titanate nanotube structure, some of the original sodium ion content still remained (~1 wt.% of total nanotube mass). A less aggressive acid wash step resulted in approximately half of the original sodium content being removed with no discernable change in the titanate nanotube structure. Based on this an estimate of the extent of hydrogen ion exchange for sodium ions can be made for the samples TNT-3 (short acid wash), TNT-4 (water only wash) and H-TNT-5 (extended acid wash). Sample TNT-4, washed only with water, is likely to contain near stochiometric $Na_2Ti_3O_7$ (assuming the structure proposed by Chen et al.[173]). Sample H-TNT-5, stirred for 2 hours in 0.1 M HCl, is likely to be near stoichiometric $H_2Ti_3O_7$ while TNT-3 is most likely to be $Na_xH_{2-x}Ti_3O_7$. However exact determination of the residual sodium content requires a quantitative analysis technique.

4.5.2. Hydrogen Adsorption

A direct comparison with the hydrogen adsorption measurements of Lim et al.[194] is difficult as the samples of Lim et al. are, strictly speaking, no longer titanate nanotubes but are titania nanotubes (TiO_2 – anatase phase) with the retention of the hollow tubular structure but without the layered wall structure of titanate. Given the nanostructure of Lim et al.'s titania nanotubes, room temperature hydrogen adsorption of 2.0 wt.% (~6 MPa) at first glance seems plausible. However, further examination reveals that they also report that the hydrogen adsorption of bulk anatase powders reaches 0.8 wt.% at room temperature and 6 MPa. This is an extraordinarily high amount for a non-porous material having a surface area of 16 m^2/g. Consequently, further comparisons seem redundant.

Based upon a comparison of the XRD patterns of Morgado et al.[197] and that of hydrogen exchanged H-TNT-5, the residual sodium content of H-TNT-5 can be assumed to be ~1 wt.%. Given this and the fact that Bavykin et al.'s[193] hydrogen exchanged nanotubes adsorb 3.8 wt.% of hydrogen at 77 K and 2.5 wt.% at room temperature, the poor hydrogen uptake of H-TNT-5 is unexpected. However, a comparison of the XRD pattern of H-TNT-5 and that of Bavykin et al. reveals that, in addition to degradation of the structure in general, the position of the XRD peak at $2\theta \sim 10^o$ has shifted to a larger angle for sample H-TNT-5 while that for Bavykin et al.'s has remained at $2\theta \sim 10^o$. The implication of this is that if the substitution of sodium ions for hydrogen ions does not result in a change in the interlayer spacing, then by virtue of the difference in size between sodium and hydrogen ions, a pore spacing large enough to allow hydrogen molecules to enter is created. In the case of H-TNT-5, the exchange of hydrogen ions for sodium ions was associated with a contraction of the interlayer spacing. The result is an interlayer spacing too small to allow the entry of hydrogen molecules.

The hydrogen adorption behaviour at 77 K of TNT-3 can therefore be explained by the partial substitution of sodium ions for hydrogen ions during the brief acid washing. During acid washing, the exchange of sodium ions for hydrogen ions is expected to start at the ends of the nanotubes and proceed towards the centre. In the case where the acid wash is insufficiently long to result in complete ion substitution,

the result would be a nanotube where hydrogen ion exchange has occurred at the ends of the nanotube but not in the centre.

Given that the hydrogen adsorption at 77 K of sample TNT-4, with interlayer sodium ions, appears to be surface only and not in the interlayer spacing and that Bavykin et al.'s hydrogen adsorption shows molecular hydrogen penetration of the interlayer spacing, the hydrogen adsorption at 77 K of TNT-3 is accounted for by partial substitution of the sodium ions for hydrogen ions near the ends of the nanotubes. The substitution of sodium ions for the smaller hydrogen ions while maintaining the same interlayer spacing results in a pore large enough to allow for hydrogen penetration. This idea is represented in Figure 4-20. Here we see that molecular hydrogen can penetrate along the interlayer spacing as far as hydrogen ions have been substituted for sodium ions.

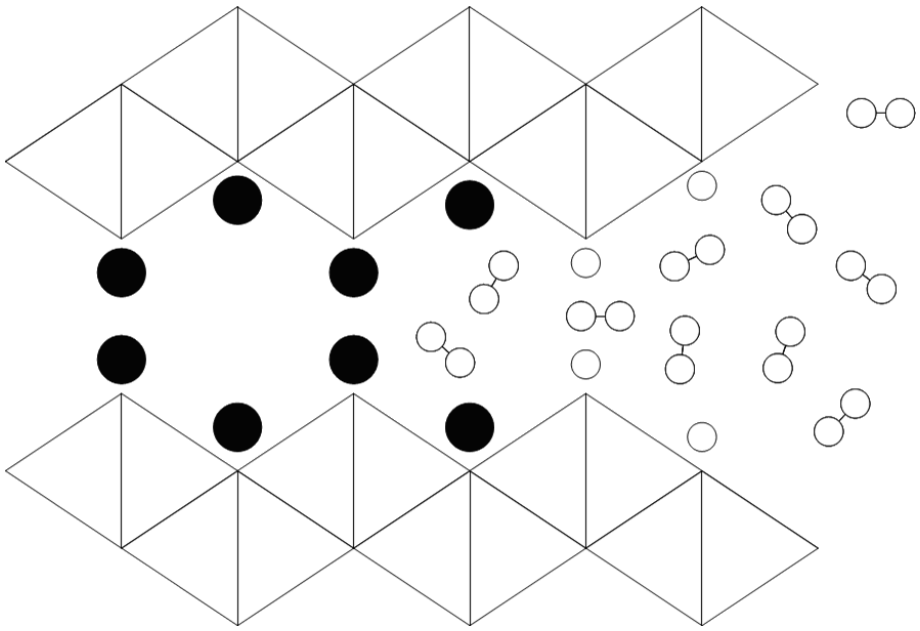

Figure 4-20: A schematic of partially ion exchanged titanate nanotubes with the $Na_2Ti_3O_7$ structure[173] with adsorption of molecular hydrogen (○-○). ● equals sodium ions and ○ equals hydrogen ions.

The hydrogen adsorption at 77 K of TNT-4, Zn-TNT-4 and Li-TNT-5 can all be interpreted with respect to the size of the interlayer spacing and whether it is large enough to allow the penetration of molecular hydrogen. XRD shows the spacing between planes in the titanate nanotube walls remains constant upon sodium ion exchange for zinc and lithium ions. However, the hydrogen adsorption curves for the

zinc and lithium exchanged nanotubes show no significant difference to that of sodium containing TNT-4. If we assume that the hydrogen adsorption for TNT-4, Zn-TNT-4 and Li-TNT-5 is on the external surfaces only and if we assume that these surfaces adsorb hydrogen at a rate 2 wt.% per 1000 m^2/g [3] then the surface area for these materials is estimated to range between 185 and 285 m^2/g. This surface area is typical for that of titanate nanotubes reported in the literature.

4.6. Conclusion

The hydrogen adsorption results of Bavykin et al.[193] and Lim et al.[194] could not be reproduced at 77 K or at room temperature. Though markedly different in total hydrogen uptake at 77 K to the results of Bavykin et al.,[193] and the shape of the adsorption and desorption curve of sample TNT-3 showed strong similarities. The adsorption curve was characterised by steep hydrogen uptake at low pressure before quickly flattening. Desorption is characterised by strong hysteresis with 85% of the maximum hydrogen uptake still remaining in the sample upon a reduction in the equilibrium pressure to 140 kPa. The difference in the total hydrogen uptake of TNT-3 (0.86 wt.%) and that of Bavykin et al.[193] (3.8 wt.%) can be attributed to a difference in acid washing procedure. The short acid wash step used for TNT-3 results in only partial substitution of interlayer sodium ions for hydrogen ions. The result is that not all of the interlayer spacing of the titanate nanotubes is made available for hydrogen molecules to penetrate. A longer acid washing step, as used for H-TNT-5, though increasing the sodium ion substitution for hydrogen ions, resulted in degradation of the nanotube structure and a reduction of the interlayer spacing of the nanotube. The result was that the interlayer spacing was impenetrable to molecular hydrogen despite near complete exchange of sodium ions for hydrogen ions.

At 77 K zinc and lithium exchanged nanotubes showed hydrogen sorption characteristic of hydrogen adsorption on the external surface area of the nanotubes. (i.e. less than 0.5 wt.% at ~5MPa). Minor hysteresis on the desorption curves suggests that some molecular hydrogen may penetrate the interlayer spacing of the nanotube.

Hydrogen adsorption at room temperature was negligible, being below 0.1 wt.% at 5 MPa for all samples studied.

4.7. Directions for Future Work

If the results of Baykin et al.[193] can be reproduced, further research on titanate nanotubes presents interesting possibilities. Bavykin et al.[193] measured hydrogen uptake after 12 hours of 2.5 wt.% with the sample yet to reach saturation. They also determined that the rate of hydrogen adsorption is dependent on the speed of hydrogen diffusion along the titanate layers. Two avenues exist for increasing this diffusion rate. The first is to increase the applied hydrogen pressure[196] while the second involves shortening the length of the titanate nanotubes via ultrasonic treatment[175]. Mixing of zeolites and MOFs with a platinum catalyst supported on activated carbon was shown to increase room temperature hydrogen uptake by a factor of between 2.6 and 3.1. A similar increase in hydrogen capacity of titanate nanotubes treated with this platinum catalyst would yield greater than 6 wt.% hydrogen storage at room temperature.

5. Titanium-Magnesium-Nickel Alloys

5.1. Motivation

Many metals and their intermetallics react with gaseous hydrogen to form metal hydrides. Metal hydrides provide a number of positive aspects with regards to hydrogen storage in mobile applications. The hydrogen can be absorbed/desorbed with changes in either temperature or pressure and the hydrogen is often stored at a density higher than that found in liquid hydrogen. The released hydrogen is also very pure while the metal hydrides themselves usually have high safety. However, since the intermetallic hydrides consist of relatively heavy transition metals they usually have a low wt.% of hydrogen while those with higher wt.% of hydrogen require impractical operating temperatures for absorption/desorption.

Magnesium, magnesium with additives and magnesium alloys have an extensive history when it comes to their interaction with hydrogen. Interest in the alloy of titanium, magnesium and nickel extends from a publication[201] in 2002 that claimed an extraordinary 11 wt.% of hydrogen uptake for a Ti-Mg-Ni sample ball milled with a molar ratio of 53:47:20. The interest in $Ti_{53}Mg_{47}Ni_{20}$ was in turn, sparked by hydrogen absorption reported for the quasi-crystal $Ti_{53}Zr_{47}Ni_{20}$[202]. The aim of examining the $Ti_{53}Mg_{47}Ni_{20}$ is to verify the claims of Lomness et al.[201] as to the effectiveness of this material as a hydrogen storage medium. Magnesium and titanium each form a hydride and a number of intermetallic compounds consisting of Ti-Ni and Mg-Ni also form hydrides. For this thesis, the work of Lomness et al.[201] will be repeated to verify the claims of 11 wt.% of hydrogen uptake. Furthermore, various stoichiometries of Ti-Mg-Ni and their effects on hydrogen sorption properties will also be examined. To provide a basis for examining the $Ti_{53}Mg_{47}Ni_{20}$ system, the interaction between the constituent elements and hydrogen should first be explored.

5.2. Ti, Mg, Ni and Their Interaction with Hydrogen

5.2.1. Magnesium - Hydrogen

Magnesium can store 7.7 wt. % of hydrogen corresponding to a stoichiometry of MgH_2. Magnesium is also a relatively cheap and abundant material making it a prime

candidate as a hydrogen storage media. In examining the viability of a metal hydride as a hydrogen storage media, there are three main criteria of importance[203]: the amount of hydrogen absorbed/desorbed; the temperature required to absorb/desorb hydrogen at a useable pressure (thermodynamics) and; the hydriding/dehydriding kinetics. Magnesium stores a large amount of hydrogen but suffers from relatively poor absorption/desorption kinetics and a high thermal stability. The examination of the literature relating to magnesium hydride will be split into two sections. The first (Section 5.2.1.1) will examine the attempts that have been made to alter the thermodynamics of magnesium hydride while the second (Section 5.2.2.2) will examine ways in which the kinetics of magnesium hydride formation have been altered.

5.2.1.1. Thermodynamics

Pressure-composition-temperature isotherms for the magnesium hydrogen system are shown in Figure 5-1 for temperatures ranging from 613 K to 833 K (340^{o}C to 560^{o}C). The curve consists of a long, almost flat plateau region[204] during which unreacted magnesium and the β-phase of MgH_2 co-exist. The existence or otherwise of an α-phase at low pressure is still a matter of debate[205]. A sharp upturn from the plateau occurs when all the magnesium has been converted to MgH_2. An upturn from the plateau may occur before the stoichiometry of MgH_2 is reached due to the encapsulation of unreacted magnesium by the hydrogen impermeable magnesium hydride layer[206].

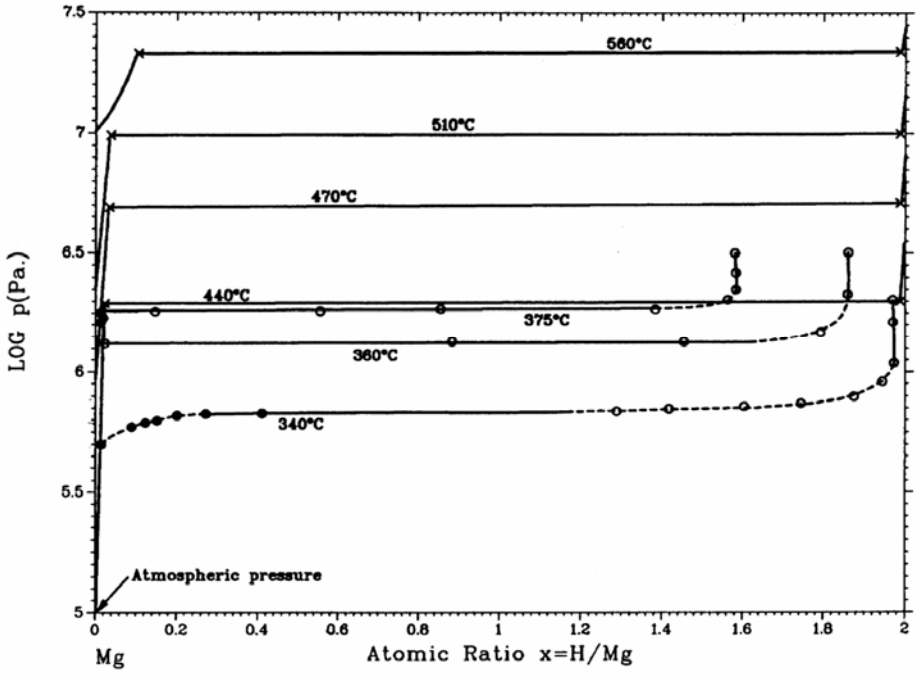

Figure 5-1: Pressure vs composition isotherm for the Mg-H system taken from Manchester and San-Martin[205]. (○) and (●) refer to adsorption and desorption data from Belkbir et al.[206] while (x) refers to data from Stampfer et al.[204] Reprinted with permission of ASM International®. All rights reserved. www.asminternational.org

The enthalpy of decomposition for magnesium hydride is approximately -74.5 kJ/mole H_2 while the enthalpy of formation has a similar value as a result of a minimal amount of hysteresis between the absorption and desorption equilibrium pressures[205]. The entropy of desorption has been measured as being -135 $Jmol^{-1}K^{-1}$ H_2.[204]. These values translate to a hydrogen equilibrium pressure with magnesium of ~1.9 MPa at 673 K (400°C), ~180 kPa at 573 K (300°C) and ~7 kPa at 473 K (200°C) respectively.

Given the high temperatures required for magnesium hydride to evolve hydrogen at a useable pressure (i.e. >0.1 MPa), much work has been done focusing on the destabilisation of magnesium hydride (that is, to decrease the magnitude of the enthalpy of formation/decomposition). This work has taken two directions. The first involves examination of Mg-rich solid solutions containing small amounts of other elements while the second involves defined compounds such Mg_2Cu[207], Mg_2Ni[208], Mg_2Ca[209,210], Mg_2Al_3, $CeMg_{12}$ and La_2Mg_{17}[211]. The intermetallic compounds can

subsequently be categorised in three classes depending on their interaction with hydrogen[212]:

i) Compounds that form a ternary hydride such as $Mg_2Ni + H_2 \rightarrow Mg_2NiH_4$;

ii) compounds that undergo a disproportionation reaction to form two hydrides, such as $2CeMg_{12} + 27H_2 \rightarrow 2CeH_3 + 24\ MgH_2$;

iii) compounds that after disproportionation give magnesium hydride and a non-hydride phase, such as $2Mg_2Cu + 3H_2 \rightarrow 3MgH_2 + MgCu_2$.

Reilly and Wiswall[208] performed early work on the destabilisation of magnesium hydride by alloying magnesium with nickel to form the intermetallic Mg_2Ni. This intermetallic then interacts with hydrogen to form a ternary hydride according to equation (5-1).

$$Mg_2Ni + 2H_2 \rightarrow Mg_2NiH_4 \qquad (5\text{-}1)$$

This intermetallic of magnesium can reversibly store 3.6 wt.% at 571 K (298^{o}C) with an equilibrium pressure of just over 0.3 MPa and an enthalpy of formation of -64.5 kJ/mole H_2. This represents modest destabilisation compared to MgH_2 and comes with a significant sacrifice in hydrogen capacity. In an effort to further reduce the stability of Mg_2Ni, transition metals have been partially substituted for nickel ($Mg_2Ni_{0.75}M_{0.25}$ where M = Cr, Cu, V[213], Fe, Co, Zn[214], Ti and Mn[215]). In general, these partially substituted materials can store ~3 wt.% of hydrogen but still require operating temperatures above 500 K (227^{o}C)[213] with measured enthalpies of formation ranging between -53 and -66 kJ/mol H_2.

Reilly and Wiswall[207] also performed the earliest work on destabilisation of magnesium hydride via a disproportionation reaction as given by equation (5-2).

$$2Mg_2Cu + 3H_2 \rightarrow 3MgH_2 + MgCu_2 \qquad (5\text{-}2)$$

This system can reversibly store 2.6 wt% of H_2 with an equilibrium pressure of 0.6 MPa at 548 K (295^{o}C); an increase by a factor of three over pure magnesium. Though the hydrogen uptake is limited by the amount of copper in the system, it was the first example of a reversible disporportionation reaction involving magnesium hydride.

Magnesium hydride also undergoes a disproportionation reaction with aluminium[216, 217, 218, 219]. A variety of stoichiometries can exist in the Mg-Al system with hydrogen storage capacities ranging between 3 wt.%[216] and 4.5 wt.%[218] at a pressure three times greater than that for magnesium at 553 K (280°C). Early work on the Mg-Al system[217] suggested the kinetics of these systems were a limiting factor due to the poor diffusion rate of aluminium through magnesium at low temperatures. However ball-milling seems to have removed this problem[218, 219].

Magnesium hydride undergoes a disproportionaion reaction with silicon[220] according to equation (5-3).

$$2MgH_2 + Si \rightarrow Mg_2Si + 2H_2 \qquad (5\text{-}3)$$

This reaction represents 5 wt.% hydrogen storage and has an enthalpy of dehydrogenation of -36.4 kJ/mol H_2, approximately half that of the enthalpy of desorption of pure magnesium hydride. The theoretically calculated equilibrium pressure is 0.01 MPa at 293 K (20°C), 10 MPa at 423 K (150°C) and 100 MPa at 573 K (300°C) but rehydrogenation could not be achieved with a pressure of 10 MPa at 423 K (150°C). This lack of rehydrogenation was believed to be due to the kinetic barrier represented by the required inter-diffusion of magnesium and silicon ions. Hydrogen generation was also kinetically limited by the build up of Mg_2Si.

Magnesium solid solutions with small amounts of other elements such as Cd[221], Ti[222], Li, Al, Pb, Sc, Zn, Ag, Ga and Sn[223] have also been examined. In a number of these cases the solid solution decomposes upon hydrogenation while modest improvements in equilibrium pressure compared to MgH_2 were obtained for Zn, Al, Ag and Ga. The exceptions to this were the solid solutions incorporating In and Cd which resulted in equilibrium pressures comparable to that of Mg_2NiH_4 at 573 K (300°C).

5.2.1.2. Kinetics

The kinetics for magnesium hydride formation are influenced by a number of factors including: the sticking coefficient of H_2 on magnesium; the rate of H_2 dissociation and; the rate of diffusion of H through the magnesium hydride layer[65].

As a hydrogen molecule approaches the magnesium surface it encounters an acitvation barrier to adsorption. This barrier is high enough to result in a very low sticking probability for hydrogen on magnesium[65]. Furthermore, once adsorbed the activation energy for dissociation strongly depends on the adsorption site geometry which, for magnesium, results in a slow dissociation rate. Lastly, hydride formation occurs via the nucleation and expansion of the β - phase at one of more points on the surface of magnesium. These nucleation sites eventually coalesce and, if the particle is sufficiently large, may form a hydride envelope with an unreacted metal core. The limiting factor in the rate of this hydride growth into the metal core is the negligible diffusion rate of hydrogen ions through this hydride[205]. The result is that magnesium has very poor hydrogen absorption kinetics with the first absorption cycle requiring pressures of up to 3 MPa, temperatures up 613 K (340^{o}C) and a time ranging from 6 hours to several weeks[212].

The main approach to increasing the absorption/desorption kinetics of magnesium has been to employ ball milling. Ball milling increases the surface area by decreasing particle size resulting in shorter diffusion lengths for hydrogen. As well as the reduction in particle size, crystal defects such as dislocations, vacancies, stacking faults as well as an increased number of grain boundaries[224] result in an increased number of sites suitable for hydrogen adsorption and dissociation.

Early efforts involving ball milling magnesium focussed on two main facets. The first was ball milling magnesium with an element that readily forms a hydride and acts as a "hydrogen pump" supplying magnesium with dissociated hydrogen. The second involves ball milling magnesium with catalytically active materials that do not themselves form hydrides but act as sites for hydrogen dissociation with subsequent diffusion to the magnesium/catalyst interface.

One of the earliest ball milling efforts consisted of milling magnesium metal with $LaNi_5$[225], an intermetallic compound that can rapidly absorb hydrogen at room temperature. The addition of this $LaNi_5$ (in amounts between 10 and 20 wt.%) resulted in the magnesium sample being able to absorb, at 618 K (345^oC), almost all of its hydrogen in 15 minutes under a hydrogen pressure of 3 MPa: a vast improvement in absorption kinetics. However, the addition of the relatively heavy $LaNi_5$ resulted in a total hydrogen uptake ranging between ~4.5 and ~5.7 wt.%.

Ivanov et al.[226] examined the effect of 5 atomic percent of the transition elements Ti, Co, Ni, Nb and Fe ball milled with magnesium and its effect on the kinetics of MgH_2 formation. At 613 K (340^oC) and an applied hydrogen pressure of 1.5 MPa, with the exception of the titanium doped sample, these materials could also absorb ~5 wt.% of hydrogen in under 20 minutes.

Imamura and co-workers[227,228,229] examined the effect of milling magnesium with graphite in the presence of various organic solvents. Magnesium and graphite milled with tetrahydrofuran or cyclohexane showed the strongest affinity for hydrogen and absorption at room temperature was even possible. They suggested that the improved kinetics were the result of intimate contact between the graphite and magnesium that was promoted by the presence of the organic additive. However, a direct comparison with the kinetics obtained by Ivanov et al.[226] and Tanguy et al.[225] is difficult as measurements performed by Imamura et al. were performed at 453 K (180^oC) under a hydrogen pressure of just 0.07 MPa.

In the late 1990's, focus shifted away from ball milling magnesium to ball milling magnesium hydride with additives. This approach has a number of advantages. The first is the elimination of process control agents (i.e. anti-sticking compounds) as magnesium hydride is brittle compared to ductile magnesium metal. The second advantage is that starting with chemically synthesized magnesium hydride (MgH_2) means that an activation process, as in the case of pure magnesium, is no longer required.

Huot et al.[230] performed some of the earliest work on ball milled MgH_2. They showed that at 623 K (350^oC) a ball-milled sample of MgH_2 could desorb nearly 7 wt.% of

hydrogen in ~600 seconds under a pressure of 0.15 MPa while the unmilled sample only yielded ~5 wt.% after 2000 seconds. Fast desorption kinetics were less pronounced at 573 K (300^{o}C) with only ~2 wt.% being desorbed from the milled MgH_2 in 2000 seconds.

Following this result, efforts were concentrated on milling MgH_2 with various catalysts including transition metals[231], transition metal oxides[232,233,234,], metal halides[235], nickel/alumina/carbon composites[236] as well as nanostructured materials such as single-walled carbon nanotubes, fullerenes, activated carbon, boron nitride nanotubes and asbestos[237]. Of these niobium oxide (Nb_2O_5) has the largest impact on both adsorption and desorption kinetics[233,234]. At 573 K (300^{o}C), absorption under a hydrogen pressure of 0.84 MPa yielded 7 wt.% uptake in as little as 60 seconds while at 523 K (250^{o}C), 6 wt.% of hydrogen was absorbed in 60 seconds. Desorption, performed under vacuum, resulted in complete desorption in 90 seconds at 573 K (300^{o}C) and 500 seconds at 523 K (250^{o}C) respectively. These results were achieved using just 0.2 mole% of the oxide suggesting that improvements in kinetics due to 5 mol% transition metals may in effect be due to trace oxide contamination. The use of metal halides[235] as well as nitrides and carbides of transition metals[238] to enhance kinetics as well as the relative lack of improvement when using very pure transition metals[238] also suggests that it is the final oxidation state of the metal catalyst that is responsible for the enhanced kinetics. The measurements on Nb_2O_5 and its effect on magnesium hydride by Bharkordarian et al.[233,234] were limited to temperatures above 523 K (250^{o}C). However, other authors[236] have reported absorption kinetics at room temperature similar to that of pure magnesium at 623 K (350^{o}C) (~6 hours) while desorption has been demonstrated, under vacuum conditions at least, at temperatures as low as 473 K (200^{o}C)[235,236].

5.2.2. Titanium - Hydrogen

As mentioned in Section 5.2.1, the three main criteria for a hydrogen storage material are: the amount of hydrogen absorbed/desorbed; the temperature required to absorb/desorb hydrogen at a useable pressure and; the hydriding/dehydriding kinetics.

Stoichiometric titanium hydride (TiH_2) corresponds to 4.0 wt. % of hydrogen. Titanium hydride can have a variety of phase structures which are dependent on both temperature and hydrogen content[239]. Titanium hydride has the disadvantage of a high enthalpy of formation/decomposition requiring elevated temperatures to generate a useable hydrogen pressure. Conversely, this high operating temperature ensures that the kinetics of hydride formation/decomposition are rapid. The examination of the literature addressing titanium hydride is again split into two sections; modification of the thermodynamics of titanium hydride (5.2.2.1) and modification of the kinetics of titanium hydride (5.2.2.2).

5.2.2.1. Thermodynamics

The pressure-composition- isotherm for the Ti-H system is shown in Figure 5-2. Hydrogen has a relatively large solubility in titanium. Above 571 K (298^{o}C), two plateau regions exist. The first corresponds to the co-existence of the α– and β–phase, two random interstitial hydrides. The second plateau corresponds to the co-existence of the β–phase and the fcc Ti-H δ-phase. Depending on the temperature and hydrogen content, titanium hydride has 8 possible phases.

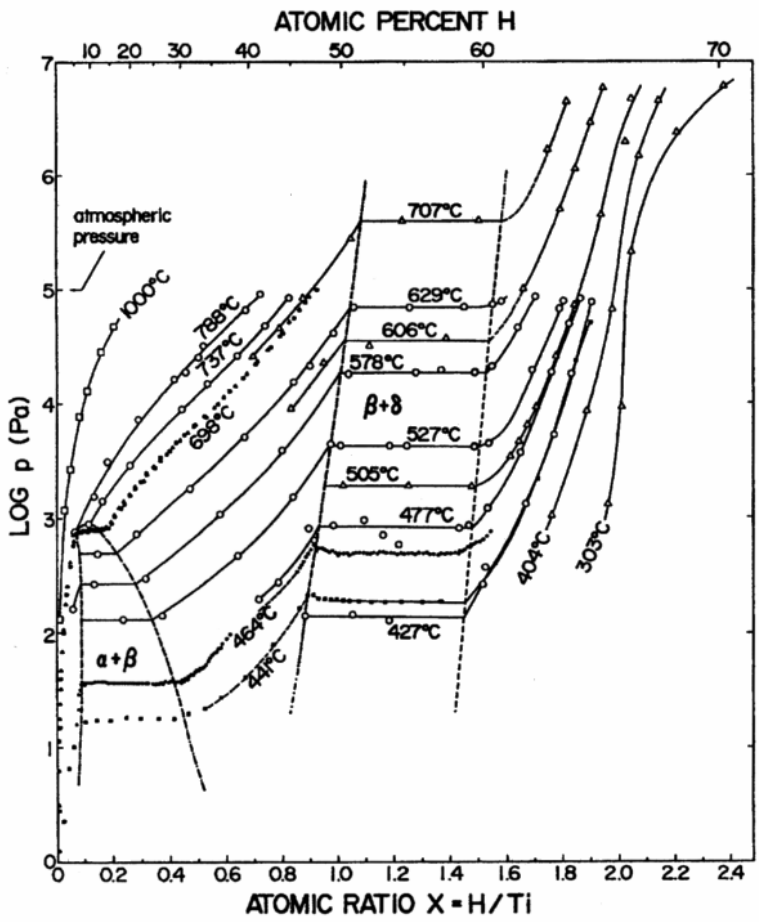

Figure 5-2: Pressure versus composition isotherm for the Ti-H system. Reproduced from [239]. Reprinted with permission of ASM International®. All rights reserved. www.asminternational.org.

The enthalpy of titanium hydride formation varies with hydrogen content and has been measured to range between -100 kJ/mol H_2 (H/M = 0.1) and -150 kJ/mol H_2 (H/M = 1.3) at 737 K (464°C) . This means that titanium hydride is very stable and a temperature of 903 K (630°C) is needed to produce a β–δ plateau pressure of 0.1 MPa (atmospheric pressure).

Unlike magnesium, the prohibitively high temperatures required for hydrogen absorption/desorption from titanium and its relatively modest hydrogen content has meant attention has not been focussed on the direct destabilisation of titanium hydride. Instead efforts have been focussed on the hydriding characteristics of intermetallics containing titanium. Three families of intermetallics have been examined: AB, AB_2 and A_2B of which titanium comprises the A element.

The intermetallic TiFe is one of the earliest examples of an AB type intermetallic hydride[240]. It absorbs hydrogen up to the composition of $TiFeH_2$, corresponding to 1.9 wt.% of hydrogen and exhibits two plateau regions. The first is at a pressure of ~0.5 MPa at 303 K (30°C) and corresponds to the H/M ratio of 0.1 - 0.5 while the second is at a pressure of ~1.0 MPa. This early titanium containing intermetallic hydride had the advantage of room-temperature operation but suffered from a sensitivity to gas contaminants, difficult activation, large hysteresis and an increase in the second plateau pressure upon cycling[66].

For the AB_2 type intermetallic compound, more than 150 intermetallics based on titanium being the A element are reported in the literature. These 150+ intermetallics broadly fall into two catergories. The first involves the partial substitution of titanium with zirconium while the B element comprises various combinations of V, Mn, Cr, Fe, Ni, Al and Co [241,242,243,244] (as a non-exhaustive list). The resulting intermetallics are usually able to absorb between 1 and 2.2 wt.% of hydrogen with plateau pressures ranging between 0.01 and 7 MPa at near ambient temperatures (273 K – 333 K). The second category is based on TiV_2 in which vanadium is partially substituted for elements such as Cr, Fe, Ni, Co and Mn[245,246,247]. These compounds can typically absorb between 2 and 3.8 wt.% of hydrogen with plateau pressures ranging between 0.004 and 0.7 MPa at near ambient temperatures (296 K – 393 K).

In the A_2B system, intermetallics have been examined in which the B element was Al[248], Ni[249], Cu[250] and Co[251]. In general, the temperatures required for hydrogen absorption of these intermetallics are in excess of 473 K (200°C)[248]. Of these, Ti_2Ni and Ti_2Co absorb up to 3.5 and 3.7 hydrogen atoms per formula unit, corresponding to 2.2 wt.% and 2.4 wt.% respectively. The closest to a conventional P-C-T diagram that exists for any of these intermetallics was performed at 353 K (180°C) by Takeshita et al.[252] who measured an equilibrium pressure of 0.01 MPa at the composition $Ti_2NiH_{\sim 1.8}$ rising to an equilibrium pressure of 2.5 MPa at the composition $Ti_2NiH_{\sim 2.7}$.

5.2.2.2. Kinetics

Hydrogen absorption by titanium is preceded by an incubation period that is dependent on applied hydrogen pressure and previous outgassing time and temperature[253]. Absorption shows two distinct stages with the first stage corresponding to hydride growth at nucleation sites on the surface. The second stage corresponds to when hydride from the nucleation sites has completely covered the surface of a particle resulting in a metal core with a hydride envelope. Further hydride formation is then determined by the rate of diffusion of hydrogen atoms through the hydride layer to the hydride/metal interface. Compared to hydrogen diffusion through magnesium hydride, hydrogen diffusion through titanium hydride is relatively rapid. At 473 K (200^{o}C), the hydride layer reaches a depth of ~50 μm within one hour while a temperature of 523 K (250^{o}C) results in a hydride depth of ~80 μm within an hour[253]. Consequently, titanium with a small grain size and a suitable activation process reacts relatively rapidly with hydrogen above 523 K (250^{o}C)[66].

Hydrogen absorption/desorption kinetics are already appreciable at the temperatures required for desorption from TiH_2. However, Maeland et al.[254] found that the high temperature body centred cubic phase of titanium can be stabilised at room temperature by the addition of >14 at.% vanadium. Further addition of 10 at.% of elements, with radii at least 5% smaller than titanium, lead to rapid reaction with hydrogen at room temperature resulting in 80% of absorption completed in under 600 seconds. The suggested mechanism for this increase in uptake is described in terms of introducing strain into the titanium lattice that results in a reduced activation energy of diffusion.

5.2.3. Nickel - Hydrogen

Molecular hydrogen has a sticky probability on nickel that approaches unity over the entire temperature range of 150 – 800 K[65]. Nickel, however, does not form a stable hydride at room temperature except under extreme pressure (>200 MPa) or via cathodic charging[255]. The main interest in nickel with respect to hydrogen is the high adsorption rate of molecular hydrogen and its facile dissociation. Hence nickel as an additive to magnesium hydride and its catalytic effect on kinetics has been extensively studied[256, 257, 258, 259, 260, 261, 262].

The role that nickel plays when milled with magnesium is dependent on a number of factors. When milled with magnesium under a hydrogen atmosphere, nickel remains in its elemental form while magnesium hydride forms[256, 262]. However, excessive milling times or the use of an inert milling atmosphere leads to the formation of Mg_2Ni. Given the nature of the phase diagram for the Mg-Ni system, decomposition of MgH_2 in the presence of elemental nickel is likely to lead to the formation of the Mg-Mg_2Ni eutectic alloy[212]. Any exposure to oxygen, through handling or as an impurity in the hydrogen supply, also add to the complexity of the system as it leads to preferential magnesium oxidation and nickel segregation[65]. Regardless of the exact composition, the presence of nickel increases kinetics either by directly dissociating hydrogen and acting as a hydrogen "pump" or as a component in Mg_2Ni which has superior kinetics compared to pure magnesium.

5.2.4. Ti-Mg-Ni Alloys: Previous Work

Examination of the Ti-Mg-Ni system in this thesis is a result of the publication of Lomness et al. [201,263] who investigated hydrogen absorption in a mechanically alloyed mixture of $Ti_{53}Mg_{47}Ni_{20}$ based on promising hydrogen absorption results published for the Ti-Zr-Ni system [202,264]. The Ti-Zr-Ni system was described as a quasicrystal and was produced by a rapid quenching technique. Lomness et al. produced their $Ti_{53}Mg_{47}Ni_{20}$ samples via a ball milling procedure using different milling times and different ball-to-powder ratios. Milling times varied slightly from sample to sample but were generally ~37, ~47, ~85 and ~115 hours while the ball-to-powder ratios used were 20:1, 40:1 and 70:1 respectively. Characterisation of the samples was limited to DSC (differential scanning calorimetry) during the hydrogen absorption process. From this, the hydriding onset temperature, the hydrogen to metal ratio and the weight percent increase in hydrogen were determined. The results are summarised in Table 5-1, Table 5-2 and Table 5-3 respectively.

Table 5-1: Differential scanning calorimetry data for hydrogen uptake by $Ti_{53}Mg_{47}Ni_{20}$ mechanically alloyed with a ball-to-powder mass ratio of 20:1. Adapted from [201].

Ball mill time (h:min)	DSC hydriding onset T (K)	H/M ratio	Wt.% H_2
0:00	-	0.0	0.0
37:19	446.9	1.3	3.4
44:20	404.6	1.33	3.5
84:22	405.9	1.03	2.5
114:41	419.8	0.79	2.0

Table 5-2: Differential scanning calorimetry data for hydrogen uptake by $Ti_{53}Mg_{47}Ni_{20}$ mechanically alloyed with a ball-to-powder mass ratio of 40:1. Adapted from [201].

Ball mill time (h:min)	DSC hydriding onset T (K)	H/M ratio	Wt.% H_2
0:00	-	0	0
37:36	375.7	1.28	3.2
47:20	387.1	1.08	2.7
90:46	395.4	0.71	1.7
115:46	403.3	0.63	1.6

Table 5-3: Differential scanning calorimetry (DSC) data for hydrogen uptake by $Ti_{53}Mg_{47}Ni_{20}$ mechanically alloyed with a ball-to-powder mass ratio of 70:1. Adapted from [201].

Ball mill time (h:min)	DSC hydriding onset T (K)	H/M ratio	Wt.% H_2
0:00	701.4	0.99	2.4
37:07	365.1	4.92	11.0
47:30	396.5	1.07	3.1
85:55	394.9	0.67	2.0
115:23	411.1	1.03	3.0

The most notable result from this publication is the absorption of 11 wt.% of hydrogen for a sample balled-milled at a ball-to-powder ratio of 70:1 for ~37 hours. If we assume that the hydrogen was absorbed as MgH_2, TiH_2 and NiH then a maximum uptake of 4.37 wt.% may be expected for a sample of $Ti_{53}Mg_{47}Ni_{20}$. Therefore the large uptake reported by Lomness et al. seems unlikely. To further compound the questionable nature of this paper are some discrepancies between the hydrogen-to-metal ratio (H/M) and the corresponding wt.% of hydrogen. For example, the sample

ball-milled for ~84 hours at a ball-to-powder (BTP) ratio of 20:1 (Table 5-1) was reported as having a H/M ratio of 1.03 with a corresponding 2.5 wt.% of hydrogen. However, the sample ball-milled for ~115 hours at a BTP ratio of 70:1 also yielded a H/M ratio of 1.03 but with a corresponding 3.0 wt.% of hydrogen.

If, for the moment, we ignore the hydrogen absorption measurements then the hydriding onset temperature as a function of BTP ratio and milling time presents some interesting results. For samples milled for ~37 hours we see an obvious decrease in hydriding onset temperature as the BTP ratio increases, though this difference becomes less obvious with longer milling time.

Hong et al.[265] also examined the Ti-Mg-Ni system and its hydrogen sorption properties for a variety of compositions. However, the approach for producing these samples is somewhat different. Rather than milling the elemental powders in an inert atmosphere as done by Lomness et al.[201], the elemental powders were milled under a reactive hydrogen atmosphere, a process known as Hydrogen Induced Mechanical Alloying (HIMA). Because of this, the elemental components react with the hydrogen atmosphere to form hydrides [266]. The stoichiometries of the samples examined by Hong et al.[265] are shown in Figure 5-4.

Table 5-4: Molar composition of Hong et al.'s[265] samples. Samples have been scaled so a direct comparison with Lomness et al. is possible[201]

Mg	Ti	Ni
198	22	0
396	44	20
198	22	20
162	40	0
324	81	20
162	40	20

After milling, XRD showed that a number of hydride phases were identifiable, including: Mg_2NiH, MgH_x, TiH_x, Ni and Ti_2NiH_x. A number of unknown phases were also present. PCT isotherms were performed at 523 K (250^{o}C) and 573 K (300^{o}C). Those performed at 523 K (250^{o}C) showed two plateaux regions attributed to the presence of intermetallics. The sample $Ti_{44}Mg_{396}Ni_{20}$ showed the highest reversible capacity of 5.3 wt.% at 573 K while all samples showed substantial hysteresis

between absorption and desorption plateau pressures (~40 kPa at 523 K and ~25 kPa at 573 K).

5.3. Experimental

The starting materials for this investigation consisted of elemental crystalline powders of titanium (99.7%) and nickel (99.8%) purchased from Sigma-Aldrich and magnesium (99.8 %) purchased from Crown Scientific. Ultra high purity hydrogen (99.999%) was purchased from BOC gases and used without further purification. Mechanical alloying of the powders was performed using a custom made cylindrical steel canister and steel balls of ~12 mm diameter designed to affix to a Turbula Type T2C shaker. This shaker is similar to the Spex 8000 widely used in the literature for ball milling. The elemental powders were combined in the ratios $Ti_{53}Mg_{47}Ni_{20}$, $Ti_{65}Mg_{133}Ni_{20}$ and $Ti_{20}Mg_{200}Ni_{20}$ inside a glovebag. Approximately 10g of powder was transferred in air to the 600 cm^3 canister along with the steel balls. The ball to powder (BTP) mass ratio was 70:1 and the canister was subsequently flushed with high purity argon (99.999% from Air Liquide) for at least 10 minutes before being sealed and milled for 36 hrs.

A fourth sample was created with the molar composition of $Ti_{62}Mg_{117}Ni_{20}$. This sample was sealed inside a Rocklabs tungsten carbide ring mill under an argon atmosphere and subsequently milled for a total of three hours. Due to the highly energetic nature of the ring mill, substantial heat was generated during the milling process. To prevent heat-induced rupture of the silicone rubber seal, the ring mill was run in 30 minute blocks with the ring mill being allowed to cool to room temperature between each block.

Hydrogen absorption experiments were performed in a volumetric apparatus [267] using the Hemmes equation of state [99] and the method of Mclennan and Gray [98] to account for the compressibility of hydrogen. The process used to initially activate the sample for hydrogen absorption is as follows. The sample was heated to 573 K (300^{o}C) under vacuum before being subjected to a constant hydrogen pressure of approximately 7 MPa for 12 hours. The sample was then evacuated, and the temperature was raised to and maintained at 723 K (450^{o}C) for 12 hours. This process was repeated three times.

The uncertainties associated with the measurements on the Ti-Mg-Ni samples are negligible and so have been excluded from the hydrogen absorption curves for clairty. X-ray diffraction was performed using a Siemens D500 diffractometer with a 2θ range of 10 – 80^{o} using 0.02^{o} steps with 3 seconds of count time per step. Scanning electron microscopy (SEM) was performed on a Philips XL30 instrument.

5.4. Results

5.4.1. $Ti_{53}Mg_{47}Ni_{20}$

After 36 hrs of ball-milling the sample has become quite amorphous (Figure 5-3(a)). Peaks can still be assigned to titanium and nickel while those for magnesium are significantly reduced in intensity. This can be expected due to the lower hardness of magnesium compared to both titanium and nickel resulting in the magnesium having lower crystallinity post ball-milling. Figure 5-3(b) shows a comparison between the hand-mixed starting powder and the post-ball milled powder. XRD also suggests that the ball-milling mixes the three elements together rather than forming an alloy. However, due to the broadness of the peaks, formation of intermetallic alloys and solid solutions can not be definitively ruled out. A small peak is evident at $2\theta =$ 25.56^{o} and is due to quartz contamination stemming from SiO_2 being used as a cleaning agent in the ball mill canister. The absence of this peak in subsequent XRD data (see Figure 5-8, Figure 5-9 and Figure 5-10) suggests that the quartz is present in trace amounts only.

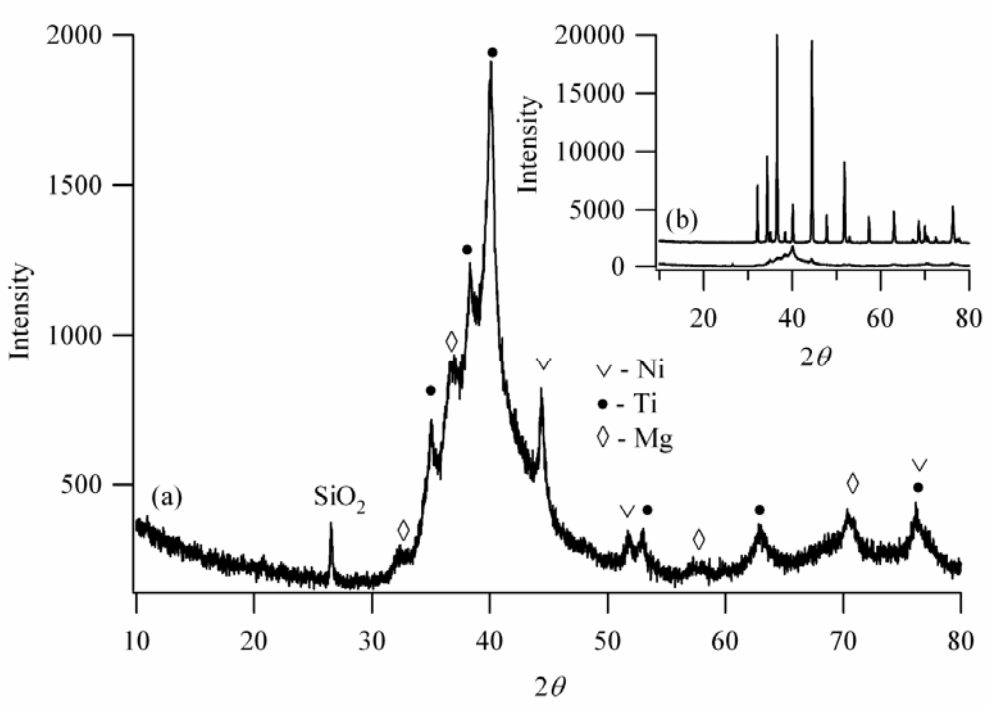

Figure 5-3: (a) XRD pattern of $Ti_{53}Mg_{47}Ni_{20}$ after ball-milling for 36 hrs. (b) X-ray diffraction patterns of $Ti_{53}Mg_{47}Ni_{20}$ pre-ball milling (TOP) and post-balling milling (BOTTOM) showing the change in peak intensities.

Scanning electron microscopy (SEM) performed on the sample after ball milling shows that a number of particle sizes and morphologies are present (Figure 5-4 and Figure 5-5). Particle sizes generally ranged from 2 μm to > 100 μm with the larger particles appearing to consist of agglomerates of small particles "fused" together during the ball milling process. Particles with platelet like morphology are also obvious in the sample (Figure 5-5). These particles seem to arise from being flattened against the side of the canister during the ball milling process. Other than these flat grain faces, all particles are rough and irregular in shape.

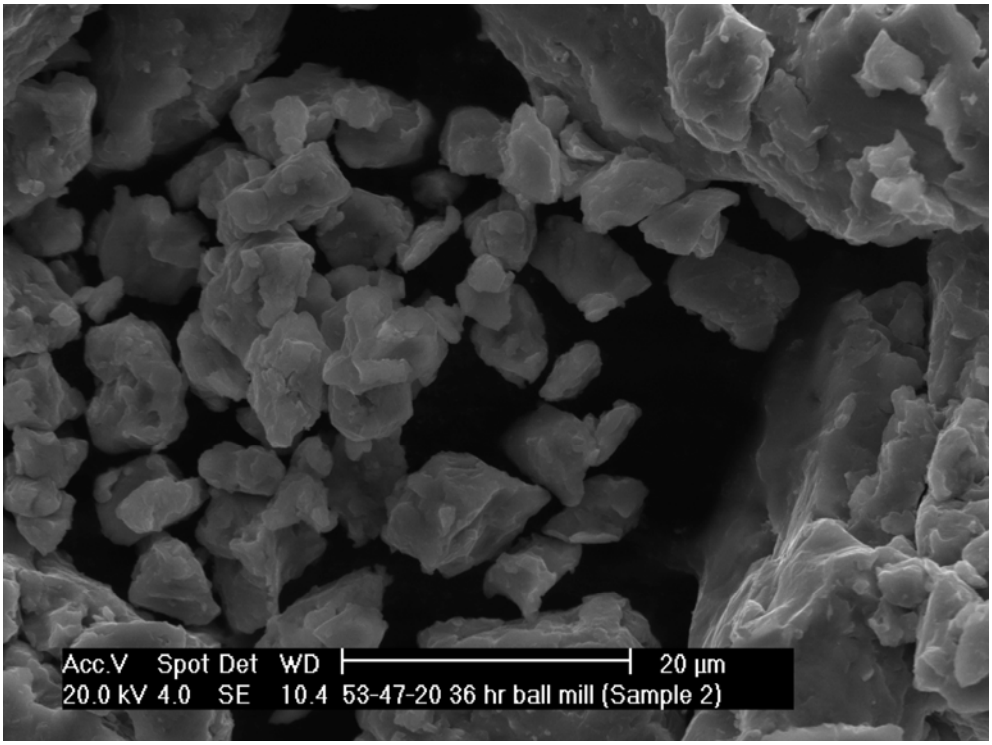

Figure 5-4: SEM of $Ti_{53}Mg_{47}Ni_{20}$ post ball-milling, showing the smallest particles present in the sample.

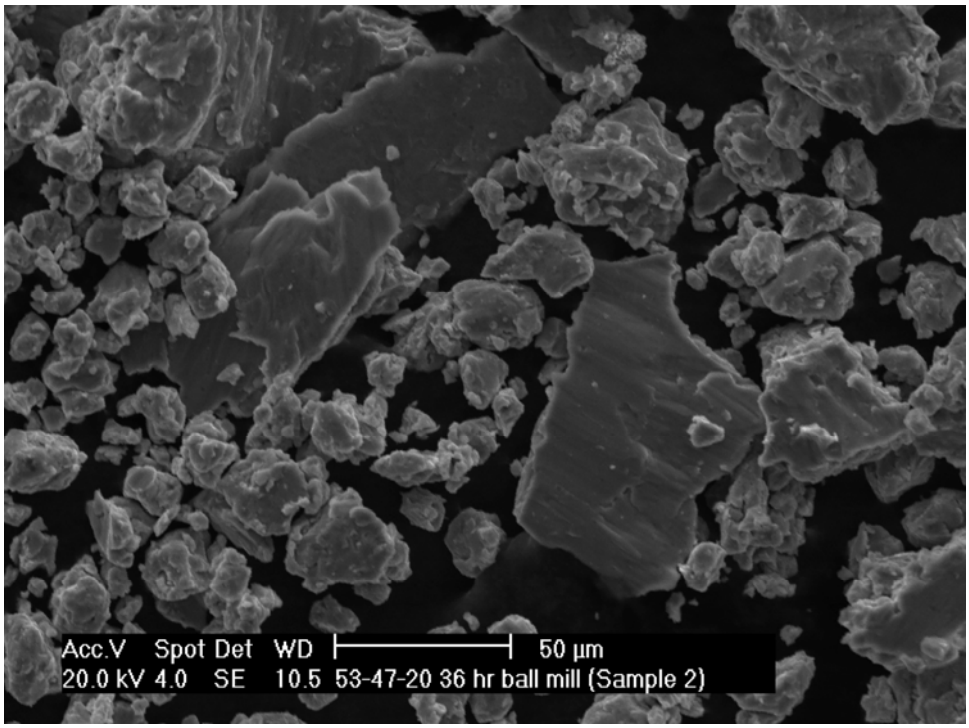

Figure 5-5: SEM of $Ti_{53}Mg_{47}Ni_{20}$ post ball-milling showing the largest grains contained within the sample.

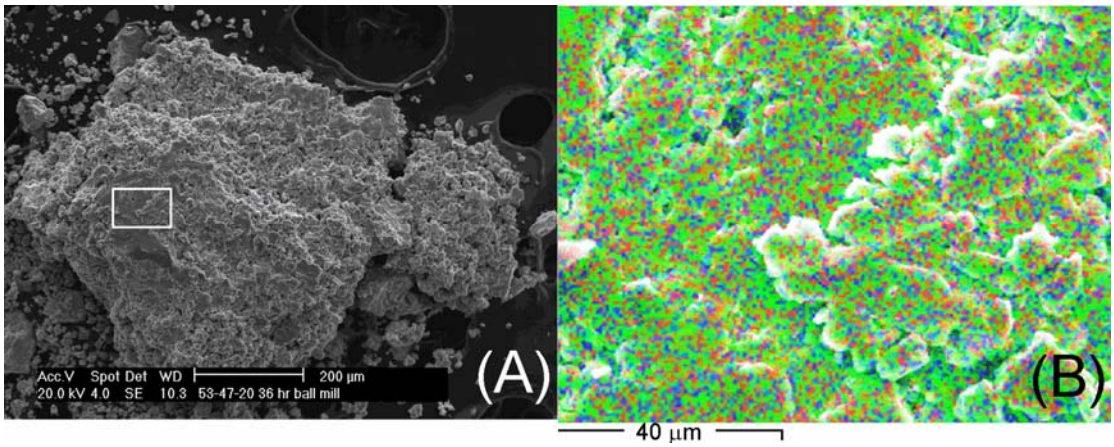

Figure 5-6: (A) A large agglomeration of particles with the rectangular region highlighting the area used for EDS area mix mapping. (B) EDS area mix map (Ti = green, Mg = red, Ni = blue) showing the distribution of the constituent elements.

Energy Dispersive Spectroscopy (EDS) area mix maps (Ti = green, Mg = red, Ni = blue) show that all three elements are well dispersed with no large collections of any one element (Figure 5-6(b)).

Following activation, hydrogen absorption was performed on the ball-milled sample at room-temperature. A significant difference between the experiments performed here and that of Lomness et al.[201] is the way in which the samples were activated. Lomness et al. used a water/humidity based method developed in their laboratory [268] while we used an activation method similar to that for magnesium based hydrides. In our experiments a temperature of 723 K (450^{o}C) was used during the out-gassing phase to ensure that any TiH_2 formed during the activation step, decomposed.

The maximum hydrogen capacity measured at 296 K, as shown in Figure 5-7, was 2.5 wt.% This corresponds to a hydrogen to metal (H/M) ratio of 1.04. The equilibrium pressure was quite low with the sample having an equilibrium pressure below the detection limit of the apparatus (1.5 kPa) at a hydrogen content of 2.1 wt.%.

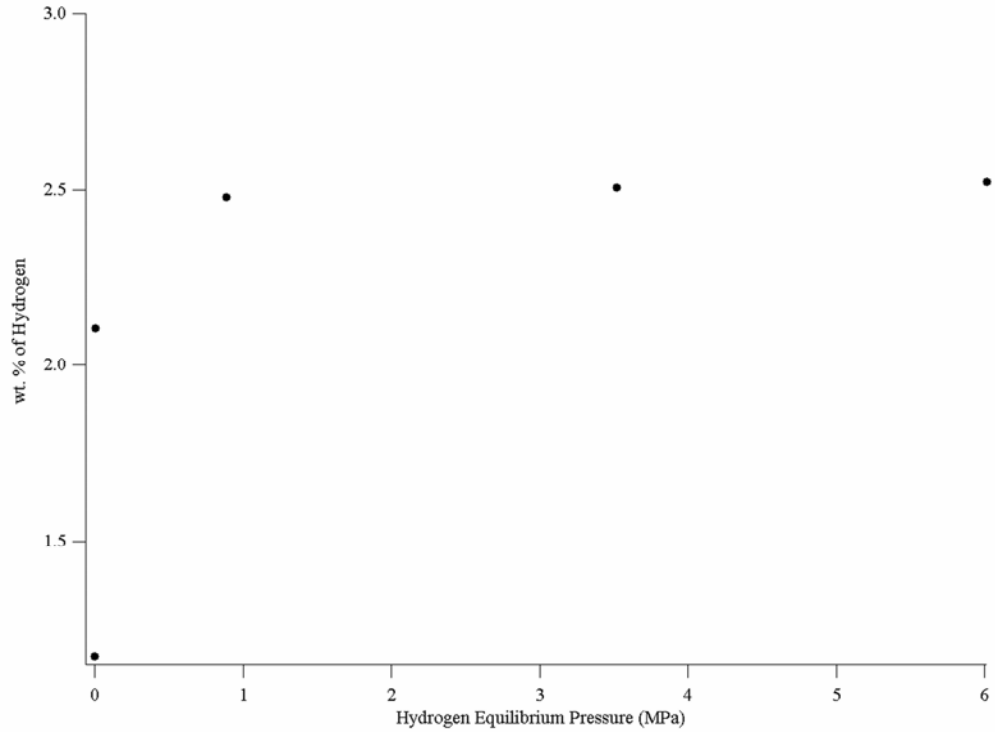

Figure 5-7: Room temperature hydrogen absorption on $Ti_{53}Mg_{47}Ni_{20}$ after activation.

The initial hydrogen absorption was quite rapid and reached 2 wt.% in approximately 700 seconds. As the sample approaches its maximum weight percent, the absorption process slowed dramatically but still continued. After hydrogen absorption had finished the sample was removed for X-ray diffraction analysis (Figure 5-8).

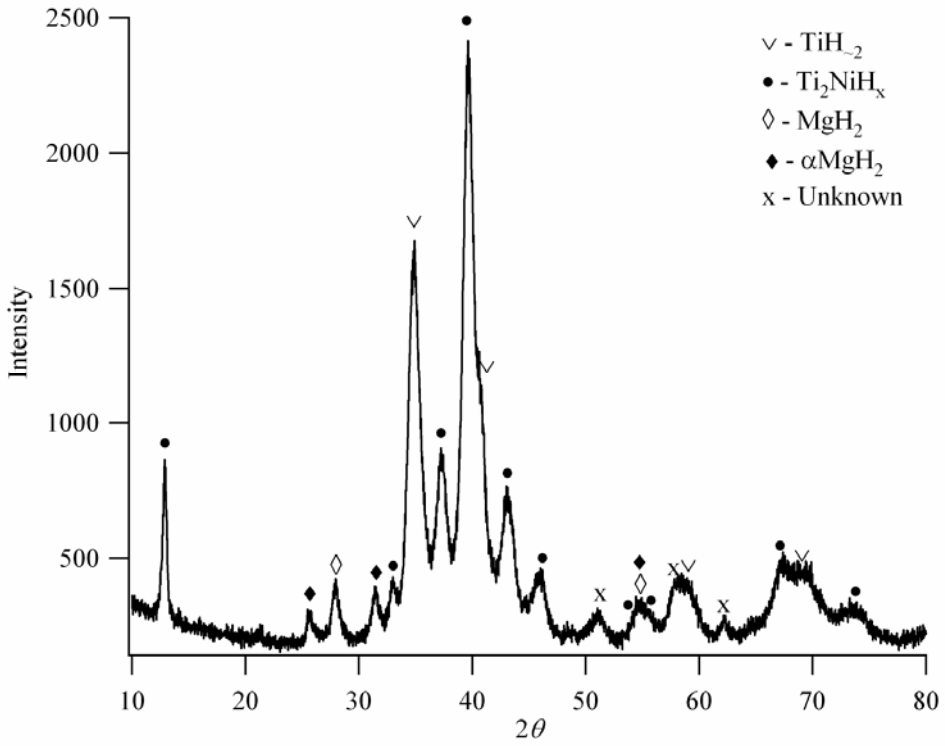

Figure 5-8: XRD pattern of $Ti_{53}Mg_{47}Ni_{20}$ hydrided at room temperature.

We see there is a sharpening of the diffraction peaks but that they are still relatively broad. It is due to this relative broadness that definitive phase identification is difficult. However Ti_2NiH_x ($x > 0.5$) is present as is small amounts of MgH_2. TiH_y ($0.7 < y < 2.0$) is also present, but the amount of peak overlap between titanium hydride phases means quantifying exactly which titanium hydride phases are present is impossible.

A second absorption run was attempted at room temperature by replacing the sample in the volumetric apparatus and out-gassing at 723 K (450^{o}C) before allowing the sample to cool. Hydrogen absorption was slow and was concluded to be due to oxide layer formation during handling in air for X-ray data collection. The sample was re-activated by heating it to 573 K (300^{o}C) under hydrogen pressure for 24 hrs before out-gassing at 723 K (450^{o}C) for 24 hrs. Following this procedure the sample once again absorbed as it had on the first absorption run and did not show early cycling capacity loss as has been reported for Ti_2Ni electrodes [269]. After subsequent out-gassing at 723 K (450^{o}C), phase analysis for this sample was investigated using XRD (Figure 5-9).

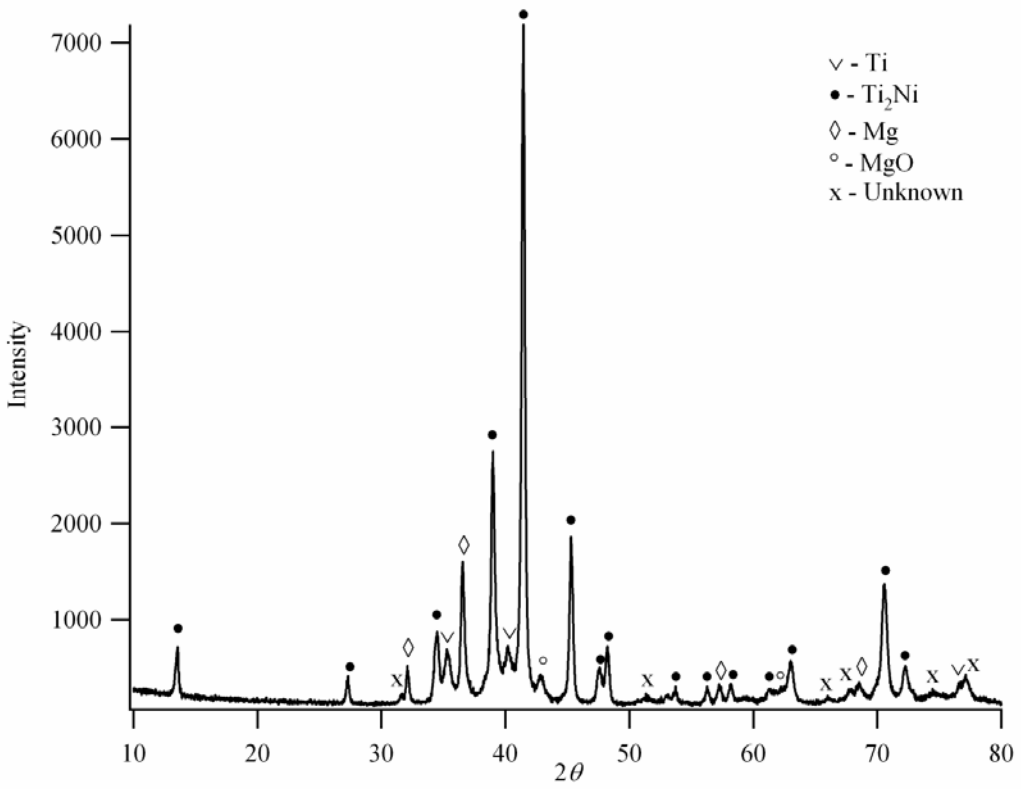

Figure 5-9: XRD of $Ti_{53}Mg_{47}Ni_{20}$ hydrided at room temperature and dehydrided at 723 K (450^{O}C) .

Figure 5-9 shows that the sample has become significantly more crystalline after cycling as well as confirming the formation of Ti_2Ni. Elemental Ti and Mg appear to comprise the remaining major phases. A small peak at 2θ = 42.9^{o} is attributed to MgO. A number of small unidentified peaks are also present. SEM on the hydrided sample (not shown) shows extensive cracking, especially in particles larger than 50 μm.

Hydrogen has been shown to act as a catalyst for the formation of Ti_2Ni at elevated temperatures [270] and therefore its formation is not surprising. In an attempt to separate the effects of temperature and hydrogen exposure, a ball-milled sample was subjected to the activation process in the absence of hydrogen (i.e., it was temperature cycled under vacuum between 573 K and 723 K). From here on this sample shall be referred to as the annealed sample. Figure 5-10 shows that once again there has been a significant increase in crystallinity as well as formation of Ti_2Ni. In this case the peaks from Ti are more intense than the peaks in the cycled sample. The similar intensity of the Ti_2Ni peaks in both patterns combined with the absence of elemental

Ni peaks in the annealed sample indicates that Ti is not left over from incomplete Ti_2Ni formation. An extremely weak MgO peak is again evident at $2\theta = 42.9$ along with numerous small unidentified peaks.

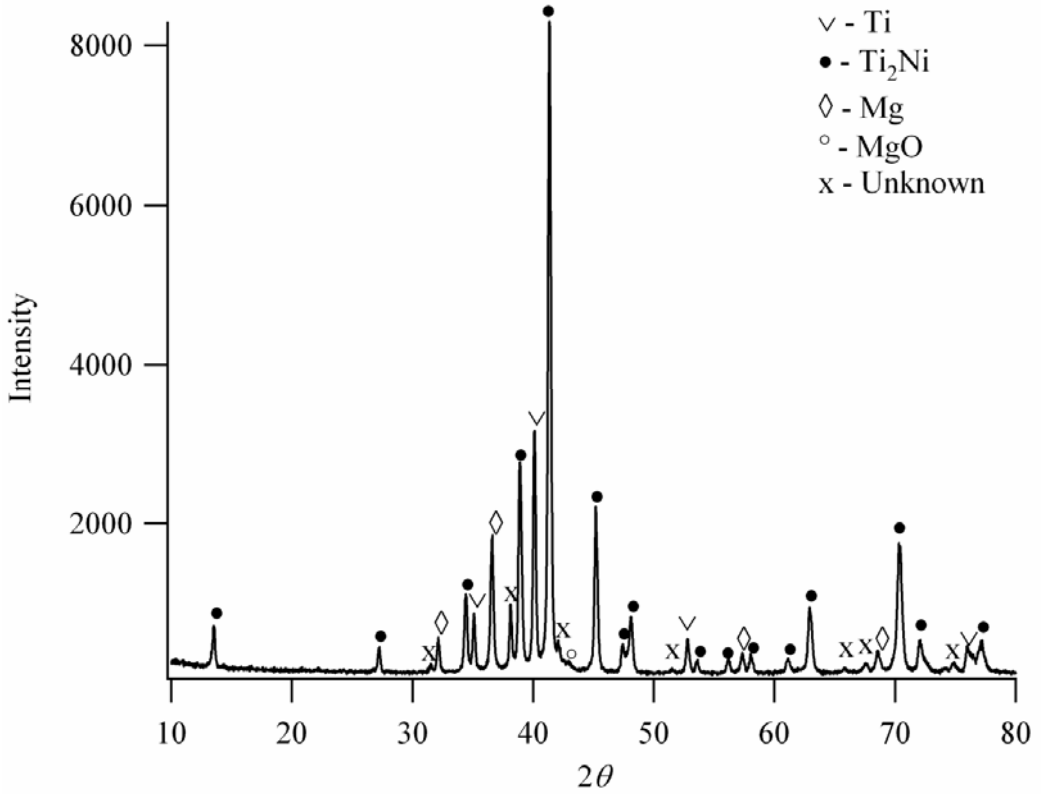

Figure 5-10: XRD pattern of $Ti_{53}Mg_{47}Ni_{20}$ subjected to temperature cycling while under vacuum.

5.4.2. $Ti_{62}Mg_{117}Ni_{20}$

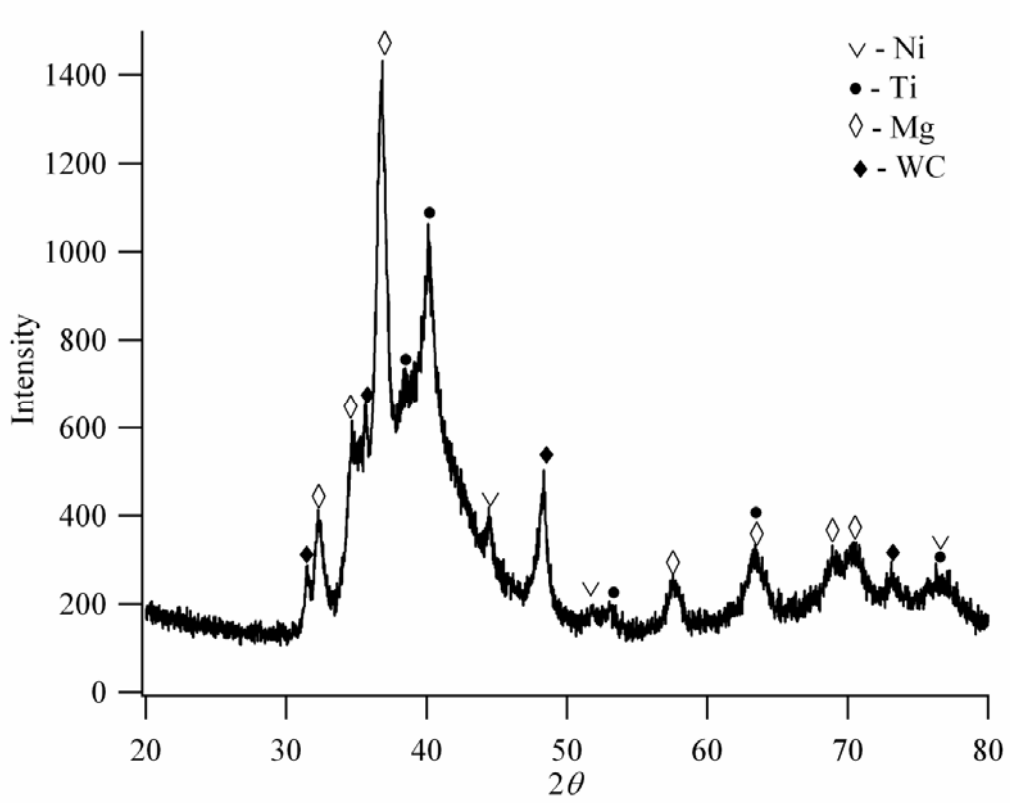

Figure 5-11: XRD pattern of $Ti_{62}Mg_{117}Ni_{20}$ after being ring milled for a total of 3 hours.

Figure 5-11 shows the X-ray diffraction pattern of the $Ti_{62}Mg_{117}Ni_{20}$ sample after three hours of ring-milling. The pattern is similar in nature to that of $Ti_{53}Mg_{47}Ni_{20}$ ball-milled for 36 hours in that it shows significant amorphisation. The starting elements can be identified while the presence of intermetallics can not be excluded due to the large amorphous hump between 30^o and 50^o 2θ. A relatively large amount of tungsten carbide (WC) is also present and originates from the milling media.

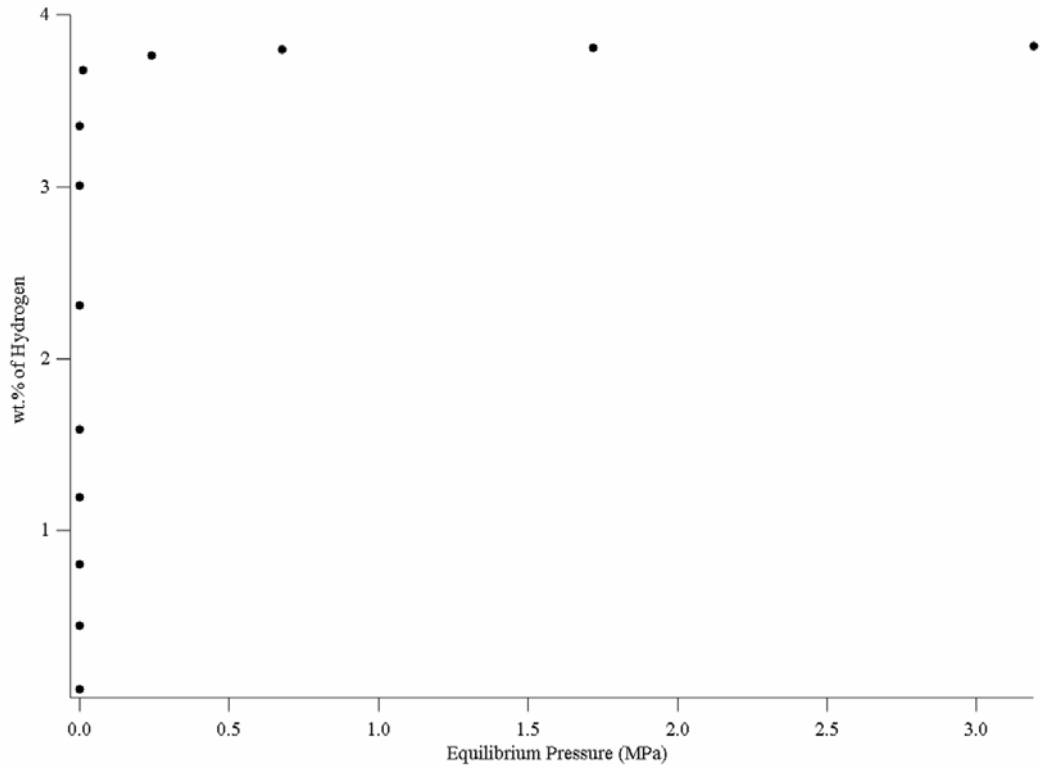

Figure 5-12: Room temperature hydrogen absorption of $Ti_{62}Mg_{117}Ni_{20}$ ring milled for 3 hours.

The hydrogen absorption at room temperature has an equilibrium pressure below the detection limit of the apparatus (1.5 kPa) up to an uptake of 3.35 wt.%. Beyond this hydrogen uptake point, there is an almost asymptotic rise in the hydrogen equilibrium pressure with minimal increase in hydrogen content. For example, an equilibrium pressure of just 12 kPa is measured at a hydrogen content of 3.68 wt.% while an equilibrium pressure of 3.2 MPa is associated with a hydrogen content of 3.82 wt.% (H/M = 1.38). The rate of absorption is dependent on how far away from equilibrium the applied hydrogen pressure is. Initally, hydrogen absorption is quite rapid and slows significantly as equilibrium is approached. Up to 24 hours may be required for final equilibrium to be reached for each data point in Figure 5-12. However, hydrogen applied as an overpressure can result in >90% of the total hydrogen uptake being absorbed in less than 60 seconds.

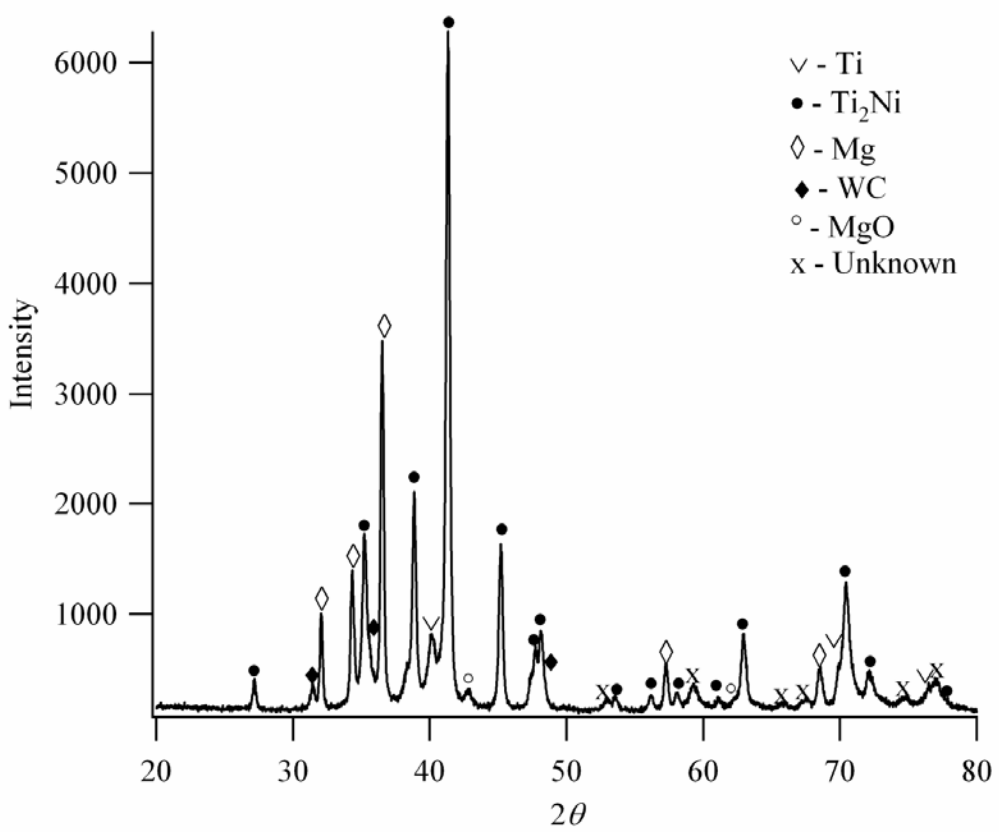

Figure 5-13: XRD pattern of $Ti_{62}Mg_{117}Ni_{20}$ after a number of hydride/dehydride cycles.

Figure 5-13 shows the XRD pattern of $Ti_{62}Mg_{117}Ni_{20}$ after a number of hydrogen absorption cycles performed at room temperature followed by desorption at 723 K (450^{o}C). As may be expected of such annealing, a substantial decrease in peak width has occurred. The major phases present are Ti_2Ni, Mg, Ti, WC and MgO. Presumably MgO was present prior to hydrogenation but is hidden in the large amorphous hump that extended between 35^{o} and 50^{o} 2θ. No elemental nickel is evident in the pattern suggesting total conversion to Ti_2Ni. A number of low intensity unidentified peaks are also present and correspond closely to the unidentified peaks in the XRD pattern of the cycled $Ti_{53}Mg_{47}Ni_{20}$ sample (Figure 5-9).

5.4.3. $Ti_{65}Mg_{133}Ni_{20}$

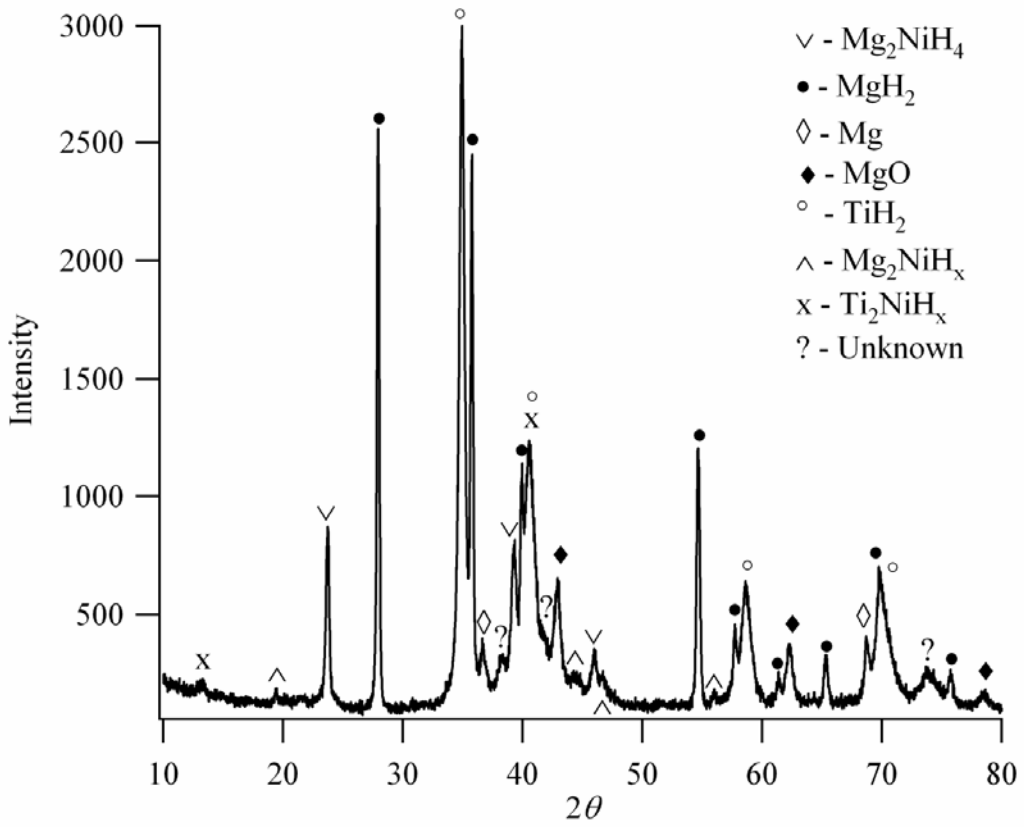

Figure 5-14: XRD pattern of $Ti_{65}Mg_{133}Ni_{20}$ hydrided at 573 K (300°C) before being cooled to room temperature.

Room temperature XRD of the $Ti_{65}Mg_{133}Ni_{20}$ sample hydrided at 573 K (300°C) (Figure 5-14) shows the formation of MgH_2, Mg_2NiH_4 and TiH_2. Partially hydrided Mg_2Ni and Ti_2Ni along with unreacted Mg are also evident. Significantly less Ti_2Ni is present as compared to $Ti_{53}Mg_{47}Ni_{20}$ and $Ti_{62}Mg_{117}Ni_{20}$. A relatively large amount of MgO is present as well as some minor unidentified peaks.

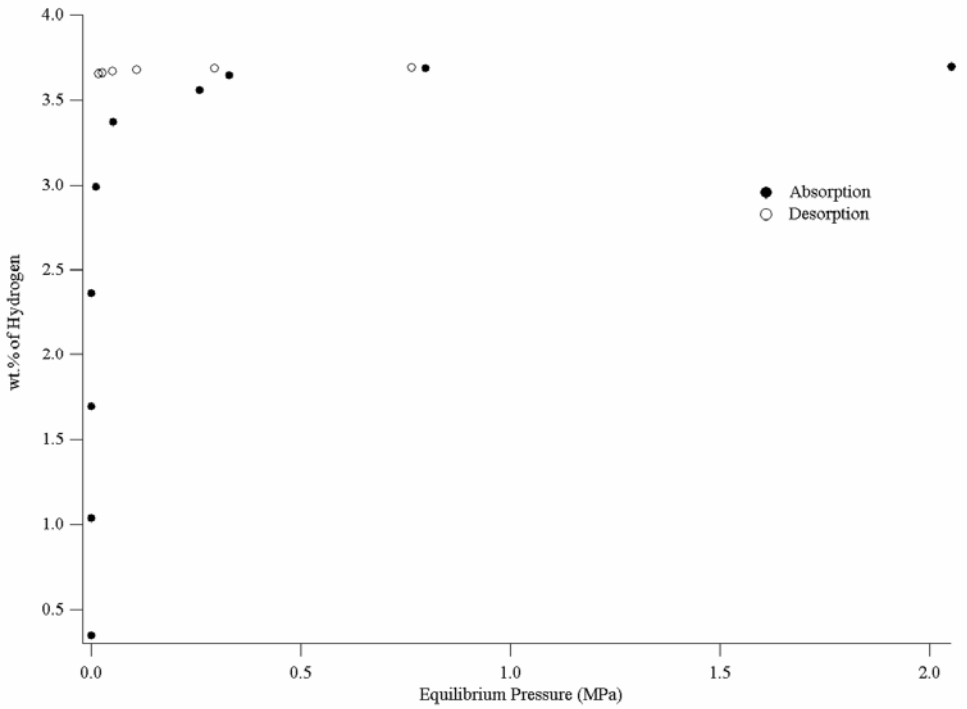

Figure 5-15: Hydrogen absorption and desorption at room temperature of $Ti_{65}Mg_{133}Ni_{20}$.

Hydrogen uptake at room temperature corresponds to 3.70 wt.% at a pressure of 2.0 MPa. The equilibrium pressure up to 2.37 wt.% is under the detection limit of the apparatus (1.5 kPa). At 2.99 wt.% and 3.56 wt.% the equilibrium pressure is 12 kPa and 53 kPa respectively. Beyond this point, an increased hydrogen pressure has little effect on the total hydrogen uptake (final H/M = 1.30). Due to the low equilibrium pressure, negligible amounts of hydrogen can be desorbed at room temperature. A desorption equilibrium pressure of 16 kPa yields just 0.05 wt.% of hydrogen desorbed.

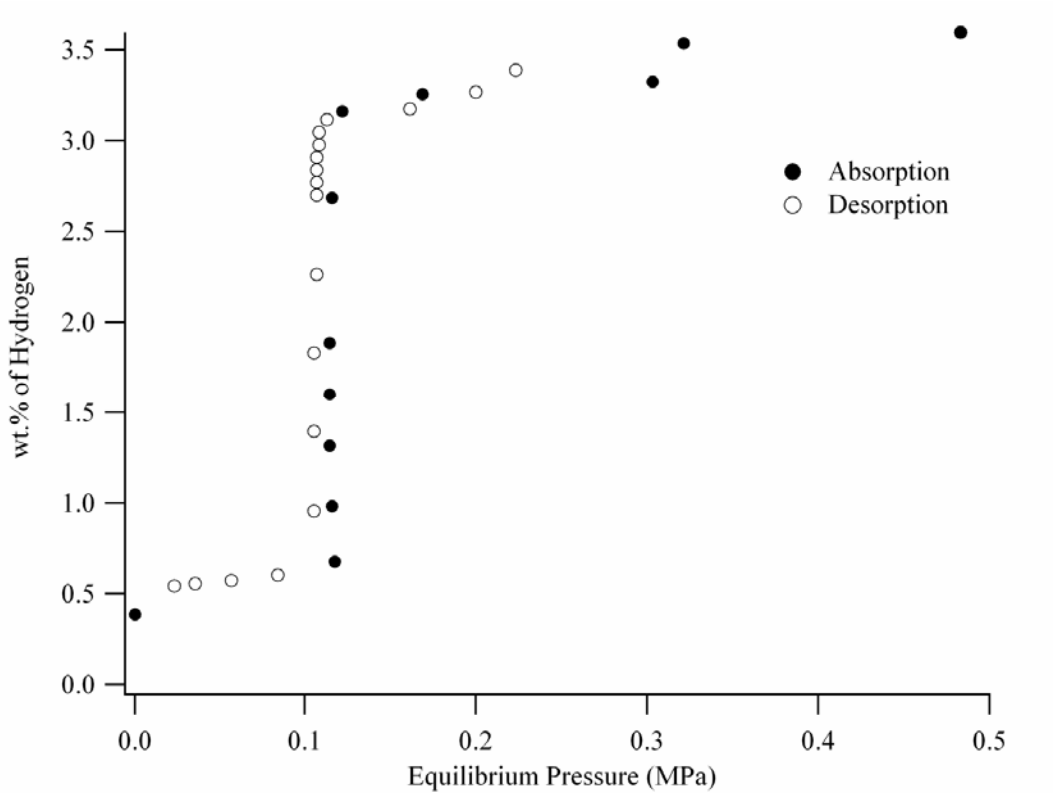

Figure 5-16: Hydrogen absorption and desorption of $Ti_{65}Mg_{133}Ni_{20}$ at 573 K (300°C)

A pressure-composition isotherm (Figure 5-16) was also obtained at 573 K (300°C). There are three distinct features on both the absorption and desorption curves of $Ti_{65}Mg_{133}Ni_{20}$ at 573 K (300°C). For absorption, the first data point corresponds to 0.39 wt.% of hydrogen with an equilibrium pressure below 1.5 kPa. Hydrogen uptake from 0.68 to ~3.2 wt.% corresponds to a plateau pressure of 115 kPa. A second short plateau between 3.32 wt.% and 3.54 wt.% exists but insufficient data points were taken in this range to determine whether a true plateau or a sloping plateau exists in this region. The start of the plateau corresponds to a pressure of ~303 kPa while the finish corresponds to a pressure of ~321 kPa. The final equilibrium point was taken at a pressure of 483 kPa and corresponds to hydrogen uptake of 3.60 wt.%.

Due to the system volume of the Sievert's apparatus, few desorption data points were obtained between the hydrogen content of 3.60 wt.% and 3.11 wt.% and little detail is evident in this region. Between 3.11 wt.% and 0.96 wt.% there is a very flat plateau with an equilibrium pressure of ~106 kPa. Desorption practically ceases with ~0.5 wt.% of hydrogen still contained in the sample as titanium hydride.

5.4.4. $Ti_{20}Mg_{200}Ni_{20}$

The kinetics of absorption for the $Ti_{20}Mg_{200}Ni_{20}$ were substantially slower than for the other samples. At room temperature, 1.5 wt.% of hydrogen was absorbed over a 17 hour period while an over pressure of hydrogen was applied. The temperature of the sample was raised to 573 K (300°C) and a further 3.53 wt.% of hydrogen was absorbed over a period of 7 hours. XRD of this $Ti_{20}Mg_{200}Ni_{20}$ sample (Figure 5-17) hydrided at 573 K (300°C) reveals that the major phase is MgH_2. Mg_2NiH_4 and TiH_2 are the other major hydride phases. Unreacted Mg and partially hydrided Mg_2Ni along with a relatively large amount of MgO are also present.

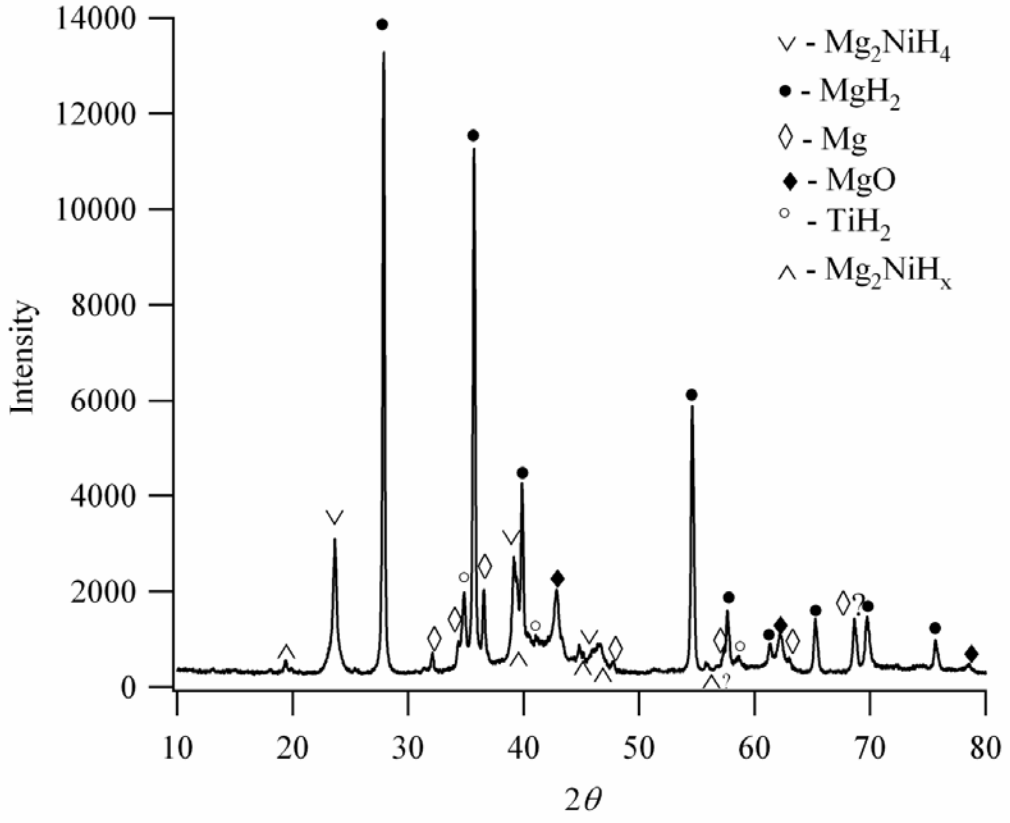

Figure 5-17: XRD pattern of $Ti_{20}Mg_{200}Ni_{20}$ hydrided at 573 K (300°C) before being cooled to room temperature.

5.5. Discussion

5.5.1. Oxide Formation

Magnesium oxide is present in all the samples indicating that the use of a glovebag to weigh the elemental powders and the transferring of the powders in air to the canister is insufficient in protecting the sample from oxygen. Oxides of titanium, nickel and the intermetallic compounds are absent. The absence of these other oxides suggests that this magnesium oxide is formed during the milling process since magnesium is known to act as a reducing agent during ball milling[271]. MgO is likely to perform a number of roles in the interaction of the Ti-Mg-Ni samples with hydrogen. Pure oxides are relatively inert towards hydrogen[65] but, in general terms, oxides with defects or partially reduced oxides have been shown to act as strong centres for hydrogen adsorption and dissociation[65,232,233,234].

Much of the research on MgO and the impact it has on hydrogen absorption in magnesium has focused on magnesium oxide layers covering magnesium[272,273]. Vigeholm et al.[272] suggested that a relatively thick oxide layer was conducive to faster hydrogen absorption kinetics in magnesium as the oxide layer is brittle and likely to flake away from the magnesium surface leaving diffusion paths for hydrogen. In contrast, they suggest that a thin oxide layer is more ductile and likely to stay adhered to the magnesium and so prevent hydrogen permeation. Hjort et al.[273] have shown that a magnesium surface exposed to a low level of oxygen can actually increase the hydrogen absorption rate of magnesium. This is because, at low exposure levels, magnesium oxide forms islands on the magnesium surface that act as sights for hydrogen adsorption and dissociation rather than forming a continuous layer. At higher oxygen exposure, these islands join up to form a magnesium oxide layer that is only marginally permeable to hydrogen. Due to the nature of the milling process, it is likely that the MgO present is highly dispersed, defected and non-stoichiometric resulting in sites for hydrogen absorption and dissociation. This is supported by a recent experiment[274] that showed MgH_2 ball-milled with MgO displayed absorption/desorption kinetics comparable to the fastest known catalysts for MgH_2 (Nb_2O_5)[234].

The second impact the magnesium oxide formation has on the Ti-Mg-Ni alloys is the reduction of the other compounds back to clean metal surfaces. The three main compounds, other than magnesium, in the samples tested here are Ti, Ti_2Ni and Mg_2Ni. Of these Ti is known to have fast hydrogen absorption kinetics when oxide free[66] while oxygen exposure of Mg_2Ni is known to result in the segregation of catalytic active Ni sites[271]. Oxygen is soluble in Ti_2Ni up to ~14 at.%[251] with little change in the lattice parameters. Given that hydrogen absorption also results in the lattice expansion of Ti_2Ni and that Ti_2NiO_x ($0<x<0.5$) can absorb hydrogen, its presence can not be ruled out.

The end result of these factors is the formation of either non-stoichiometric MgO or heavily defected MgO that acts as a site for hydrogen adsorption, dissociation and transport while the other compounds are left free of oxygen and able to act as sites of rapid hydrogen adsorption, dissociation, transport and hydride formation.

5.5.2. Magnesium Vaporisation

Following activation and cycling, all samples studied yielded a deposit sintered to the filter directly above the sample. Figure 5-18 is a SEM image of part of one of these deposits.

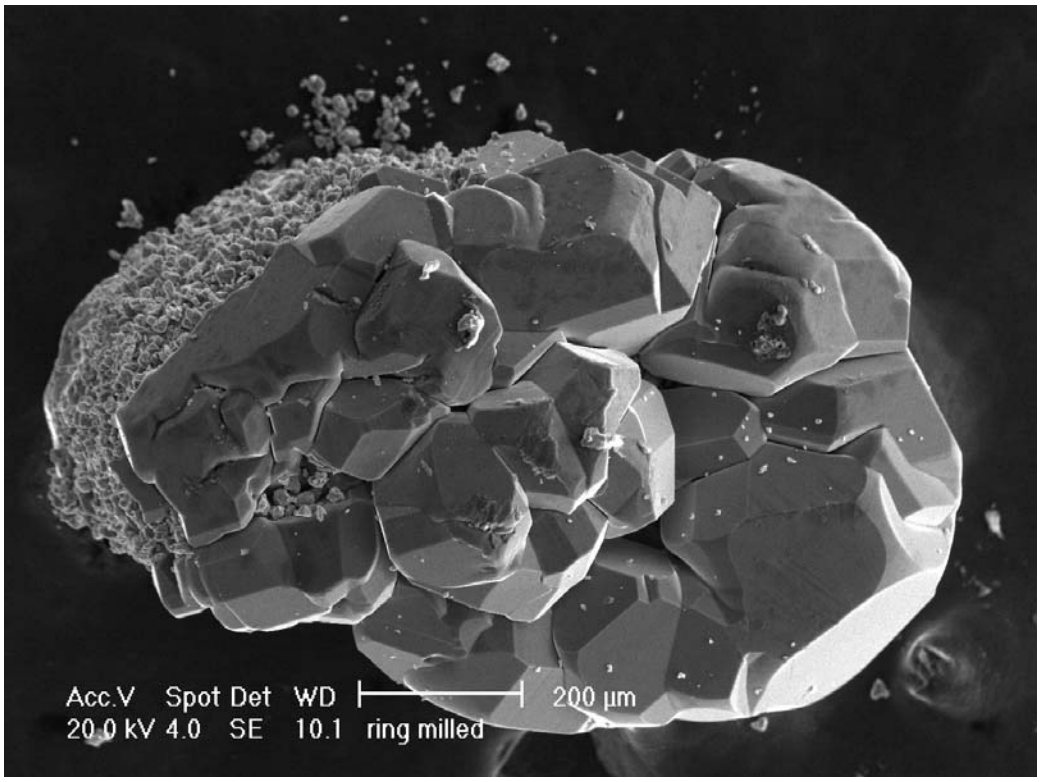

Figure 5-18: SEM image of a typical filter deposition.

SEM reveals that these deposits consist of 100 – 300 μm sized grains agglomerated together that largely have smooth faces. Energy Dispersive Spectroscopy (EDS) revealed these particles are pure magnesium. Initially, these magnesium deposits were puzzling given that the melting and boiling point of magnesium is 923 and 1363 K respectively[275]. Further investigation revealed that magnesium, despite having a boiling point of 1363 K, has a very low vapour pressure above 496 K[276,277]. A typical roughing or rotary pump, such as that used for these experiments, generates a vacuum of approximately 10^{-2} torr (1.33 Pa). At the outgassing temperature of 723 K used during the activation process, magnesium has a vapour pressure of ~5 Pa[276]. Hence, the vaporisation of magnesium would be expected under these conditions.

This vaporisation had two negative impacts on the experiments performed. The first impact is on the calculated hydrogen uptake for the sample. Following hydrogen absorption experiments, the magnesium deposited on the filter remained as metallic magnesium. This would be expected given that a defect free magnesium surface has a negligible sticking and dissociation probability for hydrogen at the temperature used for absorption studies (573 K). Given that the hydrogen uptake is measured for the

total mass of the sample, the magnesium deposition included, the result is an under reporting of the hydrogen uptake in the powdered sample contained in the rest of the sample cell volume. For the sample $Ti_{65}Mg_{133}Ni_{20}$, the magnesium deposit was able to be cleaved from the filter. The measured weight of this magnesium deposit comprised 13 wt.% of the total magnesium contained within the sample. Considering the case of absorption at 573 K (300^{o}C), if this deposit had absorbed hydrogen it would only increase the total uptake of hydrogen from 3.54 wt.% to 3.74 wt.%.

The second impact on the experiments was in relation to the measured kinetics. The $Ti_{53}Mg_{47}Ni_{20}$ sample showed reasonable kinetics absorbing 80% of its maximum uptake within 700 seconds at room temperature. However, upon removal of the sample cell volume it was determined that the magnesium deposition was partially blocking the filter. Usually when the filter is open directly to atmosphere, any pressure initially in the reference volume dissipates practically instantly through the filter. However, after measurements on the $Ti_{53}Mg_{47}Ni_{20}$, an initial reference pressure took some minutes to dissipate through the filter indicating that the actual kinetics would have been faster than that measured. The effect of the magnesium deposit was also erratic in its impact on kinetics. Both the $Ti_{65}Mg_{133}Ni_{20}$ and $Ti_{62}Mg_{117}Ni_{20}$ sample had substantial magnesium deposits on their filters with no discernable impact on the kinetics.

As a consequence of these factors, the formation of TiH_2 proves problematic for any system based on Ti-Mg-Ni. The hydrogen absorption for the T-Mg-Ni samples reported here includes that incorporated into TiH_2. Since TiH_2 formation represents irreversible absorption at the temperatures studied (573 K and below) the reversible hydrogen content is less than the total uptake. If we assume that the vacuum supplied by the rotary pump used in these experiments generates a vacuum of 1.33 Pa (10^{-2} torr) and based on the vapour pressure of magnesium[276] and the enthalpy and entropy for the α/β titanium-hydrogen plateau[239] then at 673 K (400^{o}C) magnesium has a vapour pressure lower (0.4 Pa) than that of the vacuum while Ti-H has a higher plateau pressure (4.2 Pa) than the vacuum. This means that, theoretically at least, TiH_2 can be dissociated at 673 K (400^{o}C) without vaporising magnesium. However, given

the high temperature, precise vacuum control required and modest hydrogen content it is unlikely that this research will be pursued.

5.5.3. Phase Formation

The ball milling of elemental titanium, magnesium and nickel with subsequent heating results in a rich variety of phase formation. The XRD pattern of $Ti_{53}Mg_{47}Ni_{20}$ after hydriding/dehydriding (Figure 5-9) reveals the formation of the intermetallic Ti_2Ni. Antonova et al.[270] showed that hydrogen catalyses the formation of Ti_2Ni, reducing the temperature for formation required by 200 K. However, $Ti_{53}Mg_{47}Ni_{20}$ subjected to the same temperature regime in the absence of hydrogen (Figure 5-10) also showed the formation of Ti_2Ni. This formation occurs at 450 K less than the temperature used by Antonova et al.[270] and suggests that the intimate contacting of elements provided by ball milling results in facile intermetallic formation due to reduced diffusion paths.

The XRD pattern of $Ti_{53}Mg_{47}Ni_{20}$ temperature cycled under hydrogen (Figure 5-9), the XRD pattern of $Ti_{53}Mg_{47}Ni_{20}$ cycled under vacuum (Figure 5-10) and the XRD pattern of cycled $Ti_{62}Mg_{117}Ni_{20}$ all showed the same unidentified peaks in the 2θ range of 50^o to 80^o. Antonova et al.[270] also made note of unidentified peaks in their XRD pattern of Ti_2Ni that could not be attributed to TiNi or $TiNi_3$.

As the titanium and nickel content decreases relative to the amount of magnesium, we see a decrease in the formation of Ti_2Ni and an increase in the amount of Mg_2Ni formed. As the magnesium content increases there is less contact between titanium and nickel particles and more contact between titanium-magnesium and nickel-magnesium. Since titanium and magnesium do not form an intermetallic phase, heating results in the formation of the magnesium-nickel intermetallic, Mg_2Ni.

5.5.4. Kinetics

The vaporisation and deposition of magnesium onto the filter above the sample during hydrogen absorption experiments sporadically resulted in a partial blockage of the filter. Consequently, a generalised statement about the kinetics of absorption/desorption encompassing all samples is difficult. However, for those

samples that were not affected by a blocked filter, a discussion of the factors that affected kinetics can be made.

Firstly, ball milling has the effect of reducing the grain size of titanium, magnesium and nickel. This increases the hydrogen absorption kinetics by increasing the surface area and decreasing the diffusion path of hydrogen. Secondly, ball milling introduces numerous defects, lattice strain and grain boundaries that can act as hydrogen dissociation sites. The presence of magnesium oxide is also likely to improve the kinetics of the Ti-Mg-Ni alloys in two ways. During ball milling, magnesium acts as a reducing agent for the other metals. Consequently, titanium and nickel remain oxide free. Any intermetallics that subsequently form during heating are also likely to be oxide free. This is particularly advantageous given that titanium, nickel, Ti_2Ni and Mg_2Ni have vastly superior hydrogen absorption kinetics compared to magnesium. The formation of magnesium oxide during ball milling also has a direct benefit on the hydrogen sorption kinetics. Ball milling of magnesium hydride with magnesium oxide has been shown to result in magnesium hydride with rapid absorption and desorption kinetics[274]. This improvement can be attributed to either the highly defected nature of ball milled magnesium oxide[65], or the partial oxidation state of magnesium[238], or both. Defected magnesium oxide and partially reduced magnesium act as hydrogen adsorption, dissociation and transport sites

The activation process used for the samples also contributes to an improvement in the hydrogen absorption kinetics. Figure 5-19 shows an SEM image of sample $Ti_{62}Mg_{117}Ni_{20}$ that has been activated and cycled through a number of hydrogen absorption and desorption cycles.

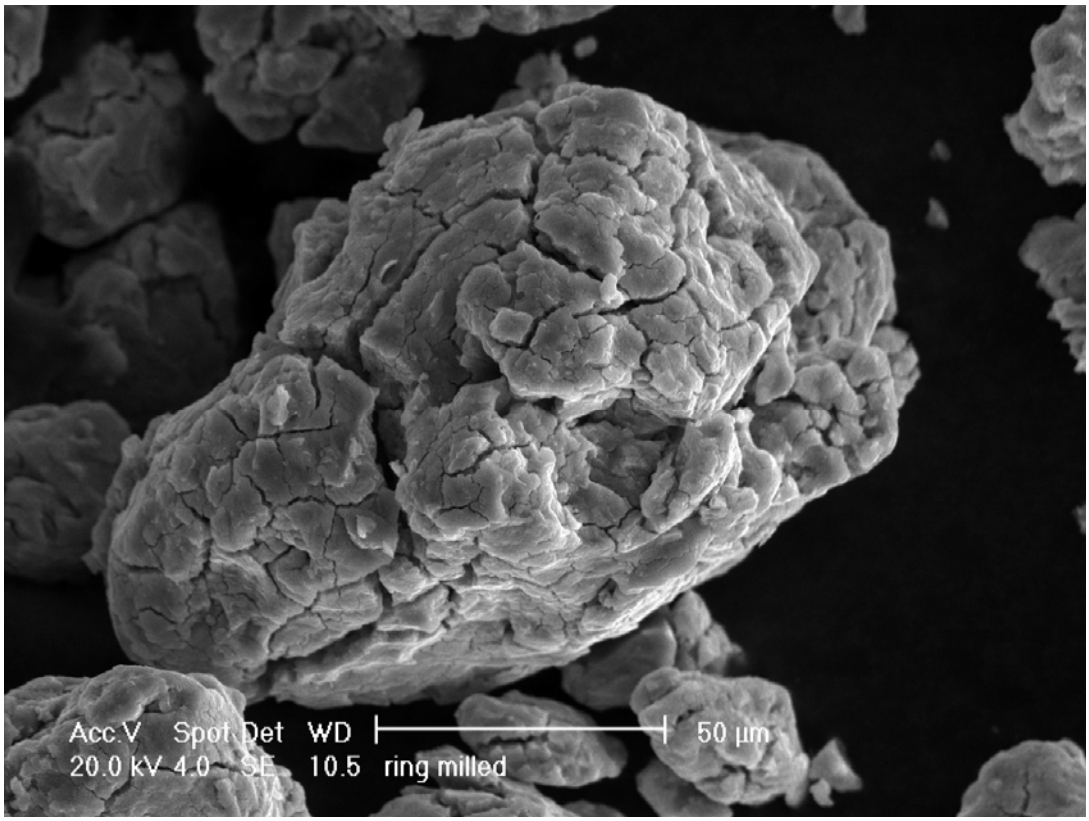

Figure 5-19: Scanning electron microscopy image of $Ti_{62}Mg_{117}Ni_{20}$ ring milled sample after several hydriding/dehydriding cycles.

The grains are characterised by extensive cracking, which enhances the kinetics by further reducing hydrogen diffusion paths and exposing fresh metallic surfaces to hydrogen.

In summation, four main factors are present that are responsible for the extraordinarily fast hydrogen absorption characteristics of these samples. The first is that the ball milling process reduces particle size and hydrogen diffusion paths as well as introducing numerous crystal defects that act as hydrogen dissociation and transport sites. The second is the oxygen impurity which results in preferential magnesium oxidation. This magnesium oxide is either heavily defected or contains partial oxidation states, which promotes hydrogen adsorption, dissociation and transport. Thirdly, the preferential oxidation of magnesium results in clean metal surfaces of nickel and/or the intermetallics Ti_2Ni and Mg_2Ni which all have superior dissociation rates of hydrogen compared to pure magnesium. Lastly, the activation process and absorption/desorption cycling results in extensive grain cracking which

works to further reduce hydrogen diffusion paths as well as exposing fresh metallic surfaces for interaction with hydrogen.

5.5.5. Comparison to Literature

Due to the divergent techniques used by Lomness et al.[201] and Hong et al.[265] a direct comparison of the hydrogen absorption properties of their Ti-Mg-Ni samples with the samples produced for this thesis is difficult. Characteristics such as kinetics and phase formation can not be compared as Lomness et al. did not report either, whereas Hong et al. only reported on phases that formed after the ball milling process. Despite this, the total hydrogen uptake for a given sample is directly comparable.

The hydrogen uptake of 11 wt.% reported for a composition of titanium, magnesium and nickel ball milled in the molar ratio of 53:47:20 with a ball to powder ratio of 70:1 for 37 hours could not be reproduced in this thesis. No combination of binary hydride formation (i.e. TiH_2, MgH_2, NiH) or ternary hydride formation (i.e. $Ti_2NiH_{3.5}$, Mg_2NiH_4) can account for the 11 wt.% reported by Lomness et al[201]. Hydrogen absorption at dislocation sites generated via the ball milling process can not account for it either[278]. Examination of the composition-temperature figures in Lomness et al.[201] reveals an anomaly. Two of the three figures reveal hydrogen absorption that continues to increase up to a temperature of 600 K before plateauing and then decreasing as the temperature continues to rise. The composition-temperature figure for the sample reported to absorb 11 wt.% shows a linear increase of hydrogen content with temperature until ~550 K. Beyond this the rate of absorption slows but continues in a linear fashion and is still increasing when the absorption run is halted at a temperature of ~725 K. The shape of this absorption curve, and its difference to the preceding two absorption curves, strongly suggests a hydrogen leak in the absorption apparatus used by Lomness et al.[201] for this sample.

For the Ti-Mg-Ni sample prepared in the molar ratio of 53:47:20 for this thesis, 2.5 wt.% hydrogen uptake was measured at room temperature. This hydrogen uptake is consistent with samples reported by Lomness et al. that were milled with different BTP ratios and milling times (1.6 - 3.5 wt.%). A significant difference to the results

reported by Lomness and those reported here is in the temperature at which hydrogen absorption takes place. Lomness et al. showed that the onset of hydrogen absorption was dependent on the BTP ratio used and the milling time. The highest BTP ratio used (70:1) and the shortest milling time used (37 hours) showed the lowest hydrogen absorption onset temperature (365 K). However, following activation of the $Ti_{53}Mg_{47}Ni_{20}$ sample produced in this thesis, hydrogen absorption occurred at room temperature 296 K. The most likely explanation for this discrepancy lies in the different activation processes used.

Of the samples produced for this thesis, the sample $Ti_{20}Mg_{200}Ni_{20}$ has stoichiometry most similar to $Ti_{22}Mg_{198}Ni_{20}$ produced by Hong et al. Maximum hydrogen absorption for Hong et al's. sample was ~5.5 wt.% at 573 K, compared to 5.0 wt.% for the $Ti_{20}Mg_{200}Ni_{20}$ sample. The discrepancy can be accounted for by the fact that XRD of the hydrided $Ti_{20}Mg_{200}Ni_{20}$ sample reveals unreacted Mg.

5.6. Conclusions

Hydrogen absorption of 11 wt.% for a sample of $Ti_{53}Mg_{47}Ni_{20}$ as reported by Lomness et al.[201] can not be accounted for by any known mechanism and as such could not be reproduced here. However, room temperature uptake of 2.5 wt.% was measured. Samples with the composition of $Ti_{62}Mg_{117}Ni_{20}$, $Ti_{65}Mg_{133}Ni_{20}$ and $Ti_{20}Mg_{200}Ni_{20}$ were measured to absorb between 3.7 and 5.0 wt.%. The formation of TiH_2 in these samples meant that temperatures greater than 673 K are required to make these systems fully reversible.

The high temperatures required for activation of the samples and the high temperatures used to decompose TiH_2 resulted in vaporisation and deposition of magnesium on the filter above the sample. This magnesium deposition did not absorb hydrogen in the temperature range studied but the difference in hydrogen uptake measured for Ti-Mg-Ni samples in this thesis and that of Lomness et al.[201] can not be accounted for by this.

Measurements of the hydrogen absorption kinetics of these samples were also hindered by deposition of magnesium on the filter above the sample. This deposition resulted in a partial blockage of the hydrogen flow in some measurements. However, in those cases where the hydrogen flow was not impeded, absorption kinetics were measured to be extremely rapid. Greater than 95 % of total hydrogen uptake occurred within 60 seconds, even for samples measured at room temperature.

The fast kinetics are due to a number of factors including: ball milling which reduces particle size and introduces defect sites; preferential oxidation of magnesium during ball milling which results in catalytically active magnesium oxide; preferential oxidation of magnesium also yields clean intermetallic sites that show superior kinetics as compared to pure magnesium; the activation process that results in extensive crack formation in particles that further reduce hydrogen diffusion lengths as well as exposing free surfaces for hydrogen absorption.

5.7. Directions for Future Work

Despite the very fast hydrogen absorption kinetics displayed by some ball milled samples of titanium, magnesium and nickel, further work for this system presents limited prospects. The presence of the relatively heavy elements in titanium and nickel limit the amount of hydrogen these samples can absorb. Ball milling of magnesium hydride with oxides presents comparable improvements in absorption kinetics with negligible impact on hydrogen content without the added difficulty of requiring activation. Hence, ball milling of magnesium hydride presents several advantages over the approached used here. However, ball milling has no effect on the thermodynamics. Theoretical calculations[279,280] suggest that reducing the crystallite size of magnesium to 1 nm or less will reduce enthalpy of hydride formation. However, ball milling of magnesium hydride can only reduce the crystallite size to 7.6 nm[274]. In addition, the crystallite size of this magnesium hydride grows to 78 nm during the first desorption performed at 573 K (300^{o}C). Aguey-Zinsou et al.[274] note that conventional ball milling techniques are unable to reach the crystallite sizes required to modify thermodynamics of magnesium hydride and that new synthesis methods must be found. Consequently, two techniques have been identified by the

author as having potential for producing magnesium hydride with crystallite sizes smaller than conventional ball milling, and preliminary investigations are underway.

6. References

[1] J. Pettersson and O. Hjortsberg, edited by Volvo Technical Division (KFB-Meddelande, Stockholm, 1999), Vol. 27, pp. 33.

[2] L. Schlapbach, Züttel. A.,, *Nature* **414**, 23 (2001).

[3] A. Züttel, *Materials Today* **6**, 24 (2003).

[4] U. S. Department of Energy, Targets for On-Board Hydrogen Storage Systems: Current R&D Focus is on 2010 Targets, Available at www1.eere.energy.gov/hydrogenandfuelcells/storage/pdfs/targets_onboard_hydro_storage.pdf.

[5] S. M. Aceves, G. D. Berry, G. D. Rambach, *International Journal of Hydrogen Energy* **23** (7), 583 (1998).

[6] S. A. Sherif, N. Zeytinoglu, T. N. Veziroğlu, *International Journal of Hydrogen Energy* **22** (7), 683 (1997).

[7] J. Wolf, *Materials Research Society Bulletin* **27** (9), 684 (2002).

[8] T. E. Rufford, Z. H. Zhu, G. Q. Lu, *Developments in Chemical Engineering and Mineral Processing* **14** (1/2), 85 (2006).

[9] L. Zhou, *Renewable and Sustainable Energy Reviews* **9**, 395 (2005).

[10] J. Zhang, T. S. Fisher, P. V. Ramachandran, J. P. Gore, I. Mudawar, *Journal of Heat Transfer* **127**, 1391 (2005).

[11] E. MacA. Gray, *Advances in Applied Ceramics* **106** (1 - 2), 25 (2007).

[12] S. Hynek, W. Fuller, J. Bentley, *Carbon* **22** (6), 601 (1997).

[13] J. Ko, K. Newell, B. Geving, W. Dubno, FY 2005 Progress Report, 2005.

[14] P. Bénard, R. Chahine, *Langmuir* **17**, 1950 (2001).

[15] X. B. Zhao, B. Xiao, A. J. Fletcher, K. M. Thomas, *Journal of Physical Chemisty B* **109**, 8880 (2005).

[16] S. K. Bhatia, A. L. Myers, *Langmuir* **22**, 1688 (2006).

[17] P. N. Cheremisinoff, F. Ellerbusch, *Carbon Adsorption Handbook*. (Ann Arbor Science Publishers, Inc., Michigan, 1978).

[18] G. G. Stavropoulus, A. A. Zabaniotou, *Microporous and Mesoporous Materials* **82**, 79 (2005).

[19] A. J. Kidnay, M. J. Hiza, *Advances in Cryogenic Engineering* **12**, 730 (1967).

[20] R. K. Agarwal, J. S. Noh, J. A. Schwarz, P. Davini, *Carbon* **25** (2), 219 (1987).

[21] L. Zhou, Y. Zhou, Y. Sun, *International Journal of Hydrogen Energy* **29**, 319 (2004).

[22] P. Bénard, R. Chahine, *Scripta Materialia* **56**, 803 (2007).

[23] M. Rzepka, P. Lamp, M. A. de la Casa-Lillo, *Journal of Physical Chemisty B* **102** (10894 - 10898) (1999).

[24] H. Kabbour, T. F. Baumann, J. H. Satcher, A. Saulnier, C. C. Ahn, *Chemistry of Materials* **18** (26), 6085 (2006).

[25] J. A. Schwarz, United States of America Patent No. 4716736 (1988).

[26] A. C. Dillon, K. M. Jones, T. A. Bekkedahl, C. H. Kiang, D. S. Bethune, M. J. Heben, *Nature* **386**, 377 (1997).

[27] M. Becher, M. Haluska, M. Hirscher, A. Quintel, V. Skakalova, U. Dettlaff-Weglikovska, X. Chen, M. Hulman, Y. Choi, S. Roth, V. Meregalli, M. Parrinello, R. Ströbel, L. Jörissen, M. M. Kappes, J. Fink, A. Züttel, I. Stepanek, P. Bernier, *C. R. Physique* **4**, 1055 (2003).

[28] V. V. Simonyan, J. K. Johnson, *Journal of Alloys and Compounds* **330-332**, 659 (2002).
[29] D. Fraenkel, J. Shabtai, *Journal of the American Chemical Society* **99**, 7074 (1977).
[30] J. -H. Yoon, *Journal of Physical Chemistry* **97**, 6066 (1993).
[31] J. Weitkamp, M. Fritz, S. Ernst, *International Journal of Hydrogen Energy* **20** (12), 967 (1995).
[32] J. Weitkamp, S. Ernst, F. Cubero, F. Wester, W. Schnick, *Advanced Materials* **9**, 247 (1997).
[33] H. W. Langmi, A. Walton, M. M. Al-Mamouri, S. R. Johnson, D. Book, J. D. Speight, P. P. Edwards, I. Gameson, P. A. Anderson, I. R. Harris, *Journal of Alloys and Compounds* **356-357**, 710 (2003).
[34] H. W. Langmi, D. Book, A. Walton, S. R. Johnson, M . M. Al-Mamouri, J. D. Speight, P. P. Edwards, I. R. Harris, P. A. Anderson, *Journal of Alloys and Compounds* **404-406**, 637 (2005).
[35] A. Zecchina, S. Bordiga, J. G. Vitillo, G. Ricchiardi, C. Lamberti, G. Spoto, M. Bjørgen, K. P. Lillerud, *Journal of the American Chemical Society* **127**, 6361 (2005).
[36] Y. Li, R. Yang, *Journal of Physical Chemistry B* **110**, 17175 (2006).
[37] L. Regli, A. Zecchina, J. G. Vitillo, D. Cocina, G. Spoto, C. Lamberti, K. P. Lillerud, U. Olsbye, S. Bordiga, *Physical Chemistry and Chemical Physics* **7**, 3197 (2005).
[38] V. B. Kazansky, V. Y. Borovkov, A. Serich, H. G. Karge, *Microporous and Mesoporous Materials* **22**, 251 (1998).
[39] F. Stéphanie-Victoire, A. Goulay, E. Cohen de Lara, *Langmuir* **14**, 7255 (1998).
[40] C. Otero Areán, O. V. Manoilova, B. Bonelli, M. Rodríguez Delgado, G. Turnes Palomino, E. Garrone, *Chemical Physics Letters* **370**, 631 (2003).
[41] C. Otero Areán, M. Rodríguez Delgado, G. Turnes Palomino, M. Tomás Rubio, N. M. Tsyganenko, E. Garrone, *Microporous and Mesoporous Materials* **80**, 247 (2005).
[42] C. Otero Areán, G. Turnes Palomino, M. R. Llop Carayol, *Applied Surface Science* **253**, 5701 (2007).
[43] A. J. Lachawiec, G. Qi, R. T. Yang, *Langmuir* **21**, 11418 (2005).
[44] Y. Li, R. Yang, *Journal of the American Chemical Society* **128**, 726 (2006).
[45] H. Li, M. Eddaoudi, M. O'Keeffe, O. M. Yaghi, *Nature* **402**, 276 (1999).
[46] J. L. C. Rowsell, O. M. Yaghi, *Angewandte Chemie International Edition* **44**, 4670 (2005).
[47] J. L. C. Rowsell, A. R. Millward, K. S. Park, O. M. Yaghi, *Journal of the American Chemical Society* **126**, 5666 (2004).
[48] D. N. Dybstev, H. Chun, K. Kim, *Angewandte Chemie International Edition* **43**, 5033 (2004).
[49] B. Chen, N. W. Ockwig, A. R. Millward, D. S. Contreras, O. M. Yaghi, *Angewandte Chemie International Edition* **44**, 4745 (2005).
[50] V. K. Peterson, Y. Liu, C. M. Brown, C. J. Kepert, *Journal of the American Chemical Society Communications* **128**, 15578 (2006).
[51] P. M. Forster, J. Eckert, B. D. Heiken, L. B. Parise, J. W. Yoon, S. H. Jhung, J. -S. Chang, A. K. Cheetham *Journal of the American Chemical Society* **128**, 16846 (2006).

[52] A. G. Wong-Foy, A. J. Matzger, O. M. Yaghi, *Journal of the American Chemical Society Communications* **128**, 3494 (2006).
[53] S. Bordiga, J. G. Vitillo, G. Ricchiardi, L. Regli,D. Cocina, A. Zecchina, B. Arstad, M. Bjørgen, J. Hafizovic, K. P. Lillerud, *Journal of Physical Chemistry B* **109**, 18237 (2005);
[54] B. Panella, M. Hirscher, H. Pütter, U. Müller, *Advanced Functional Materials* **16**, 520 (2006).
[55] B. Kesanli, Y. Cui, M. R. Smith, E. W. Bittner, B. C. Bockrath, W. Lin, *Angewandte Chemie International Edition* **44**, 72 (2005).
[56] M. Dincă, A. Dailly, Y. Liu, C. M. Brown, D. A. Neumann, J. R. Long, *Journal of the American Chemical Society* **128**, 16876 (2006).
[57] N. L. Rosi, J . Eckert, M. Eddaoudi, D. T. Vodak, J. Kim, M. O'Keeffe, O. M. Yaghi, *Science* **300**, 1127 (2003).
[58] Q. Yang, C. Zhong, *Journal of Physical Chemistry B* **110**, 655 (2006).
[59] G. Férey, Latroche, M., Serre, C., Millange, F., Loiseau, T., Percheron-Guégan, A.,, *Chemical Communications*, 2976 (2003).
[60] E. Y. Lee, Suh, M. P.,, *Angewandte Chemie International Edition* **43**, 2798 (2004).
[61] X. Zhao, Xiao, B., Fletcher, A. J., Thomas, K. M., Bradshaw, D., Rosseinsky, M. J., , *Science* **306**, 1012 (2004).
[62] D. Kim, T. B. Lee, S. B. Choi, J. H. Yoon, J. Kim, S. H. Choi, *Chemical Physics Letters* **420**, 256 (2006).
[63] F. D. Manchester ed., *Phase diagrams of binary hydrogen alloys*. (ASM International, 2000).
[64] G. Sandrock, edited by Office of Naval Research (1997), pp. 159.
[65] L. Schlapbach, in *Hydrogen in Intermetallic Compounds II*, edited by Schlapbach. L. (Springer-Verlag, 1992), Vol. 67, pp. 15
[66] G. Sandrock, Hydride-Metal Related Databases (Sandia National Laboratories) http://hydpark.ca.sandia.gov/
[67] B. Bogdanović, M. Schwikardi, *Journal of Alloys and Compunds* **253 - 254**, 1 (1997).
[68] B. Sakintuna, F. L. Darkrim, M. Hirscher, *International Journal of Hydrogen Energy* **32**, 1121 (2007).
[69] J. Chen, N. Kuriyama, Q. Xu, H. Takeshita, T. Sakai, *Journal of Physical Chemistry B* **105**, 11214 (2001).
[70] L. Zaluski, A. Zaluski, J. O. Ström-Olsen, *Journal of Alloys and Compounds* **290**, 71 (1999).
[71] M. Fichtner, O. Fuhr, O. Kircher, *Journal of Alloys and Compunds* **356-357**, 418 (2003).
[72] C. M. Jensen, R. Zidan, N. Mariels, A. Hee, C. Hagen, *International Journal of Hydrogen Energy* **24**, 461 (1999).
[73] B. Bogdanović, R. A. Brand, A. Marjanović, M. Schwickardi, J. Tölle, *Journal of Alloys and Compounds* **302**, 36 (2000).
[74] M. Resan, M. D. Hampton, J. K. Lomness, D. K. Slattery, *International Journal of Hydrogen Energy* **30**, 1417 (2005).
[75] S. Orimo, Y. Nakamori, G. Kitahara, K. Miwa, N. Ohba, S. Towata, A. Züttel, *Journal of Alloys and Compounds* **404-406**, 427 (2005).
[76] S. C. Amendola, S. L.Sharp-Goldmann, M. S. Janjua, N. C. Spencer, M. T. Kelly, P. J. Petillo, M. Binder, *International Journal of Hydrogen Energy* **25**, 969 (2000).

[77] D. K. Ross, *Vacuum* **80**, 1084 (2006).
[78] R. Aiello, J. H. Sharp, M. A. Matthew, *International Journal of Hydrogen Energy* **24**, 1123 (1999).
[79] E. Fakioğlu, Y. Yürüm, Y. N. Veziroğlu, *International Journal of Hydrogen Energy* **29**, 1371 (2004).
[80] A. Züttel, A. Borgschulte, S. -I. Orimo., *Scripta Materialia* **56**, 823 (2007).
[81] N. Ohba, K. Miwa, M. Aoki, T. Noritake, D. -I. Towata, Y. Nakamori, S. -I. Orimo, A. Züttel, *Physical Review B* **74**, 075110 (2006).
[82] A. Züttel, S. Rentsch, P. Fishcer, P. Wenger, P. Sudan, P. Mauron, C. Emmenegger, *Journal of Alloys and Compounds* **356-357**, 515 (2003).
[83] S. -I. Orimo, Y. Nakamori, J. T. Eliseo, A. Züttel, C. M. Jensen, *Chemical Reviews* **XXX** (2007).
[84] K. Miwa, N. Ohba, S. -I. Towata, Y. Nakamori, A. Züttel, S. -I. Orimo, *Journal of Alloys and Compounds* **446 - 447**, 310 (2006).
[85] H. -W. Li, S. Orimo, Y. Nakamori, K. Miwa, N. Ohba, S. Towata, A. Züttel, *Journal of Alloys and Compounds* **XX**, *In press*. (2007).
[86] P. Chen, Z. Xiong, Z. Luo, J. Lin, K. L. Tan, *Science* **402**, 302 (2002).
[87] P. Chen, Z. Xiong, G. Wu, Y. Liu, J. Hu, W. Luo, *Scripta Materialia* **56**, 817 (2007).
[88] T. Ichikawa, S. Isobe, N. Hanada, H. Fujii, *Journal of Alloys and Compounds* **365**, 271 (2004); Y. H. Yu, E. Ruckenstein, *Industrial & Engineering Chemistry Research* **43**, 2464 (2004).
[89] Z. Xiong, G. Wu, J. Hu, P. Chen, *Advanced Materials* **16**, 1522 (2004); W. Luo, *Journal of Alloys and Compounds* **381**, 284 (2004).
[90] C. E. Buckley, Griffith University, 1993.
[91] E. Poirer, R. Chahine, A. Tessier, T. K. Bose, *Review of Scientific Instruments* **76**, 055101 (2005).
[92] R. T. Yang, *Carbon* **38**, 623 (2000).
[93] T. P. Blach, E. MacA. Gray, *Journal of Alloys and Compunds* **446-447**, 692 (2007).
[94] P. Chen, X. Wu, J. Lin, K. L. Tan, *Science* **285**, 91 (1999).
[95] F. E. Pinkerton, B. G. Wicke, C. H. Olk, G. G. Tibbetts, G. P. Meisner, M. S. Meyer, J. F. Herbst, *Journal of Physical Chemisty B* **104**, 9460 (2000).
[96] R. Checchetto, G. Trettel, A. Miotello, *Measurement Science and Technology* **15**, 127 (2004).
[97] Katmar Software. http://www.katmarsoftware.com/alcodens.htm, AlcoDens (2003).
[98] K. G. McLennan, E. M. Gray, *Measurements in Science and Technology* **15**, 211 (2004).
[99] H. Hemmes, A. Driessen, R. Griessen, *Journal of Physics C: Solid State Physics* **19**, 3571 (1986).
[100] N. B. Vargaftik, *Handbook of Physical Properties of Liquids and Gases: Pure Substances and Mixtures*, Second Edition ed. (Hemisphere Publishing Corporation, 1975).
[101] H. M. Roder, L. A. Weber, R. D. Goodwin, (National Bureau of Standards, 1965), Vol. Monograph 94.
[102] R. D. McCarty, L. A. Weber, edited by Cryogenics Division (National Bureau of Standards, 1972), pp. 169.
[103] E. W. Lemmon, M. O. McLinden, D. G. Friend, in *NIST Chemistry WebBook, NIST Standard Reference Database Number 69*, edited by Mallard. W. G.

Linstrom. P. J. (National Institute of Standards and Technology, Gaithersburg, 2005).
[104] Igor Pro (WaveMetrics, Inc., Lake Oswego, Oregon, USA, 1988 - 2002).
[105] C. Chambers, C. Park, T. K. Baker, N. M. Rodriguez, *Journal of Physical Chemistry B* **102** (22), 4253 (1998).
[106] L. Kirkup, *Experimental Methods: An Introduction to the Analysis and Presentation of Data*. (John Wiley & Sons, 1994).
[107] J. R. Taylor, *An Introduction to Error Analysis: The Study of Uncertainties in Physical Measurements*, 2nd ed. (University Science Books, Sausalito, 1997).
[108] D. Frenkel, in *Computational Soft Matter: From Synthetic Polymers to Proteins*, edited by Binder. K. Attig. N., Grubmüller. H., Kremer. K., (2004), Vol. 23, pp. 29.
[109] P. N. Aukett, N. Quirke, S. Riddiford, S. R. Tennison,, *Carbon* **30** (6), 913 (1992).
[110] J. D. Gale, A. L. Rohl, *Molecular Simulation* **29** (5), 291 (2003).
[111] M. Rzepka (e-mail).
[112] Q. Wang, K. J. Johnson, *Journal of Chemical Physics* **110**, 577 (1999).
[113] M. G. Nijkamp, J. E. M. J. Raaymakers, A. J. van Dillen, K. P. de Jong, *Applied Physics A: Materials Science & Processing* **72**, 619 (2001).
[114] L. A. M. M. Barbosa, G. M. Zhidomirov, R. A. van Santen, , *Catalysis Letters* **77**, 55 (2001).
[115] P. M. Forster, J. Eckert, J. Chang, S. Park, G. Férey, A. K. Cheetham, *Journal of the American Chemical Society* **125**, 1309 (2003).
[116] B. L. Mojet, J. Eckert, R. A. van Santen, A. Albinati, R. E. Lechner, *Journal of the American Chemical Society* **123**, 8147 (2001).
[117] V. V. Simonyan, P. Diep, J. K. Johnson, *Journal of Chemical Physics* **111**, 9778 (1999).
[118] M. Selvaraj, A. Pandurangan, K. S. Seshadri, P. K. Sinha, K. B. Lal, *Applied Catalysis A* **242**, 347 (2003).
[119] J. S. Beck, J. C. Vartulli, W. J. Roth, M. E. Leonwicz, C. T. Kresge, K. D. Scmitt, C. T-W. Chu, D. H. Olson, E. W. Sheppard, S. B. McCullen, J. B. Higgins, J. L. Schlenker, *Journal of the American Chemical Society* **114**, 10834 (1992).
[120] C. T. Kresge, M. E. Leonwicz, W. J. Roth, J. C. Vartulli, J. S. Beck, *Nature* **359**, 710 (1992).
[121] X. S. Zhao, G. Q. Lu, G. J. Millar, *Industrial & Engineering Chemistry Research* **35**, 2075 (1996).
[122] S. Bhattacharyya, G. Lelong, M. -L. Saboungi, *Journal of Experimental Nanoscience* **1** (3), 375 (2006).
[123] M. Myers, *Surfactant Science and Technology*, Second Edition ed. (VCH Publishers, New York, 1992).
[124] F. Reiss-Husson, V. Luzzati, *The Journal of Physical Chemistry* **68** (12), 3504 (1964).
[125] C. -Y. Chen, S. L. Burkett, H. -X. Li, M. E. Davis, *Microporous Materials* **2**, 27 (1993).
[126] J. C. Vartulli, K. D. Schmitt, C. T. Kresge, W. J. Roth, M. E. Leonwicz, S. B. McCullen, S. D. Hellring, J. S. Beck, J. L. Schlenker, D. H. Olson, E. W. Sheppard *Chemistry of Materials* **6**, 2317 (1994).
[127] P. I. Ravikovitch, D. Wei, W. T. Chueh, G. L. Haller, A. V. Neimark, *Journal of Physical Chemistry B* **101**, 3671 (1997).

[128] U. Oberhagemann, M. Jeschke, H. Papp, *Microporous and Mesoporous Materials* **33**, 165 (1999).
[129] S. -H. Liu, H. P. Wang, *International Journal of Hydrogen Energy* **27**, 859 (2002).
[130] P. B. Amama, S. Lim, D. Ciuparu, Y. Yang, L. Pfefferle, G. L. Haller, *Journal of Physical Chemistry B* **109**, 2645 (2005).
[131] J. M. Kim, J. H. Kwak, S. Jun, R. Ryoo, *Journal of Physical Chemistry* **99**, 16742 (1995).
[132] D. Ciuparu, Y. Chen, S. Lim, G. L. Haller, L. Pfefferle, *Journal of Physical Chemistry B* **108**, 503 (2004).
[133] Y. Yang, S. Lim, G. Du, Y. Chen, D. Ciuparu, G. L. Haller, *Journal of Physical Chemistry B* **109**, 13237 (2005).
[134] M. Urbán, D. Méhn, Z. Kónya, J. Zhu, I. Kiricsi, *Diamond and Related Materials* **13**, 1322 (2004).
[135] D. Ciuparu, R. F. Klie, Y. Zhu, L. Pfefferle, *Journal of Physical Chemistry B* **108**, 3967 (2004).
[136] M. Kruk, M. Jaroniec, A. Sayari, *Journal of Physical Chemistry B* **101**, 583 (1997).
[137] Y. M. Setoguchi, Y. Teraoka, I. Moriguchi, S. Kagawa, N. Tomonaga, A. Yasutake, J. Izumi, *Journal of Porous Materials* **4**, 129 (1997).
[138] B. Marler, U. Oberhagemann, S. Vortmann, H. Gies, *Microporous Materials* **6**, 375 (1996).
[139] A. C. Voegtlin, A. Matijasic, J. Patarin, C. Sauerland, Y. Grillet, L. Huve, *Microporous Materials* **10**, 137 (1997).
[140] J. He, X. Yang, D. G. Evans, X. Duan, *Materials Chemistry and Physics* **77**, 270 (2002).
[141] P. Selvam, S. K. Bhatia, C. G. Sonwane, *Industrial & Engineering Chemistry Research* **40**, 3237 (2001).
[142] P. T. Tanev, T. J. Pinnavaia, *Science* **267**, 865 (1995).
[143] Z. Zhang, J. Suo, X. Zhang, S. Li, *Applied Catalysis A* **179**, 11 (1999).
[144] S. Hitz, R. Prins, *Journal of Catalysis* **168**, 194 (1997).
[145] W. A. Gomes, L. A. M. Cardosa, A. R. E. Gonzaga, L. G. Aguiar, H. M. C. Andrade, *Materials Chemistry and Physics* **93**, 133 (2005).
[146] E. G. Kodenev, A. N. Shmakov, A. Y. Derevyankin, A. V. Nosov, V. N. Romannikov, *Russian Chemical Bulletin. International Edition* **49** (10), 1669 (2000).
[147] S. Kawi, M. W. Lai, *Chemical Communications*, 1407 (1998).
[148] K. J. Edler, J. W. White, *Chemistry of Materials* **9**, 1226 (1997).
[149] R. Ryoo, J. M. Kim, *Journal of the Chemical Society, Chemical Communications*, 711 (1995).
[150] J. He, X. Duan, C. Li, *Materials Chemistry and Physics* **71**, 221 (2001).
[151] J. Yu, J. -L. Shi, L. -Z. Wang, M. -L. Ruan, D. -S.Yan, *Ceramics International* **26**, 359 (2000).
[152] E. P. Barrett, L. G. Joyner, P. P. Halenda, *Journal of the American Chemical Society* **73**, 373 (1951).
[153] M. Kruk, M. Jaroniec, A. Sayari, *Langmuir* **13**, 6267 (1997).
[154] M. Jaroniec, L. A. Solovyov, *Chemical Communications*, 2242 (2006).
[155] M. Broyer, S. Valange, J. P. Bellat, O. Bertrand, G. Weber, Z. Gabelica, *Langmuir* **18**, 5083 (2002).

[156] T. Dabadie, A. Ayral, C. Guizard, L. Cot, P. Lacan, *Journal of Materials Chemistry* **6**, 1789 (1996).
[157] N. Floquet, J. P. Coulomb, S. Giorgio, Y. Grillet, P. L. Llewellyn, *Studies in Surface Science and Catalysis* **117**, 583 (1998).
[158] *Cationic Surfactants: Physical Chemistry*. (Marcel Dekker Inc., New York, 1991).
[159] T. Wärnheim, A. Jönsson, *Journal of Colloid and Interface Science* **125** (2), 627 (1988).
[160] D. Maciejewska, A. Khan, B. Lindman, *Progress in Colloid & Polymer Science* **73**, 174 (1987).
[161] R. Savidha, A. Pandurangan, *Applied Catalysis A* **262**, 1 (2004).
[162] Jaroniec. M. Kruk. M., Sayari. A.,, *Langmuir* **13**, 6267 (1997).
[163] S. Biz, M. G. White, *Microporous and Mesoporous Materials* **40**, 159 (2000).
[164] A. K. Cheetham, H. Fjellvåg, T. E. Gier, K. O. Kongshaug, K. P. Lillerud, G. D. Stucky, *Studies in Surface Science and Catalysis* **135**, 158 (2001).
[165] X. D. Bai, D. Zhong, G. Y. Zhang, X. C. Ma, S. Liu, E. G. Wang, *Applied Physics Letters* **79** (10), 1552 (2001).
[166] S. Y. Kim, H. S. Kum, S. Augustine, J. K. Kang, *Applied Physics Letters* **89** (25), 253119 (2006).
[167] S. -H. Jhi, Y. -K. Kwon, K. Bradley, J. -C. P. Gabriel, *Solid State Communications* **129**, 769 (2004).
[168] S. -H. Jhi, Y. -K. Kwon, *Physical Review B* **69** (24), 245407 (2004).
[169] J. Chen, S. -L. Li, Z. -L. Tao, Y. -T. Shen, C. -X. Cui, *Journal of the American Chemical Society* **125**, 5284 (2003).
[170] T. Kasuga, M. Hiramatsu, A. Hoson, T. Sekino, K. Niihara, *Langmuir* **14**, 3160 (1998).
[171] T. Kasuga, M. Hiramatsu, A. Hoson, T. Sekino, K. Niihara, *Advanced Materials* **11** (15), 1307 (1999).
[172] G. H. Du, Q. Chen, R. C. Che, Z. Y. Yuan, L. -M. Peng,, *Applied Physics Letters* **79** (22), 3702 (2001).
[173] Q Chen, G. H. Du, S. Zhang, L. -M. Peng, *Acta Crystallographica B* **58**, 587 (2002).
[174] X. Sun, Y. Li, *Chemistry - A European Journal* **9**, 2229 (2003).
[175] D. V. Bavykin, V. N. Parmon, A. A. Lapkin, F. C. Walsh, *Journal of Materials Chemistry* **14**, 3370 (2004).
[176] D. -S. Seo, J. -K. Lee, H. Kim, *Journal of Crystal Growth* **229**, 428 (2001).
[177] Z. -Y. Yuan, B. -L. Su, *Colloids and Surfaces A: Physicochemical and Engineering Aspects* **241**, 173 (2004).
[178] Q. Chen, W. Zhou, G. Du, L. -M. Peng, *Advanced Materials* **14** (17), 1208 (2002).
[179] D. V. Bavykin, B. A. Cressey, F. C. Walsh, *Australian Journal of Chemistry* **60**, 95 (2007).
[180] D. V. Bavykin, F. C. Walsh, *Journal of Physical Chemistry C* **111**, 14644 (2007).
[181] R. Ma, T. Sasaki, Y. Bando, *Chemical Communications*, 948 (2005).
[182] D. V. Bavykin, J. M. Friedrich, *Advanced Materials* **18**, 2807 (2006).
[183] R. Ma, Y. Bando, T. Sasaki, *Chemical Physics Letters* **380**, 577 (2003).
[184] A. Nakahira, W. Kato, M. Tamai, T. Isshiki, K. Nishio, *Journal of Materials Science* **39**, 4239 (2004).

[185] J. Yang, Z. Jin, X. Wang, W. Li, J. Zhang, S. Zhang, X. Gao, Z. Zhang, *Dalton Transactions* (20), 3898 (2003).
[186] A. Liu, M. Wei, I. Honma, H. Zhou, *Advanced Functional Materials* **16**, 371 (2006).
[187] T. Kasuga, *Thin Solid Films* **496**, 141 (2006); M. Yada, Y. Inoue, M. Uota, T. Torikai, T. Watari, I. Noda, T. Hotokebuchi, *Langmuir* **23**, 2815 (2007).
[188] L. Qian, F. Teng, Z. -S. Jin, Z. -J. Zhang, T. Zhang, Y. -B. Hou, S. -Y. Yang, X. -R. Xu, *Journal of Physical Chemistry B* **108**, 13928 (2004); L. Qian, Z. -S. Jin, S. -Y. Yang, Z. -L. Du, X. -R. Xu, *Chemistry of Materials* **17**, 5334 (2005); L. Qian, S. Y. Yang, Z. S. Jin, Z. J. Zhang, T. Zhang, F. Teng, X. -R. Xu, *Physics Letters A* **335**, 56 (2005).
[189] M. Wei, Y. Konishi, H. Zhou, H. Sugihara, H. Arakawa, *Journal of the Electrochemical Society* **153** (6), A1232 (2006).
[190] A. Thorne, A. Kruth, D. Tunstall, J. T. S. Irvine, W. Zhou, *Journal of Physical Chemistry B* **109**, 5439 (2005).
[191] J. Li, Z. Tang, Z. Zhang, *Electrochemical and Solid-State Letters* **8** (11), A570 (2005); H. Zhang, G. R. Li, L. P. An, T. Y. Yan, X. P. Gao, H. Y. Zhu, *Journal of Physical Chemistry C* **111**, 6143 (2007); J. Li, Z. Tang, Z. Zhang, *Electrochemistry Communications* **7**, 62 (2005); J. Li, Z. Tang, Z. Zhang, *Chemical Physics Letters* **418**, 506 (2006).
[192] X. G. Xu, X. Ding, Q. Chen, L. -M. Peng, *Physical Review B* **75**, 035432 (2007); Y. Wang, C. Feng, Z. Jin, J. Zhang, J. Yang, S. Zhang, *Journal of Molecular Catalysis A: Chemical* **260**, 1 (2006).
[193] D. V. Bavykin, A. A. Lapkin, P. K. Plucinski, J. M. Friedrich, F. C. Walsh, *Journal of Physical Chemistry B* **109**, 19422 (2005).
[194] S. H. Lim, J. Luo, Z. Zhong, W. Ji, J. Lin,, *Inorganic Chemistry* **44**, 4124 (2005).
[195] K. Watanabe, T. Kondow, M. Soma, T. Onishi, K. Tamaru, *Proceedings of the Royal Society, London A* **333**, 51 (1973).
[196] G. Garberoglio, R. Vallauri, *Journal of Molecular Liquids* **117**, 43 (2005).
[197] E. Morgado, M. A. S. de Abreu, O. R. C. Pravia, B. A. Marinkovic, P. M. Jardim, F. C. Rizzo, A. S. Araújo, *Solid State Sciences* **8**, 888 (2006).
[198] V. A. Cardoso, A. G. de Souza, P. P. C. Sartoratto, L. M. Nunes, *Colloids and Surfaces A: Physicochemical and Engineering Aspects* **248**, 145 (2004).
[199] S. Branauer, P. H. Emmett, E. Teller, *Journal of the American Chemical Society* **60**, 309 (1938).
[200] S. J. Gregg, K. S. W. Sing, *Adsorption, Surface Area and Porosity*. (Academic Press Inc. Ltd, London, 1967).
[201] J. K. Lomness, M. D. Hampton, L. A. Gianuzzi, *International Journal of Hydrogen Energy* **27**, 915 (2002).
[202] K. F. Kelton, P. C. Gibbons, *Materials Research Society Bulletin* (22), 69 (1997).
[203] P. Selvam, B. Viswanathan, C. S. Swamy, V. Srinivasan, *International Journal of Hydrogen Energy* **11** (3), 169 (1986).
[204] J. F. Stampfer, C. E. Holley, J. F. Suttle, *Journal of the American Chemical Society* **82**, 3504 (1960).
[205] F. D. Manchester, A. San-Martin, *H-Mg (Hydrogen-Magnesium)*. (ACM International, 2000).
[206] L. Belkbir, E. Joly, N. Gerard, *International Journal of Hydrogen Energy* **6** (3), 285 (1981).

[207] J. J. Reilly, R. H. Wiswall, *Inorganic Chemistry* **6**, 2220 (1967).
[208] J. J. Reilly, R. H. Wiswall, *Inorganic Chemistry* **7**, 2254 (1968).
[209] K. N. Semenko, V. N. Verbetsky, A. N. Sytnikov, *Russian Journal of Inorganic Chemistry* **25** (5), 509 (1984).
[210] V. N. Verbetsky, A. N. Sytnikov, K. N. Semenenko, *Russian Journal of Inorganic Chemistry* **29** (3), 622 (1984).
[211] B. Darriet, M. Pezat, A. Hbika, P. Hagenmuller, *International Journal of Hydrogen Energy* **5**, 173 (1980).
[212] N. Gérard, S. Ono, in *Hydrogen in Intermetallic Compounds II. Surface and Dynamic Properties, Applications*, edited by Schlapbach. L. (Springer Verlag, 1992), Vol. 67, pp. 164
[213] J. P. Darnaudery, D. Darriet, M. Pezat, *International Journal of Hydrogen Energy* **8**, 705 (1983).
[214] P. Selvam, B. Viswanathan, C. S. Swamy, V. Srinivasan, *International Journal of Hydrogen Energy* **13**, 87 (1988).
[215] H. Yang, H. Yuan, J. Ji, H. Sun, Z. Zhou, Y. Zhang, (2002).
[216] J. J. Reilly, R. H. Wiswall, Report No. Report BNL 21322, 1976.
[217] M. H. Mintz, Z. Gavra, G. Kimmel, Z. Hadari, *Journal of the Less-Common Metals* **74**, 263 (1980).
[218] A. Zaluska, L. Zaluska, J. O. Ström-Olsen, *Applied Physics A: Materials Science & Processing* **72**, 157 (2001).
[219] A. Andreasen, M. B. Sørensen, R. Burkarl, B. Møller, A. M. Molenbroek, A. S. Pederson, J. W. Andreasen, M. M. Nielsen, T. R. Jensen, *Journal of Alloys and Compounds* **404 - 406**, 323 (2005).
[220] J. J. Vajo, C. C. Ahn, R. C. Bowman, B. Fultz, *Journal of Physical Chemistry B* **108**, 13977 (2004).
[221] G. Liang, R. Schulz, *Journal of Materials Science* **39**, 1557 (2004).
[222] G. Liang, R. Schulz, *Journal of Materials Science* **38**, 1179 (2003).
[223] G. Liang, *Journal of Alloys and Compounds* **370**, 123 (2004).
[224] C. Suryanarayana, *Progress in Materials Science* **46**, 1 (2001).
[225] B. Tanguy, J. -L. Soubeyroux, M. Pezat, J. Portier, P. Hagenmuller, *Materials Research Bulletin* **11**, 1441 (1976).
[226] E. Ivanov, I. Konstanchuk, A. Stepanov, V. Boldyrev, *Journal of the Less-Common Metals* **131**, 25 (1987).
[227] H. Imamura, N. Sakasai, *Journal of Alloys and Compounds* **231**, 810 (1995).
[228] H. Imamura, N. Sakasai, Y. Kajii, *Journal of Alloys and Compounds* **232**, 218 (1996).
[229] H. Imamura, N. Sakasai, T. Fujinaga, *Journal of Alloys and Compounds* **253 - 254**, 34 (1997).
[230] J. Huot, G. Liang, S. Boily, A. Van Neste, R. Schulz, *Journal of Alloys and Compounds* **293-295**, 495 (1999).
[231] G. Liang, J. Huot, S. Boily, A. Van Neste, R. Schulz, *Journal of Alloys and Compounds* **292**, 247 (1999).
[232] K. S. Jung, E. Y. Lee, K. S. Lee, *Journal of Alloys and Compounds* **421**, 179 (2006).
[233] G. Barkhordarian, T. Klassen, R. Bormann, *Scripta Materialia* **49**, 213 (2003).
[234] G. Barkhordarian, T. Klassen, R. Bormann, *Journal of Alloys and Compounds* **364**, 242 (2004).
[235] V. V. Bhat, A. Rougier, L. Aymard, X. Darok, G. Nazri, J. M. Tarascon, *Journal of Power Sources* **159**, 107 (2006).

[236] Y. Kojima, Y. Kawai, T. Haga, *Journal of Alloys and Compounds* **424**, 294 (2006).
[237] C. Z. Wu, P. Wang, X. Yao, C. Liu, D. M. Chen, G. Q. Lu, H. M. Cheng, *Journal of Alloys and Compounds* **414**, 259 (2006).
[238] W. Oelerich, T. Klassen, R. Bormann, *Journal of Alloys and Compounds* **322**, L5 (2001).
[239] F. D. Manchester, A. San-Martin, in *Phase Diagrams of Binary Hydrogen Alloys*, edited by Manchester. F. D. (ASM International, 2000), Vol. 13, pp. 238
[240] J. J. Reilly, R. H. Wiswall, *Inorganic Chemistry* **13**, 218 (1974).
[241] Y. -S. Hsu, Chiou, S. -L., Perng, T. -P.,, *Journal of Alloys and Compounds* **313**, 263 (2000).
[242] H. J. Chuang, Huang, S. S., Ma, C. Y., Chan, S. L. I.,, *Journal of Alloys and Compounds* **285**, 284 (1999).
[243] J.-L. Bobet, B. Chevalier, B. Darriet, *Intermetallics* **8**, 359 (2000).
[244] S. N. Klyamkin, A. Yu. Kovriga, V. N., Verbetsky, *International Journal of Hydrogen Energy* **24**, 149 (1999).
[245] I. Jacob, V. Shargorodski, D. Davidov, D. Shaltiel, *Journal of the Less-Common Metals* **82**, 391 (1981).
[246] J. -R. Chen, C. -C. Chuang, K. Hong, presented at the HYDROGEN ENERGY PROGRESS X, Proc. 10th World Hydrogen Energy Conf, 1994 (unpublished).
[247] O. Bernauer, C. Halene, *Journal of the Less-Common Metals* **131**, 213 (1987).
[248] K. N. Semenko, V. N. Verbetskii, V. S. ZOntiv, M. I. Ioffe, S. V., Tsutsuran, *Russian Journal of Inorganic Chemistry* **27**, 766 (1982).
[249] K. Yamanaka, H. Saito, M. Someno, *Journal of the Chemical Society of Japan* **8**, 1267 (1975).
[250] L. N. Padurets, E. I. Sokolova, M. E. Kost, *Russian Journal of Inorganic Chemistry* **27**, 763 (1982).
[251] M. H. Mintz, Z. Hadari, M. P. Dariel, *Journal of the Less-Common Metals* **74**, 287 (1980).
[252] H. T. Takeshita, H. Tanaka, N. Kuriyama, T. Sakai, I. Uehara, M. Haruta, *Journal of Alloys and Compounds* **311**, 188 (2000).
[253] A. Efron, Y. Lifshitz, I. Lewkowicz, M. H. Mintz, *Journal of the Less-Common Metals* **153**, 23 (1989).
[254] A. J. Maeland, G. G. Libowitz, J. F. Lynch, *Journal of the Less-Common Metals* **104**, 361 (1984).
[255] M. L. Wayman, G. C. Weatherly, in *Phase Diagrams of Binary Hydrogen Alloys*, edited by Manchester. F. D. (ASM International, 2000), Vol. 13, pp. 147
[256] J. Huot, E. Akiba, T. Takada, *Journal of Alloys and Compounds* **231**, 815 (1995).
[257] M. Au, J. Wu, Q. Wang, *International Journal of Hydrogen Energy* **20** (2), 141 (1995).
[258] P. Tessier, E. Akiba, *Journal of Alloys and Compounds* **302**, 215 (2000).
[259] R. Vijay, R. Sundaresan, M. P. Maiya, S. Srinivasa Murthy, *International Journal of Hydrogen Energy* **30**, 501 (2005).
[260] O. Gutfleisch, S. Dal Toè, M. Herrich, A. Handstein, A. Pratt, *Journal of Alloys and Compounds* **404 - 406**, 413 (2005).

[261] S. Doppiu, P. Solsona, T. Spassov, G. Barkhordarian, M. Dornheim, T. Klassen, S. Surinach, M.D. Baró, *Journal of Alloys and Compounds* **404 - 406**, 27 (2005).
[262] R. A. Varin, T. Czujko, E. B. Wasmund, Z. S. Wronski, *Journal of Alloys and Compounds* **432**, 217 (2007).
[263] J. K. Lomness, M. D. Hampton, L. A. Gianuzzi, *Materials Research Society Symposia Proceedings* **753**, 541 (2003).
[264] A. M. Viano, R. M. Stroud, P. C. Gibbons, A. F. McDowell, M. S. Conradi, K. F. Kelton, *Physical Review B* **51** (17), 12026 (1995).
[265] T. -W. Hong, Y. -J. Kim, *Journal of Alloys and Compounds* **330-332**, 584 (2002).
[266] R. A. Dunlap, D. A. Small, G. R. MacKay, J. W. O'Brien, J. R. Dahn, Z. H. Cheng, *Canadian Journal of Physics* **78** (3), 211 (2000).
[267] D. A. Sheppard, C. F. Maitland, C. E. Buckley, *Journal of Alloys and Compounds* **404-406**, 405 (2005).
[268] M. D. Hampton, J. K. Lomness, *International Journal of Hydrogen Energy* **24**, 175 (1999).
[269] B. Luan, N. Cui, H. K. Liu, H. Zhao, S. X. Dou, *Journal of Power Sources* **52**, 295 (1994).
[270] M. M. Antonova, O. T. Khorpyakov, T. V. Khomko, *Soviet Powder Metallurgy and Metal Ceramics* **30** (4), 292 (1991).
[271] M. Y. Song, M. Pezat, B. Darriet, P. Hagenmuller, *Journal of Materials Science* **28** (8), 2958 (1985).
[272] B. Vigeholm, J. Kjøller, B. Larsen, *Journal of the Less-Common Metals* **74**, 341 (1980).
[273] P. Hjort, A. Krozer, B. Kasemo, *Journal of Alloys and Compounds* **237**, 74 (1996).
[274] K. -F. Aguey-Zinsou, J. R. Ares Fernandez, T. Klassen, R. Bormann, *Materials Research Bulletin* **41**, 1118 (2006).
[275] M. Winter, Thermal properties and temperatures of magnesium, Available at http://www.webelements.com/webelements/elements/text/Mg/heat.html.
[276] J. F. Smith, R. L. Smythe, *Acta Metallurgica* **7**, 261 (1959).
[277] W. P. Gilbreath, edited by Ames Research Center (National Aeronautics and Space Administration, 1965), pp. 11.
[278] D. A. Sheppard, Z. -T. Jiang, C. E. Buckley, *International Journal of Hydrogen Energy* **32** (13), 1928 (2007).
[279] R. W. P. Wagemans, J. H. van Lenthe, P. E. de Jongh, A. J. van Dillen, K. P. de Jong, *Journal of the American Chemical Society* **127**, 16675 (2005).
[280] S. Cheung, W. -Q. Deng, A. C. T. van Duin, W. A. Goddard, *Journal of Physical Chemistry A* **109**, 851 (2005).

7. Appendices

7.1. Appendix I – The Hemmes Equation of State of Hydrogen

The Hemmes equation of state is defined as:

$$\left(P+\frac{a(P)}{V_m^{\alpha(T)}}\right)\left(V_m-b(P)\right)=RT \qquad (7\text{-}1)$$

Where P = pressure (bar)

V_m = molar volume

R = universal gas constant

T = temperature in Kelvin

$a(P)$ is given by:

$$a(P)=e^{\left(a_1+a_2\ln\left(\frac{P}{P_o}\right)-e^{\left(a_3+a_4\ln\left(\frac{P}{P_o}\right)\right)}\right)} \text{ for } P > 1 \text{ bar} \qquad (7\text{-}2)$$

Where P_o = atmospheric pressure

a_1 = 19.599

a_2 = -0.8946

a_3 = -18.608

a_4 = 2.6013

$b(P)$ is given by:

$$b(P)=\begin{cases}\sum_{i=0}^{8} b_i \ln\left(\frac{P}{P_o}\right)^i ; P \geq 100bar \\ b(100); P < 100bar\end{cases} \qquad (7\text{-}3)$$

Where b_o = 20.285 (all these constants have units of $m^3.mol^{-1}$)

b_1 = -7.44171

b_2 = 7.318565

b_3 = -3.463717

b_4 = 0.87372903

b_5 = -0.12385414

b_6 = 9.8570583 x 10^{-3}

b_7 = -4.1153723 x 10^{-4}

b_8 = 7.02499 x 10^{-6}

$\alpha(T)$ is given by:

$$\alpha(T) = \begin{cases} \alpha_o + \alpha_1 T + \alpha_2 T^2; T < 300K \\ \alpha(300); T > 300K \end{cases} \quad (7\text{-}4)$$

Where α_o = 2.9315

α_1 = -1.531 x 10^{-3} [K^{-1}]

α_2 = 4.154 x 10^{-6} [K^{-2}]

7.2. Appendix II – GCMC Simulation Data of Bulk Hydrogen Gas

Filename	Gas	μ	T	P	Geo	A	h	Iter	kon.	<n>
T600_1	H2	-0.586	600	0.99	Slit	60	2000	1000000	✓	85.91
T600_2	H2	-0.466	600	3.95	Slit	60	250	1000000	✓	107.71
T600_3	H2	-0.430	600	20.10	Slit	60	100	1000000	✓	86.67
T600_4	H2	-0.383	600	49.66	Slit	60	50	1000000	✓	105.90
T600_5	H2	-0.347	600	98.08	Slit	60	25	1000000	✓	102.56
T600_6	H2	-0.305	600	214.81	Slit	40	25	1000000	✓	95.51
T600_7	H2	-0.272	600	333.34	Slit	40	15	1000000	✓	97.99

Filename	Gas	μ	T	P	Geo	A	h	Iter	kon.	<n>
T400_1	H2	-0.376	400	1.01	Slit	60	1500	1000000	✓	99.08
T400_2	H2	-0.297	400	9.99	Slit	60	200	1000000	✓	129.61
T400_3	H2	-0.273	400	19.91	Slit	60	100	1000000	✓	128.51
T400_4	H2	-0.241	400	48.59	Slit	60	30	1000000	✓	94.60
T400_5	H2	-0.217	400	97.75	Slit	40	40	1000000	✓	107.78
T400_6	H2	-0.192	400	195.22	Slit	40	20	1000000	✓	102.21
T400_7	H2	-0.166	400	396.47	Slit	40	10	1000000	✓	93.16

Filename	Gas	μ	T	P	Geo	A	h	Iter	kon.	<n>
T250_1	H2	-0.225	250	1.00	Slit	60	1000	1000000	✓	104.68
T250_2	H2	-0.175	250	10.19	Slit	60	100	1000000	✓	105.69
T250_3	H2	-0.160	250	20.33	Slit	60	50	1000000	✓	105.04
T250_4	H2	-0.140	250	50.58	Slit	40	40	1000000	✓	90.87
T250_5	H2	-0.125	250	98.02	Slit	40	20	1000000	✓	85.24
T250_6	H2	-0.109	250	196.11	Slit	40	10	1000000	✓	79.38
T250_7	H2	-0.092	250	412.31	Slit	40	10	1000000	✓	139.81

Filename	Gas	μ	T	P	Geo	A	h	Iter	kon.	<n>
T175_1	H2	-0.152	175	1.01	Slit	60	700	1000000	✓	105.17
T175_2	H2	-0.117	175	10.18	Slit	60	70	1000000	✓	105.62
T175_3	H2	-0.107	175	19.72	Slit	60	30	1000000	✓	87.29
T175_4	H2	-0.093	175	48.53	Slit	40	30	1000000	✓	93.78
T175_5	H2	-0.082	175	97.19	Slit	40	15	1000000	✓	90.40
T175_6	H2	-0.071	175	193.08	Slit	30	15	1000000	✓	81.58
T175_7	H2	-0.058	175	443.34	Slit	30	10	1000000	✓	105.79

Filename	Gas	μ	T	P	Geo	A	h	Iter	kon.	<n>
T150_1	H2	-0.128	150	1.04	Slit	60	500	1000000	✓	50.44
T150_2	H2	-0.099	150	9.71	Slit	60	50	1000000	✓	84.16
T150_3	H2	-0.090	150	19.24	Slit	60	30	1000000	✓	99.63
T150_4	H2	-0.077	150	51.53	Slit	40	30	1000000	✓	116.51
T150_5	H2	-0.068	150	99.42	Slit	30	30	1000000	✓	121.48
T150_6	H2	-0.058	150	205.79	Slit	30	10	1000000	✓	73.73
T150_7	H2	-0.048	150	455.36	Slit	30	10	1000000	✓	117.93

Figure 7-1: Raw GCMC simulation data of bulk hydrogen gas for temperatures ranging from 150 to 600 K obtained from Rzepka[111].

Filename	Gas	μ	T	P	Geo	A	h	Iter	kon.	<n>
T125_1	H2	-0.105	125	1.01	Slit	60	400	1000000	✓	84.03
T125_2	H2	-0.080	125	10.17	Slit	60	50	1000000	✓	106.08
T125_3	H2	-0.073	125	19.25	Slit	60	30	1000000	✓	120.36
T125_4	H2	-0.063	125	48.08	Slit	40	30	1000000	✓	132.27
T125_5	H2	-0.055	125	97.60	Slit	30	20	1000000	✓	96.49
T125_6	H2	-0.046	125	216.13	Slit	20	20	1000000	✓	79.45
T125_7	H2	-0.037 40	125	403.22	Slit	20	20	1000000	✓	110.34

Filename	Gas	μ	T	P	Geo	A	h	Iter	kon.	<n>
T100_1	H2	-0.082	100	1.01	Slit	60	400	1000000	✓	105.93
T100_2	H2	-0.062	100	10.36	Slit	60	50	1000000	✓	136.12
T100_3	H2	-0.056	100	20.43	Slit	60	20	1000000	✓	108.26
T100_4	H2	-0.048	100	50.86	Slit	40	20	1000000	✓	119.79
T100_5	H2	-0.042	100	95.37	Slit	30	20	1000000	✓	125.54
T100_6	H2	-0.035	100	228.70	Slit	30	10	1000000	✓	110.35
T100_7	H2	-0.031	100	441.20	Slit	20	15	1000000	✓	95.72

Filename	Gas	μ	T	P	Geo	A	h	Iter	kon.	<n>
T60_1	H2	-0.047	60	0.94	Slit	60	300	1000000	✓	122.81
T60_2	H2	-0.035	60	9.88	Slit	60	30	1000000	✓	136.35
T60_3	H2	-0.031	60	22.02	Slit	40	30	1000000	✓	145.84
T60_4	H2	-0.027	60	48.38	Slit	30	20	1000000	✓	133.40
T60_5	H2	-0.023	60	128.75	Slit	30	10	1000000	✓	126.47
T60_6	H2	-0.021	60	273.25	Slit	20	10	1000000	✓	69.70
T60_7	H2	-0.020	60	461.61	Slit	20	10	1000000	✓	77.07

Figure 7-2: Raw GCMC simulation data of bulk hydrogen gas for temperatures ranging from 60 to 125 K obtained from Rzepka[111].

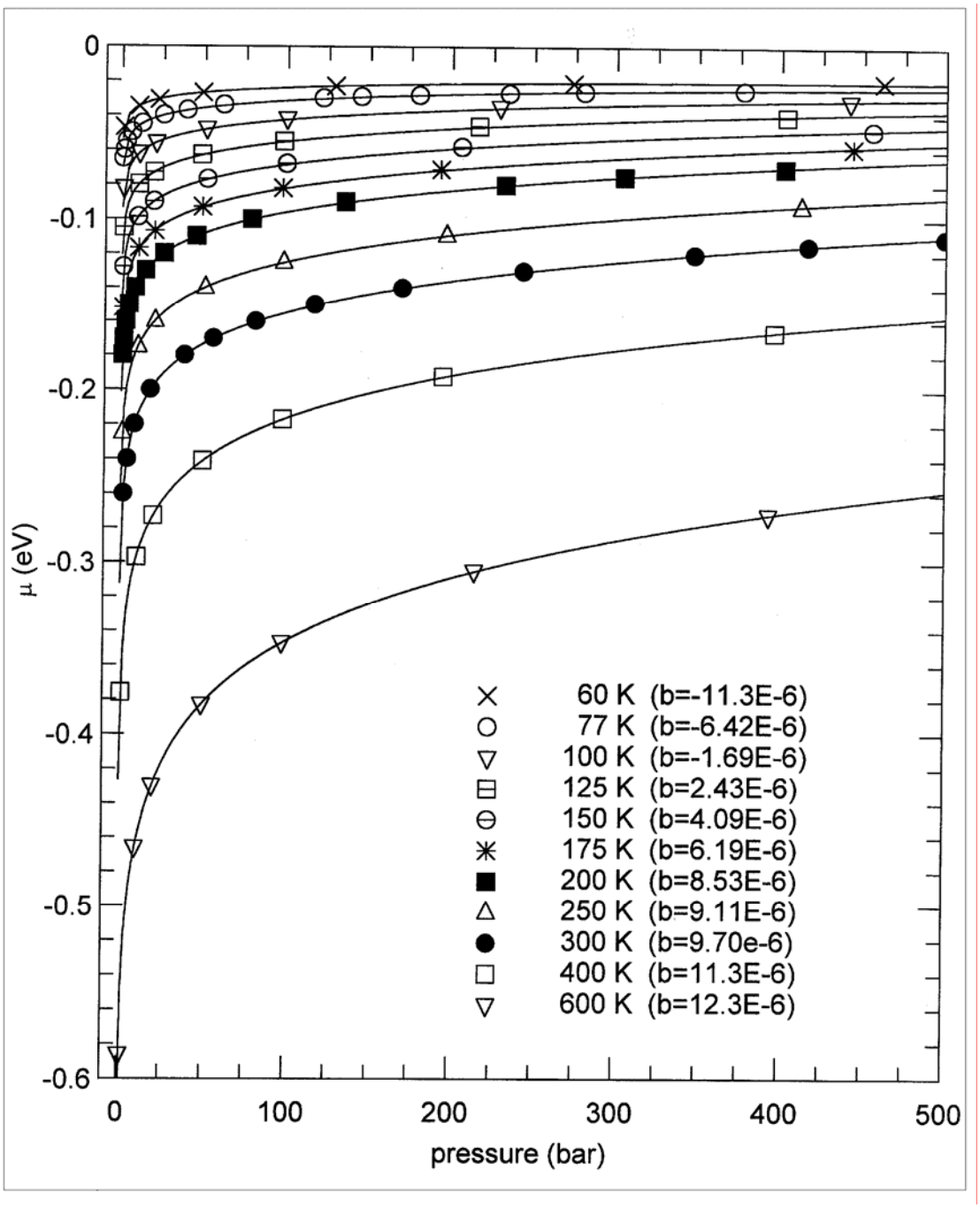

Figure 7-3: The chemical potential of bulk hydrogen gas as a function of pressure for GCMC simulations performed by Rzepka[111].

8. Peer Reviewed Publications

Chapter 8 Peer Reviewed Publications is unable to be reproduced here due to copyright restrictions.
The publications can instead be accessed via the following locations.

D.A. Sheppard, C.F. Maitland, C.E. Buckley. 2005. Preliminary results of hydrogen adsorption and SAXS modelling of mesoporous silica: MCM-41. Journal of Alloys and Compounds. 404–406: pp. 405–408. doi:10.1016/j.jallcom.2004.09.089.

D.A. Sheppard, Z.-T. Jiang, C.E. Buckley. 2007. Investigations of hydrogen uptake in ball-milled TiMgNi. International Journal of Hydrogen Energy. 32: pp. 1928 – 1932. doi:10.1016/j.ijhydene.2006.09.045.

D.A. Sheppard, C.E. Buckley. 2008. Hydrogen adsorption on porous silica. International Journal of Hydrogen Energy. 33: pp. 1688-1692. doi:10.1016/j.ijhydene.2007.12.021.